

INAUGURAL-DISSERTATION

zur

Erlangung der Doktorwürde

der

Naturwissenschaftlich-Mathematischen Gesamtfakultät

der

Ruprecht-Karls-Universität

Heidelberg

vorgelegt von

Diplom-Physiker Frank Peter Zimmermann

aus Göppingen

Tag der mündlichen Prüfung: 24. November 2006

**New approaches for optical and microoptical diagnostics
in IC engines**

**Neue Ansätze zur optischen und mikrooptischen Diagnostik
in Verbrennungsmotoren**

Gutachter:

Prof. Dr. Jürgen Wolfrum

Prof. Dr. Christof Schulz

Neue Ansätze zur optischen und mikrooptischen Diagnostik in Verbrennungsmotoren

Optische Diagnostik wird in vielen Forschungsbereichen seit Jahren erfolgreich für schnelle, berührungslose in-situ Messungen eingesetzt. Auch für die Motorenforschung sind optische Methoden heutzutage unentbehrlich. Die Schaffung der optischen Zugänge kostet jedoch Zeit und Geld. Oft werden durch makroskopische optische Zugänge auch physikalische Eigenschaften, wie Zylindergeometrie und Wärmeleitfähigkeit verändert. Zur serienreifen Weiterentwicklung von vielversprechenden Konzepten, wie Direkteinspritzung mit Schichtladung oder HCCI (homogeneous charge compression ignition), sind daher Messungen an minimal veränderten oder unmodifizierten Motoren unumgänglich. Im Rahmen eines Kooperationsprojektes mit dem Institut für Technische Optik (ITO) der Universität Stuttgart wurden hierzu mikro-invasive optische Systeme entworfen, konstruiert und getestet. So wurde ein faseroptischer Sensor entwickelt, der in einer voll funktionsfähigen Zündkerze integriert ist. Außerdem wurden ein hybrides UV Endoskop zur abbildenden Diagnostik und endoskopische Optiken zur Erzeugung von Laserlichtschnitten und Laserstrahlmustern realisiert. „Hybrid“ steht hierbei für die Kombination von refraktiven und diffraktiven optischen Elementen. Durch dieses spezielle hybride Design wird eine fast zehnmal größere Lichtstärke als mit einem vergleichbaren kommerziellen UV Endoskop erreicht. Gleichzeitig hat das hybride UV Endoskop ein besseres örtliches Auflösungsvermögen über einen definierten breiten Spektralbereich im UV. Die angewandten spektroskopischen Konzepte zur Messung von Treibstoffkonzentrationen, Mischungsverhältnissen und der Temperatur basieren auf UV-laser-induzierter Fluoreszenz (LIF). Durch die gezielte Laseranregung wird beim Zündkerzensensor mit dieser Diagnostikmethode ein definiertes Messvolumen ($\sim 2 \text{ mm}^3$) in unmittelbarer Nähe der Funkenstrecke erreicht. Mit dem Sensor wurden qualitative Treibstoff-LIF Messungen in einem handelsüblichen Vier-Zylinder-Motor durchgeführt. Für quantitative Messungen werden die Tracermoleküle Toluol und 3-Pentanon eingesetzt. Hierfür ist jedoch eine genaue Kenntnis der photophysikalischen Eigenschaften dieser Moleküle essentiell. Ein Beitrag zur besseren Charakterisierung der Toluol Fluoreszenz wurde auch im Rahmen dieser Arbeit geleistet: Anhand von hochaufgelösten Messungen der Fluoreszenzlebensdauer mit Hilfe von TCSPC (time-correlated single-photon counting) wurde ein bi-exponentielles Verhalten festgestellt und damit das bestehende photophysikalische Modell für Toluol bestätigt. Außerdem wurde eine charakteristische Abhängigkeit der zwei Lebensdauerkomponenten von Temperatur und Sauerstoffkonzentration gefunden. Diese Abhängigkeit kann zur Messung von Temperatur und Sauerstoffpartialdruck unabhängig von der lokalen Tracerkonzentration angewandt werden. Bereits vor Fertigstellung der mikrooptischen Systeme wurden Experimente in zwei optischen Ein-Zylinder-Motoren mit herkömmlichen Optiken und kommerziellen Mikrooptiken durchgeführt. Bei einem wand- und luftgeführten Verfahren wurde die Treibstoffverteilung und -ausbreitung anhand von 3-Pentanon-LIF und CN^* -Zündfunkenemission simultan gemessen. In einem spraygeführten Verfahren wurde die Wechselwirkung zwischen Treibstoffspray und Zündfunken untersucht und die Zündfunkenausdehnung beobachtet.

New approaches for optical and microoptical diagnostics in IC engines

The development of modern engine concepts like spray-guided spark-ignition direct injection (SG-SIDI) or homogeneous charge compression ignition (HCCI) requires fast, non-invasive in-situ diagnostics methods. Hence, laser-based optical diagnostics are essential for internal combustion (IC) engine research. Within this work, microoptical systems that enable the application of optical diagnostics methods on unmodified production-line engines or engines with micro-invasive optical access were designed, characterized and realized in a joint project collaborating with the Institut für Technische Optik (ITO) at the University of Stuttgart. These microoptical systems include a fiber-optic spark-plug sensor and an endoscopic UV imaging system. The used optical diagnostics are based on laser-induced fluorescence (LIF) of the fuel tracers toluene and 3-pentanone. The respective total fluorescence signal and its spectral distribution yield information about temperature, pressure and mixture composition (i.e. fuel/air-equivalence ratios). The fiber-optic spark plug is designed to perform LIF measurements in a defined small probe volume ($\sim 2 \text{ mm}^3$) close to the spark gap. Its ignition function is fully maintained. With the spark-plug sensor fuel LIF was measured in a commercial IC engine. The hybrid UV endoscope (combining refractive and diffractive optical elements) has an about ten times better light collection efficiency than a commercial UV endoscope with simultaneous high spatial resolution over a broadband spectral range. Its performance is demonstrated in various experiments. Microoptics for the generation of lightsheets and excitation beam patterns are also presented. For a quantitative application of tracer-LIF diagnostics a comprehensive knowledge of the photophysical properties of the used tracers is essential. As a contribution to this photophysical characterization, within this work, tracer-LIF lifetimes were measured via TCSPC (time-correlated single-photon counting) with unprecedented time resolution. The measured bi-exponential decay for toluene LIF could validate the prevailing model. Before the microoptical systems were finished, two experiments in optical single-cylinder engines were conducted with commercial lenses and a simple commercial fiber-optic spark plug. In an air-guided system the fuel distribution and its temporal evolution close to the spark gap were measured with 3-pentanone-LIF and CN^* spark-emission spectroscopy simultaneously. In a spray-guided SIDI engine the interaction between the fuel spray and the spark was measured and the spray induced stretching of the spark was observed.

CONTENTS

I	Introduction	1
II	Internal combustion engines	3
1	Spark-ignition direct-injection (SIDI) engines.....	5
1.1	Wall guided.....	5
1.2	Air guided	6
1.3	Spray guided.....	6
2	Homogeneous charge compression ignition (HCCI) engines	7
III	Spectroscopic background	9
1	Introduction to spectroscopic diagnostics	9
1.1	Laser spectroscopy	9
1.2	Spark emission spectroscopy.....	13
2	Photophysics of organic molecules	14
2.1	Toluene spectroscopy	14
2.2	3-Pentanone spectroscopy.....	18
3	Applications of tracer-LIF spectroscopy	20
3.1	Fuel concentration and equivalence ratio via tracer LIF	20
3.2	Toluene LIF thermometry	22
4	Equivalence ratio measurement via spark emission spectroscopy	25
4.1	CN* as an indicator for local fuel concentration.....	26
IV	Microoptical systems for diagnostics in cavities with limited optical access	27
1	Fiber-optic spark plug (FOSP).....	27
1.1	Quartz fibers for UV applications.....	28
1.2	Excitation.....	30
1.3	Detection.....	32
1.4	Development of a fiber-optic spark plug and prototypes	35
1.5	Fully functional fiber-optic spark-plug sensor.....	42
2	Hybrid UV endoscope.....	45

2.1	Specifications and requirements	45
2.2	Optical design and computer simulation.....	46
2.3	Realization	48
3	Endoscopic excitation optics.....	50
3.1	Homogeneous excitation.....	50
3.2	Inhomogeneous excitation	51
4	Outlook	52
V	Experiments in heated gas flows	53
1	General setup for experiments with a heatable flow nozzle	54
2	Demonstration experiments with fiber-optic spark plug	55
2.1	Experimental setup	55
2.2	Measurement of tracer concentrations	55
2.3	Measurement of equivalence ratios	56
2.4	Two-color toluene thermometry	58
2.5	Summary and outlook	59
3	Lifetime measurements via TCSPC with fiber-optic spark plug.....	61
3.1	Experimental setup for time-correlated single-photon counting	61
3.2	Fluorescence lifetimes of toluene LIF	62
3.3	Fluorescence lifetimes of 3-pentanone LIF	67
4	Demonstration experiments with hybrid UV endoscope.....	68
4.1	Comparison of hybrid UV endoscope to commercial UV lenses	68
4.2	Measurement of equivalence ratios	72
4.3	Flow-tagging using sensitized phosphorescence of biacetyl	76
VI	Measurements in IC engines	83
1	Fuel/air-equivalence ratio in an air-guided SIDI engine	83
1.1	Optical engine and experimental setup	83
1.2	Comparison: Tracer LIF – spark emission	86
1.3	Summary and conclusions	92
2	Spray–spark interaction in a spray-guided SIDI engine.....	94
2.1	Optical engine setup and measurement techniques.....	94
2.2	Spray fluctuations.....	96
2.3	Spray–spark interaction.....	97
2.4	Summary and conclusions	104
3	Fuel LIF measurement with fiber-optic spark plug in a commercial IC engine..	105
3.1	Experimental setup	105
3.2	Results	106

VII	Summary and conclusions	109
VIII	References	113
IX	Appendix	121
1	Filter transmission plots	121
2	Channel photomultiplier specifications.....	124
3	Guideline for using the fiber-optic spark plug	127
4	Guideline for using the hybrid UV endoscope	129
5	Automotive history	131
5.1	History of engines and cars	131
5.2	History of commercial spark-ignition direct-injection (SIDI) engines.....	136
X	Acknowledgements	139

I INTRODUCTION

Internal combustion (IC) engines began to change our lives well over a century ago. The first “Otto cycle” engine (patented in 1876 by Nicolaus August Otto) was built into a car by Gottlieb Daimler und Carl Benz in 1886. Two years later Bertha Benz (with her 14 and 15 year old sons Richard and Eugen) took the newly constructed automobile for a ride. Without her husband's knowledge, she drove from Mannheim to Pforzheim over a distance of 106 km. At this time, nobody could have imagined the full potential of the automobile. Actually, IC engine research has an even longer history: As early as 1509 and 1673, Leonardo da Vinci and Christiaan Huygens, respectively, had already described constant-pressure engines. Since then, various kinds of IC engines have been developed for a wide range of applications: They are used in cars, motorbikes, boats, in a variety of aircraft and locomotives, as electric generators and in industry. Over many years, a lot of effort was put into making IC engines powerful and durable. But with resources becoming scarce and the increasing awareness of pollution issues the main focus shifted towards the development of cleaner and more efficient engines.

Nowadays, scientists from all over the world are working on promising concepts such as modern spark-ignition direct-injection (SIDI) engines with highly stratified fuel distribution or engines with smaller cylinder volumes, but very high compression ratios, that are pushing the old Otto engine concept to its very limits. New engine concepts like controlled auto ignition (CAI), or homogeneous charge compression ignition (HCCI), for example, require the precise knowledge of in-cylinder temperature and gas composition. The main regulators for a defined start of combustion in an HCCI engine are temperature and residual gas fraction. For the development of these modern, more efficient engines with cleaner exhaust gas emissions, the old empirical development based on experience and “trial and error” reached its limits. New diagnostics methods had to be employed for a better understanding of in-cylinder processes. Fuel mixture composition is one of the key factors for efficient combustion. The variation of mixture composition is an important subject of many investigations [1,2]. In order to analyze the mixture composition in the region of the spark gap fast gas sampling valves have been integrated into spark plugs [3]. However, with methods like this it is not possible to measure single cycles, because of the small probe volume extracted from each individual engine cycle. Only phase-sampled mean values of the equivalence ratio can be delivered. Direct measurements along the spark gap like ion current sensing [4] are faster, but they are not accurate enough and can only be applied during ignition. For SIDI engines operated with stratified charge, though, especially the temporal evolution of the charge distribution before ignition is of great interest.

Required are fast, time-resolved, non-intrusive in-situ diagnostics methods, especially for the examination of the fuel/air mixing process, but also for the determination of local tempera-

tures or temperature fields, and the observation of the spray–spark interaction. Optical methods are most suitable for non-intrusive diagnostics and often allow the observation of processes in individual cycles with high temporal resolution [5,6]. Techniques using laser-induced fluorescence (LIF) [7], infrared absorption, flame luminosity and spectrally-resolved visible and ultraviolet emissions from the flame have been applied for in-cylinder measurements, e.g., the observation of fuel/air-mixing processes and flame propagation. Particularly, diagnostics methods based on LIF have been used to measure liquid fuel distribution [8], fuel concentration [9,10], oxygen distribution [11] and temperature [12], and they have been applied for the observation of flow fields [13]. During the last decade, huge progress has been made especially in the field of tracer-LIF diagnostics supported by the development of smaller and more efficient lasers (e.g., diode lasers and modern fiber and disk lasers [14]) and better sensors (especially high-resolution, high-speed, intensified CCD cameras).

However, many optical diagnostics techniques require major modifications in the engine geometry (i.e. large windows for optical access). These modifications are always time consuming and expensive, and in some cases even influence the physical properties (e.g., heat transfer, in-cylinder flow field, compression ratio) of the examined engine. This work presents three microoptical systems that minimize these modifications:

1. Fiber-optic spark-plug sensor for UV-LIF point measurements close to the ignition spark
2. Hybrid (refractive and diffractive) endoscopic UV-imaging optics
3. Hybrid excitation optics for the generation of lightsheets and illumination patterns

These systems are designed for UV-LIF diagnostics based on tracer-LIF spectroscopy using 3-pentanone and toluene. The fiber-optic spark plug is tested in various laboratory experiments under conditions relevant to an IC engine application. It is also applied in an engine experiment for the measurement of the variation in fuel distribution close to the spark gap. The hybrid UV endoscope and the excitation optics are used for the visualization of oxygen concentrations in a turbulent mixing gas flow. Additionally, a flow-tagging experiment is carried out using the microoptical laser excitation and the UV endoscope. In this experiment, sensitized phosphorescence of biacetyl is used to measure axial velocities in a laminar flow.

For quantitative tracer-LIF measurements, the used tracer must be well characterized. The systematic examination of the photophysical properties of toluene and 3-pentanone has been subject of extensive research in the last years [7,15–20]. Despite this, some questions regarding the prevailing photophysical models remain open. The measurements of 3-pentanone and toluene fluorescence lifetimes in this work make a valuable contribution to the solution of some of these questions. Respective oxygen partial pressure and temperature dependences of the tracer lifetimes are presented with unprecedented time resolution. The lifetimes were acquired with the fiber-optic sensor via time-correlated single-photon counting (TCSPC).

The growing knowledge of tracer photophysics makes spectroscopic techniques increasingly suitable for quantitative measurements in practical apparatus. Once these techniques are combined with micro-invasive optical systems that enable the application on previously inaccessible objects (e.g., production-line engines), another milestone for optical diagnostics in combustion research will be achieved.

II INTERNAL COMBUSTION ENGINES

The work on diagnostics techniques for the research on internal combustion (IC) engines requires an understanding of the fundamental methods of operation of modern IC engines. The engines investigated in this work are all based on the four-stroke engine concept as developed by Nikolaus August Otto from 1862–1866. The Diesel engine will therefore not be described here. Detailed information about the fundamentals of IC engines can be found in [21].

The idealized thermodynamic operation principle of an Otto engine can be described with the p - V diagram of the ideal constant-volume cycle shown in Figure II-1. Especially the combustion is strongly simplified by the heat quantity Q_{34} . Figure II-3 shows two p - V diagrams of realistic Otto cycles. The respective crankshaft, valve and piston positions are schematically illustrated in Figure II-2. The time scale during an engine cycle is commonly referred to as degrees crank angle before top dead center ($^{\circ}\text{CA BTDC}$, before the power stroke).

- 1→2 **Intake stroke**
- 2→3 **Compression stroke** (adiabatic compression)
- 3→4 **Ignition** shortly before top dead center (BTDC). Combustion starts around top dead center V_{TDC} and the sudden pressure increase can be approximated as an isochoric event.
- 4→5 **Power stroke (expansion)**. The combustion energy is transformed into kinetic energy of a flywheel and supports the next three strokes.
- 5→6 **Blow out**. The exhaust valves open and exhaust gases quickly expand into the exhaust pipe (isochoric). The heat Q_{56} is released.
- 6→7 **Exhaust stroke**. Remaining exhaust gas is pushed out by the piston (isobaric).

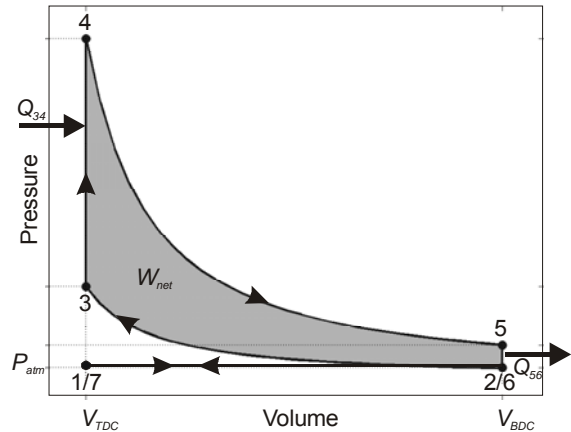


Figure II-1: p - V diagram of idealized Otto cycle. Combustion energy is approximated by the heat quantity Q_{34} . Gas exchange and losses from friction, heat conduction or throttling are not regarded.

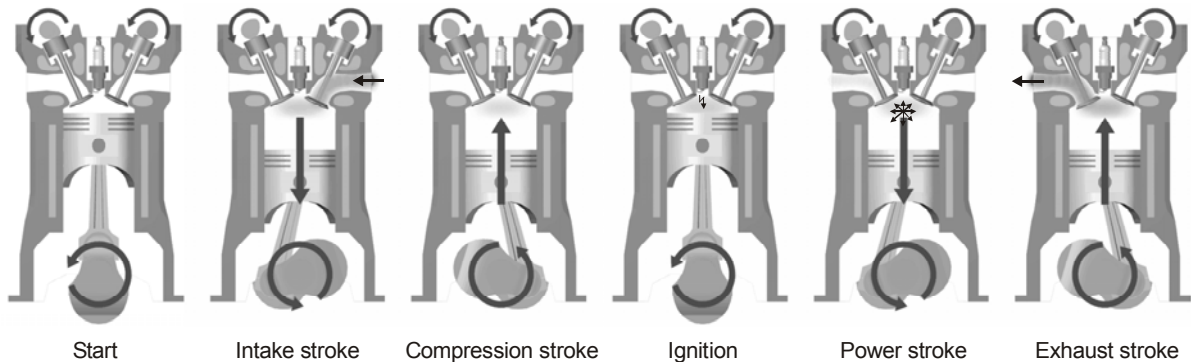


Figure II-2: Schematic of Otto engine cycle.

The efficiency of an Otto cycle is among the best for thermal engines. (Only the Diesel engine is slightly more efficient). Theoretically, it could be as high as 60%. In reality, with heat and friction losses, the efficiency of a regular car engine is between 20 – 30%. Thermodynamically, the efficiency of an Otto process η_{Otto} depends on the ratio between the maximum and minimum displacement volumes V_{BDC} and V_{TDC} , respectively (i.e. the compression ratio, cf. [22]):

$$\eta_{\text{Otto}} = 1 - \frac{1}{\left(\frac{V_{\text{BDC}}}{V_{\text{TDC}}}\right)^{\kappa-1}}; \quad \text{with } \kappa = \frac{c_p}{c_v} \quad (\text{II.1})$$

Whereas c_p and c_v are the heat capacities at constant pressure and constant volume. According to equation II.1, an optimization of the compression ratio is one way to increase engine efficiency. Thus, modern IC engines work with a very high compression ratio and resulting high peak pressures, mainly limited by the autoignition temperature of the used fuel. Sudden, uncontrolled autoignition of the endgas leads to engine knock. Therefore, the measurement of temperature (as it is the crucial control factor) is an important task for the development of engines that push the compression ratio to its limits.

A standard Otto engine works with a premixed homogeneous fuel/air distribution. The first Otto engines that could be operated with liquid fuel worked with a carburetor to vaporize the fuel and supply the gas to the intake air. Later, with the development of fuel injectors and fuel pumps, the fuel could be injected into the intake port, where the spray evaporated and mixed homogeneously with air. Within the last decade more and more engines are operated with gasoline direct injection (DI, also GDI) into the combustion chamber as described in the next section. In order to achieve an ignitable (stoichiometric) homogeneous fuel/air-equivalence ratio, in part load operation (with less fuel) the amount of air has to be reduced, too (i.e. the engine is throttled by a valve in the intake port). However, these so-called pumping losses obviously reduce the engine efficiency (cf. Figure II-3). Therefore, another way to optimize engine performance would be the unthrottled operation at all loads (i.e. over the whole engine operating map). The next section will introduce various engine concepts that employ an inhomogeneous (i.e. stratified) fuel distribution to realize this idea in modern spark ignition (SI) engines.

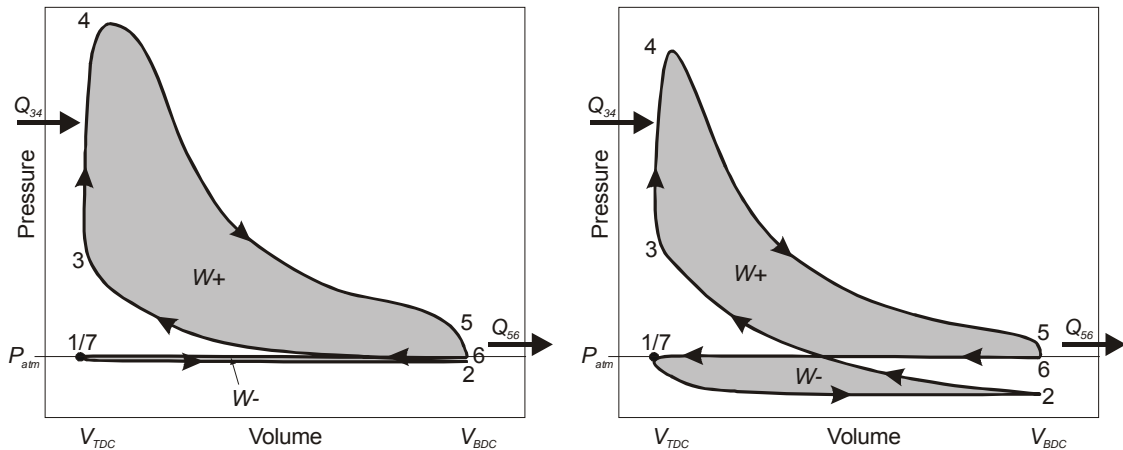


Figure II-3: Schematic of realistic Otto-cycle pV -diagrams: Left: Unthrottled, full load. Right: Throttled, part load. The throttle loss is marked as W^- .

1 Spark-ignition direct-injection (SIDI) engines

Modern spark-ignition direct-injection (SIDI) engines offer new possibilities for performance optimization. There is practically no difference in operation to a port-fuel injection engine, when the fuel is injected early during the intake stroke and hence, homogeneously premixed at the time of ignition. But with late injection during the compression stroke just before ignition, the desired fuel reduction is achieved by a stratified fuel distribution. This high stratification is necessary to ignite the overall lean mixture, which would be too lean for ignition under homogeneous conditions. Efforts to reduce pumping losses and thereby improve the part-load fuel economy of gasoline engines by unthrottled stratified-charge operation began nearly a century ago [23], but only within the last decade have advances in fuel injectors, engine controls and exhaust-catalyst technology permitted such SIDI engines to reach commercial production (see, e.g., [24,25] and references therein). Nowadays, most car manufacturers offer cars that are supplied with an engine for stratified operation at least in a certain part-load range (cf. appendix IX 5.2). These SIDI engines are very promising for a further reduction of fuel consumption and CO₂-emissions. However, because of the spatially inhomogeneous equivalence ratio, the ignition performance is very sensitive to mixture distribution and timing. In order to improve modern SIDI engine technology and extend the range of loads where stratified operation is possible, more research and development is necessary.

The major problem in the development of these SIDI engines is the cyclic variation of the combustion process, which leads to high raw emissions of soot and hydrocarbons and causes inhomogeneous temperature distributions that are responsible for increased formation of nitric oxide. These emissions can only be partially reduced using state-of-the-art exhaust after-treatment systems. Especially in stratified operation the fuel/air composition at the start of combustion is an important factor for the ignition and combustion process of the individual cycle. The equivalence ratio determines ignitability and flame speed. For lean and rich mixtures the flame speed is reduced compared to stoichiometric composition. Thus, the fuel/air mixing strongly affects cyclic variations of the combustion process.

In general, there are three different concepts for providing an ignitable fuel stratification at the right location and time, i.e. for directing the ignitable fuel cloud to the ignition spark at the time of ignition (cf. [26]). These concepts are basically characterized by the injector type, the arrangement of spark plug and injector and the geometry of the piston bowl.

1.1 Wall guided

The initial generation of wall-guided (WG) SIDI engines, in which the stratified charge is formed by directing the fuel spray obliquely towards a contoured piston surface, experienced disappointing fuel-economy gains (largely due to the limited speed-load range over which successful charge stratification could be achieved without high soot emissions), increased hydrocarbon emissions relative to a comparable-output premixed-charge engine (primarily due to inadequate fuel confinement and lean-fringe flame quenching), and soot emissions (dominated by pool fires supported by the film of liquid fuel remaining on the piston).



Figure II-4: Wall-guided fuel injection (figure from [27])

1.2 Air guided

In air- or tumble-guided systems the flow of the inlet air stream supports the fuel delivery to the spark plug. Often this tumble flow is generated by a special geometry of the inlet port or an additional regulation valve. Similar to the wall-guided concept, the piston geometry can support the tumble flow. In most cases a combination of wall- and air-guided fuel transportation is applied. Chapter VI 1 describes an experiment in an optical single-cylinder engine with tumble-guided fuel stratification. Here, the local fuel concentration in close proximity of the spark gap was measured by means of two different optical diagnostics techniques. The measurements were accomplished in cooperation with the Institut für Kolbenmaschinen (IfKM) in Karlsruhe, Germany (cf. [28]).

1.3 Spray guided

The state-of-the-art technique for controlled fuel stratification is the spray-guided (SG) approach, taking advantage of new high-pressure electronic injectors that generate a well defined fuel spray. The SG-SIDI concept, now under vigorous development worldwide, increases the speed-load range of stratified-charge operation by virtue of the close-coupled mixture preparation and ignition, while the more compact fuel cloud and reduced fuel-spray interaction with the piston reduce hydrocarbon emissions and pool-fire-generated soot. However, the close spacing of the injector and spark electrodes can also lead to high gas-phase and liquid-phase velocities, large numbers of liquid droplets, and steep, rapidly-varying gradients in velocity and fuel/air ratio, all of which can be unfavorable to robust ignition and flame-kernel growth. Occasional random misfires are typically encountered, especially as the charge is diluted to reduce the flame temperature and hence NO production.

Combined experiments and numerical simulations to examine fuel sprays, mixture preparation and combustion in an SG-SIDI engine have been performed [29,30]. These studies found that, over a substantial range of injection and spark-timing conditions, multi-cycle ensemble averages of key experimental quantities – specifically, spray structure, fuel concentration near the spark gap, combustion (both the initial partially premixed flame propagation and the later mixing-limited combustion of rich products) and the overall heat-release rate – were adequately captured by computational fluid dynamics (CFD) calculations employing $k-\varepsilon$ turbulence and two-stage combustion sub-models. Although such CFD codes predict the intensity of velocity fluctuations (via the turbulence kinetic energy), they typically do not *directly* calculate fluctuations in fuel concentration, which are important to cyclic variation in engine performance through their influence on ignition and combustion stability. The cyclic variations in fuel concentration can be very large in SG-SIDI engines [31].

Another important aspect in SG-SIDI engines is the interaction of the fuel spray with the spark-plug electrodes and the ignition spark itself. Models that calculate this interaction are currently being improved, but they do not yet suffice to predict the effects of spray-spark interaction on engine performance. Experiments for the measurement of the spray-spark interaction that were performed during a collaboration (i.e. an internship) with General Motors (GM) in Detroit, USA, are the topic of chapter VI 2 and are published in [31].



Figure II-5: Spray-guided fuel injection (figure from [27])

2 Homogeneous charge compression ignition (HCCI) engines

An Engine for the Future: This is how homogeneous charge compression ignition (HCCI) engines are sometimes referred to. In fact HCCI engines have a long history and were popular before electronic spark ignition was used, but they were never commercially used as car engines. By combining features from both spark-ignition (SI) and Diesel engines, the HCCI engine is promising the high efficiency of a Diesel engine with very low NO_x or particle emissions. In the HCCI engine, fuel is homogeneously premixed with air, as in an SI engine, but with a lean fuel/air ratio. At the end of the compression cycle the fuel autoignites from compression heating as in a Diesel engine. In an SI engine the autoignition of the endgas is what causes knock. It enhances undesired heat transfer within the cylinder, causes pressure peaks and may eventually burn or damage the piston. In an HCCI engine, with its lean fuel/air ratio, the autoignition does not damage the engine because the presence of excess air keeps the maximum temperature of the burned gases relatively low. Thus, autoignition becomes the desired mode of operation. The ignition occurs at several places at a time which makes the fuel/air mixture burn nearly simultaneously (cf. Figure II-6, right). But the timing of this autoignited combustion is critical. It must occur almost exactly at top dead center. Aggravating circumstances are that the HCCI engine gives up two timing control mechanisms: The start of ignition is not directly controlled by an external event such as the injection in a Diesel engine or the ignition spark in the SI engine. And the heat release rate is neither controlled by the rate and duration of the fuel-injection process, as in the Diesel engine, nor is it controlled by the turbulent flame propagation time, as in the SI engine. Hence, there is no direct initiator of combustion. This makes the process inherently challenging to control. And this is the reason, why it was not able to commercially use an HCCI engine in a car, yet. In order to achieve dynamic operation in an HCCI engine, the control system must change the conditions that induce combustion. Thus, either the compression ratio, inducted gas temperature, inducted gas pressure, or quantity of retained or reinducted exhaust must be controlled. Alternative control mechanisms and possible ways to expand the HCCI power range include the use of different additives to the fuel for an optimization of its flashpoint and autoignition temperature or even the use of different blends of fuel.

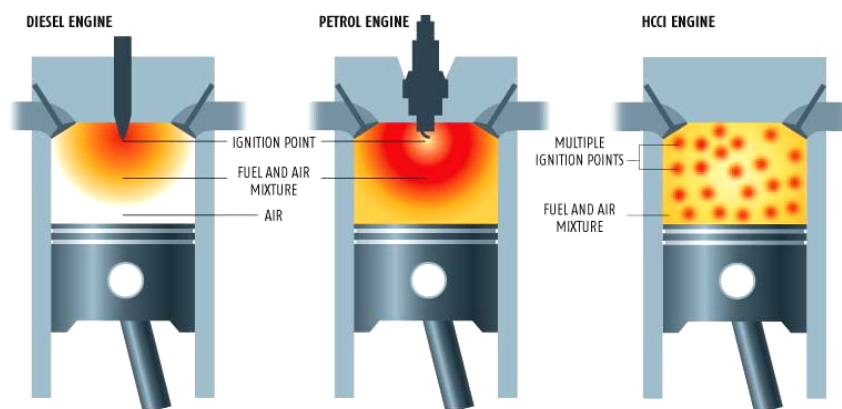


Figure II-6: Different ways of ignition in Diesel, SI and HCCI engines. Only HCCI engines have multiple simultaneous ignition points throughout the chamber. With its additional lean burn this combustion keeps temperatures low and the formation of nitric oxides to a minimum. (Figure from [32])

In spite of its disadvantages like the difficulty of control or the inherent high peak pressures and high heat release rates, like its limited power range, high carbon monoxide and hydrocarbon pre-catalyst emissions, the HCCI engine has some very convincing advantages: Lean operation leads to higher efficiency than in spark-ignited gasoline engines. The HCCI is closer to the ideal Otto cycle than spark-ignited combustion. Since HCCI it is not throttled, pumping losses are eliminated, too. And finally, homogeneous mixing of fuel and air leads to cleaner combustion and lower emissions. In fact, due to significantly lower peak temperatures than in typical SI engines, NO_x levels are almost negligible.

These advantages could indeed make the HCCI engine the “engine of the future”. Thus, worldwide intense research has been triggered. With a better physical understanding of the ignition process, HCCI can be controlled. However, for the next generation of commercial engines it is sufficient to operate the engine in HCCI mode over a certain load range. For the “engine of tomorrow” a hybrid solution will be developed, combining the benefits of each, homogeneously premixed charge spark ignition, stratified SG-SIDI and HCCI. The presented optical diagnostics techniques in this thesis and the new microoptical detection systems could be of considerable help for the development of these engines.

III SPECTROSCOPIC BACKGROUND

The measurement techniques applied in this thesis are all based on optical diagnostics with the focus on laser induced fluorescence (LIF) of fuel tracers. This chapter at first gives an overview over frequently used spectroscopic diagnostics methods for engine research, then the established photophysical properties of the used tracer molecules are discussed in more detail. Finally, the applications that were used for measurements within this work are described. These applications include toluene and 3-pentanone LIF for quantitative measurements of fuel/air-equivalence ratios and temperature. Additionally, CN* spark-emission spectroscopy is described, as it was used for the measurement of fuel concentrations at the spark gap.

1 Introduction to spectroscopic diagnostics

1.1 Laser spectroscopy

Diagnostics by means of chemiluminescence or spark emission spectroscopy does not require an external light source. However, it is restricted to investigations of the event that generates the observed signal (e.g., the luminescence from a burning flame or the radiative emissions from the ignition spark). Thus, especially the development of mixture formation in an IC engine can not be investigated with these methods. Techniques employing an external laser source for the study of absorption, scattering, or laser-induced fluorescence (LIF) are much more flexible and often enable quantitative measurements.

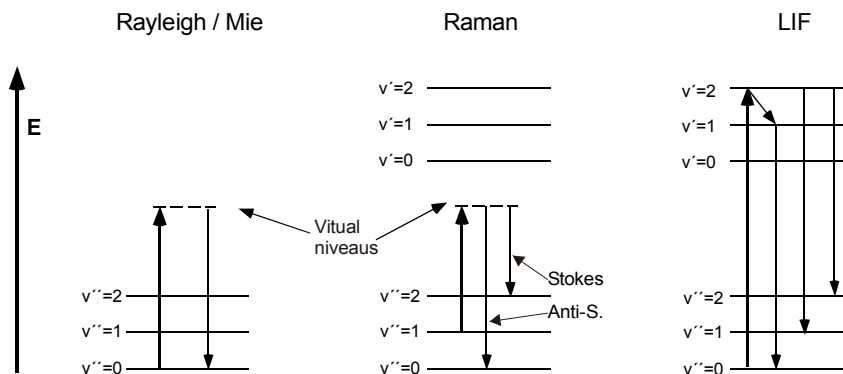


Figure III-1: Simplified diagram showing laser-induced radiative processes between electronic and vibrational states of a molecule.

The basic physical processes behind most laser-spectroscopic techniques can be explained with the simplified energy-level diagram in Figure III-1. It schematically shows different laser-induced radiative energy transfers between electronic and vibrational states in a molecule.

Spontaneous radiative emission or long lived radiative decays from an electronic triplet state (i.e. phosphorescence) are not shown. Non-radiative intramolecular processes like vibrational relaxation, intersystem crossing (ISC) between excited singlet and triplet states or internal conversion between different electronically excited states are not explained in the diagram, either. Neither does it show collisional intermolecular processes (e.g., cross-excitation or quenching). Detailed information about these processes can be found in literature (e.g., [33,34]). This section describes the basic radiative processes that are of importance for the used techniques in the experiments of this work. Other details of photophysical processes (as mentioned above) will be addressed in connection with the respective application.

1.1.1 Rayleigh scattering

Rayleigh scattering is the elastic scattering of light (i.e. photons) by particles much smaller than the wavelength of the light. It is most prominently seen in gases. Rayleigh scattering of sunlight by the atmosphere is the main reason for the observed blue color of the sky. The Rayleigh law states that the intensity of the scattered light, varies inversely with the fourth power of the wavelength. Thus the scattering cross-section is higher for ultraviolet (UV) light. In UV laser-induced fluorescence measurements Rayleigh-scattered excitation light is a source of interfering background signals and has to be suppressed by optical filters.

In contrast to Raman scattering (see 1.1.3) Rayleigh scattering is not species selective. Hence, the Rayleigh-scattering cross-section of a gas depends on the total particle density. With known pressure and the assumption of an ideal gas it is possible to use Rayleigh thermometry for a direct measurement of gas temperatures.

1.1.2 Mie scattering

Scattering from spherical particles larger than about a tenth of the illuminating wavelength (e.g., aerosols) is explained by the Mie theory. The wavelength of scattered photons remains unchanged. The cross-section is much larger than that of Rayleigh scattering. In IC engine research related experiments Mie scattering is predominantly used for the observation of flow fields with e.g., particle imaging velocimetry (PIV) or for spray diagnostics [35]. In combination with laser-induced fluorescence (see 1.1.5), Mie scattering is also used to investigate the drop-size distribution within a spray [36]. For this purpose a fluorescing tracer is added to the investigated spray. The Mie-scattered signal of the excitation laser and the fluorescence signal of the tracer are spectrally separable. The Mie/LIF dropsizing technique then uses the fact that the Mie signal is proportional to the droplet surface whereas the LIF signal is roughly a function of the droplet volume modulated by the tracer concentration.

1.1.3 Raman scattering

Raman scattering can occur with a change in vibrational, rotational or electronic energy of a molecule (see energy-level diagram in Figure III-1). Concerning the interaction of UV light between 200 – 300 nm with molecules, particularly the vibrational Raman effect is of importance. The Raman effect corresponds, in perturbation theory, to the absorption and subsequent emission of a photon via an intermediate electron state, having a virtual energy level. There are two possibilities for an energy exchange occurring between the incident photon and the

molecule: (i) The molecule absorbs energy, which is called Stokes scattering. The resulting photon of lower energy generates a Stokes line on the red side of the incident spectrum. (ii) The molecule loses energy: so called anti-Stokes scattering. Incident photons are shifted to the blue side of the spectrum, thus generating an anti-Stokes line. Obviously, this form of light scattering is species dependent and can thus be spectroscopically used. However, due to the low cross-section for Raman scattering a high excitation energy density is required for the generation of reasonable signal intensities.

1.1.4 Absorption

Apart from getting scattered, laser radiation can also selectively excite atoms or molecules. The total energy $E_{tot}(e, \nu, J)$ is thereby distributed on electronic $E_{el}(e)$, vibrational $E_{vib}(\nu)$ and rotational $E_{rot}(J)$ energy of the respective excited state [33]:

$$E_{tot}(e, \nu, J) = E_{el}(e) + E_{vib}(\nu) + E_{rot}(J) \quad (\text{III.1})$$

The quantum numbers e , ν and J represent different electronic, vibrational and rotational states of the excited molecule, whereas $e = \nu = J = 0$ denotes the ground state. In order to radiatively excite a molecule from an energetically low state $E_{tot}(e_1, \nu_1, J_1)$ to the energetically higher state $E_{tot}(e_2, \nu_2, J_2)$ a monochromatic laser beam with the frequency ν is required:

$$\nu = \frac{1}{h} [E_{tot}(e_2, \nu_2, J_2) - E_{tot}(e_1, \nu_1, J_1)] \quad (\text{III.2})$$

In this work, the ground state is referred to as S_0 . The first excited electronic singlet state (anti-parallel electron spin) is denoted S_1 , the next electronic singlet state S_2 and so on. Electronic triplet states (parallel electron spin) are denoted with a 'T'. Every molecule has a characteristic excitation spectrum that is pressure and temperature dependant. The form of this spectrum can be used to identify gaseous molecules (e.g., H_2 , O_2 , H_2O , CO_2) via infrared (IR) absorption spectroscopy. The near- and mid-infrared (approx. 800 nm – 20 μm) may be used to study the fundamental vibrations and associated rotational-vibrational structure [37]. Additionally, NIR (800 nm – 8 μm) absorption spectroscopy is frequently used to determine species concentrations [38].

Absorption of UV light excites higher electronic states of the investigated molecules. In chapters III 2.1.1 and III 2.2.1 the UV absorption spectra of toluene and 3-pentanone, are shown. Especially for larger molecules, with higher excitation energies vibrational states are getting denser. Thus, the absorption spectra of molecules in the UV (below 250 nm) are often continuous.

1.1.5 Fluorescence

After excitation to a higher electronic and vibrational state the molecule will lose its energy through different radiative and non-radiative channels. The most important decay process for many spectroscopic applications is the fast spontaneous emission of light: Fluorescence. Every molecule has a characteristic fluorescence spectrum. For larger molecules this spectrum is mostly broadband with little structure. Only for small or highly symmetric molecules discrete emission lines can be found. A spectroscopic species selection can be done via specific laser

excitation (i.e. laser-induced fluorescence, LIF) and by the choice of the spectral detection window. Similar to the absorption spectrum, the fluorescence signal from gaseous molecules is influenced by temperature, pressure and gas composition. Detailed investigations of the LIF signals of toluene and 3-pentanone are shown in chapters III 2.1 and III 2.2. Once characterized, the various distinguishable dependencies of these tracer-LIF signals can be used to measure temperature (cf. chapter III 3.2), pressure or gas composition (i.e. oxygen partial pressure, cf. chapter III 3.1).

The fluorescence intensity is influenced by many factors. An excited molecule will only transfer a certain amount of its energy into fluorescence light. Energy transferred via ISC, IC or collisional quenching by ambient molecules is lost for fluorescence. The ratio of the number of fluorescing molecules to the number of absorbed photons, i.e. excited molecules, is called the fluorescence quantum yield ϕ_{fl} of a molecule. Regarding the fact that laser excitation is an immediate process, the fluorescence quantum yield can be described as the ratio of fluorescence to all other de-excitation processes (see [39] for a detailed derivation of equation III.3):

$$\phi_{fl} = \frac{k_{rad}}{k_f + k_q n_q} \quad (\text{III.3})$$

Hereby, k_{rad} and k_f are the rate constants for fluorescence and all other non-fluorescing deactivation processes (except quenching), respectively. For molecules sensitive to de-excitation by collisions with other molecules, the rate constant for collisional quenching (k_q) multiplied by the number of quenching molecules (n_q) has to be added. Details can be found in [39]. The total intensity of the linear unsaturated fluorescence signal can then be described as the product of the intensity of the excitation laser I_ν , the number density of excited molecules n , the absorption cross-section σ_{abs} and the fluorescence quantum yield ϕ_{fl} :

$$S_{fl}(T, p, n_q, x, y) \sim I_\nu n(T, x, y) \sigma_{abs}(T, p) \phi_{fl}(T, p, n_q) \quad (\text{III.4})$$

1.2 Spark emission spectroscopy



Figure III-2: Electrical discharge spark between electrodes of fiber-optic spark plug (in air).

The advantage of spark emission spectroscopy is that it does not require an external excitation light source like the diagnostics methods mentioned in the last section. Especially in spark ignition (SI) engines the use of spark emission spectroscopy is obvious for measurements at the spark gap during ignition. However, no information about the mixture formation before ignition is gathered.

Figure III-2 shows a photo of a spark discharge in air between the electrodes of the fiber-optic spark plug presented in detail in this work. The bright white-blue illumination from the spark is clearly visible and can easily be detected with photomultipliers through adequate optical filters or with a spectrograph. (the additional red light reflections in the photo come from a HeNe-laser used to adjust the optics.)

In case of a standard spark plug the energy for the spark breakdown is supplied by high voltage ($\sim 7 - 20$ kV) between the electrodes. This high voltage is induced in the ignition coil. In the spark gap (~ 2 mm) a strong electric field builds up and eventually starts an electron avalanche and a plasma is generated. Paschen's Law states that the breakdown voltage is a non-linear function of electrode distance and gas pressure only. This relationship predicts the occurrence of a minimum breakdown voltage for a certain product of pressure times electrode distance. The phenomenon is well verified experimentally and is referred to as the Paschen minimum. More details about electrically-induced plasma can be read in [40] and [41].

Apart from electrically-induced breakdown there is also a lot of research done on the field of laser spark emission spectroscopy (LASS) [42], nowadays rather called laser-induced breakdown spectroscopy (LIBS). A similar approach is done with flame chemiluminescence, which is an important diagnostics method for combustion research as well [43]. The spectroscopic principle of all the above basically remains the same:

After ionization, radical formation and molecular recombination atoms and molecules emit light leaving their individual fingerprint, e.g. specific lines in the emission spectrum. A direct connection between signal intensity and species concentrations is complicated. But after calibration, the intensity of these lines and the shape of the spectrum yield information about species concentration and respective mixture compositions.

Spark emission spectroscopy is robust and relatively easy to apply. It has been used in numerous experiments [28,44,45]. Chapter III 4 will give a more detailed illustration, how specifically the emission from excited CN after recombination from the spark plasma can be used to measure fuel concentrations.

2 Photophysics of organic molecules

Most diagnostics applications discussed in this work are based on tracer-LIF techniques with the two organic molecules toluene and 3-pentanone, that are often used as fluorescence tracers in engine research. This chapter gives a comprehensive overview about the photophysics of these tracers, discussing their absorption and fluorescence characteristics and other important photophysical properties relevant for LIF diagnostics.

2.1 Toluene spectroscopy

The photophysical properties of the $S_0 \rightarrow S_1$ (π , π^*) transition in toluene vapor have been subject of interest since early in the last century [46,47]. The absorption around 248 nm or 266 nm is easily accessible with commercially available high-power UV lasers, and the excitation is followed by fluorescence with a high quantum yield [16,48]. These properties make the toluene molecule (along with similar aromatic molecules) attractive for diverse research fields ranging from the investigation of fundamental energy-transfer processes in larger molecules to practical applications that use toluene as a tracer for flow-field and mixing studies by laser-induced fluorescence (LIF) imaging.

Collision-induced vibrational energy transfer of toluene has been studied within the S_0 -state using UV absorption [49], IR emission [50], two-photon ionization [51], or a combined fluorescence/ionization technique [51], and within the S_1 -state by means of dispersed fluorescence spectra [52] as well as intramolecular vibrational redistribution (again by dispersed fluorescence) [53,54]. In the field of laser-based measurements in combustion systems, toluene is a promising tracer for visualizing gas-phase mixing processes. As a major component of commercial gasoline it is especially attractive to IC engine researchers [7]. More than a decade ago, Reboux et al. tried the approach of using the strong influence of molecular oxygen on the fluorescence intensity (collisional quenching) to directly access the fuel/air-mixing process [55]. Eight years later, Koban et al. showed that the fuel/air-equivalence ratio in precombustion mixing can be measured quantitatively via toluene and 3-pentanone fluorescence under certain conditions [11,15,16] (see also chapter III 3.1.2). The harsh engine environment, however, is prone to rapid variations in pressure and temperature, which triggered extensive research on the influence of temperature and oxygen partial pressure on absorption and fluorescence quantum yield of toluene [16,48], culminating in a semi-empirical model that enables the quantitative interpretation of toluene laser-induced fluorescence (LIF) at engine-relevant temperatures and pressures [15,56].

2.1.1 Absorption and emission

In [48] Koban et al. report in detail about light absorption and emission properties of toluene. Here, a brief overview will be given, only for a better understanding of the diverse LIF-diagnostics techniques in this work that use toluene as a tracer.

TEMPERATURE DEPENDENCE OF ABSORPTION CROSS-SECTION

Two excitation wavelengths are important for toluene LIF applications: 248 nm from an KrF*-excimer laser and 266 nm from the 4th harmonic of a Nd:YAG laser. At 248 nm the spectrum has no structure at room temperature and higher temperatures. At 266 nm the absorption spectrum shows distinguished lines at room temperature and only becomes continuous at higher temperatures (Figure III-3). At room temperature 266-nm excitation is in an absorption minimum. Thus, the absorption cross-section increases rapidly when this minimum disappears at higher temperatures (Figure III-4, right). For 248-nm excitation absorption can be regarded to be constant in the temperature range investigated in this work.

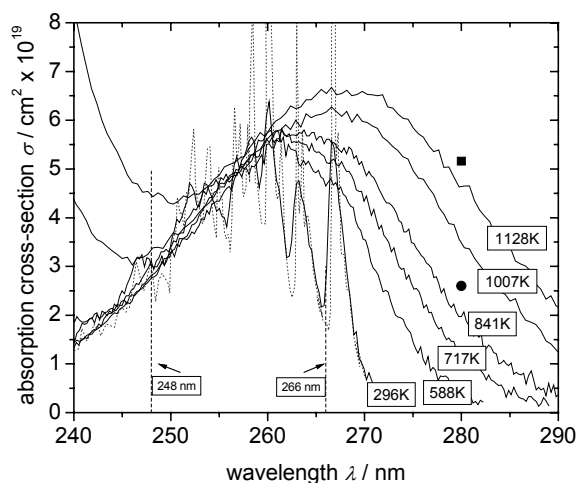


Figure III-3: Solid lines: Absorption spectra, [19] (shock tube measurements); dotted line: Room temperature spectrum from [57]; • 850 K, ▪ 1200 K from [49]; vertical lines illustrate the laser wavelengths used in this work. (Graph from [19])

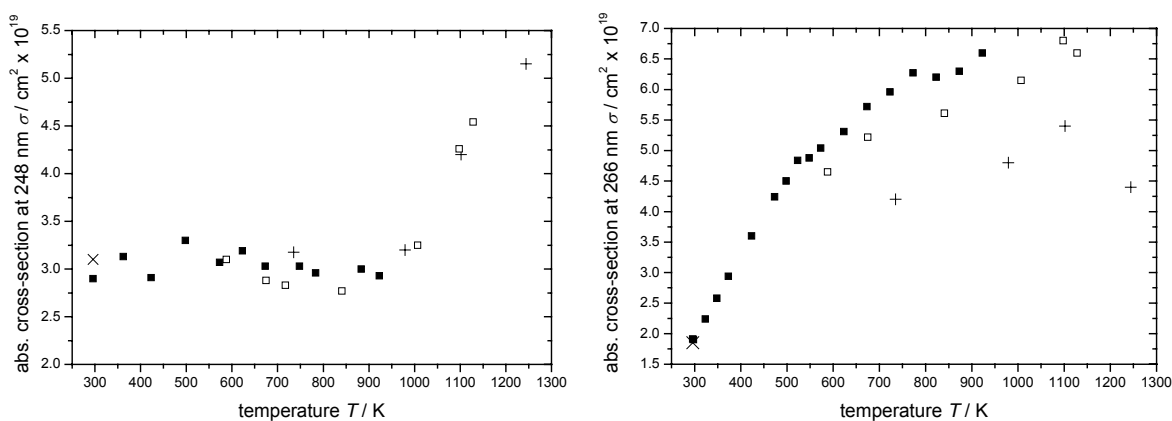


Figure III-4: Toluene absorption cross-section at 248 nm (left) and at 266 nm (right) as a function of temperature. ▪ and □ from [19]; + from [58]; × from [57]. (Graphs from [19])

TEMPERATURE DEPENDENCE OF FLUORESCENCE

All data shown here are for diluted toluene (g) in 1 bar nitrogen bath gas. Figure III-5 shows normalized fluorescence spectra of toluene after excitation at 248 nm. The room temperature spectra after 248- or 266-nm excitation have identical shape, whereas the redshift of the nor-

malized spectra is slightly stronger after 266-nm excitation. Note that the spectra shown in Figure III-5 are normalized for a better illustration of the redshift. Total intensities decrease rapidly with temperature.

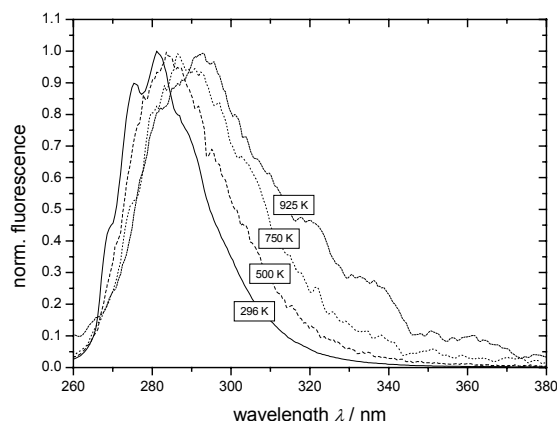


Figure III-5: Normalized fluorescence spectra; 5 mbar toluene in nitrogen at 1 bar total pressure, 248-nm excitation. (Graph from [19])

After excitation at 266 nm the fluorescence quantum yield decreases exponentially by three orders of magnitude within a 600 K temperature range. The dependence of the fluorescence yield on temperature for 248-nm excitation can be described by a double-exponential function. The initial decrease at 300 – 500 K is steeper than that found for 266-nm excitation, but signal decreases more slowly at higher temperatures. The total variation in fluorescence quantum yield after 248-nm excitation exceeds three orders of magnitude within the 600 K interval (cf. Figure III-10). More detailed information about the temperature dependence of the toluene fluorescence quantum yield on temperature can be found in [48].

2.1.2 Collisional quenching by oxygen

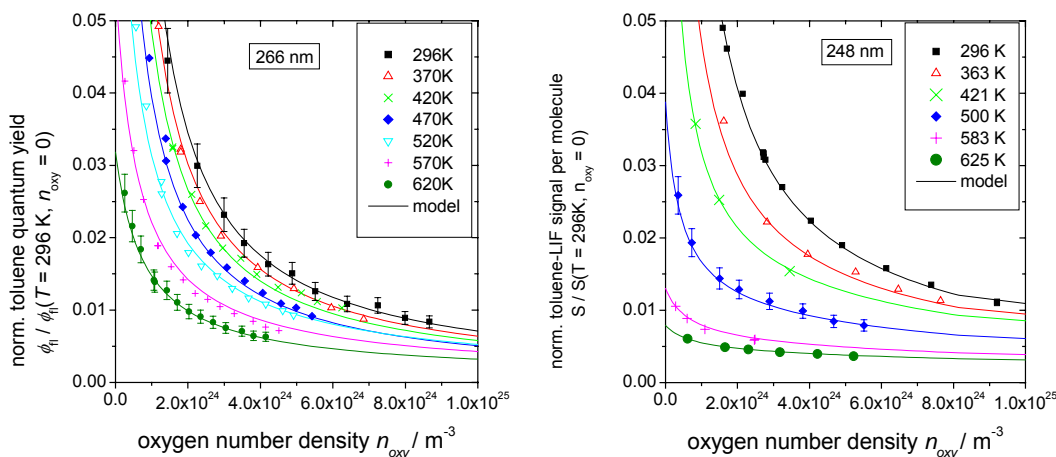


Figure III-6: Normalized (to $T = 296$ K and $n_{\text{oxy}} = 0$) toluene fluorescence quantum yield in dependence on the oxygen number density for different gas temperatures. The total signal intensity would be the product of quantum yield and absorption cross-section. (Graph from [15])

Quenching of the fluorescence from aromatic molecules by molecular oxygen is a well-known phenomenon (e.g., [59]). For toluene this behavior was first published by Burton and Noyes

[57] for 266.8-nm excitation at room-temperature. They found that the inverse fluorescence signal increases linearly with the oxygen number density (Stern-Volmer behavior). For 248 nm or at higher temperatures this linear behavior can not be observed anymore. Detailed information can be found in [15,19] and will be explained in short in the next paragraph. In spite of the complicated influences of combined temperature, pressure and oxygen partial pressure effects on the LIF of toluene, it can be used as a tracer for fuel/air-ratio measurements under well-defined boundary conditions (see chapter III 3.1.2). Figure III-6 shows the dependence of the toluene-LIF quantum yield on oxygen partial pressure for different temperatures. This dependence is used for FARLIF (fuel/air-ratio LIF) techniques.

2.1.3 Photophysical model

The photophysical model for toluene [15] can best be explained by the scheme shown in Figure III-7. The model is based on time-integrated measurements of total LIF-signal intensities. For the description of the temperature- and oxygen-partial-pressure-dependent LIF intensities it was necessary to hypothesize two different non-radiative decay channels with different lifetimes. Therefore, a bi-exponential fluorescence decay was expected, although LIF measurements with sufficient time resolution were not available at that time.

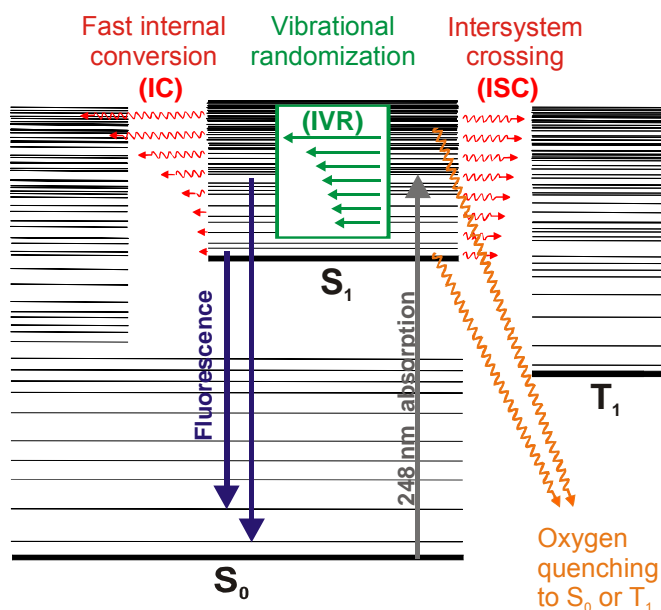


Figure III-7: Photophysical scheme of the important decay processes for toluene LIF. Intersystem crossing (ISC) and fluorescence are the dominant non-collisional processes for low vibrational excitation. Internal conversion (IC) becomes important for selected states at higher energies. ISC and IC states may be populated either directly via absorption or via intramolecular vibrational redistribution (IVR) following absorption. (Graph from [19])

The two important non-radiative internal de-excitation processes are intersystem crossing (ISC) to the spin-forbidden triplet state and the much faster internal conversion (IC) to high vibrational levels of the electronic ground state. With increasing vibrational energy both processes become more important, but IC becomes dominant. Additionally, internal vibrational relaxation (IVR) is preferably going to states that decay by IC.

The total fluorescence quantum yield $\phi_f(T, n_{O_2})$ is a combination of fluorescence from these two types of vibrational states within the electronically-excited state, distinguished by their Stern-Volmer factor $k_{SV,i}(T)$, to represent states with ISC (1) and with IC (2) occurring. The total signal can thus be written as:

$$S(T, n_{O_2}) \sim \sigma_{abs}(T) \phi_f(T, n_{O_2}) \sim \sigma_{abs}(T) \left(\frac{A_1(\lambda_{exc}, T)}{1 + k_{SV,1}(T)n_{O_2}} + \frac{A_2(\lambda_{exc}, T)}{1 + k_{SV,2}(T)n_{O_2}} \right) \quad (III.5)$$

In order to predict quantitative LIF signals, the model has to be fit to experimental data. Fit parameters are the temperature dependence of $k_{SV,i}(T)$ and the (temperature- and excitation-wavelength-dependent) relative contribution of each type of state (i.e. A_1 and A_2). A_i is the product of the relative population a_i and the fluorescence quantum yield $\phi_{f,i}^{N_2}$ of the respective state in pure nitrogen as bath gas. In the limit of zero quencher concentration, equation (III.5) must agree with the data in pure nitrogen. This is ensured by:

$$A_1(T) + A_2(T) = \phi_f^{N_2}(T) \quad (III.6)$$

The experimental part of this work (chapter V 3) will show new time-resolved LIF measurements that validate the model assumption. By measuring the temperature and oxygen-concentration dependence of the two fluorescence lifetime components of toluene more detailed information about the photophysics of toluene was acquired.

2.2 3-Pentanone spectroscopy

Ketones are the most frequently used class of fluorescent tracers for the measurement of fuel distributions. Their properties have been extensively studied [17,18,20,60-62] and they have been applied to various practical situations [8-10]. The following section will briefly introduce the important photophysical properties of 3-pentanone, which is being used as a fuel tracer in this work.

2.2.1 Absorption and emission

The absorption spectrum of 3-pentanone is the typical $n \rightarrow \pi^*$ transition for carbonyl compounds (ketones). The density of vibrational and rotational energy levels in the ground and excited electronic states is extremely high. Thus, the absorption feature appears broadband (and may be continuous at short wavelengths) at room temperature and atmospheric pressure. As a result, changes in pressure and composition have little effect on the absorption cross-section. As temperature increases, there is a known red shift in the shape of the spectrum [20].

Figure III-8 shows the absorption and fluorescence spectra of 3-pentanone compared to toluene. 3-Pentanone has a ten times weaker absorption cross-section in a much broader spectral region peaking at 280 nm. The fluorescence of pure 3-pentanone gas is more than 1000 times weaker than that of toluene. But the 3-pentanone fluorescence is not quenched by oxygen, which makes it a popular tracer for fuel concentration and enables fuel/air-ratio measurements in combination with toluene. Note that in gaseous mixtures with toluene there is a cer-

tain cross excitation from toluene that enhances the 3-pentanone-LIF signal. However, for applications in strongly diluted mixtures with low toluene concentration this effect can be neglected.

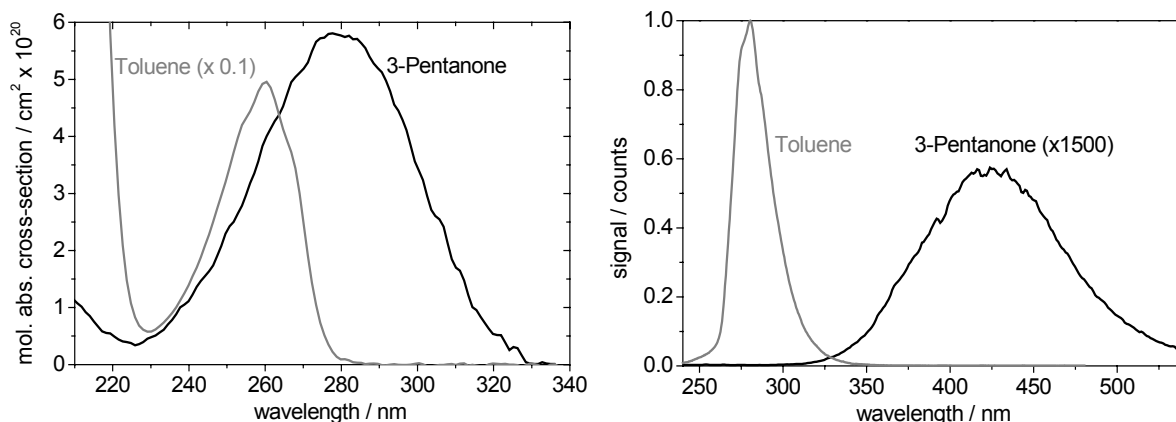


Figure III-8: left: Absorption spectrum of 3-pentanone (10 times weaker compared to toluene) right: Fluorescence spectra of toluene and 3-pentanone after excitation at 266 nm.

2.2.2 Photophysical model

The prevailing photophysical model for 3-pentanone [18] is based on a model for acetone by Thurber et al. [63]. It was established by fitting experimental data at either high temperature T or high pressure p . However, for combined high T AND high p the model fails to describe the signal behavior [56].

Due to fast ISC the fluorescence lifetime is small (<3 ns) and a low quantum yield can be expected. With increasing temperature the spin-forbidden ISC to the triplet state becomes vibrationally allowed and the total signal decreases. The prevailing model assumes a single-exponential fluorescence decay. If the decay was bi-exponential, instead, similar to that of toluene, the discrepancy between model predictions and high T / high p measurements could be explained. Hence, one goal of the lifetime measurements within this work (cf. chapter V 3.3) was the investigation of the 3-pentanone fluorescence lifetime.

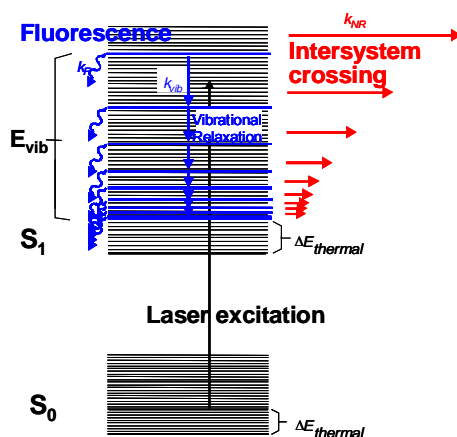


Figure III-9: Simple photophysical scheme of the important decay processes for 3-pentanone LIF. Intersystem crossing (ISC) and fluorescence are the dominant non-collisional processes.

3 Applications of tracer-LIF spectroscopy

Laser-induced fluorescence upon UV excitation provides strong signals that are frequently used for imaging of concentration distributions. Commercial fuels contain several organic compounds that emit fluorescence light in a wide spectral range after laser excitation. The physical and spectroscopic properties of these species typically vary within a wide range and the over-all signal is hard to quantify. For quantitative fuel-concentration measurements, systems are preferred where the fluorescence signal can be attributed to single species. Therefore, it is popular to add well-characterized fluorescing tracers to otherwise non- (or weakly) fluorescing fuels. The ideal tracer should behave exactly like the fluid it is added to (e.g., the fuel or the desired component of a multi-component fuel), in terms of droplet formation, evaporation, convection, diffusion, reactivity and reaction rate. It is obvious that these requirements can not be met in full. However, practical tracers are often very similar to the fuel or are components which are present in commercial fuels (like toluene). A popular model fuel is iso-octane (boiling point: 99°C). Toluene (111°C) and 3-pentanone (101°C) are two of the most frequently used tracers. The modification of the system must be kept to a minimum and the influence of the tracers on a given experimental situation must be critically reviewed. Ideally, the tracer should yield LIF signal intensities that are directly proportional to the desired quantity and should not be influenced by ambient conditions. Unfortunately, all fluorescent tracers show at least some dependence on local temperature, pressure and bath gas variation. Therefore, in experiments where ambient conditions change in time or space, the underlying interdependencies with the tracer signal must be understood in order to yield quantitative results. On the other hand, with known boundary conditions one can also take advantage of certain dependencies and use them to not only measure fuel concentrations, but also temperature or partial oxygen concentrations.

3.1 Fuel concentration and equivalence ratio via tracer LIF

Laser-induced fluorescence from toluene or 3-pentanone has been frequently used to trace the fuel concentration inside IC engines. The following two sections explain a popular technique for measuring fuel concentrations via 3-pentanone LIF, which has also been used for an engine experiment within this work, and a method for fuel/air-equivalence ratio measurements via the combined LIF signals from toluene and 3-pentanone (FARLIF).

3.1.1 Fuel concentration Measurement via 3-pentanone LIF

3-Pentanone [20,64] or mixtures of 3-pentanone and 3-hexanone [65] were suggested as tracers that mimic the boiling and transport properties of gasoline. In most experiments mixtures of iso-octane and 3-pentanone are used as fuel. The temperature and pressure dependence of acetone and 3-pentanone LIF was investigated in numerous experiments [9,18,20,61,62,66,67]. Thurber et al. succeeded to set up a conceptual model combining the various observations. This model for acetone fluorescence was extended to also include 3-pentanone [18]. It has recently been compared to results with in-cylinder measurements. This comparison shows that the photophysics is not yet fully understood [56]. Nevertheless, lacking a better model at the

time of the experiment in this thesis (see chapter VI 1) this model was still used to calculate the dependence of the 3-pentanone LIF signal on pressure and temperature for an engine experiment described in chapter VI 1 (see Table III-1). Due to the opposing effects of increasing temperature and pressure the changes are below 5% for all operating conditions relative to the homogeneous-charge condition used for calibration of the system at 45°CA BTDC (degrees crank angle before top dead center) in the experiment.

Piston pos. [°CA BTDC]	45	29	26	23
T [K]	500	590	610	625
p [bar]	2.3	8.5	9.5	10.5
ϕ / ϕ (298 K, 1 bar)	0.89	0.93	0.91	0.90
ϕ / ϕ (500 K, 2.3 bar)	1.00	1.05	1.03	1.02

Table III-1: Variation of 3-pentanone LIF intensity for different crank-angle positions, i.e. different temperatures and pressures, based on model calculations [16]. Reference points are ambient conditions and conditions during calibration measurements in a fired engine at 45°CA BTDC.

For quantitative measurements 3-pentanone is doted to iso-octane with a know concentration (i.e. 8% vol.). Within given uncertainties from model prediction the 3-pentanone LIF signal is directly proportional the number density and, assuming that the tracer is mixing well and has the same volatility than iso-octane, thus directly proportional to the fuel concentration.

3.1.2 Equivalence ratio measurement via 3-pentanone and toluene LIF

Reboux et al. [55] suggested the use of toluene LIF to measure fuel/air ratios in the compression stroke of IC engines. While the LIF signal from acetone, 3-pentanone and biacetyl [7] are relatively immune to quenching by O_2 and thus are commonly used to represent the fuel distribution, toluene fluorescence is additionally sensitive to oxygen. It thus offers the potential to directly assess the fuel/air ratio ϕ . The concept suggested by Reboux et al. is intriguing and simple: when oxygen quenching is the dominant de-excitation pathway and intra-molecular de-excitation can be neglected, the signal from an excited molecular state is proportional to the tracer number density and inversely proportional to the oxygen number density, i.e. proportional to ϕ . They found this to be true for toluene at air pressures above 3 bar for room temperature and 248-nm excitation. This concept is known in the literature as FARLIF (Fuel-Air Ratio LIF).

For a long time it was assumed that the concept of oxygen quenching as the dominant de-excitation process and the resulting proportionality of signal and fuel/air ratio can be adapted for all pressures and temperatures within the compression stroke of IC engines. However, as shown in [15,19,68,69], the non-radiative, intra-molecular decay rates feature a strong dependence on temperature T , most noticeable in the rate for internal conversion (i.e. radiationless transition to the ground state), which is known in the literature as the “third-decay-channel” [70] – but also possibly in the rates of fluorescence and intersystem crossing (i.e. transition to the triplet state). The collision rate Z , in turn, is only a weak function of temperature ($Z \propto \sqrt{T}$) because density and velocity have opposite effects. Under many practical conditions this leads to a breakdown of the FARLIF concept [68]. Nevertheless, within certain

limits the FARLIF concept can be used in various applications [16]. In chapter V 2.3 it is used to measure the oxygen partial pressure in a room temperature nitrogen flow at atmospheric pressure. In this system the FARLIF method worked perfectly:

Toluene LIF is strongly quenched by oxygen and yields oxygen concentrations. 3-Pentanone LIF is not influenced by oxygen and indicates local tracer concentrations. Thus, the local tracer concentration-independent partial oxygen pressure is obtained by ratio of the two spectrally well separable tracer LIF signals.

The following effects must additionally be corrected for:

- Toluene LIF is additionally quenched by 3-pentanone
- This energy transfer enhances the 3-pentanone fluorescence.
- There is a little spectral crosstalk between toluene and 3-pentanone LIF

With a high 3-pentanone : toluene ratio (fuel : 3-pentanone : toluene \cong 100:10:1) and appropriate filters the disturbing effects can be neglected or corrected for [11].

In an imaging experiment shown in chapter V 4.2 the two-dimensional oxygen distribution in a turbulent flow was measured this way. An excitation laser lightsheet defines the observation plane in the object. 3-pentanone- and toluene-LIF images are acquired simultaneously with intensified cameras. By means of digital image processing an oxygen distribution image can be calculated as the ratio of the two tracer-LIF images. This technique has been applied before in [11].

3.2 Toluene LIF thermometry

Although toluene has been used extensively as fuel tracer for concentration and fuel/air-ratio measurements, the temperature dependence (and its possible drawbacks and benefits) of toluene LIF has been ignored for a long time. However, investigations [71,72] have shown that toluene fluorescence varies with temperature: (i) total, integral signal intensity, (ii) the shape of the emission spectrum and (iii) the fluorescence lifetime. Thus, toluene can be used as a tracer molecule for temperature measurements in various kinds of flow and mixing diagnostics. This section will briefly discuss each effect for its applicability for temperature measurements.

The total LIF signal can be used in a simple one-color detection setup. This approach, however, is restricted to flows with a homogenous tracer distribution. In systems with inhomogeneous tracer mole fractions (e.g., mixing flows), the total signal depends on both, mole fraction *and* temperature. In this case a two-color detection method can be applied taking advantage of the redshift of the emission spectrum with increasing temperature. The ratio of the signals is a function of temperature only, as the tracer number density cancels. All results presented here are obtained with 248-nm excitation. Similar results were observed for 266-nm excitation.

Within this work, for the first time high resolution lifetime measurements of the temperature dependence of toluene LIF were performed. They will be described in detail in chapter V 3. The lifetimes of toluene LIF significantly change with temperature which has a potential for

temperature measurements as well. Obviously, lifetime measurements have the advantage of being independent of the local tracer concentration. They could thus be applied to inhomogeneous systems for temperature measurements.

3.2.1 Temperature dependence of total signal – single-color thermometry

The toluene-LIF signal S_{fl} is at each point (x,y) proportional to the product of the number density n_{tol} , the absorption cross-section σ_{abs} and the fluorescence quantum yield ϕ_{fl} of the fluorescing species and the laser intensity I (as long as not saturated):

$$S_{fl}(T, x, y) \sim I n_{tol}(T, x, y) \sigma_{abs}(T) \phi_{fl}(T) \quad (III.7)$$

where temperature may be a function of the spatial coordinates (x,y) . In constant pressure systems with homogeneous tracer mole fraction, n_{tol} depends on $1/T$ only. The LIF signal is then a function of temperature only, with $\sigma_{abs}(T)$ and $\phi_{fl}(T)$ known from cell-measurements [15,48]. The calculated calibration curve Figure III-10, left) allows the fluorescence signal to be converted to temperature. One region or condition of known temperature is then sufficient for calibration in order to obtain absolute temperatures. An example for single-shot temperature-imaging is given on the right side of Figure III-10.

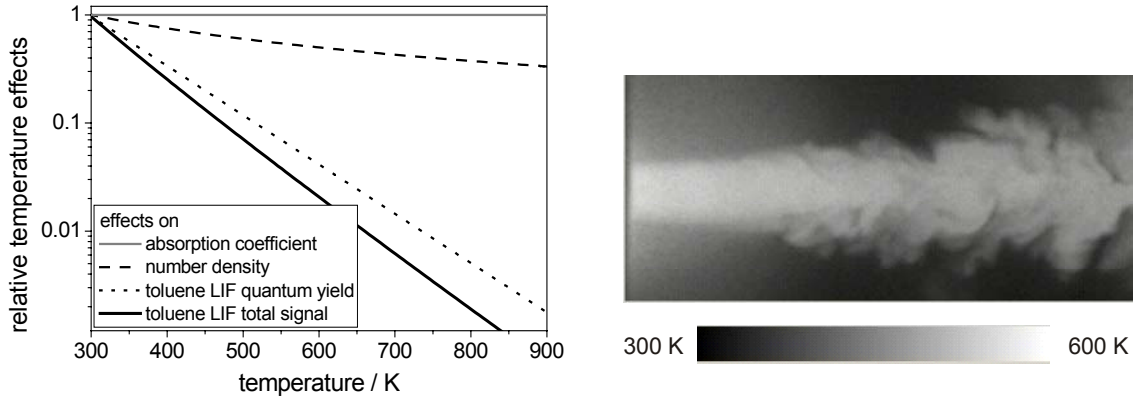


Figure III-10: Temperature dependence of toluene LIF after excitation at 248 nm (left), exemplary single-shot temperature measurement on a heated, turbulent flow with homogeneously seeded toluene (right).

3.2.2 Temperature dependence of spectra – two-color thermometry

In systems with inhomogeneous toluene mole fraction, one can take advantage of the temperature-dependent red-shift of the toluene fluorescence spectrum to measure temperature. The idea is to measure fluorescence simultaneously in two different wavelength regions with appropriate filters after excitation at a single wavelength. By taking the ratio of the signals, number density n_{tracer} and laser intensity E_{laser} cancels at each point and the result depends solely the ratio of fluorescence quantum yield which depends on local temperature $T(x,y)$:

$$S_{ratio} = \frac{S^{red}}{S^{blue}} \sim \frac{E_{laser} \cdot n_{tracer} \cdot \phi^{red}(T)}{E_{laser} \cdot n_{tracer} \cdot \phi^{blue}(T)} = \frac{\phi^{red}(T)}{\phi^{blue}(T)} \quad (III.8)$$

The temperature-sensitivity depends on the chosen combination of detection wavelength regions, i.e. the applied filters (Figure III-11, right). In previous experiments longpass filters (Schott: WG 280 and WG 320) were employed [72]. For higher temperature sensitivity, band-pass filters are suggested; e.g., 335 ± 20 nm (BP335) and 285 ± 5 nm (BP285), which imply a slight drawback on S/N-ratio. In this work a special filter combination was developed to use the two-color thermometry technique for applications with the fiber-optic spark plug (see chapter IV 1.3.1).

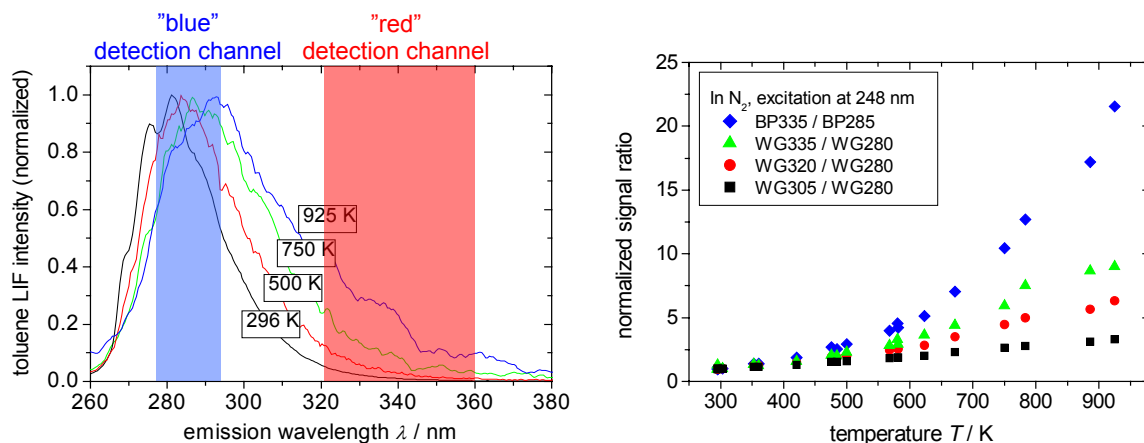


Figure III-11: Left: Temperature dependence of the normalized toluene-LIF spectra after 248-nm excitation and schematic definition of the two detection channels. Right: Temperature-dependence of the signal ratio "red channel"/"blue channel" for different filter combinations.

Figure III-12 shows the temperature dependence of the signal ratio "red channel"/"blue channel" after 266-nm excitation, which was the preferred wavelength for ns-measurements with the fiber-optic spark plug in this work. Compared are two different filter systems: (i) the special bandpass filter combination used in the photomultiplier cascade for the detector unit of the fiber-optic spark plug and (ii) regular Schott glass filters. Clearly visible, the improved filter combination yields a much better temperature sensitivity with similar S/N-ratio. Detailed information about the improved filter combination is given in chapter IV 1.3.

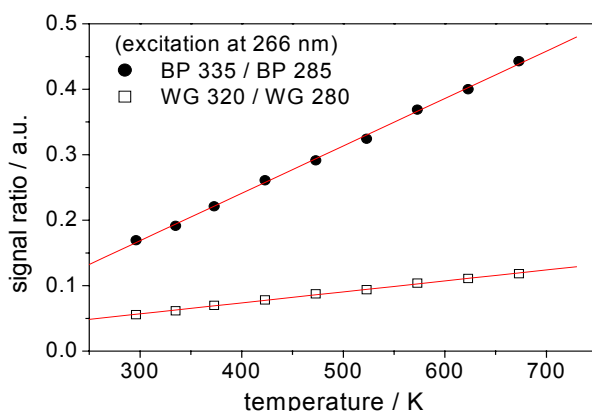


Figure III-12: Temperature dependence of the signal ratio "red channel"/"blue channel" for the special BP filter combination used in the photomultiplier cascade in the detector unit of the fiber-optic spark plug compared to the signal ratio through regular Schott glass filters (after 266-nm excitation).

4 Equivalence ratio measurement via spark emission spectroscopy

In contrast to Diesel or homogeneous charge compression ignited (HCCI, CAI, etc.) engines spark ignited (SI) engines need additional energy for the inflammation of the mixture. This energy is introduced by the electric discharge originating at the spark gap and results in a local temperature increase and the formation of radicals. (Consequently, a self-propagating flame is initialized if there is an ignitable gas mixture at the location of the spark.) The strong light signal from the spark provides another possibility to measure the equivalence ratio in close proximity of the spark gap in SI engines: Spark emission spectroscopy of signals from selected molecules like CN^* yield carbon number densities and thus equivalence ratios (with known oxygen concentration from air mass flow measurements).

Merer et al. [73] described the temporal evolution of the light-emitting processes in the spark as shown in Figure III-13. Within the first 10 ns of the spark the radiation is emitted from excited fuel and air molecules. After this phase emissions from atoms can be detected, which emit light by relaxing from multiple ionized atomic states. This period is followed by the formation of excited diatomic molecules from the recombination of atoms [74]. In this phase molecules with nitrogen, e.g., NO^* , NH^* and CN^* are spectrally dominant. In the next step chemical reactions take place and the flame kernel is formed. This can be observed in the colder fringes at the plasma.

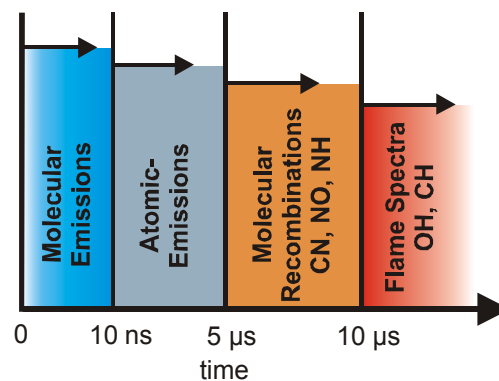


Figure III-13: Temporal evolution of spark emission [74].

Figure III-14 shows an exemplary spark-emission spectrum from measurements in a fired IC engine. The emission of CH^* (431 nm), CN^* (388 nm), NH^* (336 nm) and OH^* (306 nm) are its most important and clearly distinguishable features that can be used for the observation of mixture composition. The emission of NO^* (226 nm) can also be seen in a typical spark emission spectrum (however not in the spectral detection range of the spectrum in Figure III-14).

With increasing carbon number density the number of excited CH^* and CN^* molecules and thus the emission intensity increases. Compared to this signal, a relatively strong CH^* signal, for example, indicates deficient N_2 concentration, which could be due to locally very rich mixture or the presence of droplets or even liquid fuel on the electrodes. In this work the CN^* spark emission signal was used to measure local fuel concentrations and equivalence ratios in collaboration with the Institut für Kolbenmaschinen (IfKM) in Karlsruhe, Germany.

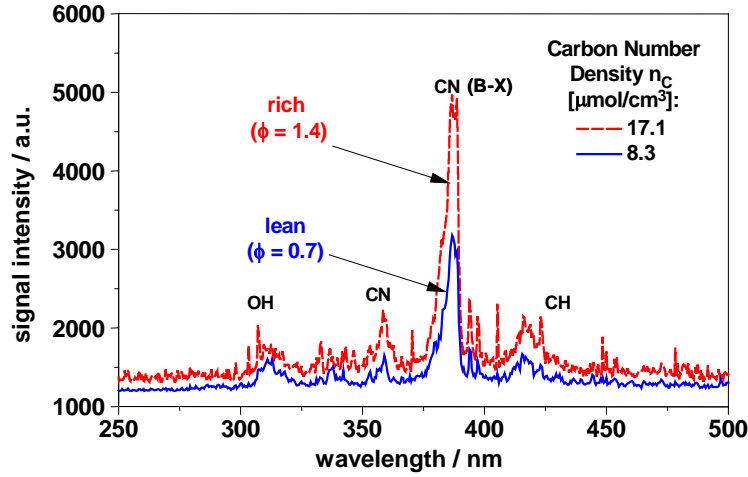


Figure III-14: Spark-emission spectra for two different carbon number densities, i.e. two different fuel/air equivalence ratios.

4.1 CN* as an indicator for local fuel concentration

According to the investigations of Merer/Wallace [73] and Fansler/Drake et al. [44] the CN* emission signal intensity shortly after the spark breakdown (see Figure III-13) can be used for the quantification of the fuel concentration at the spark gap. In order to do so the following assumptions have to be made:

- The CN* formation results from the ionization, dissociation and recombination during the spark breakdown and arc phase.
- The CN* emission intensity for a given gas density depends on the fuel concentration, respectively on the number density of fuel molecules.

Deducing from the above mentioned observations it becomes apparent, that the CN* signal intensity is directly connected to the local carbon number density n_C . For a homogeneous mixture distribution in the combustion chamber the carbon number density is calculated using the injected fuel mass m_{fuel} , its molecular weight M_{fuel} , the number of carbon atoms per fuel molecule N_C and the volume of the combustion chamber at ignition timing (spark advance: SA) V_{SA} :

$$n_C = \frac{m_{fuel}}{V_{SA}} \frac{N_C}{M_{fuel}} \quad (\text{III.9})$$

For a multi-component fuel the average carbon number of the fuel has to be used. The temporal evolution of the electrical energy shows significant cycle-to-cycle variations due to variations in local gas velocity and composition. At the beginning of the spark the energy has an influence on the radius of the plasma and therewith on the emission intensity of the CN* signal. Consequently, the CN* emission intensity must be normalized by the amount of energy dissipated in the spark during the observation interval. Residual gas has to be minimized. This method for measuring fuel concentrations has been successfully applied by various groups [28,44,45].

IV MICROOPTICAL SYSTEMS FOR DIAGNOSTICS IN CAVITIES WITH LIMITED OPTICAL ACCESS

Whenever in-situ, non-invasive measurements are needed, optical techniques are the means of choice. But for many applications major modifications of the device under investigation need to be done in order to provide optical access. These modifications are always time consuming and expensive and in some cases even influence the physical properties of the examined object (e.g., heat conduction or cylinder geometry of an IC engine). The obvious solution is the minimization of inevitable optical access. This chapter presents three microoptical systems that help keeping modifications to a minimum or even use existing access to the engine without additional modifications:

1. Fiber-optic spark-plug (FOSP) sensor for UV-LIF point measurements close to the ignition spark
2. Hybrid (refractive and diffractive) endoscopic UV-imaging optics
3. Hybrid excitation optics for the generation of lightsheets and illumination patterns

The boundary conditions imposed by an IC engine environment, like high pressure and high temperature, and the demands for UV-LIF applications make the construction of these microoptical systems a challenging task. The following sections will discuss and show solutions to the major issues that came up during the process of designing and implementing the microoptics.

1 Fiber-optic spark plug (FOSP)



Figure IV-1: Front view of fiber-optic spark plug.

In every spark-ignition (SI) engine there is at least one standard access through the cylinder head into the combustion chamber (apart from the valve openings): The spark plug access. It is frequently used for diagnostics by means of gas sampling valves, thermocouples or pressure transducers that have been integrated into modified spark plugs. Obviously one is interested in performing optical diagnostics through the spark plug as well. The standard approach is using optical fibers for signal transportation. There are several commercial fiber-optic spark plugs (FOSPs) that do not use any additional optics besides low NA fibers behind pressure-resistant windows. These FOSPs can be used to observe the start of combustion and the general direction of the flame front movement perpendicular to the optical axis. There are also FOSPs that use quite complicated optics for signal light collection, like the FOSP constructed by Ikeda et al. with Cassegrain optics for the

observation of chemiluminescence [75]. Nevertheless, all these systems are designed for the detection of spontaneous emission and are therefore working without any excitation. They often collect light from a large section of the combustion chamber, thus providing limited spatial resolution. Other FOSPs work with IR absorption [76,77] over a small, but well-defined absorption distance. Raman spectroscopy has been suggested for FOSPs, too. But because of the large cross-section of optics needed to transmit high-power laser radiation that is sufficient for Raman detection, they lack the ignition function. There has even been research on FOSPs using fuel LIF [78], but the excitation wavelength here were optically unchallenging 404 nm. So far, mainly liquid fuel was investigated with no practical approach for quantitative measurements inside an IC engine. To the best of my knowledge, a fully functional FOSP that works with 266- or 248-nm UV-laser excitation, has not been realized yet. In this chapter an optical M14 spark plug with full ignition function is presented. It uses integrated microoptics and quartz fibers to guide UV-laser excitation light to a defined probe volume and collect resulting fluorescence signals. It thus enables the use of UV LIF of fuel tracers for quantitative measurements inside fired IC engines (Figure IV-2). Any of the tracer-LIF techniques described in this work can be applied with the FOSP. Additionally, the observation of chemiluminescence from different directions or spark-emission spectroscopy can be accomplished.

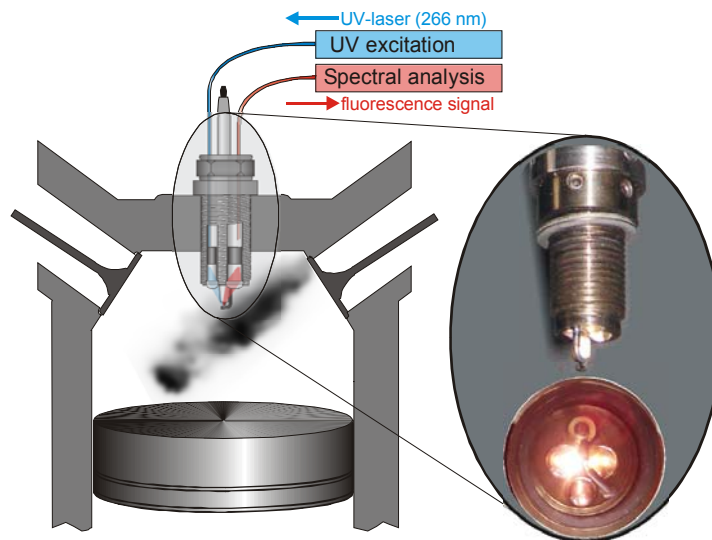


Figure IV-2: Schematic of the FOSP (fiber-optic spark plug) and its application in a SIDI (spark-ignition direct-injection) engine.

1.1 Quartz fibers for UV applications

An optical fiber is a cylindrical dielectric waveguide that transmits light along its axis by total internal reflection at the boundary between its cladding and core. In order to confine the optical signal in the core, the refractive index of the core must be greater than that of the cladding, which is realized by the respective material (i.e. different dopants in quartz glass). The boundary between the core and cladding may either be abrupt, in step-index fiber, or gradual, in graded-index fiber. The fibers used in this work were all large (i.e. multimode) step-index fibers. Such fibers with large (greater than $10\ \mu\text{m}$) core diameter may be analyzed by geometric optics. Rays that meet the core-cladding boundary at a high angle (measured relative to a line normal to the boundary) are completely reflected. The minimum angle for total internal

reflection is determined by the difference in index of refraction between the core and cladding materials. Rays that meet the boundary at a low angle are refracted from the core into the cladding, where they are lost for conveying light along the fiber. In this way, the minimum angle for total internal reflection determines the acceptance angle of the fiber and thus defines its numerical aperture (NA). A high numerical aperture makes it easier to efficiently couple a transmitter or receiver to the fiber. However, by allowing light to propagate down the fiber in rays both close to the axis and at various angles, a high numerical aperture also increases the amount of multi-path spreading, or dispersion, that affects light pulses in the fiber [79].

For the transmission of UV-light in mostly special all-silica (AS) fibers are used [80,81]. There are three different types of commercial optical AS fibers (i.e. high-OH AS, high-OH ASB for UV radiation below 200 nm and low-OH AS), differing mainly in the OH content, special dopants and different processes of fiber drawing and tempering [82]. Only high-OH fibers are suitable for UV-applications, because fibers with low-OH core material suffer from pre-existing UV-absorbing color centers [83] due to fiber drawing and generation of these defects during UV irradiation. The amount of embedded water (and resulting OH content) in a standard UV AS fiber is about 1000 ppm in contrary to less than 1 ppm in AS fibers for the infrared (IR) region. Unfortunately, especially UV irradiation with a high energy density additionally generates color centers like E'-centers (Si with an unpaired electron or H in case of high OH content) or NBOH-centers (Non Binding Oxygen Hole). For detailed information about the generation and healing of color centers in quartz fibers see [82,84-86] and references therein. Although Klein et al. [87] have done intensive research on improving low-OH core fibers even for UV-applications, they are not commercially available, yet. A special process of H-loading of commercial high-OH fibers is supposed to help these fibers to recover after a certain amount of UV-irradiation. One hour after irradiation, modern H-loaded fibers should recover almost 100% of their original transmission even with laser irradiation below 200 nm, as long as the laser power stays below a given damage threshold. However, the process of H-loading is only possible for fibers with less than 200 μm in diameter and due to diffusion the hydrogen amount gradually diminishes. After six to eight months the H-loading would have lost its effect.

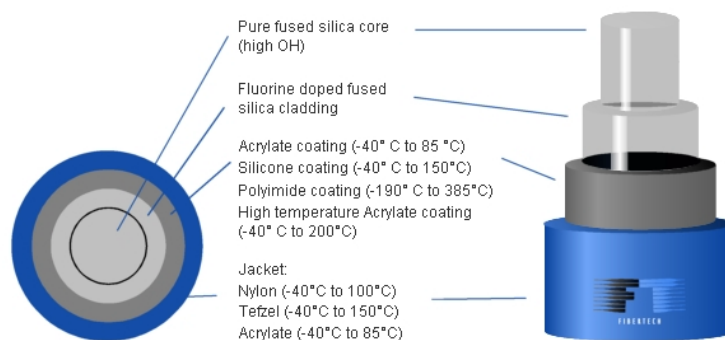


Figure IV-3: Typical cross-section of an all-silica UV-fiber (FiberTech).

For our purposes, when using 266-nm laser pulses (8 ns/pulse, 10 Hz) with pulse energies <1 mJ guided by fibers with at least 400 μm in diameter, standard high-OH AS fibers are most suitable. Such fibers are offered by *Polymicro* or *FiberTech* (Figure IV-3). After an experimental

selection and theoretical simulations with various different fibers we chose high-OH all-silica multimode fibers with a heat resistant polyimide or aluminum coating for the application in our FOSP. The fibers have core diameters of 400 μm and 1000 μm and an NA of 0.22 that is typical for all-silica fibers. It implies an acceptance cone with an opening angle of 25.4° .

Theoretical and measured transmissions of these fibers are shown in the following sections. The lifetime of a 400- μm fiber for the transmission of 266-nm laser pulses can extend several 100 hours when using less than 1 mJ/pulse. However, if the pulse energy is increased to only 2 mJ/pulse the transmission of the fiber can be significantly reduced after a couple of hours, because of the generation of absorbing color-center. From these color-centers in damaged fibers (cf. Figure IV-5) a noticeable reddish luminescence is visible.

1.2 Excitation

For most applications with the FOSP the 4th harmonic of a Nd:YAG laser (266 nm) is used for excitation. The 8-ns laser pulses are guided through an optical fiber. According to the manufacturer specifications the damage threshold for all of the used quartz-fibers is about 30 mJ/mm² (25 ns pulse at 248 nm). No direct specifications are given for 8 ns at our wavelength, but with pulses being three times shorter while depositing almost the same amount of energy, the threshold should be around 10 mJ/mm² for our application. For the excitation fiber with 400 μm core diameter this would be a damage threshold of 5 mJ/(surface of the fiber face). This value could not be achieved in our experiments, though. Surface effects on the fiber face and inhomogeneous laser profiles (hot spots) are the dominant limiting factors.

1.2.1 Laser – fiber coupling issues

Figure IV-4 shows the experimental setup for the coupling of a free laser beam into an optical fiber. The laser is focused by a spherical lens that is translatable perpendicularly to the optical axis. The focal length of the lens must fit the NA of the optical fiber, i.e. the angle of the diverging laser beam must be smaller than the acceptance angle of the fiber. For homogenization the laser beam passes through a 50 μm pinhole in its focus. A few centimeters behind the focus the laser centrally hits the fiber which is fixed inside an SMA-connector. The fiber connector is adjustable along the optical axis. Depending on the beam profile, the focal length of the used lens and on the fiber diameter an ideal distance between laser focus and the fiber face has to be adjusted to ensure a homogeneous energy distribution over the whole surface of the fiber face. In most experiments a Nd:YAG laser with a beam diameter of about 6 mm was used. With an $f = 500$ mm lens and a fiber diameter of 400 μm the fiber had to be placed at least 30 mm behind the focal point of the laser.

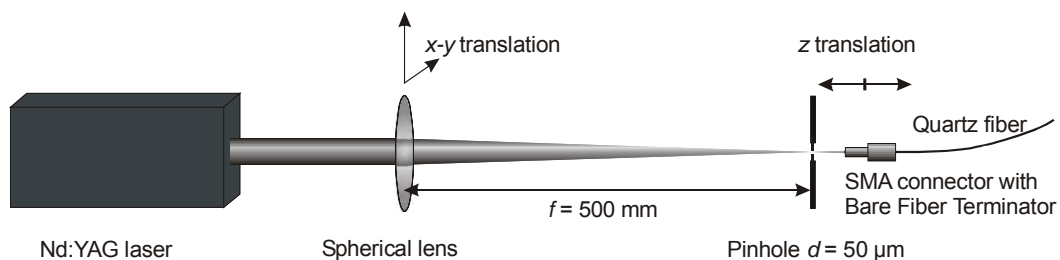


Figure IV-4: Experimental setup for the coupling of a free laser beam into an optical fiber.

In their beam profile after 4th harmonic generation, most Nd:YAG lasers have little local energy irregularities with a very high energy density, so called hot spots. These hot spots can not be completely removed by a simple pinhole. They can actually destroy the pinhole, especially with additional laser energy variations that occur during 4th harmonic generation. If such a hot spot hits the fiber surface it can be quickly damaged. A dirty fiber surface is another factor that reduces the damage threshold. Dust particles can heat up and the locally high temperature can induce the formation of color centers that further absorb the laser light, leading to more heat generation and sooner or later the destruction of the fiber. Figure IV-5 shows a photo of a damaged fiber end (right) of a 400- μm fiber with Aluminum coating that was exposed to high UV irradiation (5 mJ/pulse). The left photo shows the matt surface of the same 2 cm long fiber-end piece broken off the damaged fiber.



Figure IV-5: Photos of the two ends of a piece of damaged quartz fiber.

For future experiments with a flashlamp-pumped Nd:YAG laser a special “beam homogenizer” needs to be constructed to avoid local energy maxima and thus extend the lifetime of the excitation fiber. A homogeneous beam profile could also be achieved with a seeded Nd:YAG laser. Another way to safely transmit more power is the use of longer laser pulses by means of pulse stretching or other laser-light sources.

1.2.2 Total transmission

Figure IV-6 shows a standard attenuation curve for all-silica fibers. Whereas the attenuation in the visible and near IR is in the range of a few decibel per *kilometer*, it reaches one decibel per *meter* in the UV spectral region that is of interest for our LIF applications.

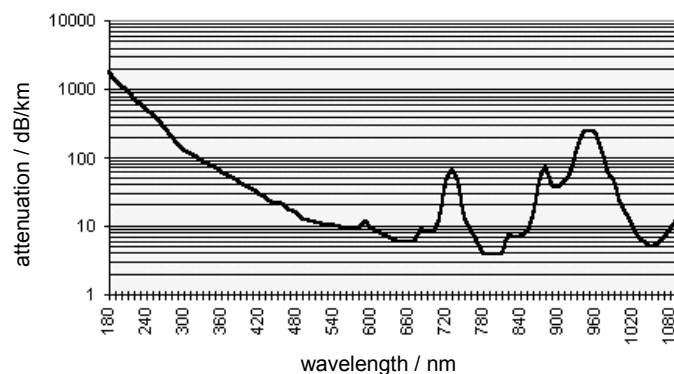


Figure IV-6: Attenuation of quartz fibers.

With optimal adjustment of the fiber coupler a total transmission of up to 70% could be achieved through a 2-m long aluminum-coated fiber with 400 μm diameter. This is in good agreement with the manufacturer specifications in Figure IV-7 (*FiberTech*). Even with a low excitation energy of about 0.5 mJ/pulse, after 30 minutes the transmission is reduced to less than 50%, though. Taking into account that minor hot spots might have been present in the beam profile, this agrees well with the theory of color-center formation [83]. After switching off the laser and another 30 minutes recovery time the transmission almost reaches 70% again.

But after permanent irradiation for several hours the fiber could not recover anymore and a drastic transmission loss down to 40% could be noticed. From two hours to three hours of irradiation there was no noticeable difference in transmission, though. For long time operation the measurements suggest a total input power of less than 0.7 mJ/pulse (8 ns, 266 nm). The measured output power, which is available for LIF experiments, is then only 0.3 mJ/pulse.

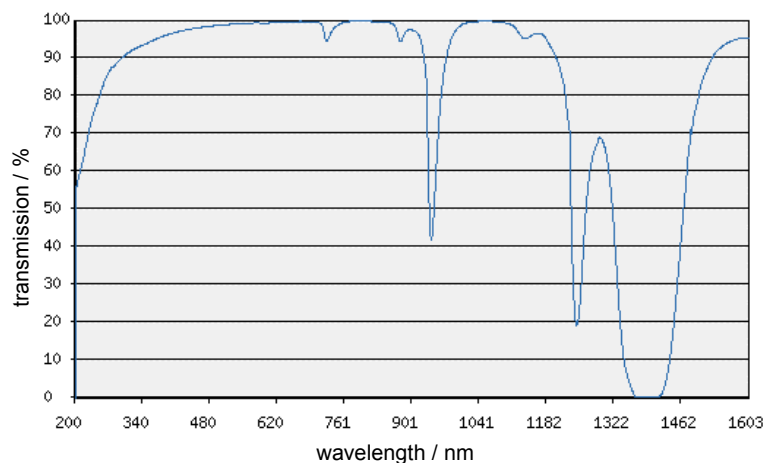


Figure IV-7: Transmission through a 2-m long (high OH) quartz fiber.

1.3 Detection

For the detection of very weak fluorescence signals a good signal-to-noise ratio (S/N-ratio) is very important. The S/N-ratio in our application is predominantly a characteristics of the used sensor. As shown in the next paragraph, photomultipliers with a very low dark noise were chosen. Even more crucial is the effective suppression of background signals. This can only be achieved by the spectral and geometric separation of signal light from unwanted scattered excitation-laser radiation, luminescence from organic molecules apart from tracers, or ambient light. Even fluorescence from the used sapphire windows has to be taken into account.

1.3.1 Channel photomultiplier (CPM) cascade and filter combination

Three highly sensitive channel photomultipliers (CPM) (*PerkinElmer, MH1943*) as shown in Figure IV-8 were used for signal detection in combination with a custom filter combination. A CPM, like conventional photomultiplier tubes, converts low light signals (i.e. single photons) into photoelectrons by a semitransparent photocathode deposited on the inner surface of the entrance window. On their way from the cathode to the anode the photoelectrons pass through a narrow, semiconductive channel. Each time the electrons hit the inner wall of the curved channel, multiple secondary electrons are emitted. This effect occurs multiple times along the path, leading to an avalanche effect with a gain exceeding 10^8 at the maximum bias voltage of 3000 V. The curved shape of the glass tube improves the multiplication effect. The advantages of a CPM in comparison to a regular dynode PM are its formidable sensitivity and simultaneously relatively large dynamic range with a very low dark noise (800 pA at 5×10^7). At 2400 V anode sensitivity is typically 3×10^6 A/W at a wavelength of 410 nm with the used bialkali photocathode. This performance surpasses conventional PMTs by one to two orders

of magnitude. A disadvantage of the used CPM is its low damage threshold: For long term operation a maximum average anode current of <100 nA is recommended. Exposition to daylight during normal operation (gain 10^7) would immediately destroy the CPM. For the application with the FOSP it must be ensured that the high voltage is off during the ignition and combustion period. Therefore, the CPM has a gating function. With a 5 V TTL trigger signal the cathode voltage can be disabled within $150 \mu\text{s}$. For details and plots of the spectral sensitivity of the CPM see appendix IX 2.

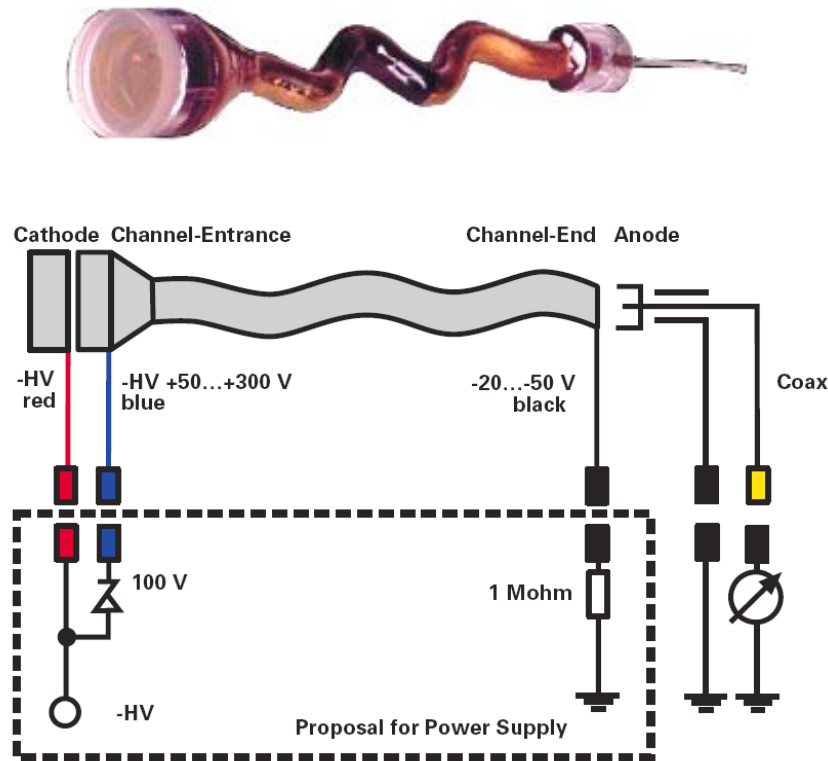


Figure IV-8: top: Picture of typical unpotted channel photomultiplier (CPM)
bottom: simplified wiring diagram.

For a complete insulation from ambient light and robust handling the CPM cascade was built into a 19"-rack module (Figure IV-9, left). The optical board with a 25-mm grit of M6 threads allows a flexible use of the module. The right scheme in Figure IV-9 shows the optical setup of the filter combination used for measurements of fuel concentrations, oxygen partial pressure and temperature with the tracer-LIF methods described in chapter III. First, the signal passes a 266 nm narrowband high-reflective mirror with a steep gradient in its transmission curve around 275 nm (at a 10° angle of incidence). This mirror effectively filters out laser stray light. (In the photo in Figure IV-9 this mirror is adjusted in the wrong angle for alignment reasons). Then, a broadband negative bandpass at 335 nm (FWHM 80 nm) reflects light (45°) between 290 and 380 nm onto the photocathode of the first CPM (CPM 1). For detection of the tail of the toluene LIF spectrum the signal light also passes a 320 nm longpass filter (Schott, WG320). Further along the cascade a 280-nm longpass filter reflects (45°) the remaining transmitted short wavelength between 275 and 295 nm onto CPM 2, thus detecting the spectral peak of the toluene LIF signal. Finally, the signal transmitted through the first three dielectric filters pass another longpass glass filter (Schott, GG385). On this signal pass, the last CPM (CPM 3) meas-

ures the integrated signal from the whole 3-pentanone-LIF spectrum. Without the GG385 the last CPM can also detect another spectral region in the toluene LIF signal (280 – 310 nm) that lies between the regions detected by CPM 1 and CPM 2. Measured transmission curves of all used filters can be found in the appendix (IX 1).

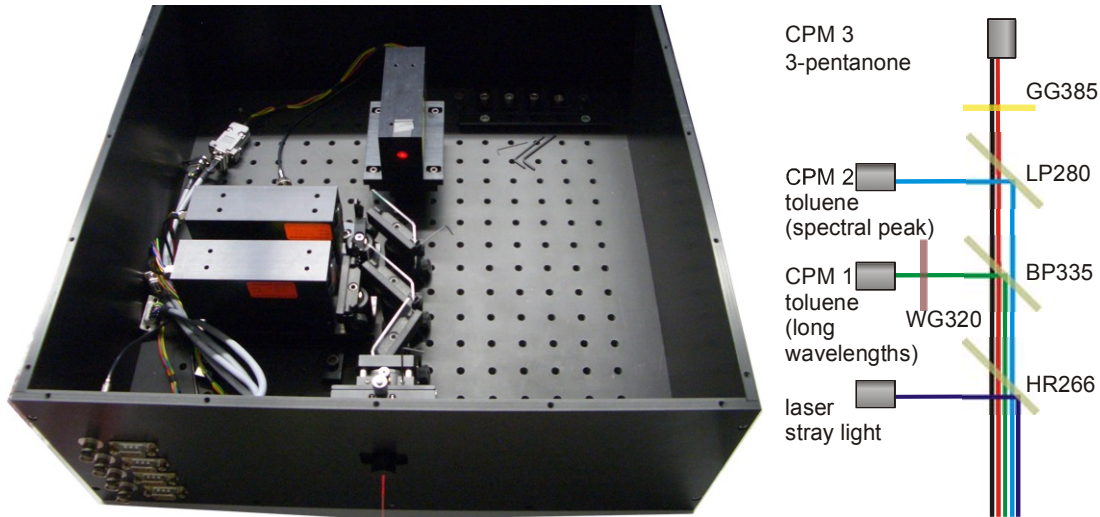


Figure IV-9: CPM cascade and filter combination in a 19'' rack module (left) schematic setup of filter combination (right).

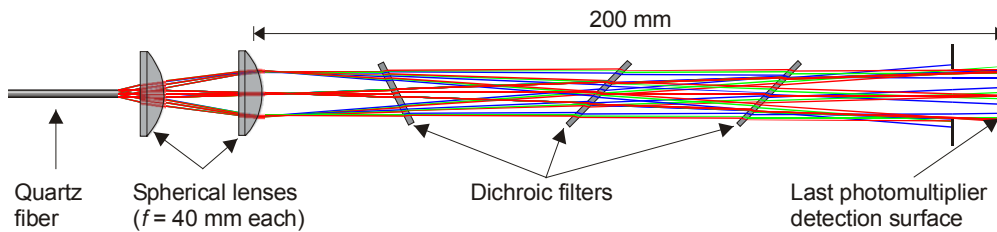


Figure IV-10: Raytracing simulation (Zemax) of signal-light collimation.

The signal light entering the detection module is guided there from the sensor head through quartz fibers with an NA of 0.22 and is therefore strongly divergent at the fiber exit (opening angle of 25.4°) after leaving the fiber. In order to efficiently pass all filters and reach all photocathode surfaces without major losses, the signal light must be collimated over a length of at least 200 mm. This would be no problem, if the diameter of the used optical fiber was small, or ideally a point source. But with our detection fibers having diameters of 1 mm and the simultaneous use of two fibers in the same detector module should be possible, the collimation is not straight forward. For the simulation of the collimation optics the raytracing software *Zemax* was used. A total fiber face diameter of 2.5 mm was assumed. A good collimation distance could be established with an optimized setup (Figure IV-10) using two spherical lenses with $f = 40$ mm each. In this setup 97% of the rays reach the photocathode of the last CPM in its worst case position 200 mm after the last collimation lens. Nevertheless, in the present setup 100% of the signal light reaches the last CPM in a position 180 mm after the last collimation lens, because the planned detection of deflected stray light, which would require another 20 mm, is not yet implemented.

The proper function of the filter combination has been tested by measuring known wavelengths and comparing the resulting CPM voltage to calculated reference values. A deuterium lamp was used as UV-light source and a spectrograph was applied for wavelength selection. A *Chromex* spectrograph with a 300 g/mm grating blazed for 500 nm was used. The wavelength selection in the UV had to be done with the second order diffraction pattern (i.e. if the spectrograph is set to 500 nm the measured wavelength is 250 nm). Certainly, this is only true, if there is no interfering signal from the first order spectrum at the set wavelength. In order to get rid of visible light, a *Schott* UG11 filter suppressed most of the light above 400 nm. However, the UG11 has another weak transmission window between 680 and 760 nm. The signal transmitted in that region is overlaid with the second order spectrum of wavelength between 340 and 380 nm. This must be taken into account when comparing the measured and calculated values. The left graph in Figure IV-11 shows calculated intensity values for the transmitted signal through different filter combinations. The right graph shows the signal measured by the respective CPM. The theoretical transmission curves are represented with the same colors and symbols as the respective measured CPM intensity signals. Calculated and measured values agree well.

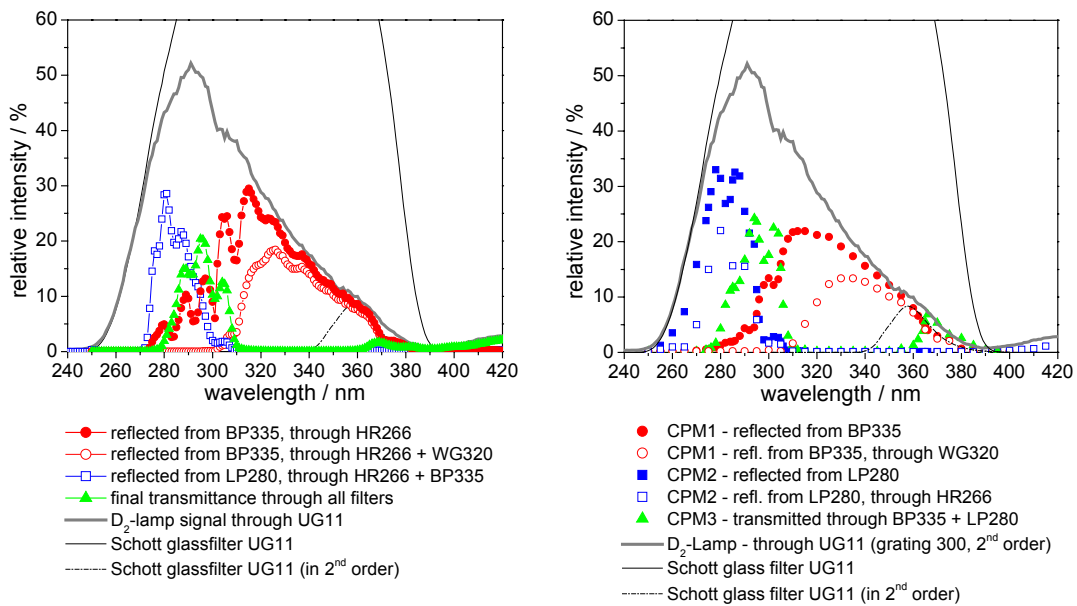


Figure IV-11: Calculated (left) and measured (right) CPM response to a deuterium lamp spectrum (after a Schott UG11 filter). The calculated values are obtained from measured filter transmission curves applied on the measured deuterium spectrum.

1.4 Development of a fiber-optic spark plug and prototypes

Before the fully-functional FOSP could be built, two different optical models were designed and simulated by the Institut für Technische Optik (ITO) at the University of Stuttgart and implemented into prototypes. The first prototype was working with only one channel for both, excitation and detection. That way, the space needed for optical elements was kept to a minimum and collection efficiency was maximized, but scattered excitation light and luminescence from the window could not be suppressed in the detection channel. The second prototype solved most of the issues that arose from the first concept by using multiple channels

and separating excitation and detection. This section shows the milestones on the way to the final FOSP and describes the factors that made us discard the first single-channel concept. Note in advance that the requirements to the sensor optics and the harsh engine environment do not leave a choice for the sensor window material. Sapphire is the only UV-transmitting material that is robust enough and can be connected pressure tight to titanium because of its similar expansion coefficient. But the usage of sapphire brings about the most challenging issue during the sensor development: Laser induced sapphire fluorescence.

1.4.1 Specifications and requirements

Any sensor designed to measure inside the combustion chamber of an IC engine must meet the following requirements:

It must stand high pressures and sudden pressure peaks up to 200 bar as well as high temperatures up to ~ 3000 K during combustion. It must cope with rapid temperature drops induced by impinging liquid fuel and fuel burning off its surface that leads to soot formation obstructing the view. For the integration in a functional spark plug, optical elements must be installed within very little available space, still maintaining the ignition function. The optical setup must be designed in a way to ensure a defined probe volume close to the ignition spark.

1.4.2 Single-channel prototype

The single-channel concept is designed for the excitation of molecules directly in front of the sensor window. For maximum coupling efficiency of the fluorescence light into the fiber with its limited NA the strong divergence of the fluorescence light is eliminated by a spherical lens behind the sensor window. The focal point of this lens is directly in front of the window, thus defining the probe volume. The image is at infinity (Figure IV-12). In this case a detection fiber bundle with the same diameter as the collecting lens positioned directly behind it would collect most of the light.

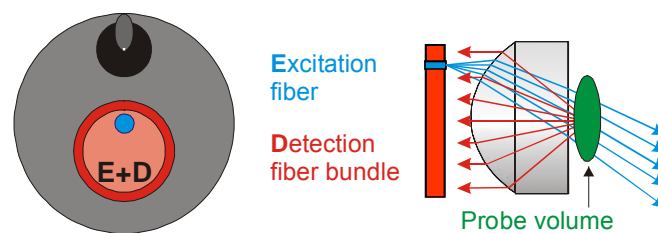


Figure IV-12: Principle of the optical design of the sensor head with one single lens. The measured area is located directly in front of the window [88].

For an ideal fluorescence source of 1 mm diameter as defined by the excitation beam, the signal rays that are coupled into the fibers have an almost homogenous power distribution in the cross-section. Hence, the detectable power scales with the covered area. The excitation fiber is positioned alongside the detection fibers. Because its place cannot be used for detection fibers there is a small inevitable loss for detection (about 5%). In order to create a divergent excitation beam the excitation fiber end is closer to the lens than the focal length. An off-axis position of the excitation fiber and thus an inclined direction of excitation helps to limit the measuring volume.

SIMULATION AND OPTIMIZATION

A variation of the lens parameters affects the measurement in two ways: (i) It changes the propagation of the excitation rays and thus the position and strength of the fluorescence, and (ii) it changes the characteristics of light collection. This dependence was considered by mapping the complete system – excitation and subsequent detection – into one nonsequential model with *Zemax* [89]. Especially the modeling of the fluorescence is not available as standard module. It is described in detail in [88].

The sensor can be optimized for different sensing characteristics, i.e. different positions and sizes of the measurement volume. Figure IV-13 shows the behavior for different optical setups. For a measuring volume very close to the sensor window, 80% of the signal power comes from a volume of about 0.5 mm^3 . If the measuring volume is moved away from the window, its extension increases.

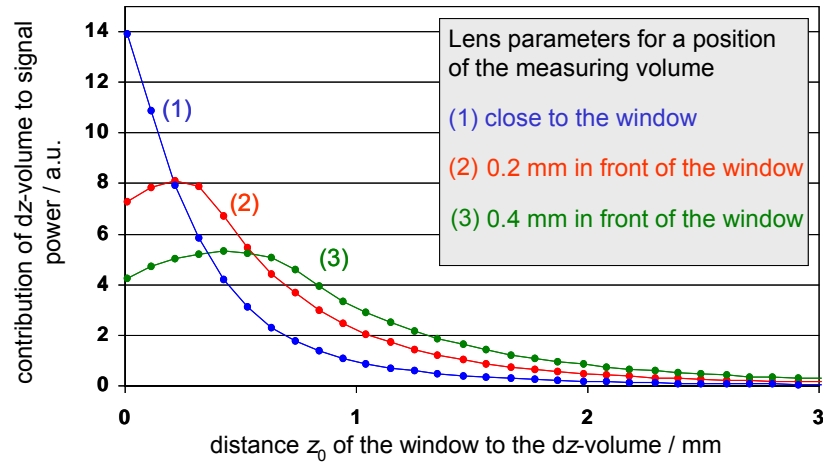


Figure IV-13: Detection characteristics of different sensor setups. The graph shows the contributions of the detected fluorescence power over the distance from the sensor window. The integral of the data is the total power. Excitation by off-axis excitation fiber ($400 \mu\text{m}$ core diameter, NA 0.22) [88].

Based on the results of the simulation a prototype was built (Figure IV-14). The sensor is sealed towards the test chamber by a sapphire-window. A custom made plano-convex sapphire lens is directly pressed against the window. Optical fibers are positioned in drilled holes (0.5 mm diameter) and fixed by high temperature ceramic adhesive.



Figure IV-14: Drawing and pictures of the prototype [88]

DISTURBING SAPPHIRE FLUORESCENCE

After first experimental tests to measure 3-pentanone (g) at vapor pressure in 1 bar air with the single-channel prototype no discernable 3-pentanone LIF signal could be detected. Instead, an interfering broadband background signal was noticed, that scaled with laser energy. Only when a droplet of liquid 3-pentanone was placed directly on the sensor window, the typical 3-pentanone spectrum could be observed. In these tests the detection fibers (400 μm diameter) were plugged directly into the wide open entrance slit of the spectrometer. A long-pass filter (Schott, WG280) was attached inside the spectrometer just behind the slit. This configuration enabled a good fluorescence-light collection, even though the numerical apertures of fiber (NA = 0.22) and spectrograph ($f/4 \rightarrow \text{NA} = 0.12$) were not optimally matched (i.e. the angle of the light cone exiting the fiber was larger than the acceptance angle of the spectrograph). It also provided sufficient spectral resolution. The left graph of Figure IV-15 shows a typical 3-pentanone spectrum and its underlying background signal from measurements in pure air. The spectrally broadened peak around 266 nm comes from strong laser stray-light and reflections from the inside of the sensor window and lens that could not be fully suppressed. After further investigations, the broadband part of the background signal could be identified as luminescence from the sapphire window. It is well known that sapphire – like many other optical materials – can be excited by UV-laser-radiation and then emits a broadband fluorescence signal with maxima in the UV and the IR [90]. The sapphire fluorescence measured after 266-nm excitation is shown in Figure IV-15 (right). The signal peaks in the UV at 335 nm with a band width of 40 nm (FWHM) and has a long spectral tail into the visible. The signal intensity of the interfering spectral tail was almost a hundred times higher than a LIF signal of 3-pentanone gas at vapor pressure.

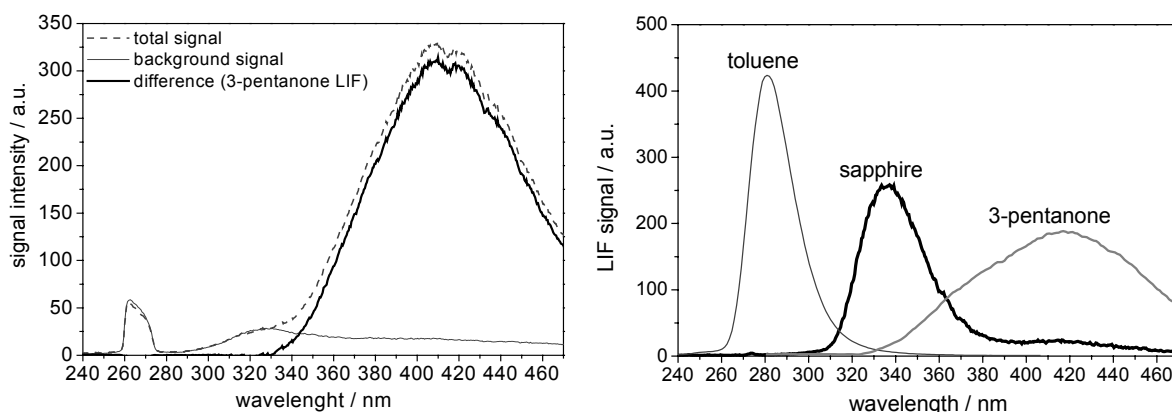


Figure IV-15: Fluorescence signal of a 3-pentanone (l) droplet after excitation with 266 nm and background signal in air (left). Measured sapphire fluorescence of the sensor window in spectral context with a toluene (g) and 3-pentanone (g) fluorescence signal from separate measurements (right).

It soon became obvious that the tracer-LIF concepts could not be applied with this kind of sensor. 3-Pentanone (g) LIF was completely buried by the sapphire fluorescence. LIF from toluene gas in nitrogen could be measured, but techniques relying on the measurement of the spectral tail of the toluene-LIF signal were impossible to apply. As long as the same window and optics were used for both excitation and detection a solution to discriminating against the

strong sapphire fluorescence signal was not in sight. Nevertheless, the background signal vanished with external excitation (not through the sensor fiber and window), which proved that the used materials are suitable for signal detection.

1.4.3 Multi-channel prototype

A completely new sensor concept with separate excitation and detection channels promised to get rid of the sapphire fluorescence and to strongly reduce scattered excitation light in the detection channel. The basic optical scheme is shown in Figure IV-16. It employs three optical channels, one for excitation and two for detection. The probe volume is defined by the overlap of the excitation beam with the field of detection. It can be positioned several millimeters in front of the sensor.

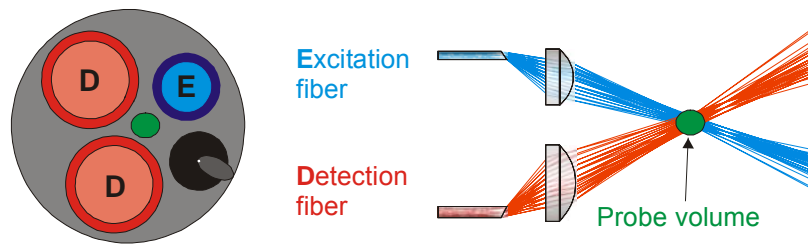


Figure IV-16: Schematic view of the general optical setup for a multi-channel fiber-optic spark plug (optical design by ITO).

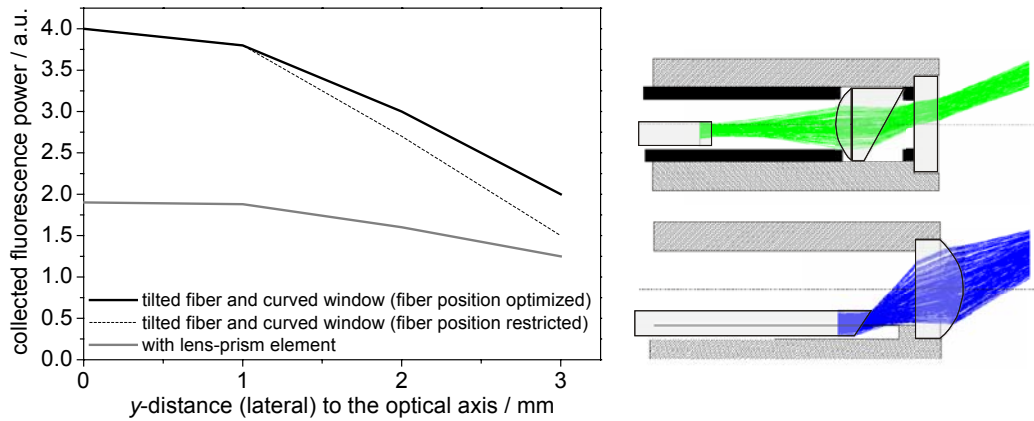


Figure IV-17: Simulated efficiency (left) and layout (right) of two principal optical designs for the collection of fluorescence light from an off-axis y -position (i.e. decentral from the optical axis) 6 mm in front of the sensor (1.2 mm source diameter). The design with a lens-prism element (right, top) has a poor detection efficiency for an off-axis light collection (gray curve in the plot). The design with a tilted fiber end and a curved window (right, bottom) yields a two times more efficient light collection from off-axis object positions [91].

Figure IV-17 shows two possible microoptical designs for the collimation and deflection of light emerging from an optical fiber. The standard approach would use a prism in combination with a lens behind the flat pressure resistant sensor window (top right). Our design uses a tilted fiber end instead of the prism and a spherical window with integrated refractive properties (bottom right). This compact optical design provides the following advantages:

- Maximum collection of fluorescence light by curved windows of maximum diameter
- Curved lens surface close to probe volume \rightarrow large solid angle for detection
- Minimal number of elements for easy handling and reduction of Fresnel losses
- Adjustability by changing the position of the fiber and the angle of its tilted face instead of creating a new lens-prism element (faster and cheaper)

The optical layout for the use of a lens and a prism behind a flat sensor window (Figure IV-17, top right) yields poor detection efficiency from an off-axis light source (i.e. decentral with regard to the optical axis, cf. gray curve in the plot in Figure IV-17, left). The layout that uses a tilted fiber end and a curved window (Figure IV-17, bottom right) is a factor two more efficient. The shown layout uses an optimized fiber position. If the fiber position was restricted by the effective diameter of the channel in the spark plug body, the light collection would be less efficient (dotted curve). In order to avoid this restriction, in the final FOSP body additional spark eroded gaps were provided in the channels for the fibers.

SIMULATION OF THE SENSOR FUNCTION (SIGNAL POWER, MEASURING VOLUME)

For the simulation and optimization of the sensor a similar *Zemax* setup as published in [88] was applied by ITO (see Figure IV-18, left). It was used to (i) optimize system parameters and (ii) calculate the contribution of the dz-volumes to the signal. The overall detected power depends on the tracer absorption, fluorescence yield and its concentration (DLL for LIF simulation). With the multi-channel configuration a z-limitation of the measuring volume is available in defined distance in front of the sensor windows. For a contribution to the measuring signal, regions have to fit to both the spatial excitation and detection characteristics of the system. The calculated z-dependence (Figure IV-18, right) was used to estimate the probe volume size by multiplication with the diameter of the excitation beam. 80% of the excitation rays are within a beam of 1.2 mm in diameter. With the expansion in z-direction being limited to about 2.5 mm an upper limit of 3 mm³ can be estimated for the probe volume.

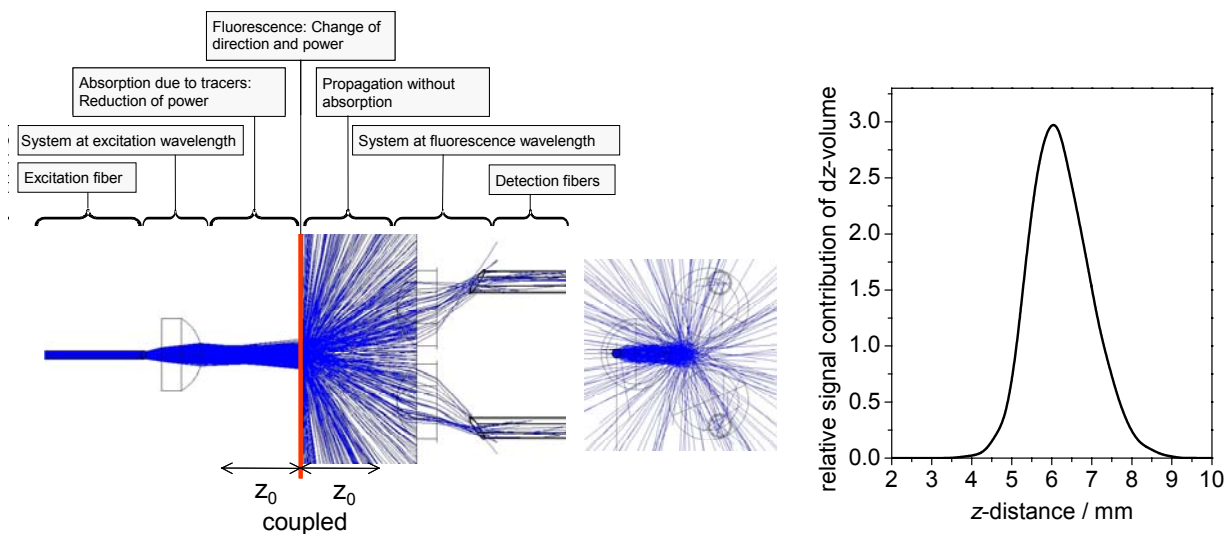


Figure IV-18: Setup for the simulation of the sensor function(left) and the resulting spatial z-resolution characteristics of the sensor (right). (Simulation and results from ITO.)

COPPER-BODY MULTI-CHANNEL PROTOTYPE

The materials for the construction of a fully-functional FOSP are expensive and the production process is challenging and has to be well planned. Therefore, at first a prototype was constructed by the fine-mechanical workshop at the Institute of Physical Chemistry in Heidelberg and tested in various experiments to ensure its proper optical behavior. The prototype body with the standard size of an M14 spark plug was made from copper and the sapphire lenses (made by ITO) were attached with silicone (see Figure IV-19). The optical fibers with tilted ends (made by ITO) were fixed in copper cylinders.



Figure IV-19: Photos of the copper-body multi-channel FOSP prototype.

A graphic way of demonstrating the probe volume definition of the prototype is to illuminate all 3 fibers with a HeNe laser and look at the power distribution on a plane (piece of paper) at varying distances in front of the sensor. In Figure IV-20 the spatial positions and dimensions of the beams and thus the characteristic of the sensor can be seen. Close to the sensor surface, the beams are separated, thus the fluorescence of excited tracers can not be detected. According to the dz -simulation at a distance of about 5 mm the sensitivity of the sensor begins and an overlap of the beams is noticeable. At 6 mm the beams have a maximum overlap which corresponds to the maximum signal. After that, the positions of the beams get separated again.

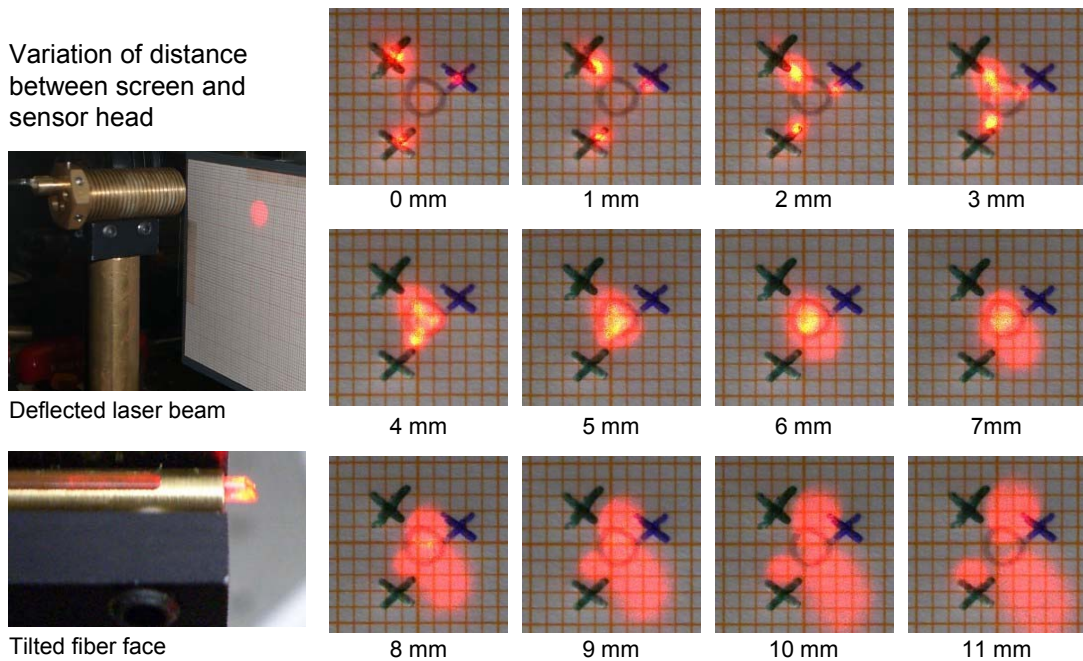


Figure IV-20: Demonstration of the probe volume definition. HeNe-laser light is coupled into all three fibers and the spatial power distribution is observed on a piece of paper in varying distances in front of the sensor.

1.5 Fully functional fiber-optic spark-plug sensor

In various experimental tests the copper-body prototype enabled the best possible reduction of interfering sapphire fluorescence and stray-light and was approved for the application of the tracer-LIF concepts. With a few performance enhancing and mechanically necessary alterations the multi-channel concept (optical design by ITO) could now be implemented into a fully-functional FOSP. The requirements of high temperature and pressure do not leave a big choice of materials for the FOSP. The only suitable combination is sapphire optics in a titanium body. Sapphire is the second hardest material after diamond and has an extreme chemical resistance. Because of its high transparency and high refractive index in the UV it is the ideal material for the microoptics, i.e. the curved sensor windows. Titanium is the only metal that has a similarly high tensile strength (even at high temperatures) as sapphire, is light weight, extraordinarily corrosion resistant and able to withstand extreme temperatures.

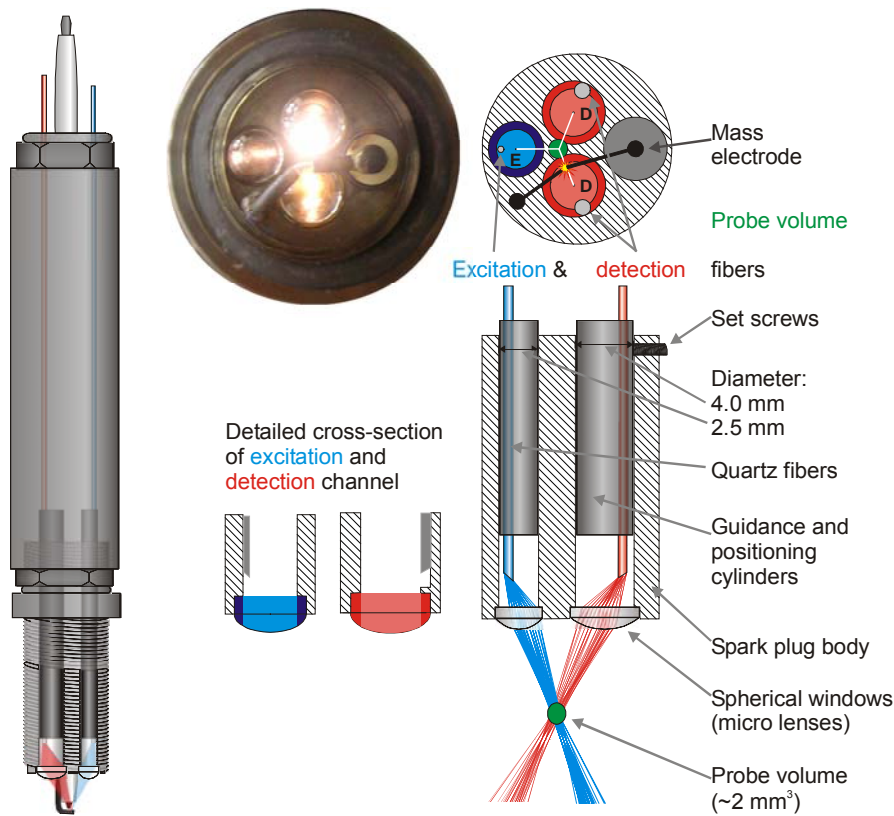


Figure IV-21: Schematic view of the integration of microoptics and fibers into the FOSP.

Based on the fundamental considerations described before we used the available space in the modified spark plug for an arrangement of two detection windows (3 mm diameter each) and one excitation window (2.5 mm diameter) symmetrically at adjacent positions. Maximum window diameters increase the angle between the beams and therefore help to limit the measuring volume and increase the collection of fluorescence light up to a diameter defined by the fiber. For excitation we use an aluminum-coated all-silica fiber with a core diameter of 400 μm . It showed the best resistivity against temporary laser energy peaks or hot-spots in the laser profile. For convenient fiber adjustment the fibers are fixed in a duct along titanium cylinders. With the help of these adjustment cylinders the fibers are positioned off-axis in spark-eroded gaps that extend to about 1 mm above the windows. The mounting of the windows is

not affected by this gap. Because of the similar expansion coefficients of titanium and sapphire the windows can be pressed into the FOSP body and sealed by a thin gold gasket. A detailed schematic view of the channel positions and the optical fiber adjustment is shown in Figure IV-21. The FOSP was manufactured by FOS-Messtechnik GmbH in Schacht-Audorf, Germany. Figure IV-22 shows some assembly parts of the FOSP.



Figure IV-22: Selected photos of some FOSP parts and the assembled sensor head. Top row: positioning cylinders with optical fibers, tilted fiber end. Middle row: Raw sensor body, disk with pressure-resistant spherical lenses, adjustment of assembled spark plug. Bottom row: Fully functional FOSP.

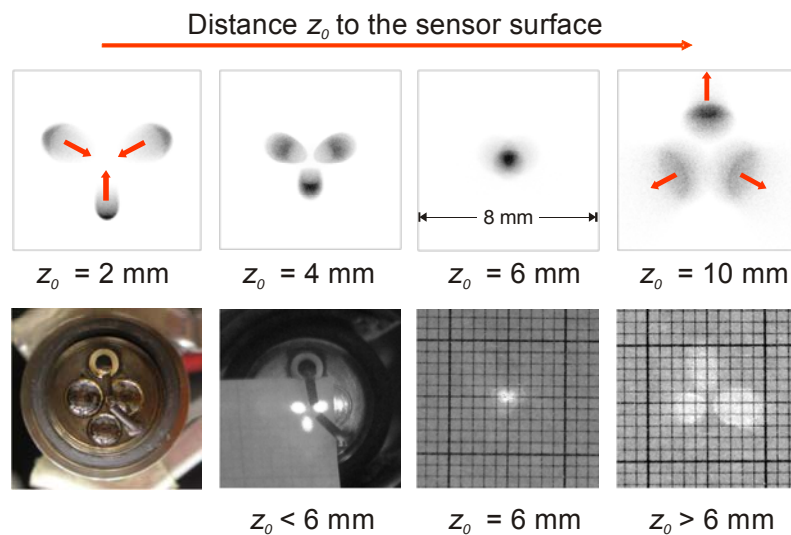


Figure IV-23: Simulation of the power distribution in several planes in front of the sensor. The overlap corresponds to the resulting signal power. That way, the measuring volume is defined. (top) Front view of sensor and experimental validation of the probe volume definition (bottom) (cf. [91]).

The FOSP is modularly constructed for the flexible exchange of parts. This is especially important considering the limited lifetime of the excitation fiber. By the adjustability of the three fibers the probe volume position can be easily changed within a range of several millimeters. The right photo in the middle row of Figure IV-22 shows the sensor head while the probe volume position was adjusted. Figure IV-23 shows the probe volume definition in comparison to the simulation (top). With the symmetrical layout of the lenses a slightly more accurate definition of the probe volume could be achieved ($\sim 2 \text{ mm}^3$). More detailed information about the optical design, simulation and realization of the FOSP was published in [91].

For future applications with appropriate laser sources the excitation peak powers can be reduced by longer pulse durations and more homogeneous beam profiles (e.g., seeded lasers). This would not only entail a longer lifetime of the excitation fiber, but would also allow for the use of a smaller excitation fiber and thus larger possible deflection angles. That way the lateral position of the measuring volume could be set further towards the detection windows and the probe volume could be reduced.

2 Hybrid UV endoscope

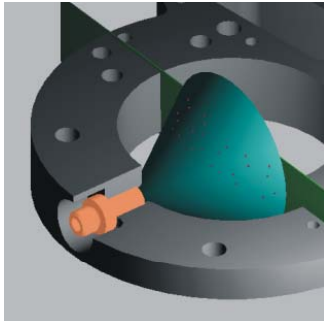


Figure IV-24: Schematic example of endoscope application.

The presented multi-wavelength imaging system is designed for UV-LIF diagnostics in cavities with limited optical access. The focus is set on IC engine applications. The endoscope was built to fit into a cylinder-wall-socket for optical access previously used by *Volkswagen* for measurements with standard endoscopes (for visible light) and with a commercial UV endoscope (*LaVision*). Therefore, the diameter of the endoscope was restricted to one centimeter. In spite of this small “keyhole” the endoscope achieves a very good light collection efficiency with high resolution over a broad spectral range. In comparison with a commercial UV endoscope the new hybrid UV endoscope yields about ten times higher signal sensitivity. This is enabled by means of an optical system that was designed and realized by the Institut für Technische Optik (ITO) at the University of Stuttgart, Germany. It comprises a small, uncorrected “front endoscope” and hybrid relay optics. These relay elements are referred to as “hybrid”, because a combination of a standard refractive lens and a diffractive optical element (DOE) is used in each relay element for the correction of spatial and chromatic aberrations over a broad spectral range. This chapter describes the construction of the hybrid UV endoscope laid out for the detection of toluene- and 3-pentanone-LIF signals. It can also be adapted for the detection of other wavelength, though. Information about the UV endoscope was published in [92], with the focus on optical design and computer simulation.

2.1 Specifications and requirements

Because of the limited choice of optical materials for the UV range and their high dispersion in this spectral range, it is a challenging task to build UV optics in general. Downsizing for endoscopic application does not make it easier and an engine environment imposes further restrictions. These are the requirements the endoscope has to fulfill for UV-LIF imaging applications in an engine:

- Entry diameter: 10 mm
- Observed area: $30 \times 30 \text{ mm}^2$
- Object distance: 35 mm (to sealing window in the cylinder wall)
- Detector size: 25 mm diameter (intensified CCD camera)
- Paraxial magnification: 0.5
- Resolution: better than 100×100 pixel
- Detection wavelength range: 275 – 350 nm and 380 – 440 nm
- Robust sealing towards combustion chamber (peak pressures over 100 bar and temperatures up to 3000 K.)

2.2 Optical design and computer simulation

On the one hand the demanding requirements of a minimal-invasive wide-angle system with a long distance between object and detector must be met. On the other hand, only a small, light-weight endoscope is feasible for the application in a production-line engine. Therefore, the optical concept was laid out as a multi-stage system: The front endoscope is fixed in the cylinder wall of the engine. It consists of only two quartz lenses and an additional replaceable field lens that deflects the uncorrected image towards large multifunctional relay optics (50 mm diameter). These relay optics are set in a fixed position with the camera(s) in a safe distance (20 cm) from the engine. Spacial and chromatic aberrations are corrected for by means of diffractive optical elements (DOEs) that are integrated in the relay optics. The principle of this multi-stage concept is illustrated in Figure IV-25.

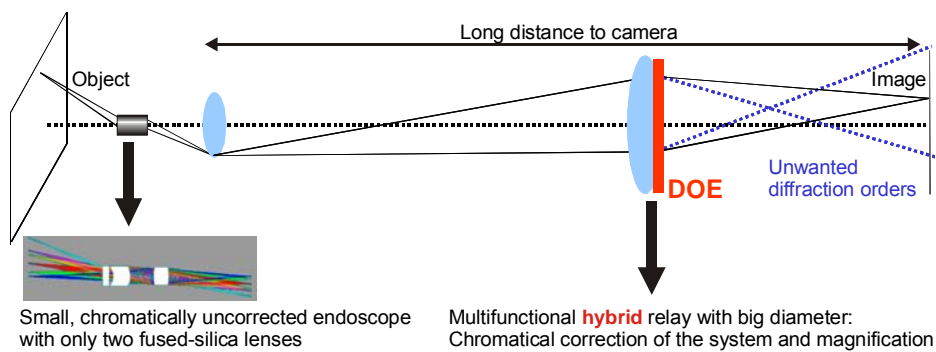


Figure IV-25: Design concept with simple front endoscope and main correction in the hybrid relay.

2.2.1 Chromatic correction by diffractive components

The chromatic correction of the final image is achieved by the strong negative dispersion of a diffractive collection lens in the hybrid relay. This negative dispersion with an Abbe-number of -3.45 is a property of all optical elements that deflect light by diffraction (cf. Figure IV-26). Unfortunately, there is not only the first order of diffraction, but also further orders that can lead to unwanted effects. These effects are strongly reduced by an optimized phase-modulation of the blaze structure of the DOE and its relative position to the refractive lens in the relay. This adaptation of the DOE on a limited spectral detection range enables the suppression of unwanted diffractive orders. Only a small amount of light from interfering unwanted diffraction orders hits the detector.

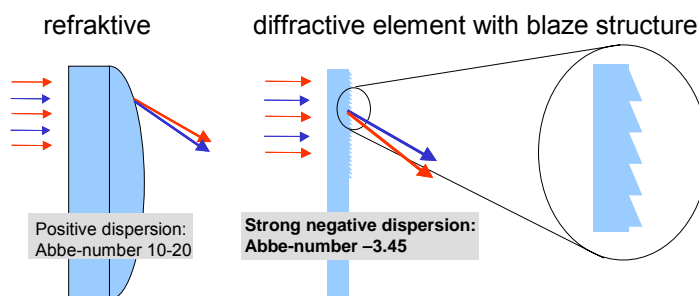


Figure IV-26: Principle of chromatic correction by means of the negative dispersion of diffractive optical elements.

Figure IV-27 shows the computer simulation (*Zemax*) results for a chromatic correction in the spectral range from 275 – 350 nm (i.e. the toluene-LIF spectrum). The focal spot has a minimal diameter at two optimized wavelengths at the boundaries of the detection spectrum. The simulated intensity distribution of an imaged line pattern shows that also the spectral region in between has a good resolution. Because of the negative dispersion of the DOEs, in combination with a refractive lens in the relay optics a “turnaround” of the focal position is achieved that minimizes the deviation from the desired focal position over the entire wavelength range.

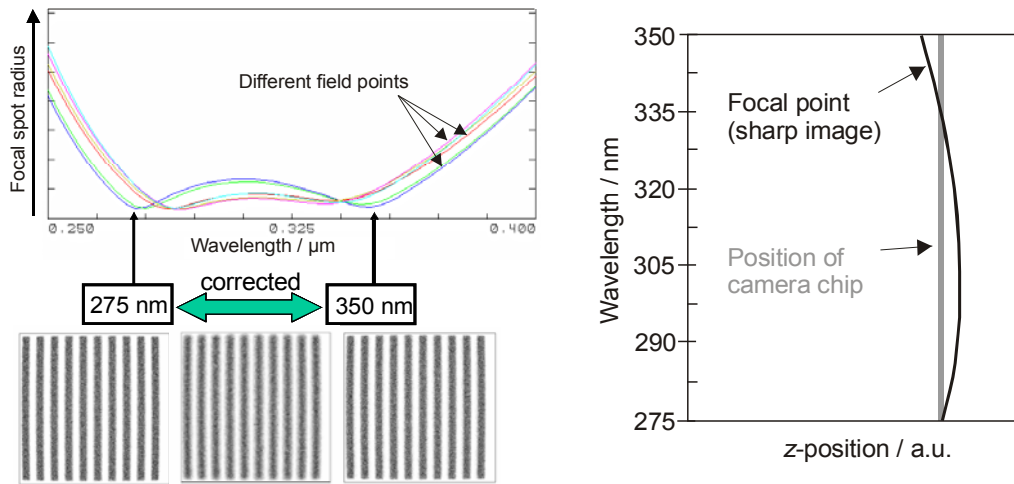


Figure IV-27: Chromatic correction in the desired spectral range. The focal spot has a minimal diameter at two optimized wavelength (left, top). The simulated intensity distribution of a line pattern shows that also the spectral region in between has an acceptably good resolution (left, bottom). This is to blame on the “turnaround” of the focal position (right), because of the negative dispersion of the DOEs (cf. [92]).

2.2.2 Optical setup

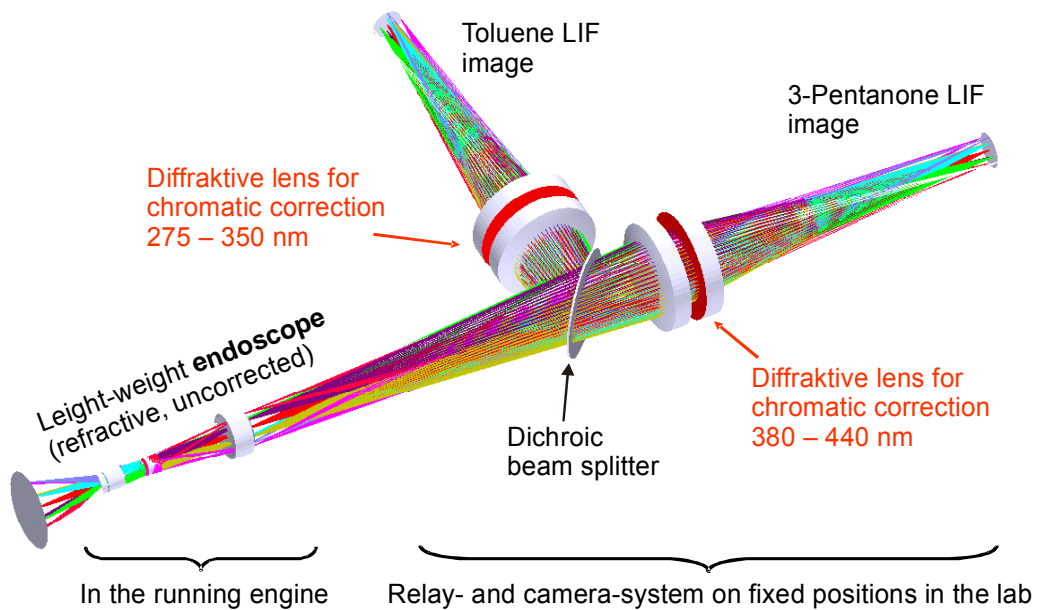


Figure IV-28: Computer simulation of the complete hybrid endoscopic UV imaging system with two relay elements for two different spectral detection regions (i.e. for toluene- and 3-pentanone-LIF signal detection) [92].

The setup was designed for simultaneous acquisition of 3-pentanone-LIF (380 – 500 nm) and toluene-LIF (275 – 350 nm) signals. A dichroic beam splitter in combination with other optical filters defines the two imaging channels (cf. chapter V 4.2.1). The multifunctional hybrid relay in each channel is adapted to the specific spectral detection region. Apart from its correction on chromatic aberrations, the optimized aspheric phase function of the diffractive elements also corrects on further aberrations of the system. In the final engine application the front endoscope will be fixed in the engine and thus vibrate relative to the stationary relay optics and cameras. Therefore, the system is corrected for a relative movement of 0.5 mm in x -, y - and z -direction between endoscope and relay. A 3D-plot from *Zemax* is shown in Figure IV-28. It illustrates the arrangement of the optics for a two-camera experiment through only one “keyhole” in the engine.

2.3 Realization

Figure IV-29 shows a selection of photos of the endoscopic imaging system delivered by ITO. The refractive lenses and the mountings for both the front endoscope and the relays were manufactured by *Sill Optics*, Wendelstein, Germany. The steel employed for the front endoscope matches the thermal properties of the steel the pressure tight engine socket is built of. The diffractive elements were manufactured and characterized at ITO.



Figure IV-29: Hybrid endoscope system: Front endoscope (left), front endoscope with demounted field lens (top middle), looking through the endoscope (top right), disassembled relay element with refractive (left) and diffractive (right) lenses (bottom middle), relay element (bottom right).

The experimental setup for a characterization of the endoscopic optics was established at ITO in Stuttgart. The setup provided a spectrally-adjustable but spatially invariable illumination of a target and the acquisition of test images on a UV-sensitive CCD camera (Figure IV-30, top). Isotropic fluorescence light was simulated by an integrating, so called Ulbricht sphere that ideally emits light with Lambert-radiation characteristics. A high-pressure Hg lamp and a spectrometer provided the wavelength selection. Single images at different wavelengths are recorded, and subsequently added with different weights to simulate a polychromatic image

for a given spectral distribution. This image (cf. Figure IV-30, bottom) is analyzed in order to determine the respective polychromatic resolution. That way, a square wave response >0.8 is obtained within an object diameter of 30 mm for a constant spectral power distribution inside the respective spectral range. This resolution could be maintained even with variations of ± 0.5 mm in x , y , z between the front endoscope and the relay (simulating engine vibrations). According to these measurements the broadband resolution of the new hybrid endoscope is better than the resolution of a commercially-available UV endoscope.

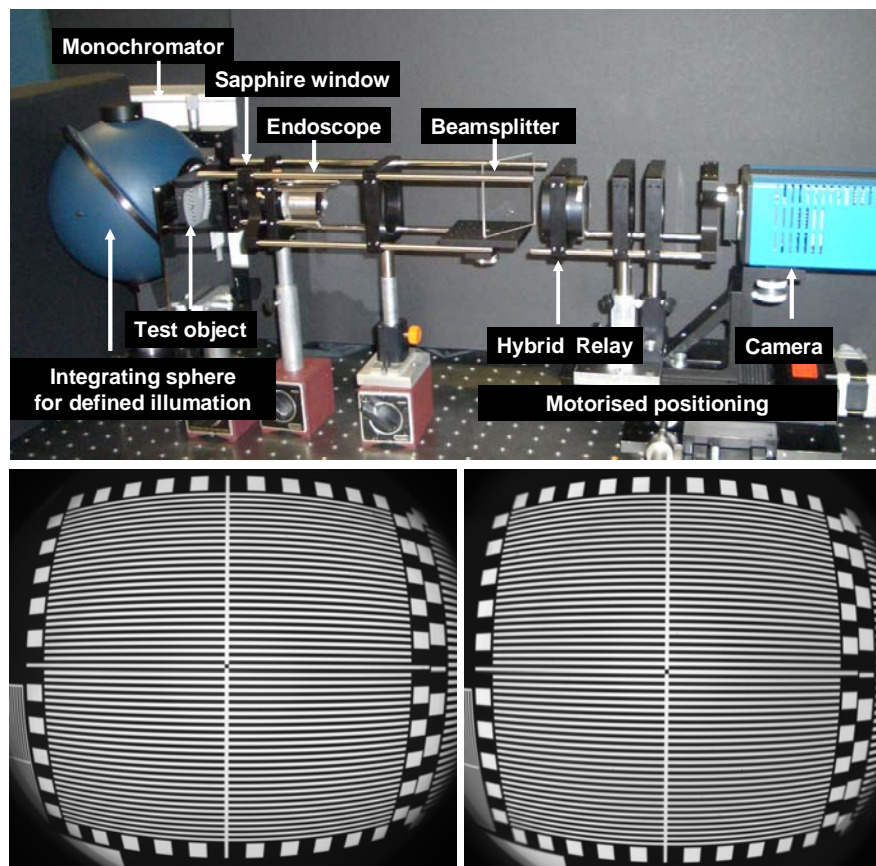


Figure IV-30: Top: Experimental setup for the characterization of the hybrid imaging system at ITO. Bottom: Polychromatic test images (object 30 x 30 mm² with a test pattern of 100 lines). Single-wavelength measurements of 285, 313 and 335 nm (left) and 380, 400, 420 and 440 nm (right) are overlaid. (Results from ITO)

With the setup shown in Figure IV-30 (top) at ITO the efficiency in light collection of the hybrid endoscope was compared to that of a commercial UV endoscope (*LaVision*) and a commercial 105 mm UV lens (*Nikkor*). With an arrangement leading to a similar paraxial object magnification at 313 nm (Hg line) the new hybrid endoscope collects about 1.4 times more amount of light than the *Nikkor* lens (1.8 times more with improved aperture) and up to seven times more than the commercial endoscope. In chapter V 4.1 toluene LIF measurements are presented that show similar results. Over a broader spectral detection range (280 – 440 nm) the relative efficiency in light collection of the hybrid endoscope is even better. In comparison to the *Nikkor* lens about twice the amount of light is gathered and for the commercial endoscope a factor >10 is obtained. (All values are preliminary results from ITO).

3 Endoscopic excitation optics

LIF diagnostics require laser excitation. For a complete minimal invasive LIF-diagnostics system both, endoscopic signal detection and generation must be considered. In this section two microoptical beam-shaping optics are introduced that have an outer diameter of $D = 9$ mm. They convert an incoming high-power Gaussian UV-laser beam into (i) a divergent homogeneous excitation lightsheet and (ii) an inhomogeneous beam pattern for flow-tagging applications. Both optics have been designed and realized by ITO according to our specifications. They are adapted to fit into a cylindrical steel housing with an outer diameter of only nine millimeters. Figure IV-31 illustrates the size of the endoscopic excitation optics compared to a standard pen. The steel housing mounts cylindrical lenses inside a square, spark-eroded carrier channel (Figure IV-31, bottom). Exchangeable spacers between the optical elements enable an adaptation to different excitation wavelengths. The required diffractive and aspheric refractive optical elements were made by ITO. The mountings were manufactured by FOS-Messtechnik GmbH in Schacht-Audorf. They also processed the commercial lenses to fit into the carrier. The design of the endoscopic excitation optics is published in [93].



Figure IV-31: Photos of the endoscopic excitation optics ($D = 9$ mm): Side view in comparison to a pen (left); front view of the beam exit (right); demonstration model of homogeneous excitation optics interior, mounting channel with lenses and spacers (bottom).

3.1 Homogeneous excitation

Figure IV-32 shows the design of the homogeneous excitation optics and its simulated and measured intensity profile. The divergent top-hat profile is generated by two refractive cylindrical lenses (1 and 4). Lens 1 has an optimized aspheric shape for the conversion of the incoming Gaussian laser beam into a beam with homogeneous power distribution. Lens 4 is a commercial plano-concave cylindrical lens ($f = -8$ mm) providing a 22° divergence angle of the lightsheet relative to the beam axis (i.e. 44° opening angle of the lightsheet “fan”). The lightsheet (width < 0.5 mm) is generated by two commercial cylindrical lenses (2 and 3) that form a telescope. At high laser energies, especially with an inhomogeneous laser profile and hot-spots, the last divergent lens (4) is likely to be harmed by the high laser power density. In experimental tests with the 4th harmonic of a Nd:YAG laser at 266 nm (8 ns/pulse) a total power

of 10 mJ/pulse was transmitted without damaging the optics. For an excitation laser beam with a smooth Gaussian profile the damage threshold of the excitation optics can be as high as 20 mJ. In chapter V 4.1 experiments with the new excitation optics are presented.

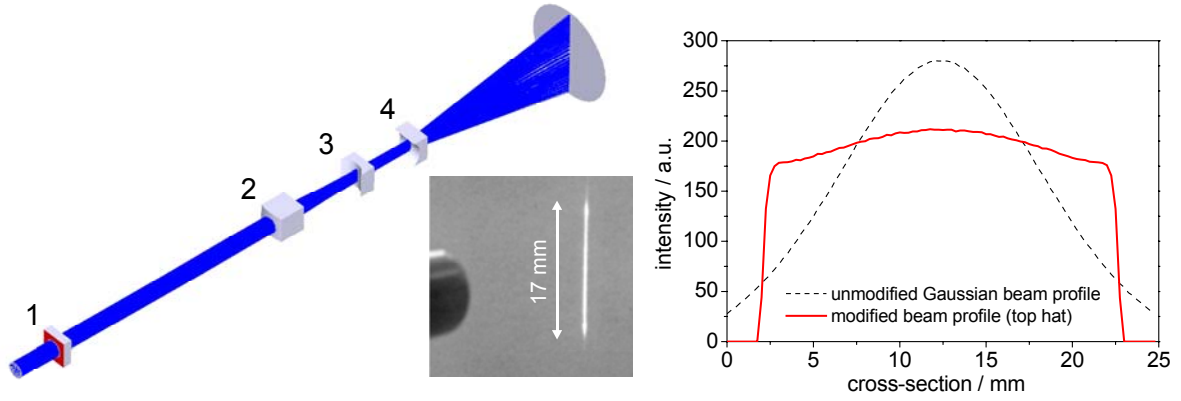


Figure IV-32: Left: Computer simulation of homogeneous excitation optics with refractive elements for the conversion of a Gaussian profile into a top-hat profile (1 and 4) and telescope optics for the generation of a lightsheet with 0.5 mm width (2 and 3). Middle: Resulting intensity profile on a white sheet of paper. Right: Simulated intensity profile in 25 mm distance after the beam exit.

3.2 Inhomogeneous excitation

The microoptics for inhomogeneous excitation were designed for flow-tagging applications. As illustrated in Figure IV-33 the optics transform a high-power laser beam into five separate spread lines with a maximum diameter of 0.5 mm each. For the generation of this inhomogeneous excitation pattern the ITO in Stuttgart created a diffractive optical element (1a). In order to increase the damage threshold of the optics (in comparison to a standard approach, e.g., with a Dammann grating), an optical element with five diffractive microlenses covers the whole incoming beam diameter of 4 mm (cf. [93]). Each microlens creates a convergent beam with a diameter of ~ 0.5 mm in the measuring z -distance (30 – 50 mm).

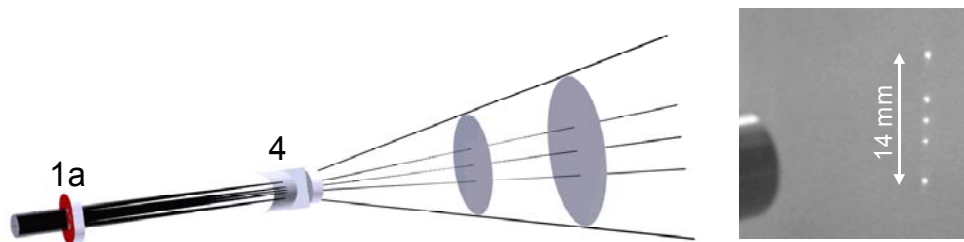


Figure IV-33: Design (left) and illumination pattern (right) of the microoptics for inhomogeneous laser excitation. The diffractive element (1a) comprises five diffractive microlenses. The diverging plano-concave lens (4) is the same as used in the optics for homogeneous excitation.

Note, that in this case telescope optics are not necessary for beam collimation in contrast to the design of the optics for homogeneous excitation. The microlenses are sufficient, because of the smaller individual sub-apertures. For an equal energy distribution on the single beams, the sizes of the sub-apertures differ according to the included power in the covered cross-section

of the incoming Gaussian beam. Aberrations are corrected for by different phase functions in x and y of each diffractive lens. For the generation of the required divergence, the same plano-concave lens (4) is used as for the homogeneous light-sheet optics. In experimental tests with the 4th harmonic of a Nd:YAG laser at 266 nm (8 ns/pulse) the optics transmitted a total power of up to 5 mJ/pulse. Successful flow-tagging experiments were performed using the phosphorescence of biacetyl (cf. chapter V 4.3).

4 Outlook

FIBER-OPTIC SPARK PLUG

The presented concept of a fiber-optic spark plug with separated excitation and detection channels works best for a flexible probe-volume definition and an optimum suppression of straylight in the detection channel. Also the detection of interfering signals from laser-induced color centers in the excitation fiber and sapphire fluorescence from the excitation channel window are effectively suppressed. However, further investigation must be done regarding a complete elimination of interfering sapphire fluorescence. In chapter V 2.5 possible ways of improvement are suggested. The development of the electronic control and realization of a trigger unit for the detector module is not finished, yet. This control unit includes a gating function to automatically shut off the sensitive photomultipliers just before light-intense events like ignition or flame luminescence could harm the photomultipliers. A computer-based control system is currently being implemented. For most measurements with the fiber-optic spark plug (e.g., in the experiments in chapter VI 3 and V 2) a flashlamp-pumped Nd:YAG laser was used. In future experiments with other laser sources like seeded Nd:YAG lasers or diode-laser-pumped solid state lasers, high-repetition fiber lasers or lasers with longer pulse durations, more excitation energy can be coupled into the probe volume and high-repetition in-situ measurements will be possible. A patent on the optical concept of the fiber-optic spark plug in combination with UV-LIF diagnostics is pending.

HYBRID UV ENDOSCOPE

As shown in chapter IV 2.3 the new hybrid UV endoscope has a superior light collection efficiency and good resolution for spectrally broad detection in the UV. Currently available, there is no commercial product with comparably good characteristics and the advantages of the flexible and modular design of the hybrid endoscope. This is confirmed in the demonstration experiments shown in chapter V 4. Therefore, a commercialization of the hybrid UV endoscope is planned.

V EXPERIMENTS IN HEATED GAS FLOWS

In order to show the feasibility of various tracer-LIF concepts with our new microoptical devices a series of measurements was performed in a heated atmospheric-pressure gas flow under well-defined laboratory conditions. Section 2 of this chapter demonstrates the proper function of the fiber-optic spark plug in combination with the detector cascade and novel filter combination. This includes the demonstration of the two-color thermometry method (chapter III 3.2.2) and oxygen-concentration measurements via the two-tracer technique described in chapter III 3.1.2.

Section 3 shows highly time-resolved 3-pentanone- and toluene-LIF measurements with the aim of providing data for the development of energy-transfer models. The measurements were performed with the fiber-optic spark-plug sensor and the results look promising for an application of toluene-LIF lifetime measurements as a concentration-independent technique for the simultaneous determination of temperature and oxygen partial pressure, especially in combination with the prevailing LIF techniques.

Section 4 then features the new hybrid UV-endoscope and micro-invasive excitation optics. The endoscope is compared to a commercial UV lens and an UV endoscope. Flow mixing processes are observed and the oxygen distribution in a plane through a room-temperature gas flow is visualized via 3-pentanone and toluene LIF (chapter III 3.1.2). Additionally, a new flow-tagging technique by means of toluene sensitized biacetyl phosphorescence is presented.

1 General setup for experiments with a heatable flow nozzle

All of the experiments in this chapter were performed in non-reacting gas flows with a setup using the flow nozzle shown in Figure V-1 (*Sylvania heater, model 014683*). The nozzle exit is 1.7 mm in diameter. The nozzle is surrounded by an aluminum tube with 50 mm diameter for the creation of a coflow that prevents the flow from mixing with ambient air and thus provides defined conditions. The flow through the nozzle was electrically heated to 295 – 700 K by varying the applied heating voltage. After calibration, for a set flow speed the exit flow temperature could directly be derived from this applied voltage. In some experiments a simultaneous temperature control via a K-type thermocouple was possible. The gas composition was adjusted by mass flow controllers (*Tylan*). In most experiments the desired tracers were seeded to an atmospheric-pressure nitrogen gas flow using fritted wash bottles. That way, maximum tracer concentrations equivalent to the respective vapor pressure were achieved, assuming the flow through the bottles was kept slow enough. The final tracer concentration was set by diluting the seeded flow with known amounts of nitrogen and/or oxygen.

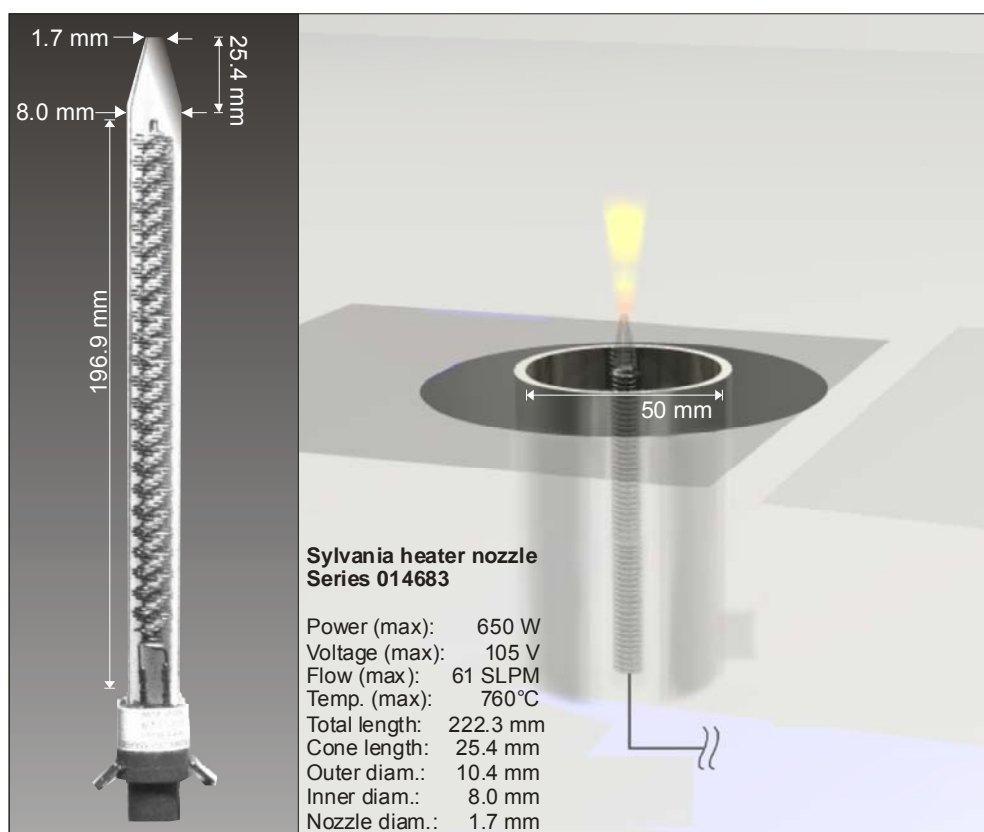


Figure V-1: Heatable flow nozzle (left) and setup of the nozzle surrounded by an unheated coflow (right).

2 Demonstration experiments with fiber-optic spark plug

2.1 Experimental setup

In all experiments, except for the lifetime measurements, the 4th harmonic of a Nd:YAG was used for fluorescence excitation of the tracers toluene and 3-pentanone. The 266 nm, 8 ns laser pulses were coupled into the excitation fiber as described in chapter IV 1.2. The FOSP sensor was fixed on an x -, y -, z -translation stage for an ideal adjustment of the sensor probe volume with the flow directly above the flow nozzle. The fluorescence signals were guided through two fibers to the channel-photomultiplier detection unit and/or to a spectrograph. All signals were digitally recorded.

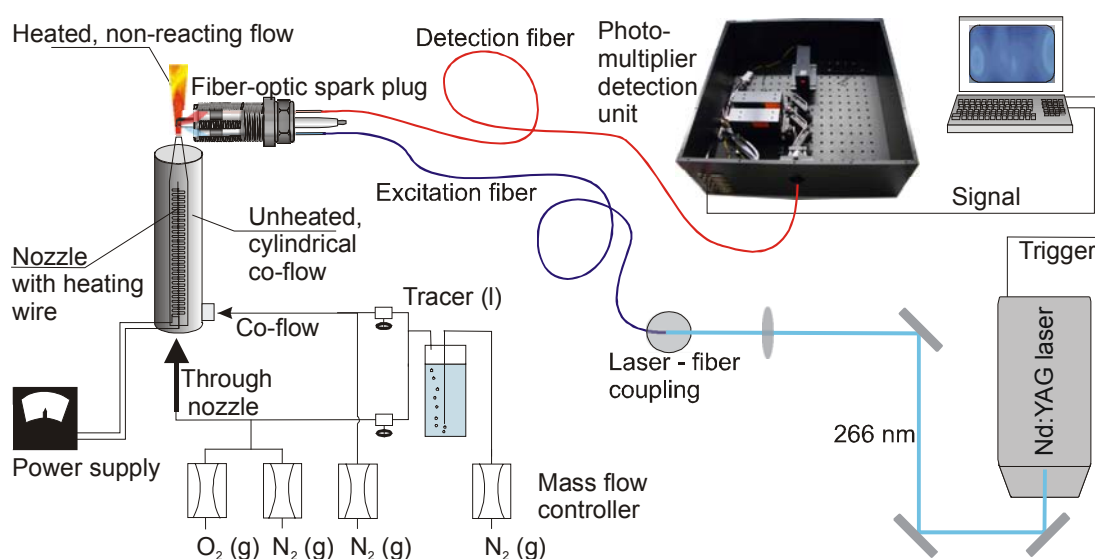


Figure V-2: Experimental setup for measurements with the fiber-optic spark-plug sensor in a heated flow.

2.2 Measurement of tracer concentrations

Although saturation effects were not expected with excitation energies of less than 1 mJ in the 2 mm³ probe volume, the first experimental tests simply checked the linearity between tracer concentration and detected signal. These tests were performed with 3-pentanone and toluene in 1 bar nitrogen gas for a range of tracer partial pressures relevant for subsequent applications (0 – 20 mbar). Simultaneously, that way, the linearity of the used detectors could be tested, i.e. the intensified CCD camera (*LaVision, FlameStarII*) behind the spectrometer (*Chromex*), the photomultiplier (*Hamamatsu, 1P28*) and the channel photomultipliers (*Perkin-Elmer, CPM MH1943*, cf. appendix IX 2). In all tests a satisfying linear behavior was found. Sometimes with an offset due to various kinds of background signals, that could be subtracted. With suitable filters, in most cases a line through the origin was measured. It is not worth showing several straight lines through a bunch of measured data points. Therefore, only one exemplary measurement will be presented here: Figure V-3 illustrates spectrally resolved LIF measurements of toluene in pure nitrogen. The fluorescence was measured with

the spectrometer and the intensified CCD camera. The left graph shows four toluene spectra for different toluene partial pressures. On the right, total integrated LIF intensities are plotted versus the respective toluene partial pressures.

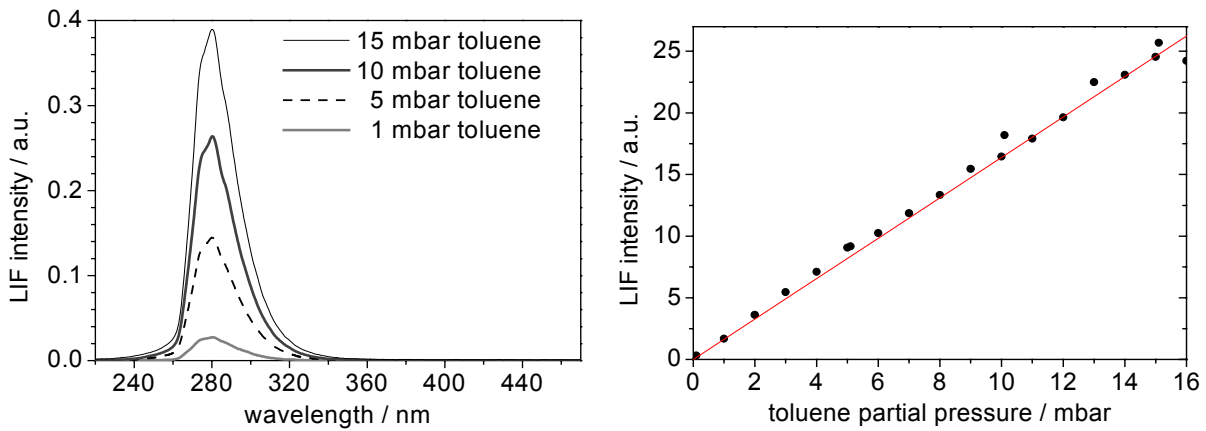


Figure V-3: Exemplary toluene LIF spectra after excitation at 266 nm for different tracer concentrations (left). Total integrated LIF intensity versus toluene partial pressure in 1 bar nitrogen.

2.3 Measurement of equivalence ratios

For the measurement of oxygen concentrations the flow was seeded with 1.4 mbar toluene and 1.7 mbar 3-pentanone. These partial pressures resemble the tracer concentrations a stoichiometric 1 bar fuel/air mixture would have with fuel containing less than 10% of each tracer. In an engine application similar tracer concentrations would be used. The partial oxygen pressure in the flow was varied from 30 to 250 mbar. The fluorescence signals were guided through the detection fibers to the photomultiplier cascade described in chapter IV 1.3.1. Due to the custom filter combination toluene- and 3-pentanone-LIF signals were spectrally separated and simultaneously detected as shown in Figure V-4. Figure V-5 shows the respective photomultiplier signals. The time resolution of the used photomultipliers is not high enough to reproduce the real LIF signal behavior. Thus, the width of a curve in Figure V-5 basically resembles the system response time. Nevertheless, the total time-integrated signal is directly proportional to the respective LIF intensity. Figure V-6 shows fluorescence intensities versus oxygen partial pressure. The constant background signal visible in Figure V-5 was subtracted before plotting this graph. In the summary of this section the origin and influence of this still prominent background signal will be discussed in detail. The background-corrected signal is normalized on the intensity in pure nitrogen. Laser energy variation cancels out. The uncertainties of presented averaged measurements are less than 5%. Measured data (green boxes) agrees well with calculated values (black boxes) derived from filter transmission curves applied on measured spectra by Koban et al. [11]. Also shown is the comparison to imaging results (blue triangles) through the same filter combination. The respective imaging experiment will be described in chapter V 4.2. 3-Pentanone LIF (red circles) is not influenced by the oxygen partial pressure variation and indicates the local tracer concentration. If the fuel concentration in the final application (and thus the tracer concentration) was inhomogeneous, the ratio of 3-pentanone LIF and toluene LIF would yield fuel/air-equivalence ratios.

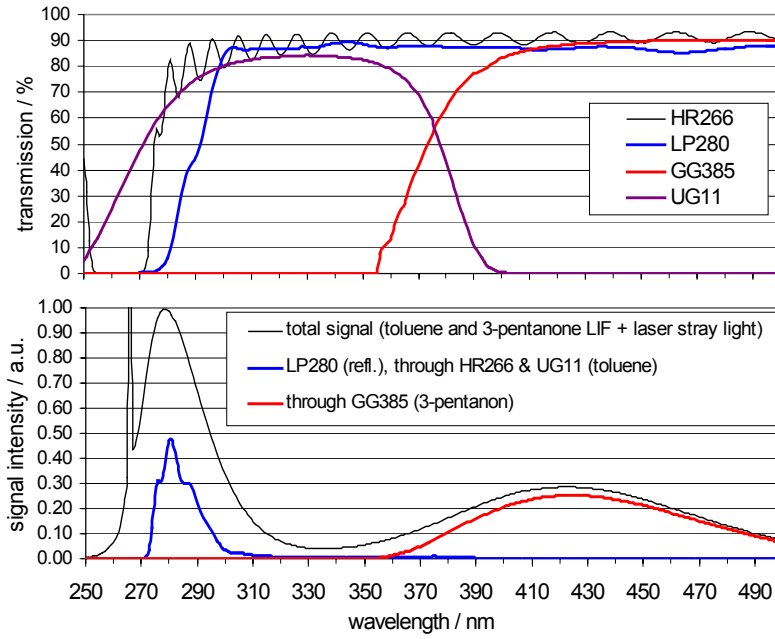


Figure V-4: Filter combination (top) and resulting spectral separation of LIF signals from toluene and 3-pentanone (bottom).

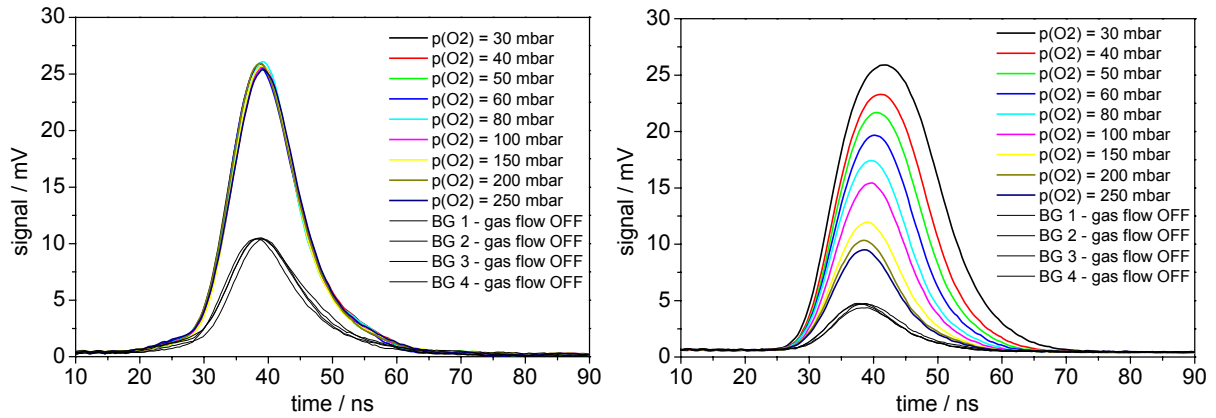


Figure V-5: Exemplary photomultiplier response to detected 3-pentanone- (left) and toluene- (right) LIF signals (average over 50 individual measurements).

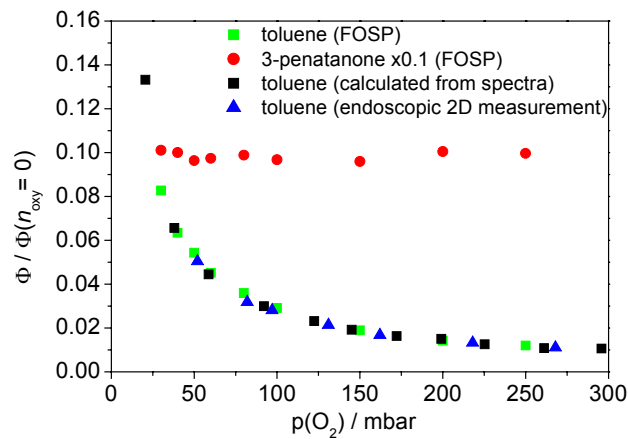


Figure V-6: Normalized fluorescence intensities. Measured data (green boxes) agrees well with calculated values (black boxes from Koban et al. [11]) and imaging results from chapter V 4.2 (blue triangles). 3-Pentanone LIF (red circles) is not influenced by the presence of oxygen.

2.4 Two-color toluene thermometry

1.2 mbar toluene was seeded to an atmospheric-pressure nitrogen flow, for the measurement of temperatures via the two-color thermometry technique described in chapter III 3.2.2. Again, this toluene concentration resembles realistic conditions for engine measurements. Figure V-7 shows the spectral regions selected by the filter combination in the photomultiplier-cascade detector module. The resulting filter transmissions can be referred to as a bandpass filter around 285 nm (BP285) for detection of the spectral toluene-LIF peak and a BP335 for detection of the long-wavelength tail of the spectrum. In Figure V-8 exemplary photomultiplier signals (averages over 50 individual measurements) are presented. In the absence of oxygen the toluene-LIF lifetimes are long enough to be resolved by the used channel photomultipliers. Therefore, for temperatures up to 200°C fluorescence lifetime information can be derived from the signals additionally to the measurement of time-integrated signal intensities. In principle the two-color method also works in the presence of oxygen, but for the long-wavelength part of the emission spectra the intensity is too small relative to its underlying background. This issue will be discussed in more detail in the summary of this section in the next paragraph. Background-corrected signal ratios (normalized on room temperature) are plotted in Figure V-9. The comparison to calculated values (filter transmission applied on measured spectra by Koban et al. [48]) shows convincingly good agreement. The accuracy of the presented measurements is about 15°C.

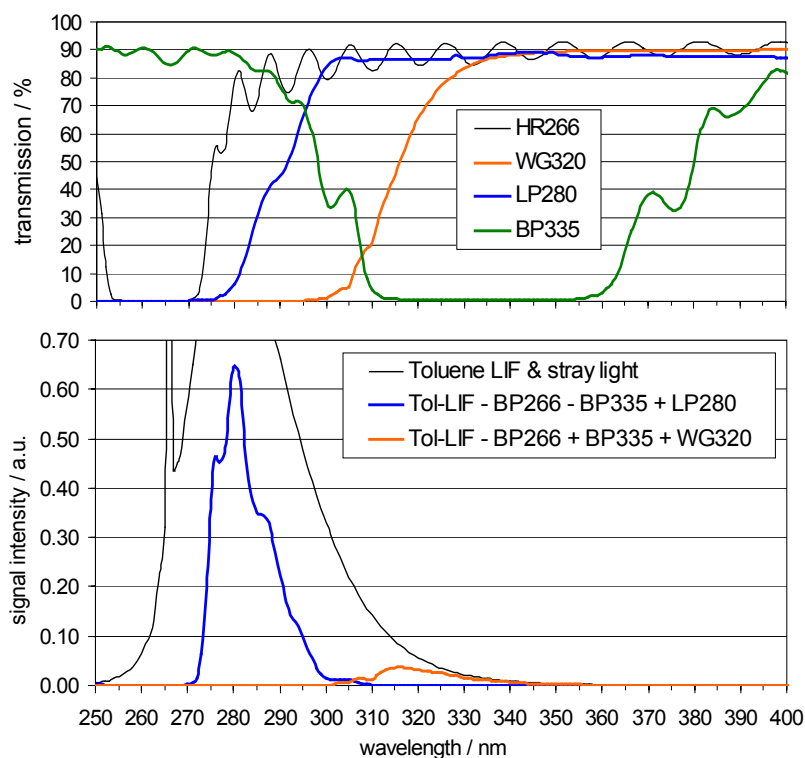


Figure V-7: Filter combination (top) and resulting separated detection of two spectral regions in the toluene LIF signal (bottom).

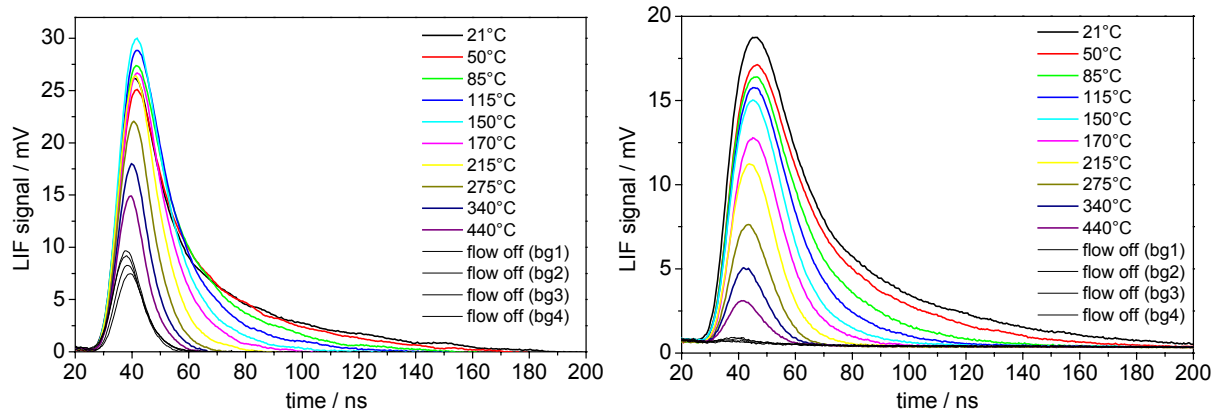


Figure V-8: Exemplary photomultiplier response to detected toluene-LIF signals (averages over 50 individual measurements). Left: Long-wavelength tail of the spectrum. Right: Spectral peak.

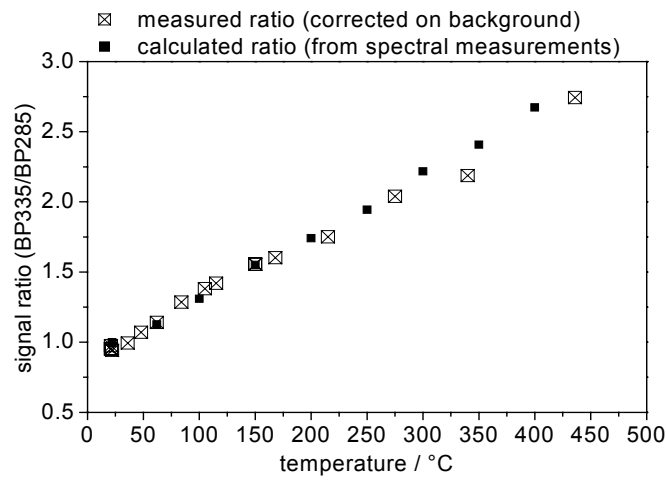


Figure V-9: Temperature dependence of toluene-LIF signal ratio (BP335 / BP285) in comparison to calculated values (filter transmission applied on measured spectra by Koban et al. [48]).

2.5 Summary and outlook

The presented results from measurements with the fiber-optic spark plug agree well with previous measurements and data from literature. The applicability of the tracer concepts for the determination of equivalence ratios and temperature was shown in lab experiments under well-defined conditions. The results suggest that quantitative tracer-LIF measurements can be performed in an IC engine with the fiber-optic spark plug, if certain restrictions are considered: The most important limiting factor is the still prominent background signal. In spite of the separation of excitation and detection channels, this disturbing background could not be completely suppressed. Although, this problem seemed to be solved in experiments with the copper-body prototype using less sensitive detectors, several experiments now suggest that the origin of the background signal remains the sapphire fluorescence, predominantly from the excitation window. One indication is the spectral power distribution of the background signal on the three spectrally different detection regions. The fact that the background signal vanishes when exciting externally (not through the sapphire window) is the prove for its origin in the excitation channel (cf. Figure V-10). Fluorescence light from the excitation window

can directly hit the detection windows, because the curved windows slightly protrude from the sensor body. Although the acceptance angle of the window would not allow a direct light-collection into the detection fiber, there is a certain amount of light, that gets scattered in a way to be coupled into the detection fiber, anyway. A barrier between the windows (thin, 2 mm high aluminum plate) strongly reduced the background signal, but could not completely block it. Scattering off the electrodes might be an explanation. Another possible source for the background signal could be broadband fluorescence of color-centers in the excitation fiber itself. The only solution so far is the further optimization of the sensor geometry. One idea would be to dimple the sensor windows into the body and thus block their intervisibility. Then, however, sediments from unburned fuel and soot could more easily accumulate in front of the windows and disturb the visibility.

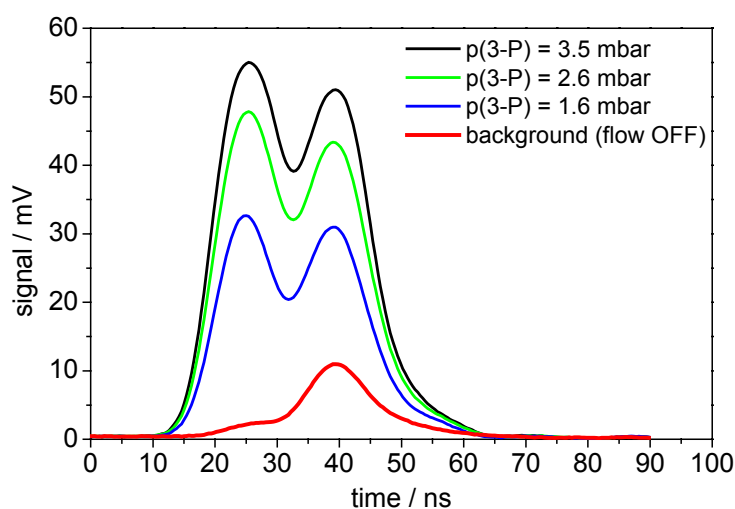


Figure V-10: Detected 3-pentanone-LIF signals with simultaneous time-advanced external excitation (left peak). The background signal almost vanishes.

3 Lifetime measurements via TCSPC with fiber-optic spark plug

The fluorescence lifetimes of toluene and 3-pentanone have been determined in the gas phase by time-correlated single-photon counting (TCSPC) with excitation of the sample by a pulsed Ti:Sapphire laser. TCSPC has become a standard method for the determination of fluorescence lifetimes in condensed matter down to 100 ps upon excitation with pulsed light sources, e.g., lasers or sub-nanosecond-LEDs (the TCSPC principle allows lifetime measurements below the duration of the excitation pulse, and if necessary the system response can be deconvoluted). In addition, TCSPC gained reasonable interest in the field of fluorescence microscopy because of the rather simple implementation of commercially-available TCSPC data evaluation boards [94] in combination with highly-sensitive avalanche photo diodes (APD). It is even suitable for the detection and identification of single molecules in solution at room temperature [95,96]. The same strategy has been adopted here to gas-phase experiments. Because of the very low excitation laser energy needed (or actually desired) this method is very suitable for use with the fiber-optic spark plug. The following experiments show, how the microoptical acquisition of fluorescence lifetimes can supply temperature and concentration information in practical applications.

3.1 Experimental setup for time-correlated single-photon counting

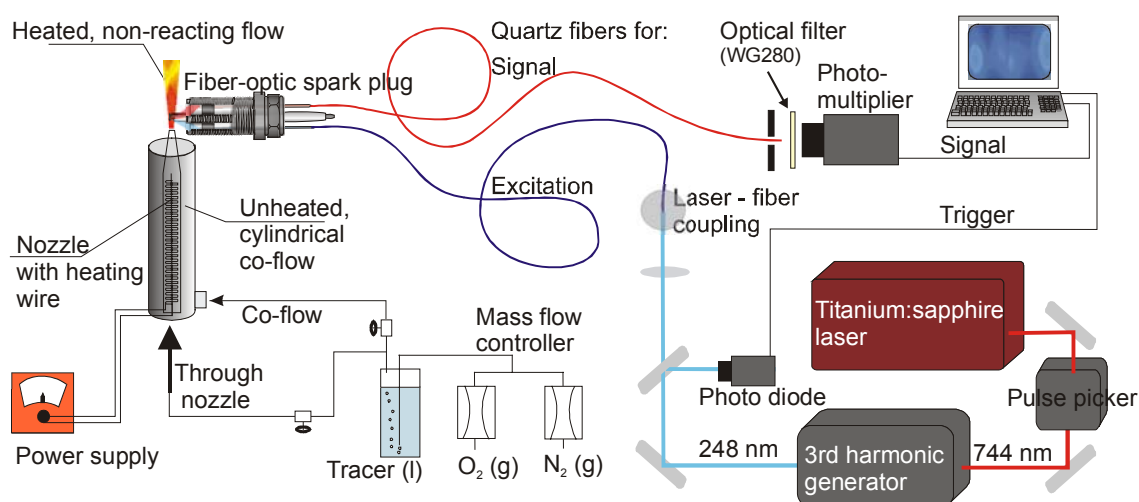


Figure V-11: Experimental setup for time-correlated single-photon counting with the fiber-optic spark plug sensor.

The experimental setup is displayed in Figure V-11. A Ti:Sapphire laser (*MIRA Optima 900-P*, Coherent) was operated at 76 MHz and 744 nm with pulse lengths of approximately 300 fs. As toluene fluorescence lifetimes range up to several tens of nanoseconds, a pulse picker (*APE, pulse select*) was used to ensure an interval of 200 – 80 ns (depending on measurement conditions) in between two successive laser pulses. A 3rd harmonic generator (*MIRA 9300*, Coherent) allowed for wavelength conversion to 248 nm. We selected this wavelength because of the frequently used 248-nm light from KrF*-excimer lasers in practical toluene-LIF imaging applications. Due to the short pulse length in the time domain, the laser has a significant broaden-

ing in the frequency (i.e. wavelength) domain. According to the manufacturer the FWHM is ~ 3 nm at 248 nm. It is, therefore, important to note that our results form an average over a wider spectral excitation bandwidth compared to nanosecond-laser sources. However, since the toluene and the 3-pentanone absorption spectra are continuous around 248 nm the introduced deviation is small for both experiments. This does not apply to toluene at 266-nm excitation which restrains the applicability of the system in that case. Fluorescence signals are detected by a UV-sensitive photomultiplier (*PMH 100, Becker & Hickl*) and processed by a TCSPC card (*SPC-132, Becker & Hickl*). TCSPC is a statistical method for lifetime measurements. After every excitation pulse statistically less than one fluorescence photon is emitted into the detection NA of the sensor. This photon is acquired together with its time delay relative to the excitation pulse. Actually, for practical reasons the delay to the next pulse is recorded, but with the pulse frequency being constant and jitter free the actual time from excitation to emitting a photon is easily calculated. Statistically there is no difference if the fluorescence signal from a molecule ensemble is detected at once or, as is the case for TCSPC, consecutively. One must ensure, however, that from the observed probe volume no more than one photon is detected per laser pulse, in order to avoid a pile-up effect: If more than one photon was emitted, always only the first one would be detected. With this special technique a system-response time

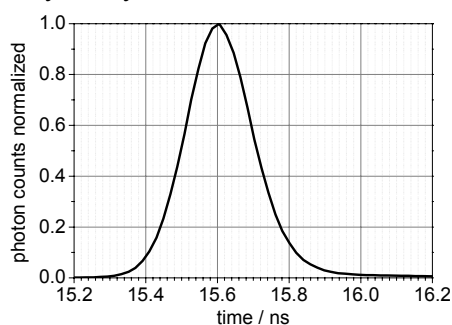


Figure V-12: System response function for TCSPC measurements.

can be achieved that is even shorter than the rise time of the used PMT. The system response function was determined from the measurement of Rayleigh-scattered laser light. The time resolution of the system is shown in Figure V-12. It was shorter than 250 ps (FWHM). A long-pass filter with 280 nm cut-off wavelength (*Schott WG280*) eliminated elastically-scattered laser light. The probe volume directly above the nozzle was defined by the optical specifications of the FOSP as described in detail in previous chapters.

Measurements without the fiber-optic spark plug, but instead with excitation by a focused laser beam and detection through a lens and a 100- μ m pinhole for NA reduction and probe volume definition were also carried out in the same setup [97]. Data from both measurements agree well within the presented temperature range. Although, with the fiber-optic spark plug a larger probe volume is observed and thus the measured temperature is rather an average over a small temperature field.

3.2 Fluorescence lifetimes of toluene LIF

Effective excited-state lifetimes of the S_1 state in toluene have been published by several groups [54,70,98], the most recent being 86 ns in the absence of vibrational excess energy [54]. Most of the measurements, however, have been conducted for low vibrational excitation and at room temperature or below (e.g., cooled jet). Only in the study of Jacon et al. [70] vibrational excitation corresponding to laser excitation at 250 nm or higher has been investigated. The time resolution of those measurements, however, was limited to >1 ns. In the experiments presented here a time resolution of ~ 250 ps was achieved. To the best of our knowledge this is the first study of toluene fluorescence lifetimes at elevated temperatures.

As expected from the photophysical model (chapter III 2.1.3) the fluorescence decay can be represented by a bi-exponential function. Lifetimes are decreasing with increasing temperature, with the long lifetime component ranging from 45 – 2 ns and the short component from 2 – 0.4 ns in the investigated temperature range. The effect of quenching by molecular oxygen could also be observed. It has a strong effect on both lifetimes, but especially on the long component. The experimental setup is shown in Figure V-11. Toluene was seeded to a nitrogen/oxygen gas flow with a total pressure of 1 bar. The oxygen concentration was varied from 0 – 100 mbar. The flow was heated to 295 – 650 K through the nozzle as described in chapter V 1. Measurements were taken directly above the 1.7-mm-diameter nozzle exit, where the flow has not yet mixed with ambient air. Nevertheless, a cylindrical co-flow with nitrogen (or the respective nitrogen/oxygen mixture) was used to keep from mixing with ambient air and ensure well-controlled gas composition. Gas exit temperatures were determined by a type-K thermocouple. As an independent check, time-integrated LIF signal intensities were measured with varying voltage and the results compared to the temperature dependence of toluene LIF that has been determined in previous measurements in a stainless-steel cell with nanosecond laser excitation [48]. The comparison showed satisfactory agreement within 10% over the investigated temperature range.

Exemplary raw data is shown in Figure V-13. Data is collected over approximately one million events (i.e. detected photons). The signal-to-noise ratio was better than 10 for all measurements and ~1000 at room temperature in nitrogen. The results show a pronounced bi-exponential behavior. The data were fitted according to a bi-exponential model:

$$I = I_0 + A_l \exp\left(\frac{-(t - t_0)}{\tau_l}\right) + A_s \exp\left(\frac{-(t - t_0)}{\tau_s}\right) \quad (\text{V.1})$$

Fit results are shown in Figure V-13 alongside the measured data. The stability of the fit was tested by using different starting parameters. Measured lifetimes are significantly longer than our system response. Hence, a deconvolution was not necessary.

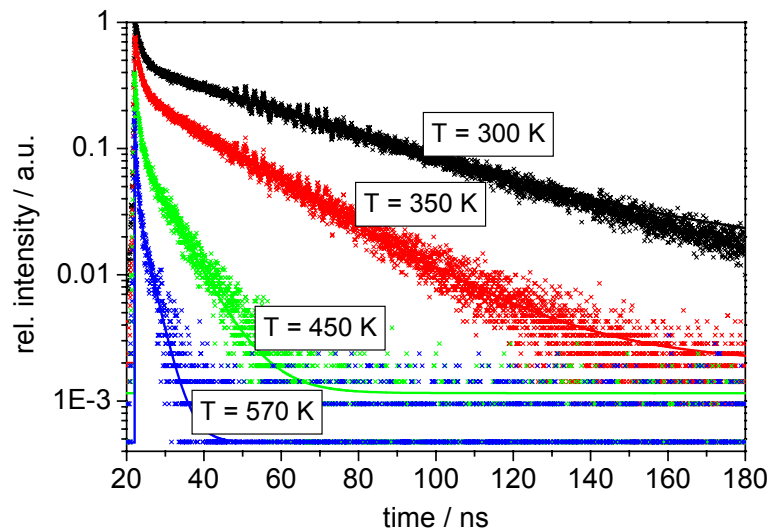


Figure V-13: Exemplary TCSPC raw data and bi-exponential fit.

3.2.1 Temperature dependence

Toluene fluorescence lifetimes in nitrogen upon excitation at 248 nm are presented in Figure V-14 as a function of temperature. The two lifetime components differ by more than a factor of ten, with the long component ranging from 45 – 2 ns and the short component from 2 – 0.4 ns in the 300 – 650 K temperature range. The only comparable data with 248-nm excitation in literature was for room temperatures at much lower pressure (0.13 – 0.66 mbar): Jacon et al. [70] measured a long lifetime component of 26 ns and a short component of 3 ns. The discrepancy between the long lifetime components could be due to vibrational relaxation to longer-living states in the case of higher pressure in our experiments. For the short lifetime component the time resolution in [70] might not have been good enough.

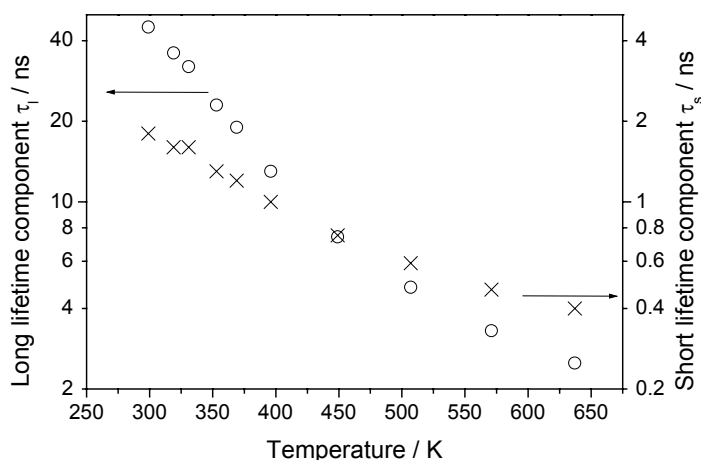


Figure V-14: Fluorescence lifetimes of toluene in a 1-bar nitrogen bath gas as a function of temperature (X: short lifetime component, O: long lifetime component).

T / K	τ_l / ns	τ_s / ns	$A_s / (A_l + A_s)$
300	45	1.8	0.56
320	36	1.6	0.60
331	32	1.6	0.60
353	23	1.3	0.65
370	19	1.2	0.67
396	13	1.0	0.71
450	7.4	0.75	0.75
507	4.8	0.59	0.78
570	3.3	0.47	0.80
637	2.5	0.40	0.81

Table V-1: Fluorescence lifetimes of toluene and their relative amplitude as a function of temperature for 248-nm excitation in 1 bar nitrogen bath gas.

The bi-exponential decay can be interpreted in terms of the “third decay channel” (e.g., [70]). This expression has been introduced in the literature and means the opening of a new decay path in addition to fluorescence and intersystem crossing above a certain energy threshold. For toluene this threshold is reached for an excitation energy corresponding to ~250 nm and can thus be seen in this experiment even at room temperature. The process through which the

molecules decay depends on the vibrational state, resulting in a bi-exponential decay function. The nature of this “third decay channel” is interpreted by Smalley [53] as internal conversion (IC) after internal vibrational randomization (IVR). With increasing temperature IVR becomes faster resulting in a decreasing lifetime component τ_s , and an increasing relevance of this fast decay channel, i.e. an increase of the ratio $A_s / (A_I + A_s)$ (cf. Table V-1). The temperature dependence of the long-lived state on the other hand is due to more effective intersystem crossing (ISC) to the triplet state. This spin-forbidden process becomes vibrationally allowed with increasing temperature.

3.2.2 Quenching by molecular oxygen

Collisional quenching by oxygen has a strong effect on both lifetimes, but especially on the long component (cf. Figure V-16, left). The time between collisions is in the order of a few nanoseconds and thus does not significantly affect the short component. Figure V-15 shows the influence of oxygen on the toluene-LIF lifetimes for three different temperatures. In the set of curves one can already see that for higher oxygen partial pressures there is no distinguishable difference in the slope of the steeper curves (with higher oxygen partial pressure). At 70 mbar oxygen partial pressure a temperature increase did not influence the long lifetime component anymore. However, it still caused the reduction of the short lifetime component (cf. Figure V-16, right).

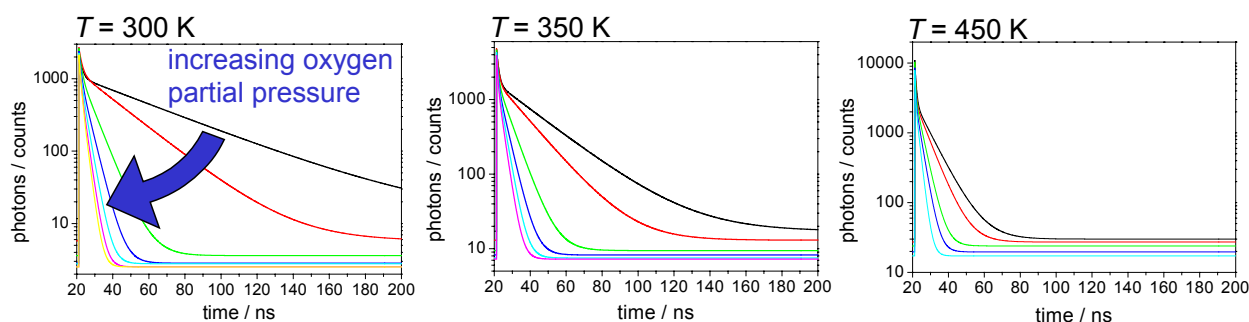


Figure V-15.: Effect of collisional quenching by molecular oxygen on toluene LIF lifetimes for different temperatures. Mainly the long lifetime component is influenced.

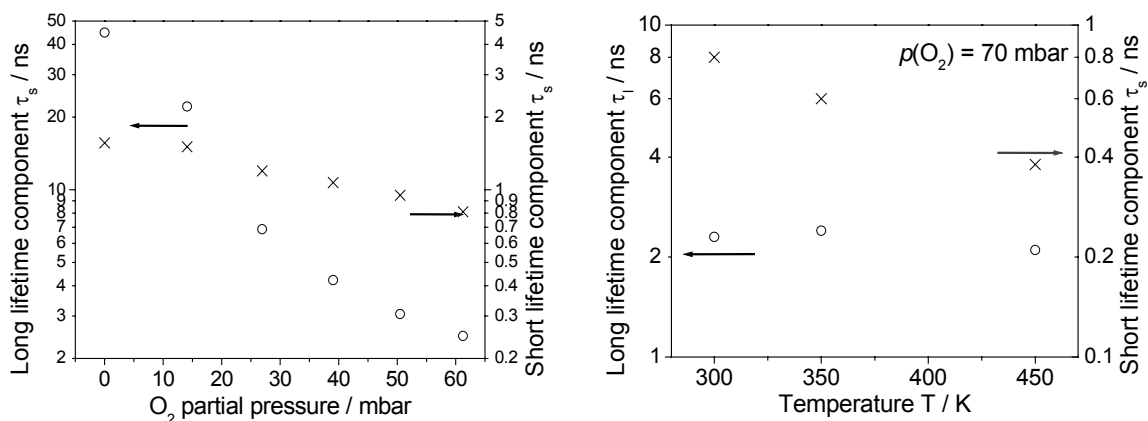


Figure V-16: Toluene fluorescence lifetime as a function of O_2 partial pressure; the long lifetime component is strongly affected by collisional quenching of O_2 (left) which causes a reduction of temperature sensitivity (right).

3.2.3 Conclusions

After excitation of toluene at 248 nm ($S_0 \rightarrow S_1$) depending on the vibrational state either ISC or much faster IC are predominantly determining the total fluorescence lifetime resulting in a bi-exponential decay. Because of strongly temperature-dependent IVR, internal conversion becomes more and more important (cf. Table V-1). In the investigated temperature range from 296 – 625 K a long lifetime component (45 – 2 ns) and a short component (2 – 0.4 ns) could be measured. The short component is not affected by collisional quenching by O_2 as strongly as the long lifetime component and thus still shows a temperature dependence even in the presence of oxygen. These results suggest the use of high-repetition-rate laser excitation of tracers like toluene in combination with time-correlated single-photon counting as a novel method for the determination of temperatures in the gas phase independent from the total fluorescence intensity and, hence, local tracer concentration. Regarding the different effects temperature variation has on both lifetime components in the presence of O_2 it might even be possible to separate temperature and oxygen partial pressure effects by recording both lifetime components which would enable the simultaneous determination of tracer concentration, oxygen partial pressure and temperature in mixing gas flows.

3.3 Fluorescence lifetimes of 3-pentanone LIF

3-pentanone lifetimes were acquired in the same experimental setup as for the toluene measurements. 3-Pentanone is not sensitive to quenching by oxygen, but has an even lower fluorescence quantum yield than oxygen-quenched toluene (in air: ~20 times lower signal). Because of the emission spectra of 3-pentanone being mainly in the visible region, the suppression of ambient room-light is a major challenge. Photons collected from this background signal show a random distribution in the time domain. Therefore this signal is regarded as noise, although it has nothing to do with the electronic noise of the photomultiplier and TCSPC-card. In order to achieve reasonable S/N-ratios, in the experimental setup maximum effort was put into noise reduction.

3.3.1 Temperature dependence

With the available time resolution no evidence for a bi-exponential decay could be found. Figure V-17 shows the temperature dependence of the fluorescence lifetime. Because of the poor S/N-ratio the single exponential fits were affected by relatively large errors of about ± 300 ps. Nevertheless, a rapid decrease with increasing temperature is visible, which is due to more efficient IS-crossing. The lifetimes measured here are similar to those found in literature with 266-nm excitation [62].

The prevailing photophysical model for 3-pentanone that is based on a single exponential decay does not explain the simultaneous effects of high pressure and temperature. Thus, we expected to measure a bi-exponential decay that could explain this discrepancy. Planned higher resolution lifetime measurements have the potential of resolving this expected bi-exponential decay, which would indicate an additional decay path similarly to the case of toluene.

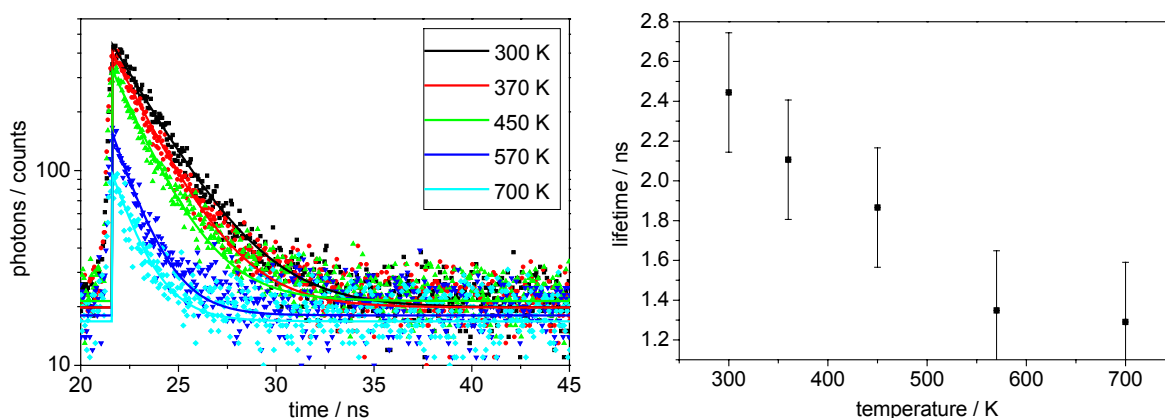


Figure V-17: temperature dependence of LIF lifetimes of 3-pentanone: exemplary raw data and single exponential best fits (left), decreasing lifetimes with temperature (right).

4 Demonstration experiments with hybrid UV endoscope

This section features the new hybrid microoptical imaging system. At first the new hybrid UV endoscope is compared to a commercial UV endoscope and a 105 mm UV lens in a standard flow application (4.1). In the results the new endoscope comes off very well: Two times more signal light is collected compared to the UV lens and almost ten times more light could be measured in comparison to the commercial UV endoscope. Additionally, for a spectrally broad detection signal our endoscope has a much better spatial resolution than the commercial endoscope. After these tests the hybrid endoscope and the homogeneous excitation optics were used in a two-camera experiment for the observation of mixing processes in a turbulent flow and the determination of local oxygen concentrations (4.2). Finally, the UV endoscope was used in combination with the inhomogeneous excitation optics to perform a new line-tagging method via sensitized phosphorescence of biacetyl (4.3).

4.1 Comparison of hybrid UV endoscope to commercial UV lenses

4.1.1 Experimental setup

For a direct comparison of the hybrid UV endoscope with two commercially available devices the experimental setup shown in Figure V-18 was used. A turbulent atmospheric pressure nitrogen flow was seeded with 5 mbar toluene. A lightsheet (266 nm, 8 ns, 10 mJ) was generated and guided through the flow by the microoptical excitation optics. The resulting laser-induced fluorescence was detected simultaneously with both, the hybrid UV endoscope and the respective commercial optics. The distance of the used *Nikkor* and the *LaVision* UV endoscope from the object was 500 mm and 50 mm, respectively.

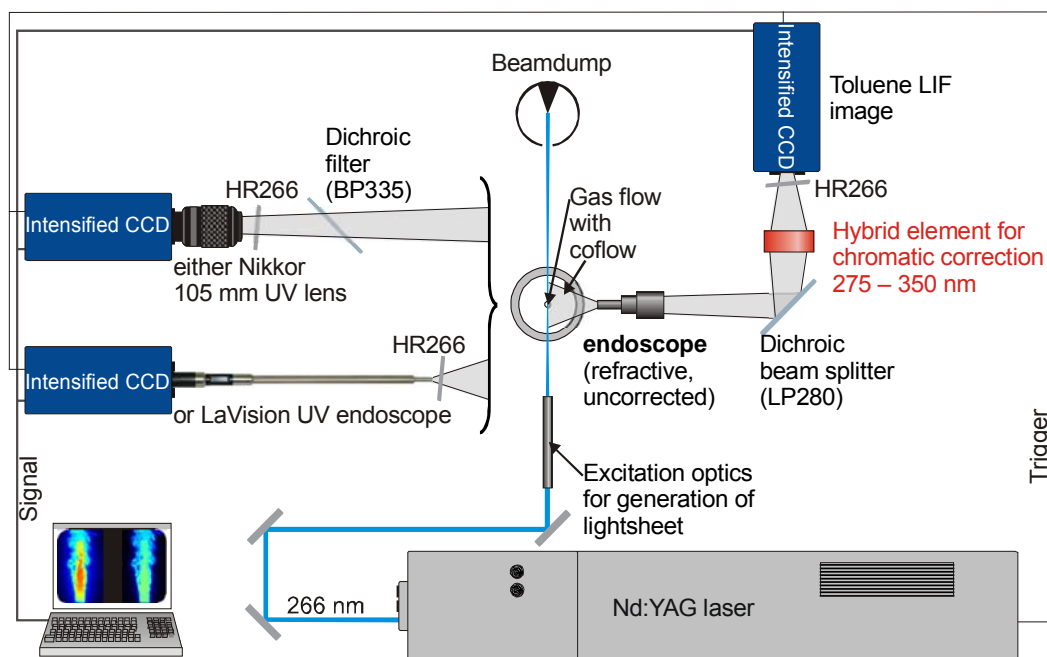


Figure V-18: Experimental setup for the direct comparison of the hybrid UV endoscope with a commercial UV endoscope and UV lens in a flow application.

In order to correct on the different sensitivities of the two used cameras (*LaVision*, *FlameStarII*), they were both calibrated by measuring toluene-LIF signals through the same optics. These calibration measurements were performed with known tracer concentrations and monitoring of the excitation-laser energy. A series of different tracer concentrations / signal intensities was measured with both cameras simultaneously using the *Nikkor* lens and the new hybrid endoscope. Then the cameras were exchanged and the same series was measured again.

Unfortunately, the experimental setup did not allow the same combination of optical filters for all three detection systems. With the hybrid UV endoscope toluene-LIF signals were reflected by the dichroic LP280 beam splitter and transmitted through a HR266 filter before detection (cf. Figure V-18). The use of reflective filters for signal pre-processing is generally not possible with the *LaVision* endoscope, because it has to be fixed to the camera and close to the object (see also Figure V-22). With the *Nikkor* lens an additional BP335 could be employed to reduce the spectral width of the detected toluene-LIF signal. The resulting detected signal for each system is shown in Figure V-19. The different spectral detection widths cause a difference in total integrated signal intensities. This has to be corrected for when comparing measured total signal intensities with the different systems. Correction factors can be derived from the integration of the signal curves in Figure V-19. The *LaVision* system sees ~ 1.7 times more total signal than the hybrid endoscopic system, and for the *Nikkor* setup a factor of ~ 1.3 can be calculated. A broader detection window also influences the resolution of the used UV optics. The wider the spectral detection range, the more difficult are corrections of chromatic aberrations. This effect has to be taken into account when comparing the resolution of our hybrid system with the *LaVision* endoscope.

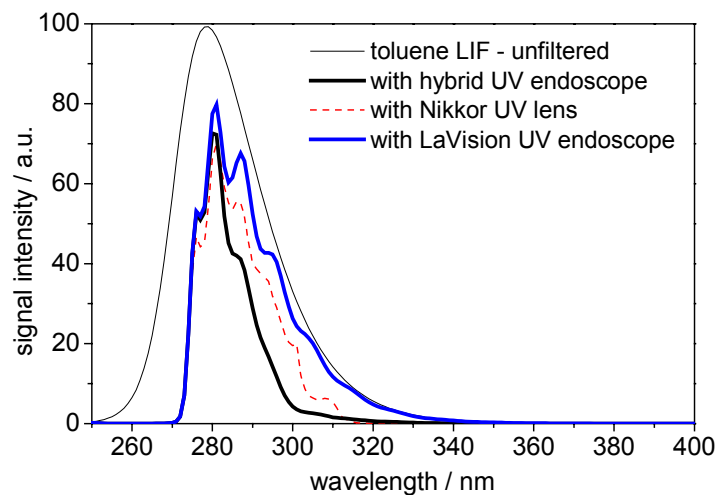


Figure V-19: Technically caused differences in the spectral width of the detected signal for each optical system during their comparison.

4.1.2 Comparison to commercial 105mm UV lens (*Nikkor*)

Because of the very good chromatic correction of the *Nikkor* UV lens, its resolution did not get visibly influenced by a variation of the spectral width of the detected signals. In tests with and without an additional BP335 dichroic mirror (for filtering out wavelength longer than 300 nm) no change in image quality could be registered. For the comparative measurements with the

hybrid system this filter was used anyhow. The resolution of our endoscopic system is slightly inferior, but compared to a standard commercial UV lens it is remarkably good. The corona of diffuse light that is clearly visible in the left image in Figure V-20 is less distinct in the image acquired with the *Nikkor* UV lens (right). However, with a different intensity scaling (i.e. a different LUT, look up table) a less intense corona of diffuse light with the same relative intensity gradient is also visible in the images acquired with the *Nikkor* lens. This effect may partly be due to scattering on the filter surfaces. In the pictures acquired with the endoscope a small amount of scattered light can also come from the surface of the used DOE. Due to an improved production process for the DOE at ITO, the next generation DOEs promise even better results. An additional low background signal results from unwanted diffraction orders of the DOE. These unwanted diffraction orders are visible as almost homogeneous spheres of light around every imaged object point. Because in the image the smallest sphere diameter is 8 mm the total background signal after overlaying all unwanted diffraction orders is quasi-homogeneous over the whole camera chip.

The most convincing property of the hybrid UV endoscope is its very high numerical aperture of $NA = 0.05$ (object side, cf. endoscope specifications in appendix IX 4). In spite of the keyhole access to the observed object our new hybrid system collects ~ 1.3 times more amount of light than the standard UV lens (in the spectral range shown in Figure V-19, with the same paraxial object magnification). This might look contradictory at first, regarding the large diameter of the *Nikkor* lens ($f/4.5$). However, the geometrical restrictions for the same object magnification (0.5) cause a strongly reduced acceptance angle for the *Nikkor* lens and a theoretically resulting NA of ~ 0.07 (image side). The hybrid endoscope has an NA of ~ 0.1 (image side). Even when taking into account the transmittance of the optical elements, the endoscope remains with a higher efficiency of light collection for the presented experimental setup. Over a broader spectral detection range (280 – 440 nm) about twice the amount of light can be collected with the new hybrid system compared to the *Nikkor* UV lens (preliminary results from ITO).

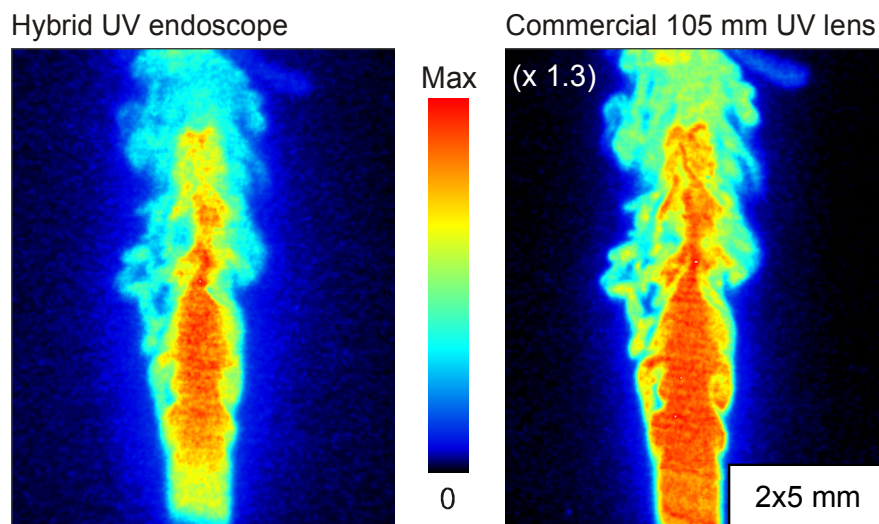


Figure V-20: Comparison of toluene-LIF images of a turbulent flow acquired with the hybrid UV endoscope (left) and the *Nikkor* UV lens (right). The images are corrected for signal intensity differences due to different spectral detection widths. The image acquired with the endoscope is corrected for distortion, but not for intensity decline towards the image boarder (vignette). Note that the intensity values in the image acquired with the *Nikkor* lens have been multiplied by a factor of 1.3.

4.1.3 Comparison to commercial UV endoscope (*LaVision*)

The immediately visible difference between images acquired with the hybrid endoscope or the *LaVision* endoscope is the apparently poor resolution of the commercial endoscope (cf. Figure V-21). However, this effect is most probably due to the broad spectral detection range. According to specifications and calculations for a smaller detection range the resolution of the *LaVision* endoscope should be as good as the resolution of our hybrid optics. Nevertheless, the resolution of the hybrid endoscope remains good even with broader spectral detection. It is optimized for a detection range between 275 – 350 nm. Over this whole spectral range the resolution will remain just as good as seen in the left image in Figure V-21. This has been validated in various experiments (cf. chapter IV 2.3). The whole toluene spectrum could be imaged with optimum resolution. Actually, the peak of the toluene-LIF spectrum experiences a relatively weak chromatic correction compared to the optimum correction around 275 and 335 nm. To cut a long story short: In an imaging experiment observing the complete toluene-LIF signal, the images acquired through our hybrid UV endoscope or the *LaVision* UV endoscope would look just like those presented in Figure V-21. Additionally, with the hybrid system almost seven times more light is collected in comparison to the *LaVision* endoscope (in the spectral range shown in Figure V-19, with the setup shown in Figure V-18). Other measurements from ITO (chapter IV 2.3) show that over a broader spectral range more than ten times the amount of light can be collected with the new hybrid endoscope (preliminary results).

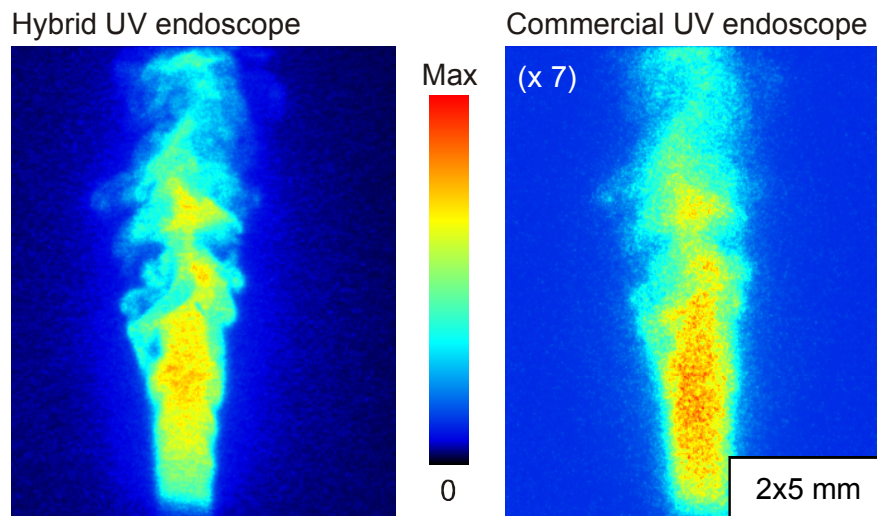


Figure V-21: Comparison of toluene-LIF images of a turbulent flow acquired with the hybrid UV endoscope (left) and the *LaVision* UV endoscope (right). The images are corrected for signal intensity differences due to different spectral detection widths. Vignette and distortion in both images are not corrected for. Note that the intensity values in the image acquired with the *LaVision* UV endoscope (right) have been multiplied by a factor of seven.



Figure V-22: *LaVision* UV endoscope mounted to camera.

4.2 Measurement of equivalence ratios

4.2.1 Setup of two-camera experiment

For the simultaneous measurement of two spectrally separable signals a two camera experiment was set up as shown in Figure V-23. The atmospheric-pressure nitrogen flow and/or the coflow were seeded with approximately 3 mbar toluene and 30 mbar 3-pentanone. The oxygen concentration of the flow and/or the coflow could be varied by flow controllers. Fluorescence was excited by a 266-nm laser beam. The microoptical excitation optics were used to form a homogeneous lightsheet and guide it through the center of the gas flow. Both 3-pentanone- and toluene-LIF images are acquired through the same “keyhole” access with the front endoscope. The signals are separated by a dichroic beamsplitter. This longpass filter (LP280) reflects wavelength shorter than 285 nm onto the first camera. The signal of this optical branch is corrected by the relay for 275 – 350 nm and passes an additional high reflective mirror (HR266) for the elimination of Rayleigh-scattered laser light. The second optical branch is defined by light passing the LP280. These signals are corrected and guided to the camera through the optical relay optimized on 380 – 440 nm. Wavelengths shorter than 380 nm are eliminated by another longpass filter (GG385) in front of the camera. The cameras are triggered to the laser pulses and synchronized to each other. That way image pairs of toluene- and 3-pentanone-LIF signals were recorded simultaneously.

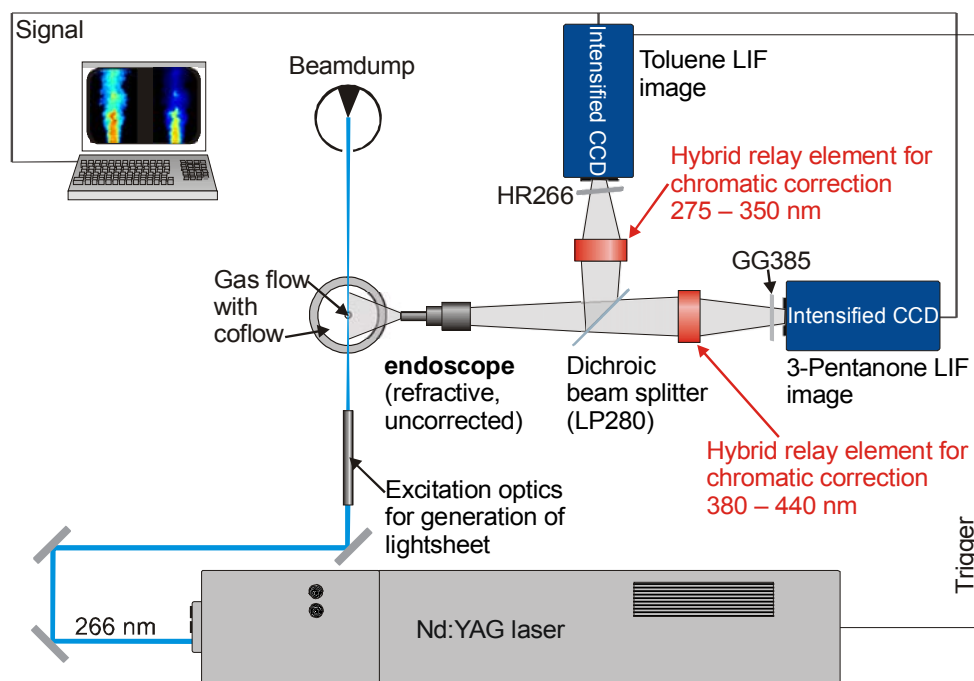


Figure V-23: Setup of two-camera experiment for the simultaneous acquisition of two spectrally separable fluorescence signals through only one keyhole access to the object.

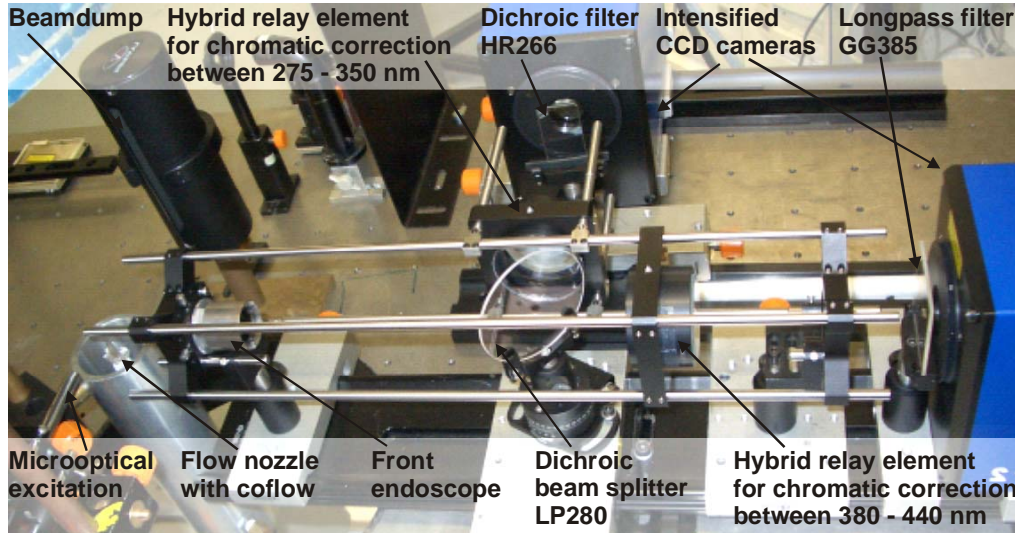


Figure V-24: Photograph of the experimental setup for the simultaneous acquisition of two spectrally separable fluorescence signals through only one "keyhole" access to the object.

Before each test series a calibration target with maltese-crosses (cf. Figure V-25, left) was imaged. For these calibration measurements the nitrogen coflow was seeded homogeneously with 3-pentanone and toluene and the central flow was off. The target was aligned in less than 1 mm distance exactly parallel to the lightsheet between lightsheet and endoscope. Thus, homogeneous fluorescence light illuminated the target and the calibration could be performed with the same wavelengths as in the actual experiments.

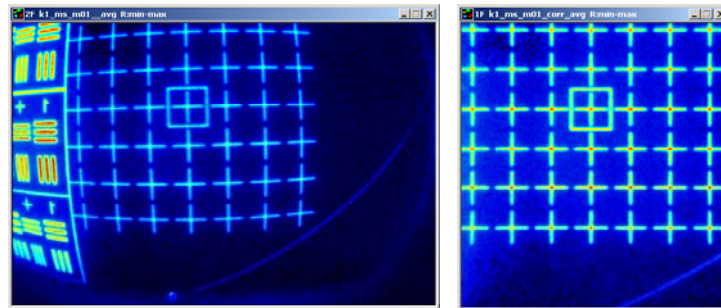


Figure V-25: Example of the distortion correction for mapping of two simultaneously acquired images. Additionally, an accurate object size can be determined: Distance between centers of maltese-crosses: 5 mm.

4.2.2 Image post processing

For all image post processing operations the software *Davis* by *LaVision* and its macro programming language "cl" was used. The often tedious correction on spatial energy inhomogeneities in the excitation laser-lightsheet is not necessary, because these inhomogeneities cancel out, when taking the image ratio of two LIF images from the same excitation-laser pulse. The first step in digital image processing is to correct for the distortion of the images by the optical system. Within the distortion-correction routine the image pairs are mapped to each other with sub-pixel accuracy. For this mapping routine a set of parameters is determined for an analytical function that describes the distortion of the maltese-cross target (i.e. the exact

alignment of respective crosses in the two target images. Figure V-25 shows an image of the target before (left) and after (right) distortion correction. After mapping of the images and cropping to the area of interest, the respective 3-pentanone- and toluene-LIF images are normalized and divided by each other for the determination of oxygen concentrations. The images are both normalized on the maximum signal intensity for a known oxygen concentration (i.e. in pure nitrogen). With the known calibration curve (cf. chapter V 2.3) only one initial value has to be matched for a quantification of the measurement. Because of the known correlation between the oxygen partial pressure and the reciprocal toluene-LIF intensity a scale for the oxygen partial pressure is easily set. For the calculation only regions with tracer concentrations (i.e. 3-pentanone-LIF signals) above a certain threshold were considered. With a thresholding function the pixel values of all pixels below the minimum value are set to zero. These areas are black in the presented images.

4.2.3 Results

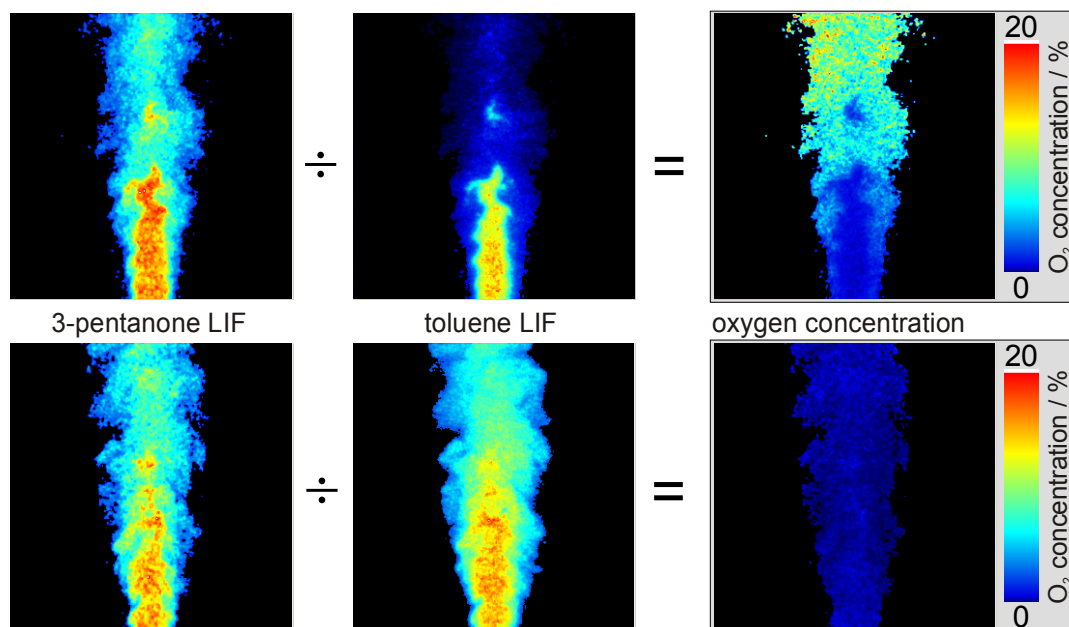


Figure V-26: Measurement of the local oxygen concentration in a central plane through a turbulent atmospheric-pressure nitrogen flow. Flow seeded with 3 mbar toluene and 30 mbar 3-pentanone. Top row: Nitrogen flow mixing with surrounding air. Bottom row: Nitrogen flow mixing with fast nitrogen coflow.

The results presented here are exemplary in-situ measurements from three different series. In two measurement series only the flow through the nozzle was seeded with the two tracers. In one of these cases there was no coflow and the mixing process with the surrounding air could be observed (cf. top row in Figure V-26). Because the intensity was normalized on the signal in pure nitrogen, the resulting ratio of the two LIF images is '1' for 0 % oxygen concentration. Note, that the LUT starts with dark blue for pure nitrogen. Black regions are areas where no tracer was present or not enough signal was detected. The bottom row in Figure V-26 can be regarded as an indicator for the accuracy of these measurements. Here, flow and coflow consisted of pure nitrogen (flow seeded with tracers). The pixel values in the resulting oxygen

concentration image should all be '1' in the ideal case. In the presented measurements the variation was less than 5%.

Another measurement series is shown in Figure V-27. Both, flow and coflow were seeded with tracers. In order to achieve the required minimum tracer concentrations, it was technically not possible to have a fast coflow in this case. This is why one can see mixing of the flow with ambient air in spite of the surrounding nitrogen coflow. Only to the flow 8% oxygen were added, and thus a slightly reduced tracer concentration can be observed there in the 3-pentanone-LIF image. The inverse intensities in the toluene-LIF image illustratively show the increased oxygen concentration. Again, areas with no tracer present are marked black in the images. The bottom row in Figure V-27 shows an event that could be observed in more than half of all images: Ambient air (without tracers) is blown through the slow coflow and meets the turbulent flow. The oxygen concentration on the boundary layer reaches 20% just before a measurement was not possible anymore, because of the strong dilution with unseeded air.

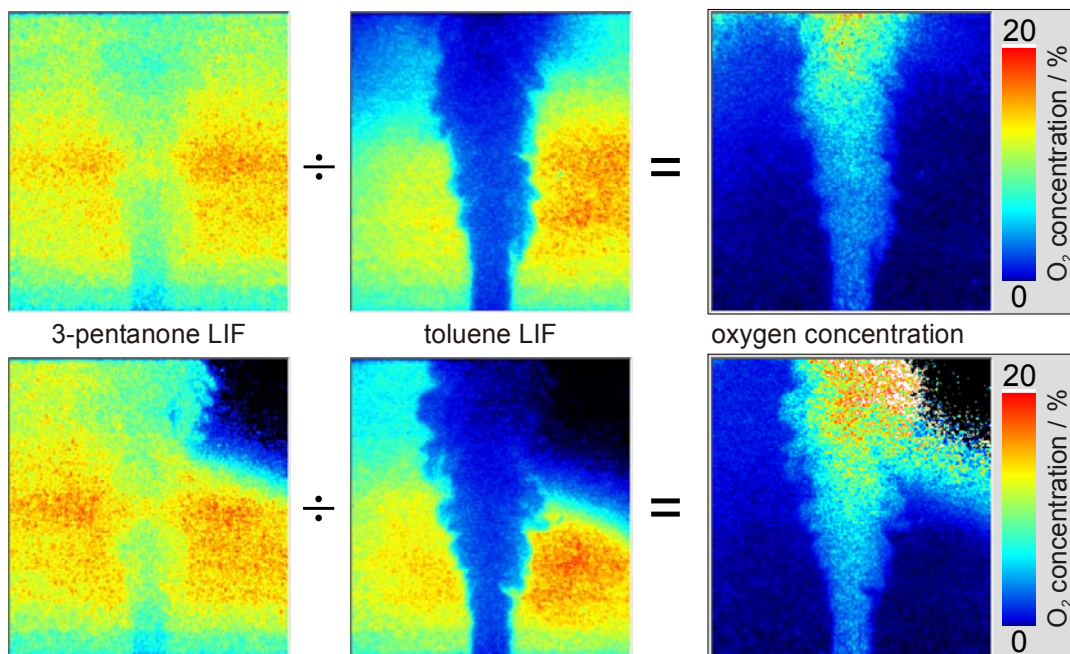


Figure V-27: Measurement of the local oxygen concentration in a central plane through a turbulent atmospheric-pressure flow. Flow and coflow: nitrogen seeded with 3 mbar toluene and 30 mbar 3-pentanone. 8% oxygen added to the central flow. Because of the slow nitrogen coflow, in the top part of the images the mixing with ambient air is visible (especially in the measurement shown in the bottom row).

4.3 Flow-tagging using sensitized phosphorescence of biacetyl

Flow-tagging (or line-tagging) is a non-intrusive optical method for the visualization of flow fields. The advantage of flow-tagging compared to other flow visualization methods like particle image velocimetry (PIV) or particle tracking velocimetry (PTV) is that the flow does not have to be seeded with particles. Due to their interaction with the wall and the flow by the use of particles, the resolution of small scale structures is often impossible, especially in the boundary layer. Flow-tagging methods use molecules to track the movement of a structure (one or more lines, often a grid) that has been “written” in the flow. This structure is created by the selective laser-excitation of the tracer molecules. There are various ways of performing a flow-tagging experiment, mainly due to different molecules that are excited. Different applications require different tracers with adequate characteristics. In a frequently used flow-tagging application the “writing” process is based on the photodissociation of one of the species present in the flow. That way a new species is generated that can be selectively visualized by means of laser-spectroscopic methods, i.e. laser-induced fluorescence. After a certain time interval between generation and detection (and successive detection) the shape of the structure is altered according to the flow field. The observation of this alteration yields information about flow velocities and their direction. This flow-tagging method requires two different laser pulses: A “write-“ and a “read-“ laser. A frequently used application is the flow-tagging of NO by photodissociation of NO₂ [99]: NO₂ is dissociated by a 355 nm laser pulse and the created NO molecules are visualized via planar laser induced fluorescence (PLIF) after excitation at 226 nm. There are other flow-tagging methods that only require one laser pulse and use the long lived phosphorescence of excited tracer molecules. Because of phosphorescence lifetimes often being in the range of milliseconds, consecutive time delayed detection of the phosphorescence signal directly visualizes the displacement of excited molecules.

In the presented experiments we used sensitized phosphorescence of biacetyl to measure flow velocities with the hybrid UV endoscope in combination with the inhomogeneous excitation optics. The axial velocity component of relatively slow (5 – 30 m/s) laminar flow fields could be measured.

4.3.1 Toluene-sensitized phosphorescence of biacetyl

Biacetyl (2,3-butanedione) is a non-toxic and highly flammable yellow liquid (flashpoint 22°C) with a vapor pressure of 40 mbar at room temperature. Biacetyl is frequently used as a flavoring substance. It smells very strong like the synthetic butter-odor of cheap microwave popcorn. Hiller et al. [87] writes ironically: “It has a sweet odor, which is commonly perceived as unpleasant by persons not directly involved in the experiment.”

Biacetyl has been frequently used as a fuel LIF tracer in engine research [100] and its photophysical behavior has been investigated [101]. After excitation with 266 nm biacetyl emits a broadband fluorescence signal and a strong phosphorescence signal peaking around 520 nm (Figure V-28 ,right). The phosphorescence signal originates from a spin-forbidden radiative decay ($T_1 \rightarrow S_0$ transition) that is very slow. The phosphorescence lifetime of biacetyl has been studied by various groups [101-103]. It is reported to be as long as 1.5 ms [102], but can be lower due to a variety of reasons [104]: The biacetyl triplet state is extremely sensitive to colli-

sional quenching by molecular oxygen (five orders of magnitude more sensitive than to self quenching or quenching by nitrogen). Unless all oxygen is completely purged from the flow system, a strong reduction in lifetime was observed [105]. Another effect that reduces the phosphorescence lifetime is the annihilation reaction between two molecules in the triplet state [103]. Its otherwise long phosphorescence lifetime makes biacetyl an attractive tracer for molecular tagging velocimetry (MTV) measurements in gas phase flows [104,105]. Only recently laser excited biacetyl phosphorescence has been used for a flow-tagging experiment inside an optical engine, again [13].

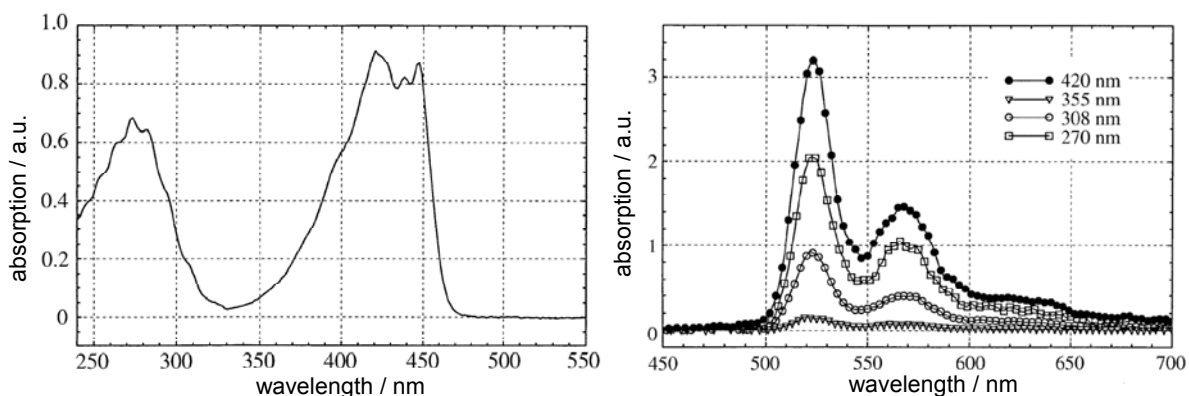


Figure V-28: Absorption spectrum (left) and phosphorescence spectra (right) of biacetyl. (Graphs from [105]).

The spin-forbidden radiative decay that follows the collisional excitation of the triplet state by an excited donor molecule is called sensitized phosphorescence. Sensitized phosphorescence with acetone as donor has been used to measure gas phase molecular mixing processes before [106]. We applied sensitized phosphorescence in our flow-tagging experiment, because it yields stronger signals. We used a mixture of toluene as donor and biacetyl as acceptor in 1 bar nitrogen. Toluene is excited to its first singlet state by the 4th harmonic of a Nd:YAG laser (266 nm). According to [106], there are two major processes for the population of the biacetyl triplet state by the collision with aromatic donor molecules: (i) The biacetyl triplet state can be directly excited from toluene molecules in the triplet state (after intersystem crossing from the laser-excited singlet state). (ii) After collision with toluene in the excited singlet state the biacetyl molecule is typically promoted to its second excited singlet state, which then relaxes to the first excited singlet state under the aid of molecular collisions and finally enters the triplet state by intersystem crossing. With an optimized mixture fraction of donor and acceptor [106] much higher phosphorescence intensities could be achieved than with direct laser excitation of biacetyl.

4.3.2 Experimental setup for line-tagging with microoptical excitation

The experimental setup is very similar to the one already shown in Figure V-23. The only difference is the use of the inhomogeneous excitation optics instead of the homogeneous. The total gas flow was reduced to generate an atmospheric pressure laminar nitrogen gas flow at the nozzle exit. It was seeded with biacetyl (~10 mbar) and toluene (~25 mbar) from two fritted wash-bottles.

For experimental reasons, we used toluene as donor, which enabled the spectrally well separable simultaneous measurement of the toluene LIF signal. In order to achieve a high phosphorescence quantum yield, toluene and biacetyl were excited with a relatively low laser pulse energy of about 2 mJ/pulse at 266 nm (distributed on the five tagging lines), which reduces annihilation effects [103].

The biacetyl phosphorescence signal peaks around 520 nm. Yet, the hybrid endoscopic UV-imaging optics used for the acquisition of these images is optimized for a spectral region from 380 – 450 nm and was not intentionally designed to work that far in the visible light spectrum. Nevertheless, after readjusting the camera position and thus correcting for the slightly different focal length at 520 nm, sufficiently sharp images could be acquired.

4.3.3 Results and comparison to simulation

With the novel excitation microoptics and the flow-tagging method using toluene sensitized phosphorescence of biacetyl, instantaneous snapshots of five velocity profiles could be acquired simultaneously. The movement of the lines could be observed within a time interval of up to 0.2 ms after excitation. After that time the phosphorescence signal was too small and the lines too broad because of molecular diffusion processes. Figure V-29 shows exemplary single shots for a measurement-time delay of 55 μ s after excitation.

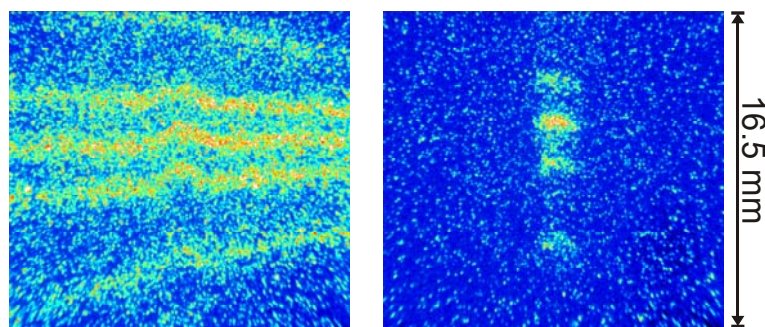


Figure V-29: Exemplary single shot images of five distorted lines of phosphorescing biacetyl molecules 55 μ s after excitation, with tracer in flow and co-flow (left) or tracer only in the flow through the nozzle (right).

The two examples presented here are measurements in laminar flows with different flow-controller settings (1.9 l/min and 3.5 l/min), and thus different velocity fields. Figure V-30 shows averages over 50 images for each time interval. The first image at 0 μ s is a toluene-LIF image and presents a snapshot of the non-displaced line. The phosphorescence line was tagged at five different times (start of exposure from 0 to 100 μ s). In order to collect enough light the exposure time for each single phosphorescence image was set to 10 μ s. Within this time a phosphorescing molecule moved about 150 and 250 μ m respectively in the slow and fast flow. This causes a broadening of the measured lines. In spite of this, the systematic error is still smaller than the width of the line, because the center of a line can be detected with about two pixel accuracy ($\sim 100 \mu$ m). For evaluation not the start of exposure, but the center of each exposure interval was regarded.

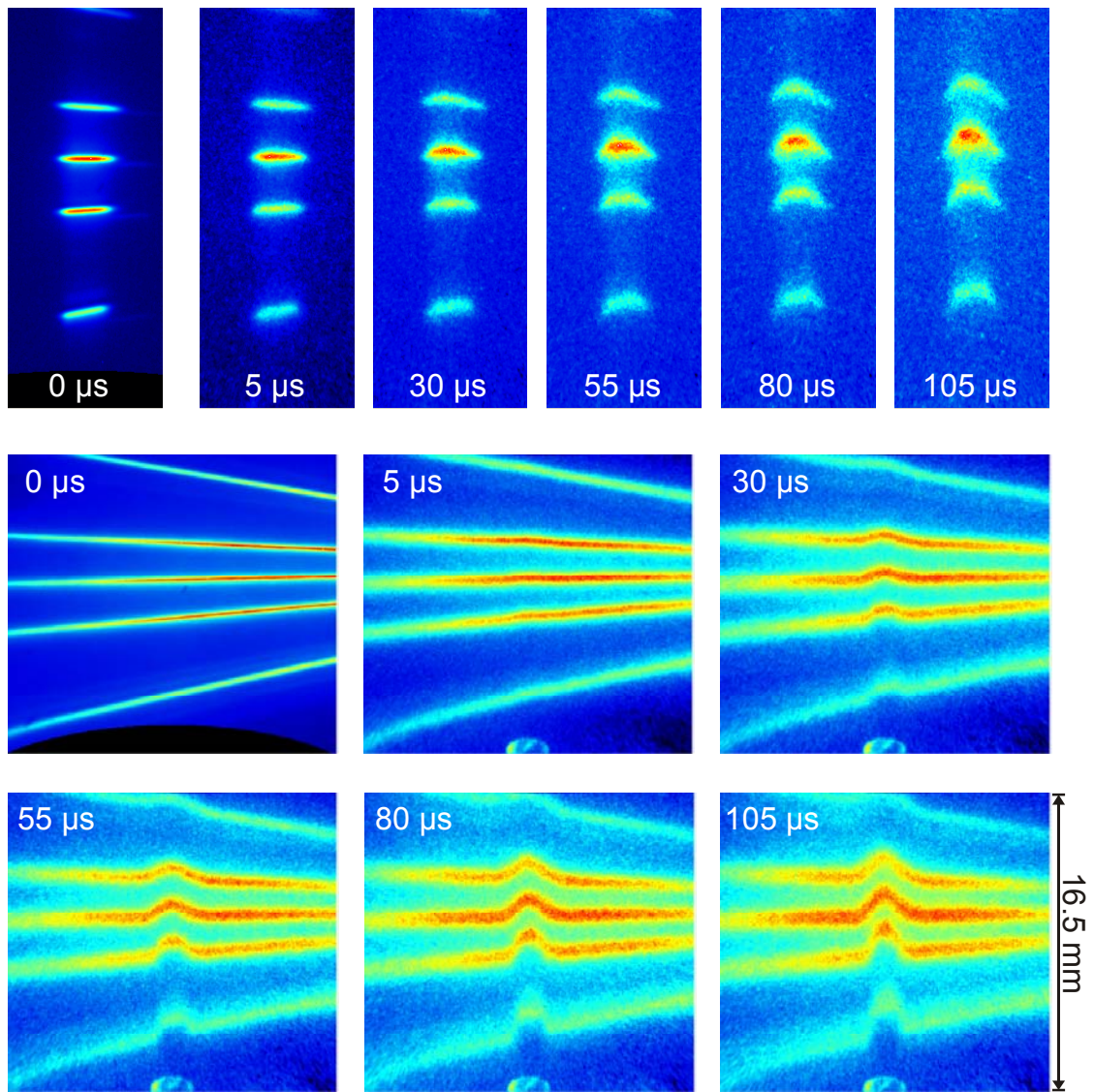


Figure V-30: Line-tagging images (averages over 50 instantaneous measurements): With a sequence of consecutive detection timings velocity profiles of the flow field in different distances above a nozzle with a slow surrounding co-flow can be measured. Top: Only flow seeded; bottom: Flow and co-flow seeded with tracer.

In Table V-2 axial velocity components of the flow are calculated from the measured displacement of the central phosphorescence line about 10 mm above the nozzle. For both, the slow and the faster flow, this central axial velocity component is getting smaller for later detection times, which could partly be explained by the broadening of the flow-cone diameter with increasing distance above the nozzle exit. However, the comparison to the simulation shows that in a height of 10 mm above the nozzle within 2 mm height difference the broadening is negligible (cf. Figure V-31). Disturbances from surrounding air that are not completely shielded off by the slow coflow in the measuring height play an increasingly important role with longer delay times. Therefore the radial unsteadiness of the flow becomes visible and averaged axial velocity components become smaller.

Flow [l/min]	Time delay [μs]	Displacement [pixel]	Displacement [mm]	Axial velocity [m/s]
1.94	30	9	0.42	14.15
	55	15	0.75	13.72
	80	23	1.08	13.56
	105	27	1.27	12.13
3.48	30	14	0.71	23.58
	55	25	1.23	22.30
	80	33	1.56	19.46
	105	41	2.03	19.32

Table V-2: Measured flow velocities for two different flow-controller settings. The axial displacement of the central pixel of the middle phosphorescence line (about 10 mm above nozzle exit) is measured.

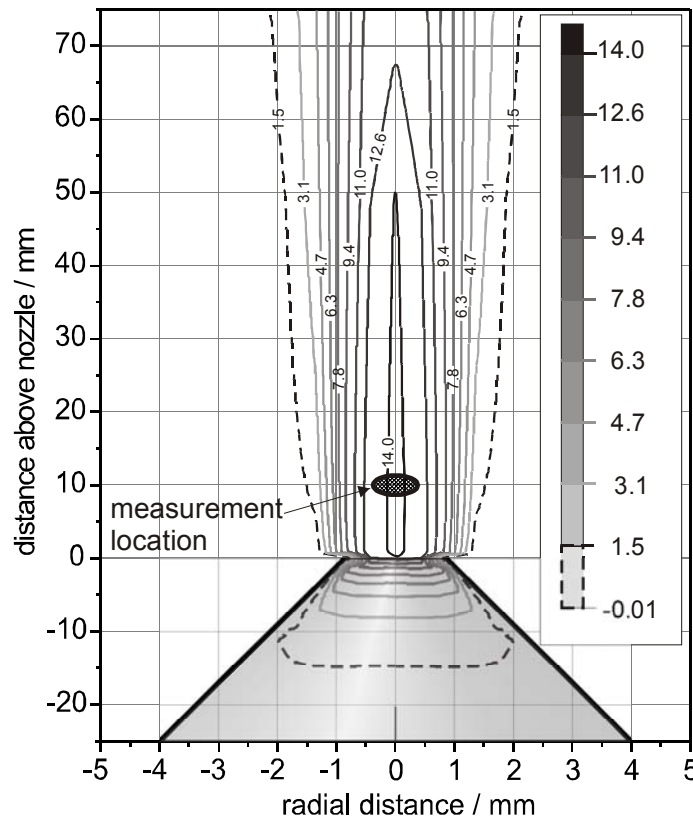


Figure V-31: Computer simulation of the axial flow velocity components of an axial symmetric laminar flow (1.94 l/min). The curves illustrate surfaces with an equal axial velocity component. Note that within the observed volume the velocity profile remains almost unchanged. (The radius of the nozzle is stretched for better illustration.)

In spite of the experimental uncertainties, in the case for the slow flow velocities (1.94 l/min, top row of images in Figure V-30) simulation and measurements agree very well for the smaller time delays. Figure V-32 shows the computer simulation of the axial velocity component centrally inside and above the nozzle. The calculated velocity of 14 m/s ($v_{\text{sim}, 1.94 \text{ l/min}}$ marked by the bar) is virtually the same as the measured one ($v_{\text{exp}, 1.94 \text{ l/min}}$).

The simulation was done with FLUENT. A total of 200,000 knots was used for the calculation with a denser mesh around the nozzle exit. For both flow controller settings (i.e. 1.94 and 3.48 l/min) a laminar flow was assumed. For the slow flow with a Reynolds-number of $Re < 1800$ the laminar model yields correct flow results and thus the good agreement with the measurement is found (cf. Figure V-32 and Table V-2). In the case of the faster flow a Reynolds-number of $Re < 3200$ can be calculated. Although in the imaging experiments the flow close to the nozzle looked fairly laminar, higher above the nozzle eddies could be observed. This case is probably not correctly treated with the laminar model and thus the discrepancies to the measured values could be explained. The laminar model yields $v_{\text{sim.}, 3.48 \text{ l/min}} = 25 \text{ m/s}$ axial velocity 10 mm above the nozzle exit. The highest measured average axial velocity at this location is $v_{\text{exp.}, 3.48 \text{ l/min}} = 23.6 \text{ m/s}$.

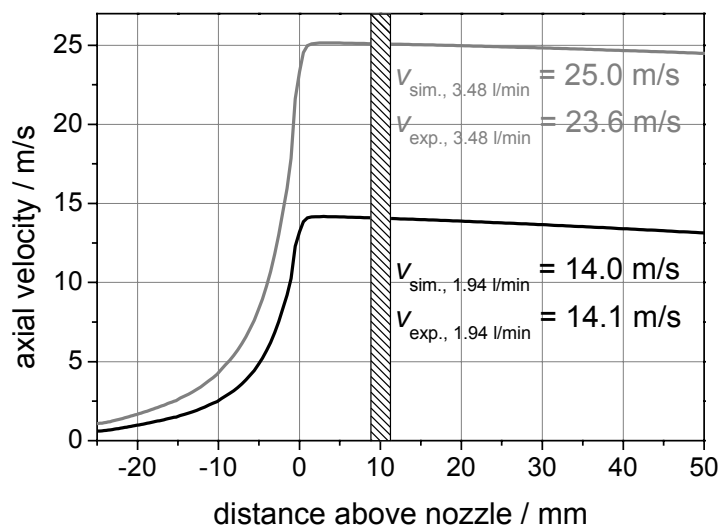


Figure V-32: Computer simulation of axial velocity component centrally above the nozzle. Values at negative distances represent flow velocities in the cone end of the nozzle. The bar at 10 mm marks the height above the nozzle where a comparison to the measurements can be made.

VI MEASUREMENTS IN IC ENGINES

The following chapter discusses different applications of optical and microoptical measurement techniques in IC engines. The focus is set on the comparison of the new microoptical methods with simultaneously applied well known, approved techniques. The experiments described in the first two paragraphs are performed in two different optical one cylinder engines, i.e. an air-guided (tumble flow) and a spray-guided direct-injection (DI) engine. The first engine experiment was done in cooperation with the Institut für Kolbenmaschinen (IfKM) in Karlsruhe, Germany. The second experiment was conducted during a collaboration with General Motors (GM) in Detroit, Michigan, USA. At the time of these experiments, neither the optical spark plug, nor the hybrid endoscope were ready for use. Therefore, the measurements were performed with commercial optics and microoptics. In the last paragraph a first fuel-LIF experiment with the novel fiber-optic spark plug in a standard four-cylinder port-fuel-injection engine is presented that was carried out at the Institut für Verbrennung und Gasdynamik (IVG) in Duisburg, Germany.

1 Fuel/air-equivalence ratio in an air-guided SIDI engine

The main objective of the investigations presented here is the comparison of two different measurement techniques for analyzing the fuel/air composition in the spark plug region in an engine. Both techniques are described in detail in chapters III 3.1.1 and III 4 and in literature: 3-Pentanone LIF [1,18,20,56,64,66,107] and spark-emission spectroscopy from CN* [28,31,44,45]. With both techniques it is possible to characterize the cycle-to-cycle variations of the equivalence ratio at the spark gap region before or at the time of ignition, respectively, which is a key factor for a reliable and reproducible combustion process in SIDI engines.

1.1 Optical engine and experimental setup

For the investigations, an air-guided concept with wide spacing between the fuel injector and the spark plug was used. In this concept the air flow moves the fuel towards the spark plug. The test engine was a single cylinder engine with optical access and a flat piston. An adjustable tumble system was mounted on the cylinder head to achieve variable in-cylinder air-flow conditions with different levels of tumble intensity.

1.1.1 Optical engine

The single-cylinder engine used for this study featured a four-valve pent-roof chamber with central spark-plug position. The injector was positioned between the inlet valves with an angle of 25° relative to the horizontal plane. A hollow-cone swirl injector was used that generates a 70° cone-angle spray with an injection pressure of 100 bar. For all measurements with

stratified charge the start of injection was 60°CA BTDC (degrees crank angle before top dead center). For the operating point with homogeneous charge the fuel was injected at 320°CA BTDC. The fuel used for this study was iso-octane : 3-pentanone (92:8% vol.). The engine was lubricated with standard 15W40 oil. All measurements were performed at an engine speed of 2,000 rpm.

The engine was equipped with an adjustable tumble system to increase the tumble motion of the in-cylinder flow. With this system a section of the intake port can be closed and thus the velocity of the air flow increased. Moreover, the air-guiding system is adjustable so that it is possible to vary the mean direction of the inlet air flow [108]. In all measurements presented here the configuration with a concentrated inlet flow (opening reduced to 1/3 of its original cross-section) directed towards the center of the cylinder was used. The high kinetic energy of the intake flow is maintained throughout the compression stroke which enhances the transport of the fuel cloud towards the spark plug.

1.1.2 Measurement of fuel concentration via spark emission spectroscopy

For the determination of the local fuel concentration during ignition within the spark the CN* emission signal at 388 nm was used as described in chapter III 4 and in [28,45,73]. The setup (Figure VI-1) that combined spark emission detection with signal transmission through an optical fiber had been applied for measurements in a SIDI engine with stratified load before [109]. The light emission of the spark was detected with an optical probe positioned in front of the glass ring between

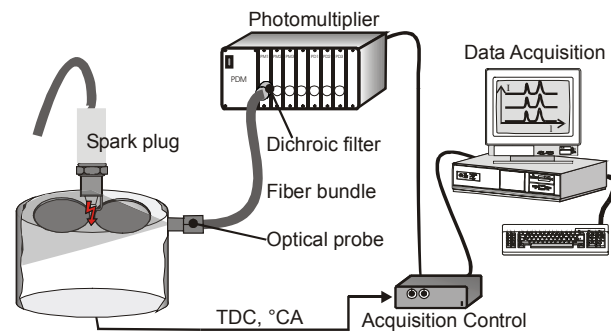


Figure VI-1: Setup for spark-emission spectroscopy.

intake and the exhaust valves with an acceptance angle of 28° and was transmitted to the photomultiplier through a quartz fiber bundle. In front of the photomultiplier an interference filter with its center wavelength at 390 nm and a bandwidth of 10 nm (FWHM) was mounted. A computer-based data-acquisition system was used to record the light-to-voltage converted signals of the photomultiplier together with pressure, spark voltage and current as well as the photodiode signal representing the laser energy with a resolution of 0.1°CA. The photomultiplier intensity was normalized by the amount of measured spark-discharge energy during the measurement interval of 150 μs after spark breakdown. The presented CN*-emission signals imply this correction.

The signal intensities from the spark emission depend on the experimental setup and quantitative measurements require calibration. For calibration, the engine is operated with homogeneous charge and known amounts of air and fuel. For each condition the carbon number density n_c is calculated using measured pressures and calculated temperatures. Fansler et al. investigated equivalence ratios ϕ in the range $\phi = 0 - 3$ while running the engine skip-fired, where one fired cycle was followed by eleven non-fired cycles. For the experiments presented here the engine was continuously fired, with a nearly constant residual gas fraction of 10% over the whole range of operating points. Without skip-firing we must ensure reproducible

composition of the residual gases and thus prevent misfire. The calibration measurements are therefore limited to the $0.7 < \phi < 1.6$ range in order to prevent misfiring. Misfiring causes a strong variation in unburned fuel concentrations in the residual gases and hence causes a significant variation in over-all fuel density in the subsequent cycles.

1.1.3 Measurement of fuel concentration via 3-pentanone LIF

Laser-induced fluorescence (LIF) of 3-pentanone was introduced in chapter III 3.1.1 for measuring fuel concentrations (see also [1,64]). 3-Pentanone-LIF imaging was performed quasi-simultaneously with the spark emission measurements. An offset of 0.5°CA before ignition had to be set for the imaging trigger, in order to prevent the acquisition of the much stronger spark emission signal on the sensitive intensified CCD camera. 3-Pentanone (8% vol. in iso-octane) was excited at 266 nm with the 4th harmonic of a Nd:YAG laser (*Quantel Twins*). Figure VI-2 shows the experimental setup. The light sheet was adjusted in a way to precisely fit through the spark plug gap. In order to reach the spark plug position on the cylinder head, additionally to the optics forming the light sheet a cylindrical lens close to the engine window was installed to spread the beam in vertical direction. The fluorescence signal was detected with an intensified CCD camera (*LaVision NanoStar*) through a regular Nikon 50 mm lens, that transmits wavelengths above 350 nm and thus blocks elastically-scattered laser light. The camera and the laser Q-switch were triggered simultaneously. At 2,000 rpm a LIF measurement could be performed in every second cycle, which implies a stable repetition rate of 8.33 Hz of the Nd:YAG laser. In order to correct for varying pulse energies a photodiode measured the relative energy of the incident beam.

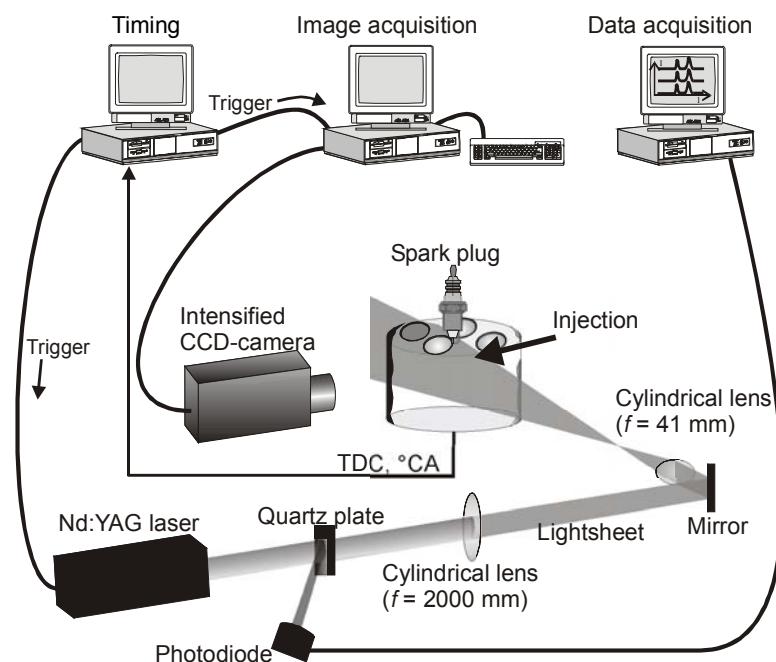


Figure VI-2: Setup for LIF measurements synchronized with CN-emission measurements.

The calibration measurements that assign LIF-signals to known fuel densities were carried out in the same cycle as the calibration of the spark emission measurement. LIF is measured at 45°CA BTDC, i.e. 36°CA before ignition (at 9°CA BTDC). This delay was necessary to guaran-

tee both stable operating conditions of the engine and an observation field of the LIF-signal large enough to check on homogeneity of the fuel gas distribution. For later detection times the rising piston blocked the incident light sheet significantly (at ignition the observation window is blocked almost completely). A cycle-resolved comparison of the CN emission and the LIF-signal in the homogeneously operated engine was therefore not possible. However, as a fairly homogeneous fuel gas distribution could be seen (Figure VI-6), the corresponding average signals correlate well within the cycle-to-cycle variations, which will be shown in the following paragraph. The LIF intensities are corrected for pulse-to-pulse as well as for spatial variations in laser energy. For each operating condition background signal was determined in motored engine without fuel injection.

Limitations of concentration measurements with 3-pentanone LIF apply when liquid fuel is in the observed area. Even small regions with remaining spray droplets contribute signal that can surmount the gas-phase signal by a factor of 100. As a consequence of the experimental setup the laser lightsheet partly hits the cylinder head which was necessary to reach the spark plug position. Therefore, in the presence of droplets, interfering LIF signal originates not only from the observed plane itself, but also from droplets that are excited by scattered laser light. This signal contribution can not easily be corrected for and only operating conditions without remaining droplets around the observed plane are suitable for quantitative fuel vapor measurements. A quantitative evaluation of the measurements could only be made for the latest observation time in stratified mode (23°CA BTDC). Here the slight variation in the fluorescence yield because of different pressure and temperature compared to the homogeneous calibration measurements was neglected (see Table III-1).

1.2 Comparison: Tracer LIF – spark emission

1.2.1 Spray propagation

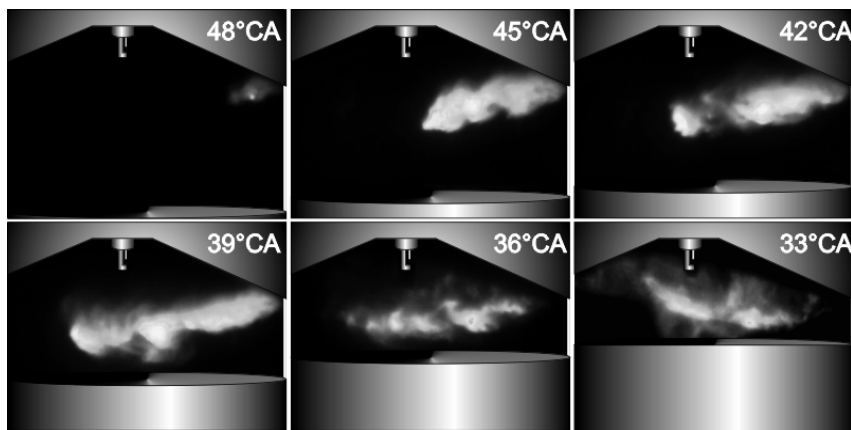


Figure VI-3: Exemplary instantaneous images of the spray propagation from 48° to 33°CA BTDC.

The observation of the liquid spray development shows when the fuel arrives at the spark plug and when it is completely vaporized. In the presence of droplets the LIF signal from the liquid phase dominates the over-all LIF intensity. The area with droplets can therefore be determined via a threshold analysis (10% of the peak signal). The fuel spray propagation was

analyzed in 3°CA steps from the start of injection until ignition. Figure VI-3 shows examples of the instantaneous spray distribution for each step from consecutive engine cycles. For all crank angles the pre-spray can clearly be observed at the front of the spray. This portion of the spray leaves the injector without swirl. Consequently, this part of the spray shows a fast axial velocity component and therefore high penetration depth. Additionally, the influence of turbulent in-cylinder air motion can be observed in the instantaneous images. Especially for later crank angles the spray looks very ragged. This gives a first impression on the cyclic variations of fuel distribution at the spark plug location.

From the spray images the mean spray propagation was calculated. Figure VI-4 shows the probability of the presence of liquid spray for the observed configuration with increased tumble motion. The injection parameters were held constant as mentioned above. Images of the spray were recorded from 48° to 33°CA BTDC. For each crank angle 100 images were evaluated and the probability distribution of the presence of spray was calculated via a threshold value analysis. It can be seen, that there is a significant influence of the in-cylinder air motion on the spray propagation already at the beginning of injection. The dependence of spray propagation on the ambient conditions is well known from literature [110]. Hence, it is obvious that compared to the spray at atmospheric pressure the in-cylinder pressure causes the collapse of the spray cone angle and a compact spray propagation can be observed. The tumble motion results in a deflection of the spray towards the upper part of the combustion chamber and therefore towards the spark plug. This behavior can be observed especially for later crank angles, when more fuel has been evaporated and the spray droplets have less conserved kinetic energy. For later crank angles the fuel is positioned in the spark plug region for a reliable ignition. In this period the fuel moves slowly, which allows one to adjust the ignition time within a broad range for thermodynamical optimization. Previous investigations showed that the tumble motion also reduces piston wall wetting [108].

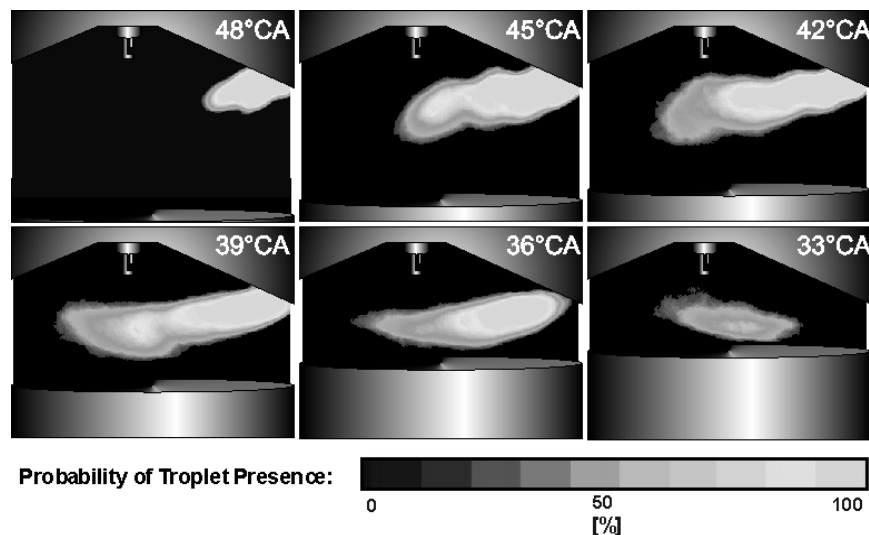


Figure VI-4: Probability of the occurrence of liquid fuel from 48° to 33°CA BTDC.

1.2.2 Homogeneous mode

The LIF and spark emission signals were calibrated under known homogeneous operating conditions. Therefore, the homogeneity of the fuel distribution after early injection (320°CA BTDC) was observed in the central area of the cylinder. The following LIF images show the area that is marked by the white frame in Figure VI-5. Its size is about 20x40 mm². The two black rectangles mark the regions where spatially averaged intensities were measured. Rectangle 1 marks the area for measurements in the engine in the homogeneous mode (early injection), and rectangle 2 to the left of the spark plug shows the measurement location for LIF measurements with stratified operation.

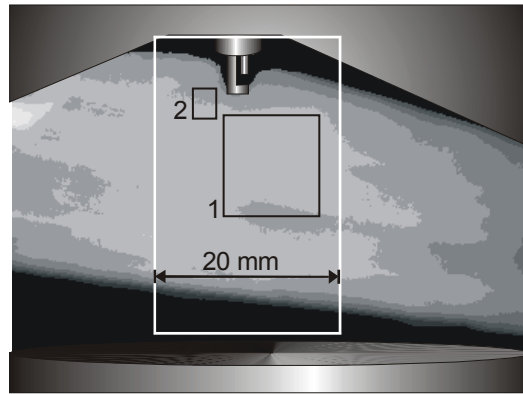


Figure VI-5: Position of the selected observation area (white rectangle) in an exemplary average image (100 individual images) with homogeneous charge distribution. The black rectangles mark the regions where spatially-averaged intensities were calculated.

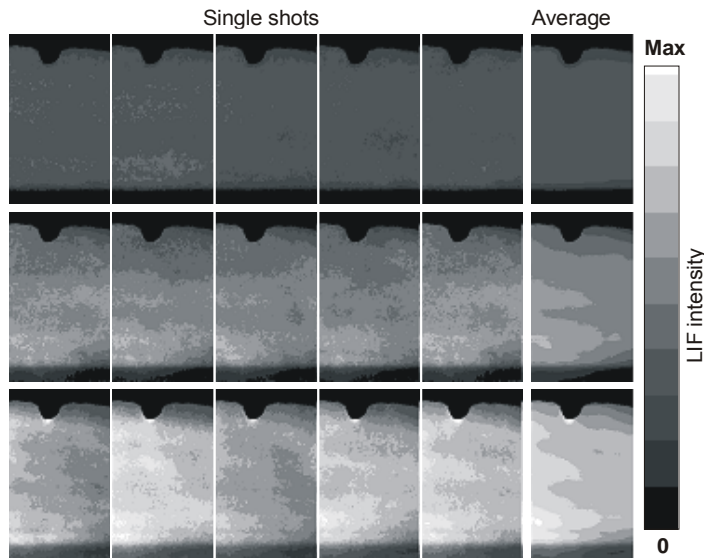


Figure VI-6: In-cylinder distribution of 3-pentanone LIF with early injection and 3 different injection durations (top to bottom: 1.2, 3, and 4 ms). Left five frames per row: Instantaneous images, right frame: Average of 100 images.

Figure VI-6 shows exemplary LIF images of the fuel distribution with early injection for 3 different injection durations (top to bottom: 1.2, 3, and 4 ms). On the left side five examples for instantaneous fuel concentrations are shown; the right frame in each row shows the averaged

fuel distribution. The cyclic variations increase with longer injection times according to richer fuel/air mixtures. Figure VI-7 shows the resulting 3-pentanone (left) and spark emission (right) for 200 consecutive cycles for three different fuel injection durations. The LIF signal is averaged in rectangle 1, Figure VI-5. Both methods show that cyclic variation increase with long injection duration due to misfire and hence variation in the residual gas composition. As mentioned before, calibration measurements can therefore only be performed for operating modes where reproducible combustion ensured ($\phi = 0.7 - 1.6$).

Compared to the CN*-emission signal the 3-pentanone LIF signal has an additional offset. The acquired LIF images are corrected for background signal, as well as spatial inhomogeneity and pulse-to-pulse energy variations of the light sheet. The background images were taken in the motored engine without fuel injection. This condition is not fully comparable to the fired engine. Additional background in the fired case is due to (i) fluorescence from oil contaminations on the quartz ring that build up during engine operation and can not be spectrally separated and (ii) reflections of the laser light sheet from the cylinder head that cause subsequent excitation of molecules outside the plane of the laser light sheet.

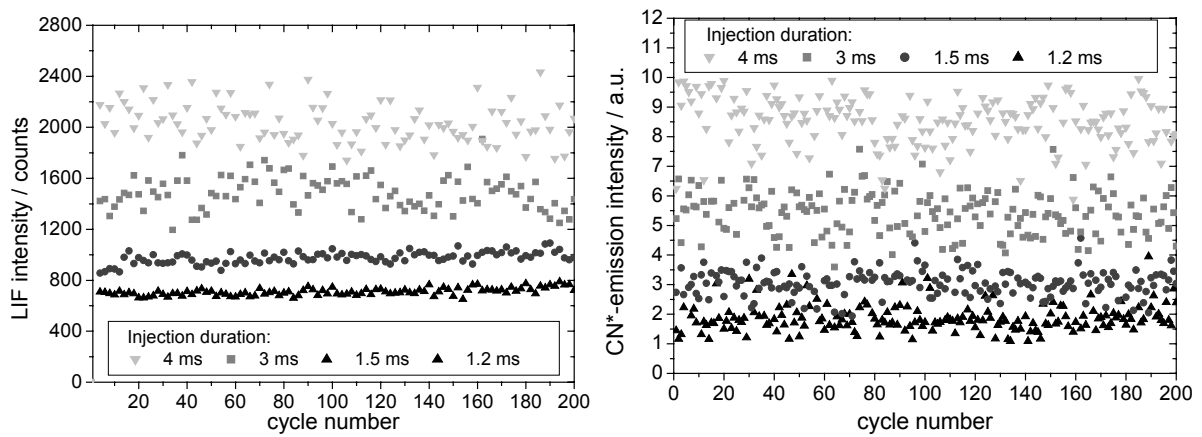


Figure VI-7: Cycle-to-cycle variations of the LIF signal measured from area 1 in Figure VI-5 (left) and the CN*-emission signal (right) for 4 exemplary fuel concentrations.

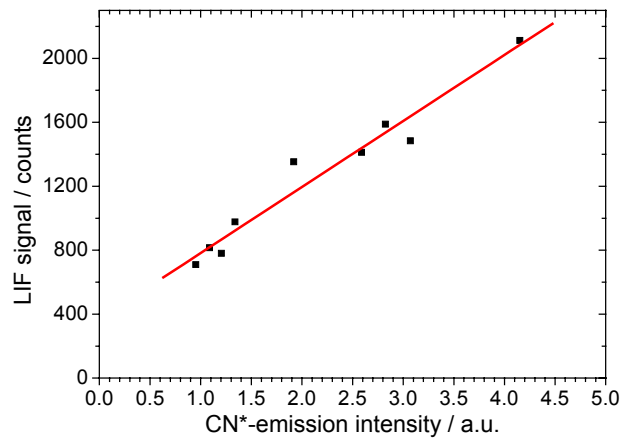


Figure VI-8: Correlation of averaged CN*-emission and 3-pentanone-LIF signals for different homogeneous charge distributions.

A qualitative comparison of the two methods is shown in Figure VI-8. Synchronous measurement series with different homogeneous fuel concentrations were made, and for each series the averages over all measured cycles were calculated. Even in series with strong cycle-to-cycle variations, there is a good correlation between the averaged CN*-emission and 3-pentanone-LIF signals.

The dependencies of the LIF signal on known fuel concentrations and of the CN*-emission signal on known carbon number densities are shown in Figure VI-9. Five different homogeneous operating conditions could be used. The error margins represent the statistical cycle-to-cycle variations. Both plots suggest a linear dependence and will be applied as a calibration for the stratified mode.

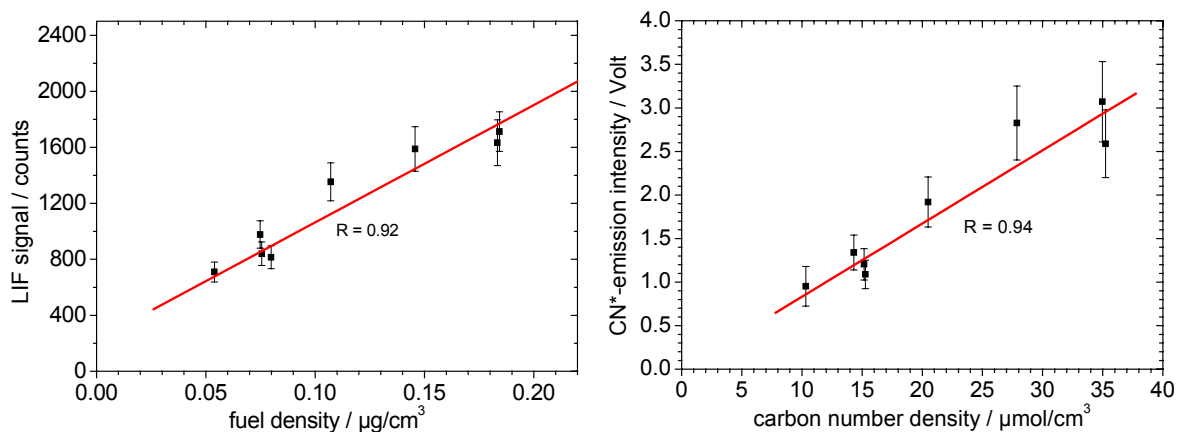


Figure VI-9: Calibration curves: 3-pentanone-LIF signal vs. fuel density (left) and CN*-emission intensity vs. carbon number density (right). The observed dependence is used for calibration.

1.2.3 Stratified mode

With the calibrated system, quantitative measurements on stratified charge distributions were attempted. Three different ignition times (spark advance, SA) (29, 26 and 23°CA BTDC) with a fixed injection time (60°CA BTDC) were observed for the configuration with increased tumble motion. The spray propagation for this configuration was discussed above and is shown in Figure VI-3 and Figure VI-4. Quantitative measurements of the fuel concentration are possible for ignition at 23°CA BTDC. For earlier observation timings (29 and 26°CA BTDC) the signal of fuel droplets disturb the vapor-phase signal. At these comparably early times in the mixing process, a very strong inhomogeneity can be seen.

Figure VI-10 shows the observed variations of the spatial distribution of the equivalence ratio next to the spark plug at 23°CA BTDC for five exemplary images and the average of 100 images. The location of areas with $\phi \sim 1$ vary significantly, but for all displayed instantaneous measurements the spark plug is located in this area. This implies good conditions for ignition and combustion of these cycles. The strong variation of the equivalence ratio in surrounding regions, however, implies a strong local variation in flame propagation velocities. This might cause considerable cycle-to-cycle fluctuations.

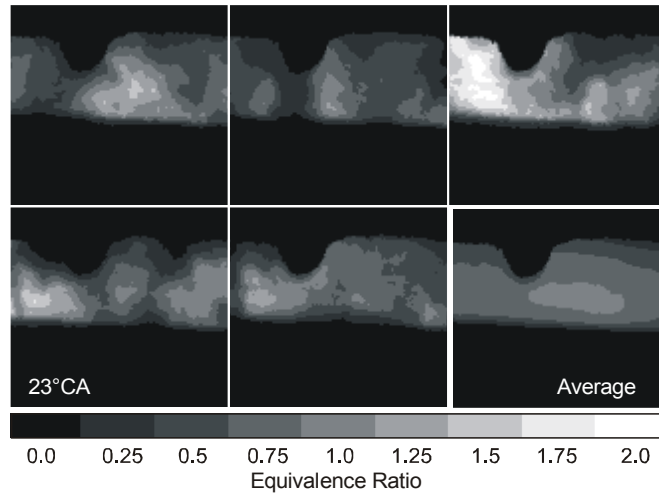


Figure VI-10: Quantitative evaluation of the equivalence ratio for five exemplary instantaneous measurements. The average (bottom right) is taken over 100 images.

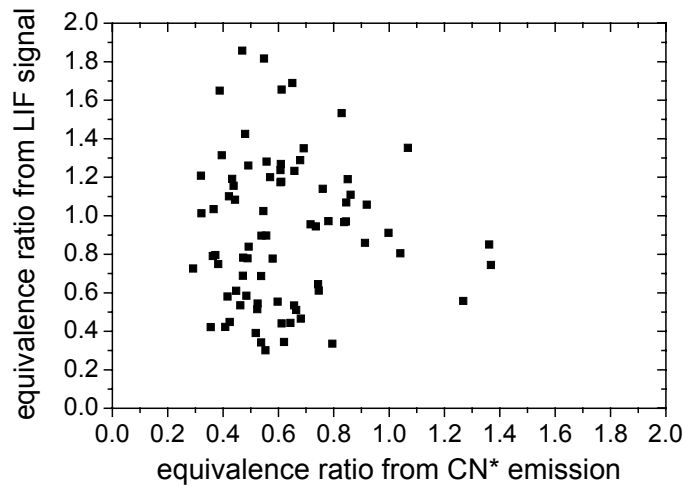


Figure VI-11: Correlation of cycle-resolved equivalence ratio measurements in stratified mode at 23°C A BTDC evaluated with the two methods.

Figure VI-11 shows the cycle-resolved comparison of the measured equivalence ratios. There is no correlation of the results observed with LIF and spark emission spectroscopy. LIF is observed about 3 mm (cf. Figure VI-5) off the spark gap, from where the spark signal is emitted. This spatial and the additional temporal offset (0.5°CA) between both measurements is responsible for the loss of correlation in cases with strong fuel stratification.

Although there is no correlation on a cycle-by-cycle basis, the probability density functions (PDFs) of the equivalence ratio for both methods agree well (Figure VI-12). The similar distributions confirm that the measurement techniques also work when the engine is operated with stratified fuel/air composition.

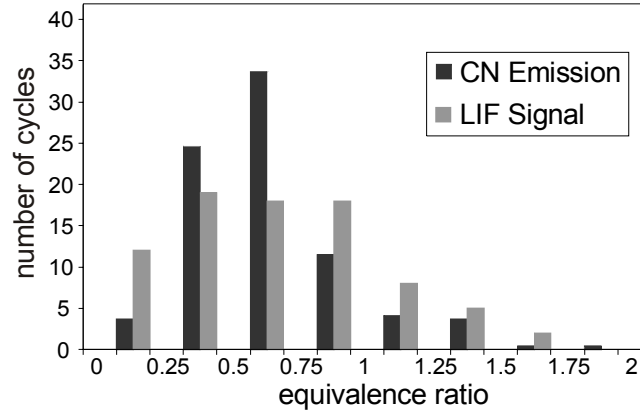


Figure VI-12: Comparison of the equivalence ratio PDFs generated from LIF and spark emission spectroscopy in stratified mode at 23°C BTDC.

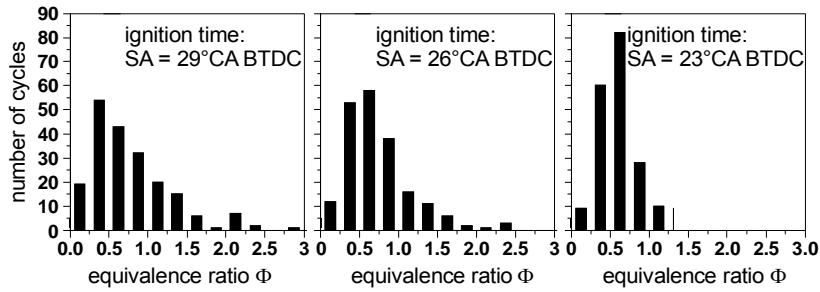


Figure VI-13: Development of the equivalence ratio PDF at the spark gap for different ignition timings (start of injection fixed at 60°C BTDC).

The CN* spark-emission measurements allow the investigation of the reproducibility of the mixture composition at different engine operating conditions. In Figure VI-13 equivalence ratio PDFs (from 200 fired engine cycles) are shown. Three cases with different ignition timing are compared. As shown before, the engine configuration that conserves high kinetic energy in the in-cylinder air motion has a strong influence on the spray propagation. For early ignition (SA = 29°C BTDC) the PDF is broad with an average at $\phi = 0.8$. This indicates that the outer region of the spray reaches the spark plug which results in strong cycle-to-cycle variations of the fuel distribution. With later ignition the PDF gets narrower and the average fuel concentration moves towards the stoichiometric ($\phi = 1.0$) point. The latest ignition timing shows less cycle-to-cycle variations with a slightly lean average equivalence ratio of $\phi = 0.6$. This indicates that during ignition a large fuel cloud is reproducibly located at the spark plug.

1.3 Summary and conclusions

Two different optical measurement techniques that determine the equivalence ratio next to the spark plug were applied quasi-simultaneously in a continuously-fired gasoline engine with air-guided direct injection. Laser-induced fluorescence was used to image the fuel concentration in the injection-ignition plane. 3-Pentanone was applied as a fluorescent tracer and added to the iso-octane fuel. Fluorescence intensities are corrected for pressure and temperature effects. At the same time, the luminescence of the spark was observed. The CN* emission at 388 nm was detected within an interval of 150 μ s after the spark breakdown. After normal-

izing the signal on spark-discharge energy, local carbon densities are obtained. Additionally, strong LIF from the liquid phase discriminated areas with droplets from those with fully-evaporated fuel. This allowed the observation of the liquid-fuel penetration. The instantaneous images show strong spatial cycle-to-cycle variations especially late after injection. The probability distribution of droplets were evaluated from 100 images for each detection timing. The observed distribution indicates a strong interaction between the high tumble motion of the investigated configuration and the propagation of the liquid fuel. The tumble motion deflects the spray towards the spark plug.

During engine operation with homogeneous mixture distribution (early injection) the LIF and the CN*-emission technique correlate well. Both signals increase linearly with the fuel concentration that was varied by changing the injection duration. These measurements were used to calibrate the measured signals within the range of equivalence ratios that ensured stable combustion ($\phi = 0.7 - 1.6$). Outside this range incomplete combustion occurs, resulting in a variation of the fuel concentration in the residual gases and hence in the overall fuel density in the subsequent cycle. Based on the calibration in the homogeneous mode both techniques are compared in the engine under stratified conditions. Only operating conditions with late ignition are used where no droplets are close to the investigated region. Both methods show a similar histogram of measured fuel concentrations. This is a good indication that the techniques yield reliable information about local equivalence ratios even under stratified conditions. A direct correlation for each cycle, however, was not observed because the measurement locations from both measurement techniques are ~ 4 mm apart. Spatial concentration variations over this distance are comparable to cycle-to-cycle fluctuations. Additionally, in the next section we will see how far a spark can be elongated, especially if a strong tumble flow is present. The fluctuations in the spark position due to spark stretching (up to 10 mm) could actually be the crucial factor for the observed signal fluctuations.

The results of the spark-emission measurements are compared for three different ignition times with fixed injection time to demonstrate the potential of this tool. It can be clearly seen that the magnitude of cyclic variations depends on the delay between injection and ignition. For the observed configuration ignition at SA = 23°CA BTDC showed less cyclic variation of the equivalence ratio at the spark gap than with earlier spark advance.

2 Spray–spark interaction in a spray-guided SIDI engine

This chapter describes results from a cooperation with General Motors in Detroit, Michigan, USA. Most of the results shown here and additional measurements regarding fuel spray fluctuations are also published in [31]. Experiments on a spray-guided spark-ignition direct-injection (SG-SIDI) optical test engine are demonstrated. One goal was to quantify the interaction of the fuel spray with the spark plug and the effect on the spark as potential sources of misfires and unstable combustion in a SG-SIDI engine. Another motivation for the experiments was to find out how a commercial fiber-optic spark plug could be used for observing spray-spark interaction by comparing high-speed imaging and standard diagnostics techniques with simultaneously performed fiber-optical spark-emission measurements. The results helped to design a fiber-optic spark plug that is better adapted to the given task.

Spray-guided spark-ignition direct-injection (SG-SIDI) engines can operate in a stratified-charge mode over a wider speed-load range than wall- and tumble-guided SIDI engines, but the close proximity of the fuel spray to the spark electrodes can lead to conditions near the spark gap that are unfavorable for reliable ignition and robust flame propagation: High gas-phase and liquid-phase velocities, high liquid droplet density, and steep, rapidly-varying gradients in velocity and fuel/air ratio. These quantities, which fluctuate significantly from cycle to cycle, depend strongly on spray structure and targeting and on spark-electrode geometry and orientation. Their effects are quantified in a firing SG-SIDI engine using high-speed (up to 60,000 frame/s), high-resolution (nominally 65 μm per pixel) imaging of visible-light spray illumination, laser Mie scattering and CN* spark emission. Simultaneous spark current and voltage measurements from both conventional and fiber-optic spark plugs and engine IMEP data determined from cylinder pressure analysis allow the investigation of sources of misfires and poor flame propagation.

2.1 Optical engine setup and measurement techniques

Figure VI-14 shows a schematic diagram of the four-valve, single-cylinder optical SG-SIDI engine (86 mm bore, 86 mm stroke; compression ratio: 9.7). The piston had a centered, cylindrical combustion bowl whose bottom was formed by a flat quartz window. Flat quartz side windows permitted a view of the spark plug at TDC. A water-cooled pressure transducer measured the cylinder pressure. The spark current and voltage were also digitized at a rate of 500 kHz.

All experiments were performed at conditions corresponding to a part-load cruise for a mid-size vehicle equipped with a four-cylinder naturally-aspirated engine: an engine speed of 2000 rpm, a manifold absolute pressure (MAP) of 95 kPa, and 10 mg gasoline (indolene) fuel injected per cycle, producing an fuel/air ratio of approximately 1:50 without dilution.

For the experiments a multi-hole injector operated at an injection pressure of 110 bar was used. The injector produced eight spray plumes in an axisymmetric pattern, with a nominal angle of 70° between opposite plumes. Extended-electrode spark plugs (a J-gap plug and a special pointed-electrode plug) were used with the 70° injector. To simulate exhaust-gas recirculation (EGR), the intake charge was diluted with nitrogen, typically to a level of 30%. For

continuous firing, this produces an oxygen concentration in the cylinder equivalent to approximately 42% EGR. For this dilution, the optimal end-of-injection (EOI) command timing and spark-advance (SA) timing were $\text{EOI} = 48^\circ\text{BTDC}$ and $\text{SA} = 40^\circ\text{BTDC}$.

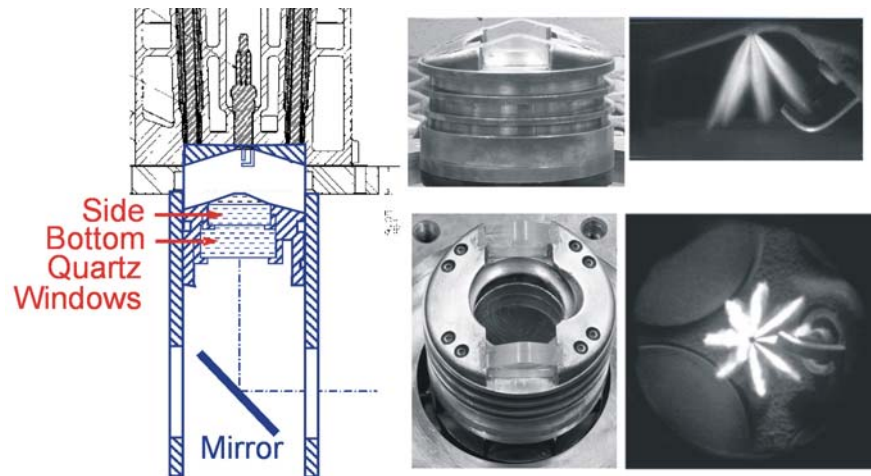


Figure VI-14: Left: Schematic of optical SG-SIDI engine. Center: Photographs of piston. Right: Views of fuel spray through piston side and bottom windows (from [31]).

The experiment with the fiber-optic spark plug (required a 90° injector along with a J-gap plug with a conventional electrode length, as discussed in more detail in paragraph 2.3. Figure VI-14 shows typical spray images (70° injector, extended-electrode J-gap spark plug) recorded with tungsten floodlight illumination. For the high-speed imaging of spark emissions a *Phantom 7.1* monochrome camera was used (12-bit dynamic range, operated here at 368×360 pixels at 12,000 frames/s or 128×144 pixels at 60,000 frames/s).

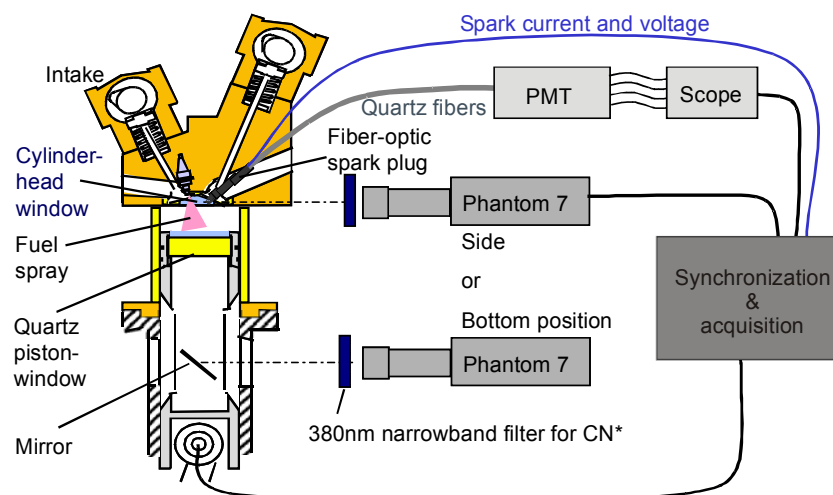


Figure VI-15: Experimental setup for simultaneous high-speed imaging and fiber-optic spark-plug measurements.

For the simultaneous high-speed imaging and fiber-optic spark-plug measurements the camera was used in either side or bottom view position as shown in Figure VI-15. For the evaluation of spark movement and stretching (2.3.3) the side view position was preferred, because it lead to better results during image post processing.

2.2 Spray fluctuations

For a better understanding of the spray-spark interaction as such this section gives a short excursion on measurements of spray fluctuation and spray/spark-plug interaction that were carried out within a cooperation of Isabell Düwel with General Motors beforehand [111].

In those experiments the spray plumes generated by the 70° multi-hole injector were investigated. Variations in spray angles and in liquid distribution within individual cycles as well as from cycle to cycle have been observed. Fluctuations in spray angle within an engine cycle and from cycle to cycle were small (a range of about 6° for the spray plume nearest the spark gap). Fluctuations in liquid distribution as measured by the Mie-scattering intensity were significant: ~25% rms relative to the mean when integrated along the spray plume and several times larger when integrated over small (1.5-mm) regions near the spark plug. These variations must be considered as potential sources of misfires and partial burns [112].

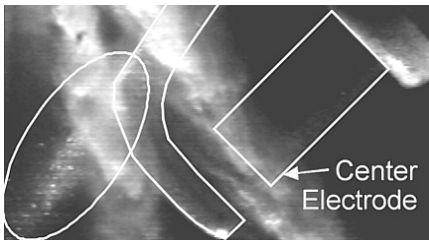


Figure VI-16: Extreme example of spray/spark-plug interaction in a fired SG-SIDI engine (from [31]).

The effects of spark-plug and injector orientation on engine performance were also examined, as well as the effect of spray-plume targeting on the vapor-phase and (relative) liquid-phase fuel concentrations at the gap of the pointed-electrode spark plug as measured by high-speed spectrally-resolved imaging of CN* and C₂* spark emission, respectively [30,44,113]. Despite the large differences in the ensemble-average vapor and liquid fuel concentrations, there was scarcely any difference in ignition stability. Furthermore, the J-gap plug could be rotated up to $\pm 90^\circ$ from

the orientation shown in Figure VI-14 without significantly affecting performance. Larger changes in spark-plug orientation caused the spray to interact strongly with the J-gap ground electrode and degraded ignition stability. Figure VI-16 shows an extreme example of spray/spark-plug interaction in the fired SG-SIDI engine imaged by means of volume illumination from a copper-vapor laser. In this orientation, the spark plug ground electrode faces the approaching spray. One spray plume strikes the ground electrode and produces a stream of large droplets (marked by the ellipse). Although the ground electrode shields the spark gap from the spray plume and reduces the local velocity at the time of spark, the resulting wake causes strong fluctuations, leading to significantly increased misfires.

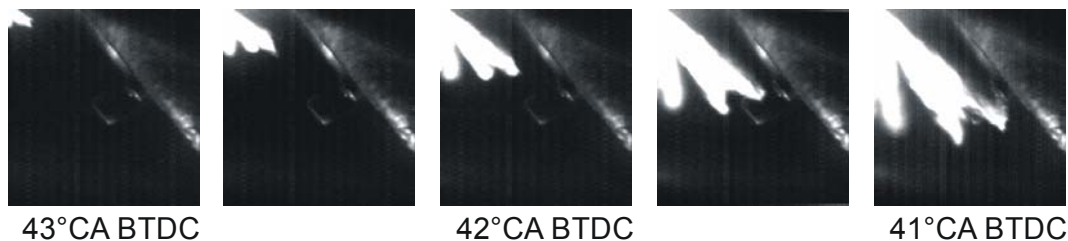


Figure VI-17: Visualization of the spray impact (90° 8-hole injector) on short electrodes of the fiber-optic spark plug.

Most of the experiments described in the next section were carried out with the fiber-optic spark plug. For reasonable engine performance with this optical spark-plug (no elongated

electrodes) a 90° multi-hole injector had to be used instead of the 70° injector. In order to check the interaction of the spray with the spark-plug electrodes, Mie-scattering images were acquired after volume illumination from a tungsten lamp. A good engine performance could be achieved with the electrodes in a 90° position to the spray as shown in Figure VI-17. For a better view of the electrode orientation also see Figure VI-21 (top, left image). In this orientation one spray plume aimed directly for the spark gap and impinged on the ground electrode. In the next section we will see how the spray induced tumble predominantly influences the spark stretching.

2.3 Spray-spark interaction

2.3.1 Spark stretching and restrikes

Spray-guided spark-ignition direct-injection (SG-SIDI) engines typically employ a high-energy inductive ignition system (e.g., approximately 120 mJ spark energy, as in this work). As illustrated by the 60,000-frames/s images in Figure VI-18 (see also [114]), the ignition event is then definitely *not* a nearly instantaneous, localized process, as one might naïvely expect. The overall spark duration here is about 2 ms, or 24° crank angle at 2,000 rpm engine speed. The spark is highly distorted and stretched out of the gap to distances of at least a few mm. The glowing fireballs as well as the more diffuse light extending from the bright spark represent predominantly thermal emission from soot resulting from locally rich combustion ignited by the spark. (The broadband visible-wavelength images here do not show ultraviolet OH* chemiluminescence from partially-premixed stoichiometric or lean combustion.)

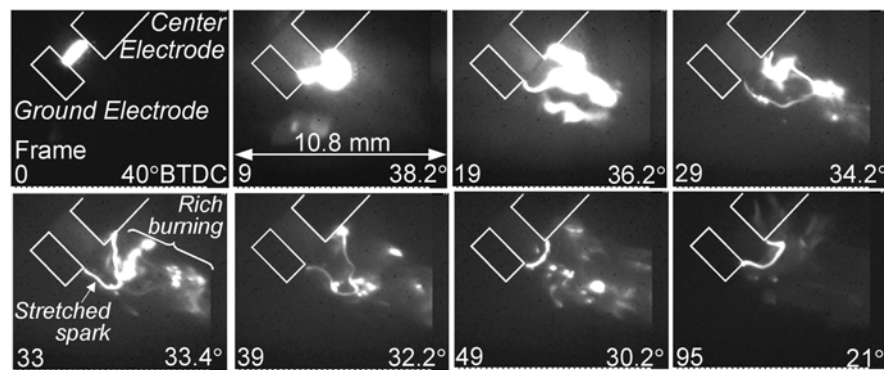


Figure VI-18. Broadband visible-wavelength (400-800 nm) images of ignition in a spray-guided SIDI engine selected from a sequence recorded at 60,000 frames/s with 7.5- $\mu\text{m}/\text{pixel}$ nominal spatial resolution. The spark-plug electrodes (overlaid in white) are oriented so that the camera looks directly into the opening of the J-gap. A spray plume from the multi-hole injector approaches the spark plug from the upper left. (Figure from [31]).

Spark voltage and current measurements can provide useful information, especially when combined with high-speed imaging [114]. Figure VI-19 shows relatively slow spark stretching for non-injected (premixed-charge) operation with the pointed-electrode spark plug. As the spark is stretched, its electrical resistance and the voltage drop across the spark increase until eventually the available coil voltage can no longer sustain the spark. Unless this occurs when the coil is almost fully discharged, there will usually be enough energy left to cause another

breakdown, i.e. a restrike, sometimes directly across the spark gap (e.g., between frames 39 and 49 of Figure VI-18 and at 1.19 ms in Figure VI-19) and sometimes into the existing ionization channel, which can be seen to persist in Figure VI-19 even though in this case the restrike occurred across the gap.

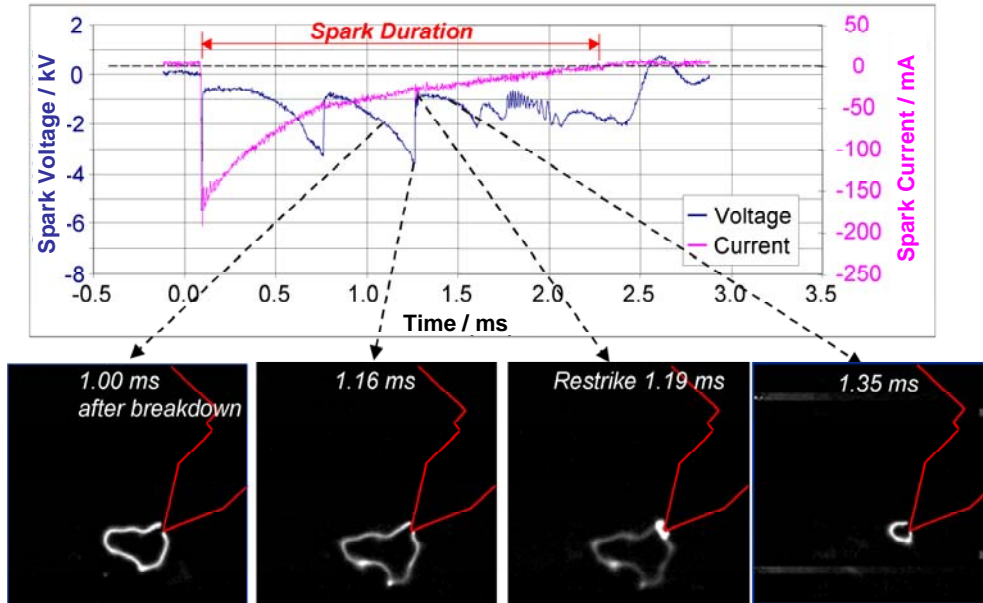


Figure VI-19: Spark voltage and current traces together with images from a 60,000-frames/s sequence selected to illustrate spark stretching and a restrike during premixed-charge (non-injected) operation. (Figure from [31])

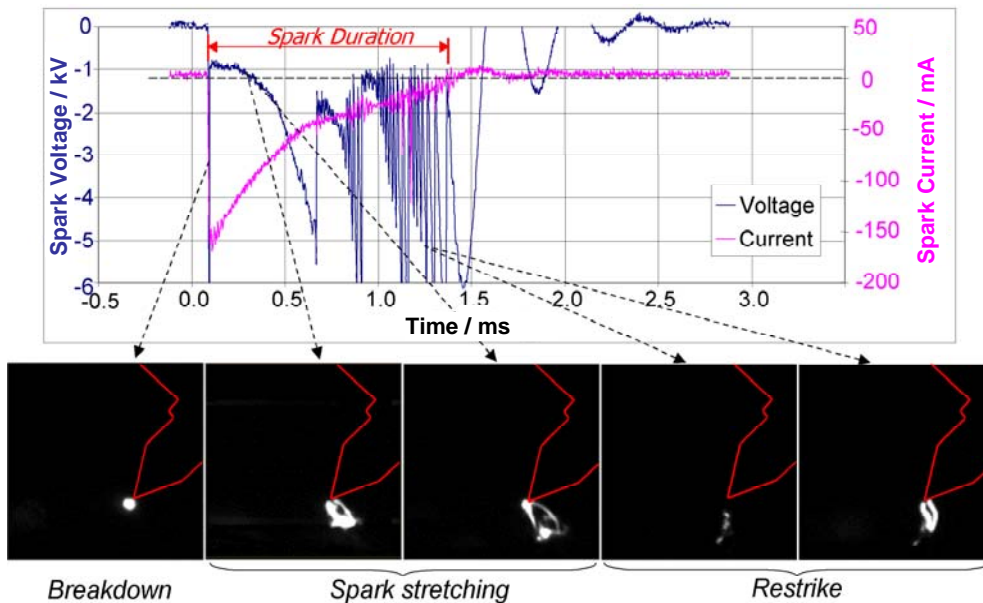


Figure VI-20. Spark voltage and current traces and selected high-speed images during direct-injection operation. (Figure from [31])

In contrast, Figure VI-20 shows similar results selected from a dataset of 1,000 continuously-fired cycles recorded during direct-injection stratified-charge operation ($\text{EOI} = 48^\circ\text{CA BTDC}$, $\text{SA} = 40^\circ\text{CA BTDC}$). The strong spray-induced motion here leads to locally higher velocities and more rapid spark stretching, as shown by the steeper slope of the spark voltage curve

around 0.5 ms. Furthermore, from 0.8 ms to the end of the spark discharge at 1.4 ms (indicated by the return of the spark current to zero), the voltage trace shows a series of very rapid restrikes. This occurs when the spray interacts very strongly with the spark, producing such high local velocities and such rapid stretching that the available voltage cannot sustain the spark for more than a few tens of microseconds. This rapid restriking also shortens the spark duration (≈ 1.3 ms here compared to ≈ 2.4 ms in the non-injected example of Figure VI-19).

The cycle-to-cycle variability in the spark current and voltage traces and in the spark images is large, but no straightforward correlation of these features (e.g., spark energy or frequency of restrikes) with misfires or partial burns could be found.

2.3.2 Combined imaging, fiber-optic and spark diagnostics

Fiber-optic spark plugs (FOSPs) have previously been used extensively for analysis of early flame-kernel motion in premixed-charge engines (see, e.g., [115,116]) and less extensively for spectroscopic measurements [45,73], including the CN* technique for fuel-concentration measurements originally developed using imaging techniques [44]. This section describes initial experiments that combine a FOSP with the high-speed imaging and spark voltage-current diagnostics discussed above. The principal objectives were to use the high-speed imaging to help interpret the spark- and combustion-emission signals detected using the FOSP and to assess prospects for using a FOSP in SIDI engines where imaging is not possible.

FIBER-OPTIC SPARK PLUG

The available fiber-optic spark plug (FOSP, *Smetec ACR40LTSMP*), shown in Figure VI-21, had considerably shorter J-gap electrodes and was therefore not well matched to the 70° spray angle used with the extended-electrode plugs discussed above. An 8-hole injector with a 90° included angle between opposite spray plumes directed fuel close to the FOSP spark gap and, together with a reduction in nitrogen dilution to 20%, provided adequate engine performance to allow evaluation of the combined diagnostics approach. The optimum injection and spark timings under these conditions were $\text{EOI} = 36^\circ\text{CA BTDC}$ and $\text{SA} = 28^\circ\text{CA BTDC}$.

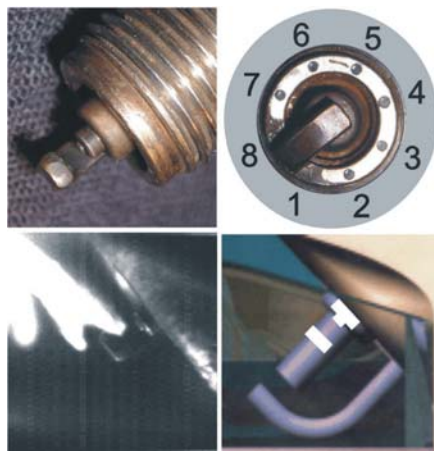


Figure VI-21. Upper: Photographs of fiber-optic spark plug in side and end-on views in orientation in which plug was installed. Lower left: Image of fuel spray from 90° injector impinging on fiber-optic spark plug in engine. Lower right: Comparison of electrode lengths and orientation of fiber-optic (white overlay) and extended-electrode spark plugs.

Light collected by the eight optical fibers (7° field of view) passed through colored glass filters en route to photomultiplier tubes, providing a combined optical bandpass of 280–500 nm. The resulting signals were digitized together with the spark voltage and current at a 500 kHz sample rate. The spectral bandwidth of the signals detected with the FOSP resulted from the combination of the photomultiplier sensitivity and the transmission of an optical bandpass filter. As shown in Figure VI-22 the spark-emission signal from CN^* at 388 nm is in the peak of the detection bandwidth, but also OH^* chemiluminescence at 308 nm, and thus, flame front movements and the early flame kernel were detected.

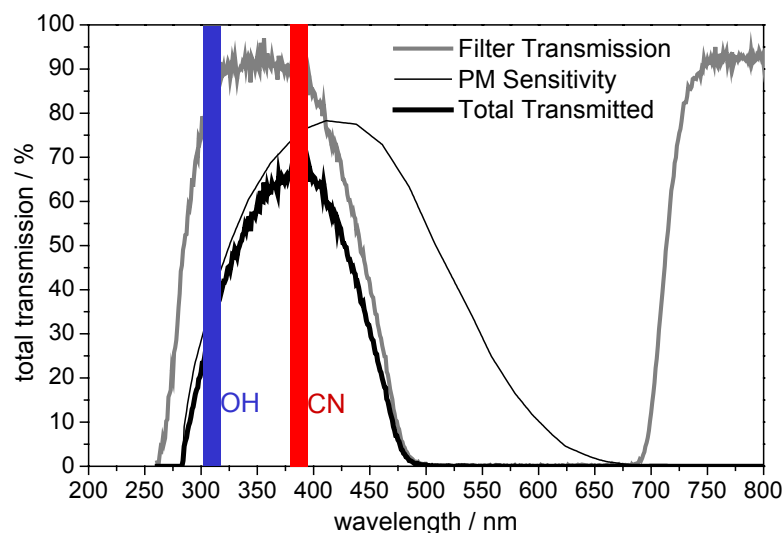


Figure VI-22: Spectral detection window of photomultiplier for fiber-optic spark plug measurements.

EXEMPLARY SPARK CURRENT-VOLTAGE TRACES AND OPTICAL SIGNALS

An example of simultaneous spark current/voltage traces and optical signals is shown in Figure VI-23. Features associated with the spark and combustion can be distinguished fairly easily. However, a preliminary conclusion from inspection of a few thousand such datasets and companion images is that it is difficult to extract *quantitative* information about features of interest (e.g., spark-stretching velocity or the arrive time of the early flame kernel at a fiber location) from the fiber-optical signals alone because of the long spark duration, the extensive spark stretching, the line-of-sight integration implicit in the technique, and the rapid variation of intensity due to the strong spark emission, the weak luminosity from the early partially premixed flame kernel, and the strong luminosity from locally-rich combustion. The situation in stoichiometric homogeneous-charge engines is considerably simpler since they typically operate with significantly lower ignition energy (hence shorter spark duration and less stretching) and with less variation in light intensity during combustion.

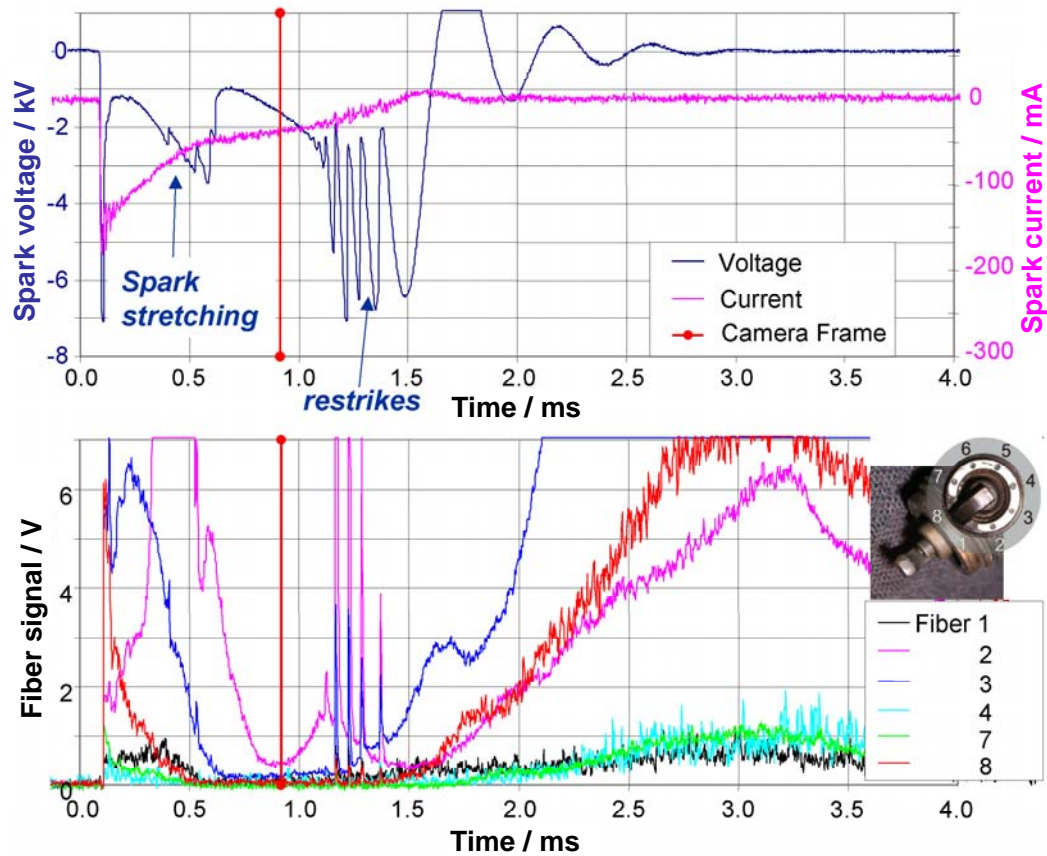


Figure VI-23. Example of individual-cycle current/voltage traces (upper) and optical signals (lower) from fiber-optic spark plug during spark (0 – 1.6 ms) and flame growth (1.6 – 4 ms) in SG-SIDI engine

2.3.3 Spark stretching from CN* image analysis

High-speed (60,000-frame/s) images of the spark recorded in conjunction with the fiber-optic data nevertheless proved of considerable interest and use in themselves. These spark images were recorded through the cylinder-head and piston side windows using a 10-nm bandpass filter to select the CN* emission from the spark at 385 nm wavelength. Figure VI-24 shows example images of a stretched spark from a typical series of highspeed CN* images. Note that one series comprises up to 100 spark images per ignition event. These images provide a measure of fuel concentration [44] and allow the spark to be imaged during its lifetime without interference from combustion luminosity, providing measures of spark stretching and local velocity.

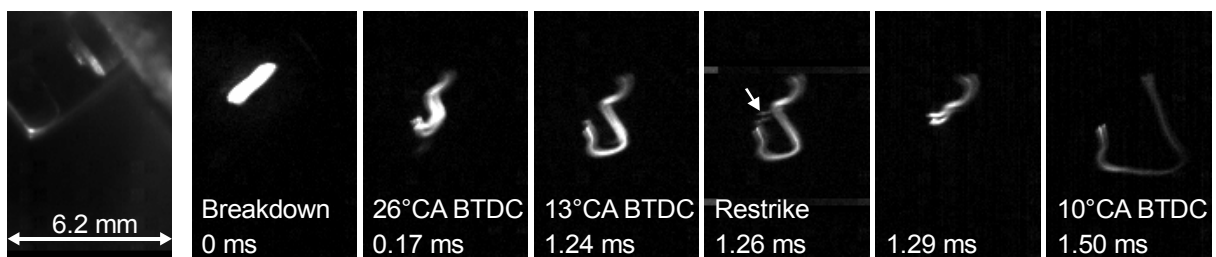


Figure VI-24: Exemplary high-speed CN* images of stretched spark.

To extract systematic information on spark stretching and velocity required an automated analysis of thousands of images. The first step was to remove low-intensity structured background artifacts (horizontal bars) that appeared in about 25% of the images in addition to very-low-level electronic noise and spark light scattered from engine surfaces (see the middle frame of Figure VI-25). Unfortunately, the horizontal bars appeared in three distinct patterns and varied in intensity depending on the overall intensity level of the image. The starting point of the background correction was to construct averaged images of the three bar patterns without a spark present and to determine unique features that allowed the identification of which pattern, if any, was present in the image. When present, the bar artifacts were then subtracted out using the appropriate averaged artifact image multiplied by a scaling factor that was evaluated from the average intensity in a small region in each image where the bar artifacts never appeared.

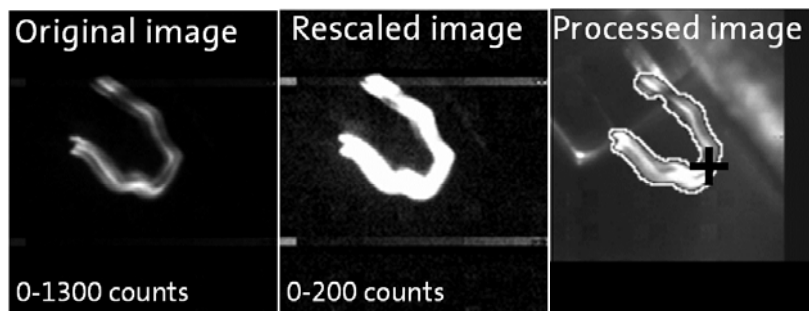


Figure VI-25: Example of high-speed CN* image of stretched spark from fiber-optic spark plug and image analysis (right) in which the spark image, the identified spark outline (highlighted in white) and the centroid (marked by large cross) are overlaid on a reference image of the spark plug.

After background removal, the spark was identified and reduced to a binary image by a combination of intensity and gradient thresholding. The thresholds were selected automatically using a variance method within bounds determined by a multiple of the residual noise level in the image (i.e. form an area in the image where a spark was never detected) and a fraction of the maximum intensity. After thresholding, a continuous spark, as recognized by the eye, would sometimes appear as two or more disconnected pieces. When more than one object was identified by the thresholding algorithm, therefore, a morphological closing operation with a radius of a few pixels was applied. In many cases, this reconnected the portions of the spark into a single entity. If more than one object remained after the closing operation, the image was not used for further evaluation.

For successfully identified sparks, the spark outline and the centroid position were calculated from the binary image. Note that the centroid, which was generated by an erosion procedure, is preferable for evaluating the spark stretch since the centroid is always located within the object, unlike the center of mass, which can be a considerable distance outside a sausage-shaped object like the example in Figure VI-25 (right).

Figure VI-26 shows results of this analysis for both non-injected (homogeneous propane-air) and SG-SIDI operation with the fiber-optic spark plug. Note that the positive direction is taken as the direction of the spray plume that approaches the spark gap, i.e. the spark in Figure VI-25 is positively stretched. Clearly, the direct-injected case exhibits higher stretching

speeds. For this case, Figure VI-27 suggests that there is perhaps a weak correlation of partial burns with low stretch speed. Note, however, that not all sparks in the ensemble are included in this graph.

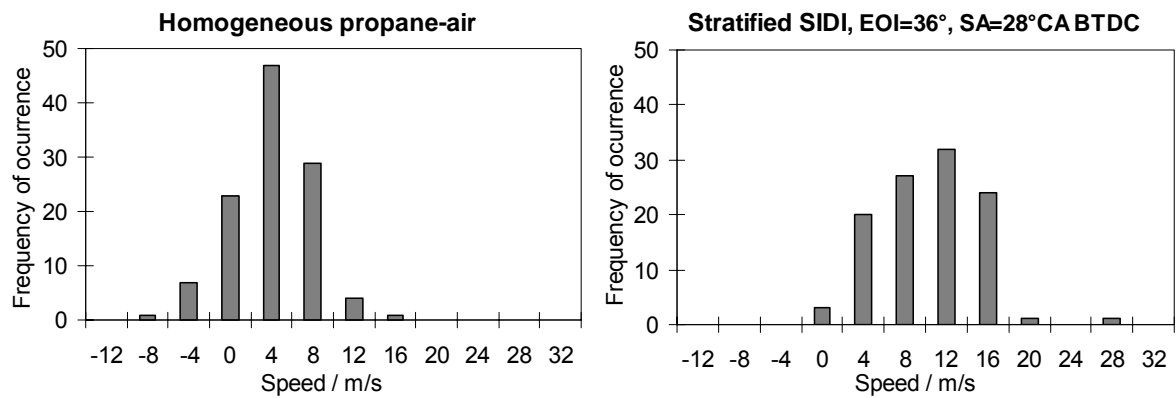


Figure VI-26 Histograms of spark-stretching speed obtained from CN* image analysis for homogeneous (non-injected) and direct-injected operation. Positive speed is taken in the direction of the fuel spray plume.

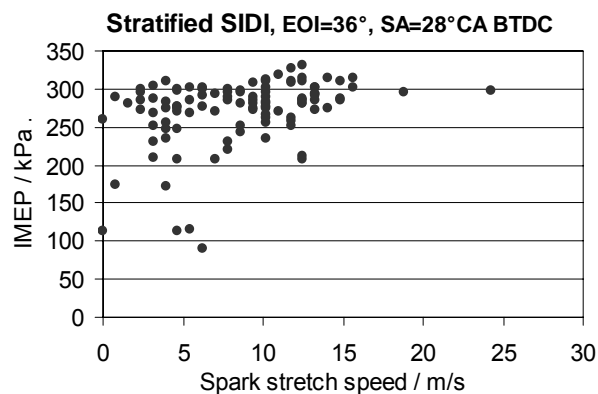


Figure VI-27. Correlation of IMEP with spark stretch speed (surface sparks not included).

Although surface spark discharges were *never* seen over tens of thousands of cycles with the extended electrode spark plugs, they were observed in 10–20% of the cases with the short-electrode fiber-optic spark plug, as illustrated in Figure VI-28. As one might expect from the image of the spray plume impinging on the spark electrodes in Figure VI-17, the surface sparks tend not to encounter much fuel. Indeed, Figure VI-29 shows that in this 200-cycle example, all the misfires and most of the partial burns were associated with surface discharges.

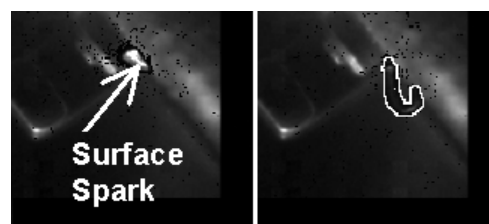


Figure VI-28. Two examples of surface sparks observed with short-electrode fiber-optic spark plug.

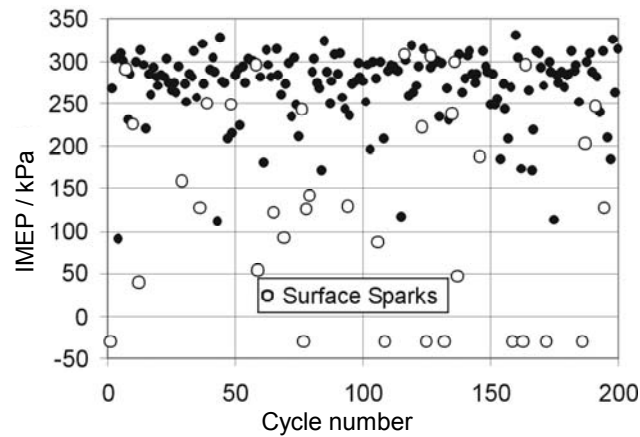


Figure VI-29. IMEP for 200 continuously fired cycles using the short-electrode fiber-optic spark plug ($EOI=36^\circ BTDC$, $SA=28^\circ BTDC$). Open circles identify cycles with surface sparks.

2.4 Summary and conclusions

High-speed imaging, image analysis and spark diagnostics were used to characterize aspects of the fuel spray, its interaction with the spark electrodes, and its effect on the spark in a spray-guided direct-injection gasoline engine. The principal conclusions regarding the spray-spark interaction are: (i) The high spray velocities present near the spark gap at the time of ignition, coupled with the long spark duration, lead to dramatic spark stretching and frequent restrikes, which shorten the spark duration. (ii) The effects listed above show no significant correlation to misfires and partial burns in the engine configuration examined here. (iii) Surface sparks, which have been recognized as a source of misfires in spray-guided engines (e.g., [114]), were never observed with the extended-electrode spark plugs normally used in this engine. Surface sparks were observed only with a short-electrode spark plug that placed the spark gap within about 3 mm of the cylinder head. In this case, misfires and partial burns were dominated by surface sparks.

3 Fuel LIF measurement with fiber-optic spark plug in a commercial IC engine

This section shows an experiment that proves the feasibility of the fiber-optic spark plug (FOSP) for LIF measurements in a commercial unmodified engine. The FOSP was used instead of a regular M14 spark plug. This test was performed soon after the FOSP was ready for use and before the proper detection module was finished. The engine is operated with regular fuel and thus quantitative tracer-LIF measurements as described in this thesis were not possible. Nevertheless, there are many fluorescing species in regular fuel allowing a qualitative measurement of fuel concentrations.

3.1 Experimental setup

3.1.1 Ford engine with port fuel injection

The test engine was a commercial four-cylinder 16-valve port fuel injection SI engine with a displacement of 1242 cm³ (1.25 Zetec-SE, Ford). This model has been used in the *Ford Fiesta* until 2002. The maximum engine power is 55 kW at 5200 rpm and the maximum torque of 110 Nm is reached at 4000 rpm. For the presented measurements the engine was operated throttled at 2000 rpm and 20 Nm.

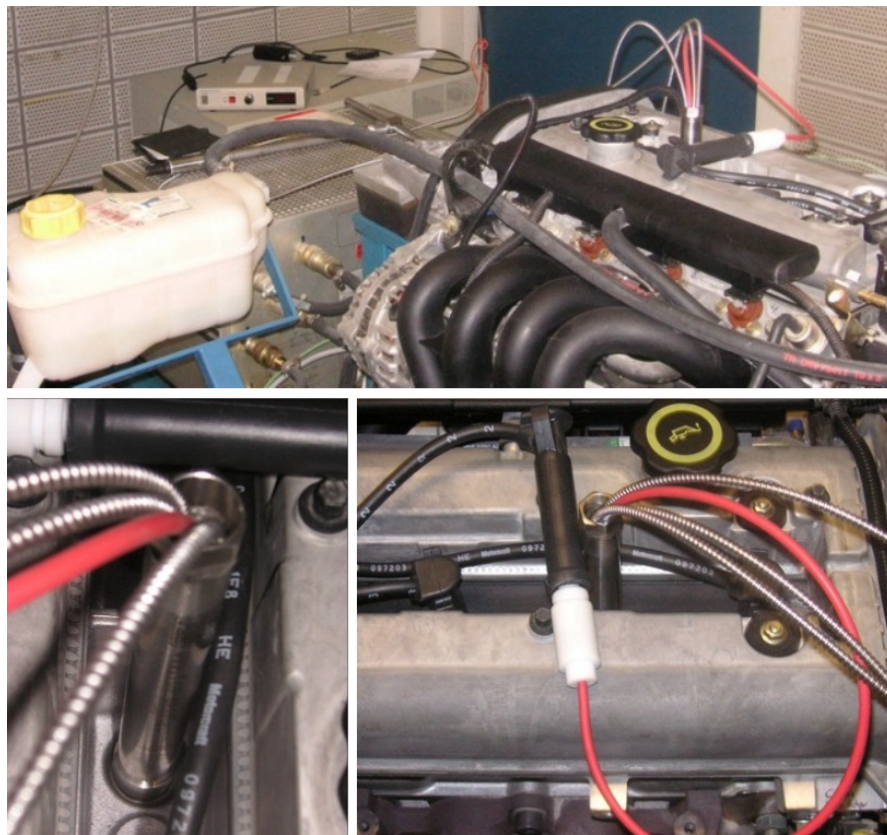


Figure VI-30: Photos of the fiber-optic spark plug in Ford Fiesta engine for fuel LIF measurements.

Spark advance and injection timing were triggered by the original engine control unit. Therefore, no influence could be taken on the mixture formation. Crank-angle (CA) resolved trigger signals and the trigger for the top dead center (TDC) were not available. Therefore, the spark advance for a set engine speed and load was used as master trigger signal within the engine cycle. This trigger signal was created from the inductive signal from the high-voltage discharge of the ignition coil that can be easily measured with an unshielded wire. Time delays between the time of ignition and the triggering of the excitation laser and thus acquisition of a LIF signal were converted into crank angles. This was possible because the engine was running stable at 2000 rpm. The deviation was about 3°CA . For the measurements the engine was fired for about 10 to 20 minutes. In between measurements the engine was motored and background signals could be acquired.

3.1.2 Optical setup

Figure VI-31 shows the experimental setup for LIF measurements in an engine with the fiber-optic spark plug. The Nd:YAG laser was triggered externally for a crank angle synchronization. At the engine speed of 2000 rpm in every second engine cycle at a given crank angle a laser pulse was triggered. This results in a repetition rate for the laser of 8.33 Hz, which is just within the acceptable range for a flashlamp pumped Nd:YAG laser. The laser beam (266 nm, 8 ns, 1 mJ) was coupled into the excitation fiber and guided to the probe volume close to the spark gap of the FOSP. The fluorescence signals are collected by the two detection fibers that were plugged into a photomultiplier (*Hamamatsu, 1P28*). Before reaching the photomultiplier the signal light passed two optical glass filters (*Schott, WG295, UG5*), resulting in a spectral detection window between 290 and 430 nm (for filter transmission plots see appendix IX 1). The photomultiplier voltage traces were then recorded with a digital oscilloscope (*LeCroy*) and could be printed out or saved to floppy disk for further evaluation.

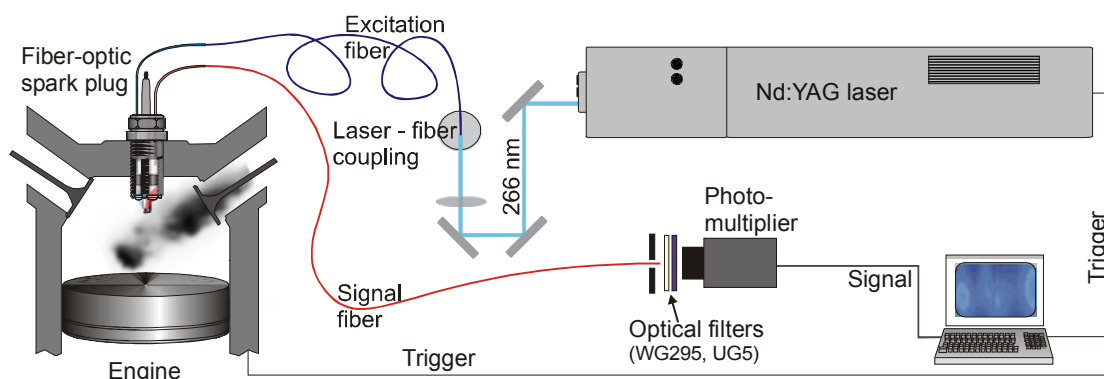


Figure VI-31: Experimental setup for fuel LIF measurements with fiber-optic spark plug.

3.2 Results

Within the spectral detection window not only fluorescence signals could be observed. The emission signal from the ignition spark was clearly distinguishable (cf. previous section), and a few milliseconds after the spark emission the strong flame chemiluminescence could be detected. The absence of these two signals are good indicators for misfires and the correct ignition function of the FOSP could be checked. Figure VI-32 shows two printouts from the oscil-

oscope display. The left graph shows an example for a spark emission signal (top trace) acquired in the *Ford* engine. The bottom trace is the laser trigger monitor signal. The time scale in this graph is 1 ms per unit. The average duration of a spark emission signal is between 1 – 2 ms. In a various of random tests observing this emission signal the spark plug never failed. Throughout the whole experiment, the engine was running smoothly with the FOSP.

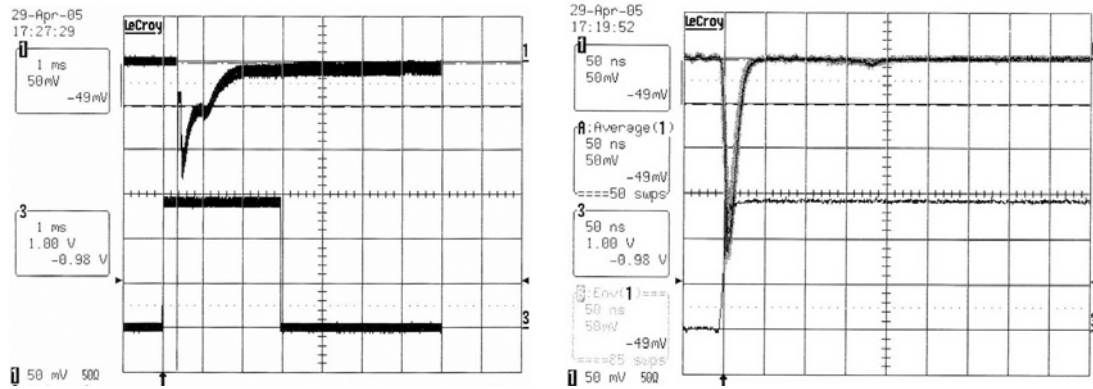


Figure VI-32: Exemplary photomultiplier signals. Left: Spark emission signal (note that the photomultiplier gain was strongly reduced for these measurements). Right: Average over 50 single fuel LIF signals at the same crank angle in 50 independent cycles (with standard deviation in gray).

The actual fuel LIF measurements were performed during the intake stroke of the engine. An example of an average LIF signal as seen on the oscilloscope monitor is shown in Figure VI-32 (right). The graph shows the average signal for a given crank angle (280°CA before ignition) from 50 independent cycles. The standard deviation is plotted as a gray shade beneath the curve. For some measurements presented here this deviation was as high as 50% due to cycle-to-cycle variations. The time resolution in the right graph in Figure VI-32 is 50 ns per unit. The time resolution of the used photomultiplier is ~10 ns. Thus, the relatively long lifetimes of fuel LIF could be seen in the photomultiplier signals. Note, that the photomultiplier cathode voltage was 500 V for the observation of spark emission signals and 700 V for the detection of LIF signals.

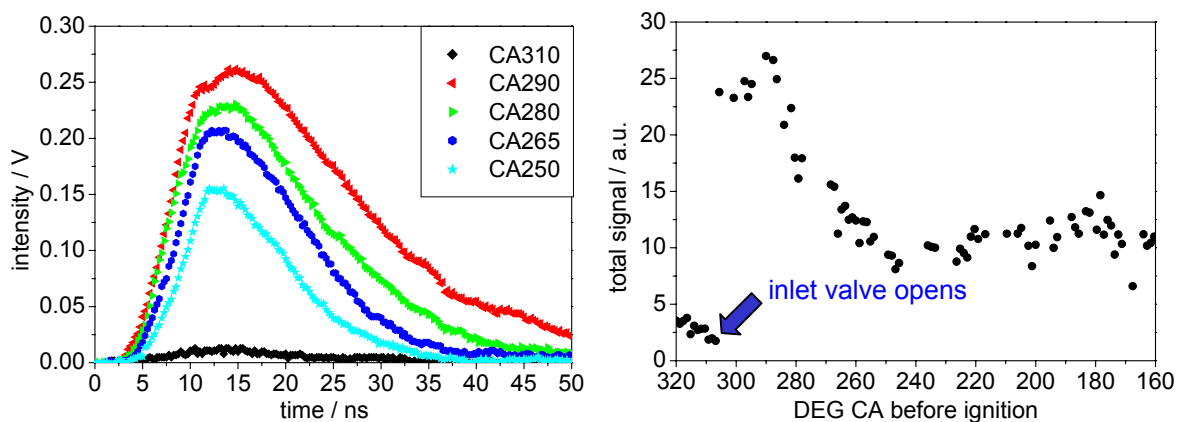


Figure VI-33: Fuel LIF signals during the inlet stroke. Left: Exemplary average signals for different crank angles measured in independent cycles. Right: Total integrated LIF signal intensities versus degree crank angle before ignition. Each data point is an average from 50 independent cycles.

The left graph in Figure VI-33 shows another five average LIF signals at exemplary crank angles before ignition. The right graph shows the development of the cycle averaged fuel LIF intensity during the intake stroke. Shortly after top dead center a strong increase in signal intensity was measured. Within the next 40°CA this signal drops to a third of its maximum and remains there until the end of the intake stroke. Not shown here is the observed pressure dependent increase of the signal during the end of the compression stroke just before ignition.

Provided that the temperature and pressure changes during the intake stroke are small and do not significantly influence the LIF signal, a linear connection between LIF signals and fuel concentration can be assumed. The strong signal increase around 305°CA before ignition could then be associated with an opening of the intake valves. At that moment a relatively rich fuel/air mixture is sucked into the engine. After the end of injection in the intake port the mixture gets more and more lean until only air is breathed in. This can be seen in the gradual decrease of the signal until about 220°CA before ignition, when the mixture seems to have homogenized.

VII SUMMARY AND CONCLUSIONS

The lack of fossil fuels will inevitably change the propulsion systems of future cars. Nevertheless, it is not yet foreseeable when alternative energy concepts like hydrogen-powered fuel cells will finally take the place of internal combustion (IC) engines. On the way to this changeover IC engines may have to use renewable fuels or gas. Fuel efficiency is becoming an even more important factor and the improvement of IC engines towards better efficiency and cleaner exhaust must continue. Gasoline engines have a large potential for the near future. Promising concepts like spark-ignition direct injection (SIDI) or homogeneous charge compression ignition (HCCI) could make gasoline engines as efficient as Diesel engines, whereas almost no NO_x and soot are emitted (e.g., in the case of an HCCI engine). However, the further improvement of modern IC engines requires non-invasive, quantitative diagnostics on engines that are not substantially modified or not changed at all (i.e. production-line engines). With the commercial availability of lasers, optical methods have become popular for these diagnostics, but the required optical access often prevents an application on unmodified engines.

With the presented microoptical systems the necessary diagnostics can be accomplished with minimal invasive optical access. The fiber-optic spark plug enables UV-laser-induced fluorescence (LIF) point measurements close to the spark gap. These UV-LIF diagnostics can be carried out in any unmodified, commercial spark-ignition (SI) engine that uses spark plugs with M14 threads. The presented endoscopic excitation and imaging optics provide optical access through a “keyhole” of only one centimeter. Besides, their applicability is not restricted to engine research. Wherever fast, in-situ non-invasive diagnostics are needed (e.g., in gas-turbines, fuel-cells or for the observation of flows and mixing processes in general), optical measuring techniques can be applied with these new microoptical systems.

The outline of this work is divided into four major sections. First, the spectroscopic background and its respective applications are described (chapter III). Then, the design and realization of the new microoptical systems are presented (chapter IV). The optical design and computer simulations were made by the Institut für Technische Optik (ITO) at the University of Stuttgart within a joint project cooperation. The following chapter (V) shows experimental results from measurements with the hybrid UV endoscope and the fiber-optic spark plug. In the last chapter (VI), three different engine experiments are discussed.

In various experiments, particularly LIF of fuel tracers was investigated. For quantitative measurements in engines, fuel tracers are added to weakly- or non-fluorescing model fuels. The used tracers were toluene (being a major aromatic component of commercial fuel) and 3-pentanone which have similar volatilities and boiling points as the model fuel iso-octane. Before spectroscopic methods can be applied quantitatively, the photophysical characteristics of the investigated species must be well known. The photophysical properties of these two tracer molecules have been extensively studied in the past. Characteristic dependences of the respec-

tive LIF signal on temperature, pressure or gas composition (e.g., oxygen partial pressure dependence of toluene-LIF) have been found. In this work, two applications that use these dependences are described and tested for their feasibility with the new microoptical systems. A novel two-color thermometry method uses the red-shift of the toluene emission spectrum after 266-nm excitation. The ratio of two well-defined spectral regions in the emission spectra yields temperature information independent of the local tracer concentration [69,71]. Another method combines both tracers and uses the fact, that toluene LIF is quenched by molecular oxygen whereas 3-pentanone LIF is not [11]. By the simultaneous acquisition of both spectrally-separable emission signals the local oxygen concentration can be calculated and thus the fuel/air-equivalence ratio in combustion systems can be measured.

The described spectroscopic concepts can be quantitatively applied under certain conditions. However, in order to completely understand the photophysical properties of toluene and 3-pentanone and for respective model calculations some questions remain and will be subject of future research. Within this work, a contribution to this area of research has been made by highly time-resolved measurements of the 3-pentanone- and toluene-LIF lifetimes. The measurements were performed with the fiber-optic spark plug via time-correlated single-photon counting (TCSPC) using a Ti:Sapphire laser. For the first time, the bi-exponential decay of toluene LIF was directly measured and the prevailing photophysical model could be validated. Additionally, the characteristic dependence of the toluene-LIF lifetimes on temperature and oxygen partial pressure can be used for concentration-independent temperature and fuel/air-equivalence ratio measurements.

With the *fiber-optic sensor*, temperature and species concentration information in the area close to the ignition spark can be acquired via UV-LIF. Because all optical components are completely integrated into a spark-plug, the sensor can be applied to unmodified production line engines. The probe volume of about 2 mm³ is defined by the optical characteristics of the sensor, i.e. the combination and arrangement of tilted fiber ends and spherical sapphire windows. It can be adjusted within a small area around the spark gap. Excitation and fluorescence light are separately guided through all-silica fibers. The signal fiber is plugged into a 19"-rack detector module. In this module three highly-sensitive channel photomultipliers (CPM) are arranged in a custom-designed filter cascade for the spectral signal separation and simultaneous detection of fluorescence signals. The spark-plug sensor was tested in various experiments including the measurement of flow temperatures and oxygen partial pressures via the described tracer-LIF methods. Hence, the feasibility of the fiber-optic spark plug for quantitative tracer-LIF measurements was shown. In a commercial four-cylinder engine, the spark plug proved its full functionality including the proper ignition function as well as a good pressure and temperature resistance. Fuel-LIF measurements qualitatively showed the development of fuel concentrations at the spark gap. Besides the suggested use of the sensor for UV-LIF measurements, it can also be used for spark emission-spectroscopy.

The novel *hybrid microoptical system*, consisting of a UV endoscope and two microoptics for the generation of lightsheets or illumination patterns, was realized for the two-dimensional observation of processes in cavities with limited optical access. It is denoted "hybrid" because of the combination of refractive and diffractive optical elements. The diffractive elements are employed to define the specific excitation beam shaping and they help to reduce aberrations

in the imaging system. The design of the endoscope comprises a small light weight front endoscope that is chromatically uncorrected and hybrid relay elements for the correction of spatial and chromatic aberrations. By means of two relay elements, two spectral detection ranges are defined and optimized for the imaging of toluene-LIF (275 – 350 nm) and 3-pentanone-LIF (380 – 440 nm) signals. Different spectral detection regions can be selected by changing the respective relay element. Its modular design makes the endoscope flexible for the use with different filter combinations and enables multiple camera experiments with only one “keyhole” access into the examined object. The endoscope was characterized and tested in laboratory experiments. In a two-camera experiment, the local oxygen concentration was measured in an atmospheric-pressure mixing flow with the combined use of the endoscopic excitation and imaging optics. Under application-relevant conditions, the new hybrid UV endoscope proved to be about ten times more light efficient than a commercial UV endoscope and showed a better spatial resolution over a broadband spectral detection range. Even in comparison to a regular 105 mm UV lens with the same paraxial object magnification the hybrid UV endoscope gathers more light (i.e. a factor of 1.3 at 300 nm and about twice the amount of light over a broader spectral detection range up to 440 nm). In another experiment the hybrid UV endoscope was used together with the inhomogeneous excitation optics for the measurement of flow velocities in a laminar flow. In this flow-tagging experiment the displacement of marked lines in the flow was observed via sensitized phosphorescence of biacetyl. Measured and calculated axial velocity components showed a good agreement.

Before the microoptical systems were finished, two engine experiments on optical single-cylinder engines were carried out with a commercial fiber-optic spark plug and standard lenses. In the first experiment, the spray movement in a tumble-guided SIDI engine was observed and simultaneous measurement of fuel concentrations via 3-pentanone LIF and CN* spark-emission spectroscopy were performed in cooperation with the Institut für Kolbenmaschinen (IfKM) at the University of Karlsruhe, Germany. In these measurements, a good correlation was found between cycle-averaged mean values obtained with the two methods, which confirmed that both techniques are applicable for quantitative measurements. A correlation within an individual cycle could not be seen. This discrepancy was possibly due to the slightly different positions of the observed probe volumes of the two diagnostics methods. Additionally, the position of the spark (i.e. the probe volume for CN* emission measurements) is not fixed. The goal of the second experiment that was carried out in cooperation with General Motors Research & Development in Detroit, USA, was the detailed investigation of the spark movement and the spray-spark interaction in a spray-guided (SG) SIDI engine. Various measurements showed that the spray induced flow stretched the spark up to 10 mm from its original position of breakdown between the spark-plug electrodes. Results from simultaneous measurements with high-speed imaging and a commercial fiber-optic spark plug suggested that an adapted fiber-optic spark plug could also yield valuable information about the spark movement in non-modified engines.

Eventually, microoptical techniques in combination with the proper spectroscopic concepts will provide quantitative information about in-cylinder processes in production-line engines. Hence, the microoptical systems described in this work together with the suggested optical diagnostics methods make a major contribution to future IC engine research.

VIII REFERENCES

1. B. Johansson, H. Neij, M. Alden, and G. Juhlin, "Investigations of the Influence of Mixture Preparation on Cyclic Variations in a SI-Engine, Using Laser Induced Fluorescence," SAE Technical Paper **950108** (1995).
2. O. Pajot and C. Mounaïm-Rousselle, "Instantaneous Flow Field Effects on the Flame Kernel in S.I. Engine by Simultaneous Optical Diagnostics," SAE Technical Paper **2001-01-1796** (2000).
3. A. Kölmel, U. Spicher, R. Düsterwald, and F. M. Wytrykus, "Analysis of Mixture Distribution and Mixture Formation Using a Fast Gas Sampling Valve," SAE Technical Paper **982473** (1998).
4. M. Lai, K. Ratton, E. Balles, E. Vandyne, A. Wahl, B. Darin, and G. Hirschlieb, "In-Cylinder Equivalence ratio Approximation Using Spark Gap Ionization," SAE Technical Paper **980166** (1998).
5. C. Schulz, A. Dreizler, V. Ebert, and J. Wolfrum, *Combustion Diagnostics*. Springer Handbook of Experimental Fluid Dynamics, ed. C. Tropea, J. Foss, and A. Yarin (Springer, 2006, in press about 80 pages).
6. J. Wolfrum, "Lasers in combustion: From basic theory to practical devices," Proc. Combust. Inst. **27**, 1-42 (1998).
7. C. Schulz and V. Sick, "Tracer-LIF Diagnostics: Quantitative Measurement of fuel concentration, temperature and air/fuel ratio in practical combustion situations," Prog. Energy Combust. Sci. **31**, 75-121 (2005).
8. M. Dawson and S. Hochgreb, "Liquid Fuel Visualization Using Laser-Induced Fluorescence During Cold Start," SAE Technical Paper **982466** (1998).
9. D. Wolff, H. Schlüter, V. Beushausen, and P. Andresen, "Quantitative determination of fuel air mixture distributions in an internal combustion engine using PLIF of acetone," Ber. Bunsenges. Phys. Chem. **97**, 1738-1741 (1993).
10. N. P. Tait and D. A. Greenhalgh, "2D laser induced fluorescence imaging of parent fuel fraction in nonpremixed combustion," Proc. Combust. Inst., 1621-1628 (1992).
11. W. Koban, J. Schorr, and C. Schulz, "Oxygen distribution imaging with a novel two-tracer laser-induced fluorescence technique," Appl. Phys. B **74**, 111-114 (2002).
12. S. Einecke, C. Schulz, and V. Sick, "Measurement of temperature, fuel concentration and equivalence ratio fields using tracer LIF in IC engine combustion," Appl. Phys. B **71**, 717-723 (2000).
13. M. M. Ismailov, H. J. Schock, and A. M. Fedewa, "Gaseous flow measurements in an internal combustion engine assembly using molecular tagging velocimetry," Exp. in Fluids **41**, 57-65 (2006).
14. A. Ostendorf, "Mit neuen Strahlquellen und erweiterten Parametern zu innovativen Anwendungen," Akademie-Journal **1**, 12-18 (2004).
15. W. Koban, J. D. Koch, R. K. Hanson, and C. Schulz, "Oxygen quenching of toluene fluorescence at elevated temperatures," Appl. Phys. B **80**, 777-784 (2005).

16. W. Koban, J. D. Koch, R. K. Hanson, and C. Schulz, "Toluene LIF at elevated temperatures: implications for fuel-air ratio measurements," *Appl. Phys. B* **80**, 147-150 (2005).
17. J. D. Koch and R. K. Hanson, "Ketone photophysics for quantitative PLIF imaging," AIAA paper **2001-0413** (2001).
18. J. D. Koch and R. K. Hanson, "Temperature and excitation wavelength dependences of 3-pentanone absorption and fluorescence for PLIF applications," *Appl. Phys. B* **76**, 319-324 (2003).
19. W. Koban, "Photophysical characterization of toluene and 3-pentanone for quantitative imaging of fuel/air ratio and temperature in combustion systems," Dissertation, Institute of Physical Chemistry, University of Heidelberg (2005).
20. F. Großmann, P. B. Monkhouse, M. Ridder, V. Sick, and J. Wolfrum, "Temperature and pressure dependences of the laser-induced fluorescence of gas-phase acetone and 3-pentanone," *Appl. Phys. B* **62**, 249-253 (1996).
21. J. B. Heywood, *Internal Combustion Engine Fundamentals* (McGraw-Hill Book Company, New York, USA, 1988).
22. G. P. Merker and G. Stiesch, *Motorische Verbrennung. Technische Verbrennung. Vol. 1* (Teubner, 1999, 159).
23. H. R. Ricardo, "Recent Research Work on the Internal Combustion Engine," *SAE Trans.* **14**, 30-32 (1922).
24. A. S. Solomon, R. W. Anderson, P. M. Najt, and F.-Q. Zhao, *Direct Fuel Injection for Gasoline Engines*. PT-80 (Soc. Autom. Engrs., Warrendale PA, 2000).
25. F.-Q. Zhao, D. L. Harrington, and M.-C. Lai, *Automotive gasoline direct-injection engines* (Soc. Autom. Engrs., Warrendale PA, 2002).
26. Bosch, *Kraftfahrtechnisches Taschenbuch*, 25 ed (Vieweg, 2003).
27. T. D. Fansler and M. C. Drake, "Designer diagnostics for developing direct-injection gasoline engines," *Journal of Physics: Conference Series* **45**, 1-17 (2006).
28. J. Fischer, A. Velji, U. Spicher, F. Zimmermann, and C. Schulz, "Measurement of the equivalence ratio in the spark gap region of a gasoline direct injection engine with spark emission spectroscopy and tracer-LIF," *SAE Technical Paper* **2001-01-1295** (2004).
29. M. C. Drake, T. D. Fansler, and A. M. Lippert, "Stratified-charge combustion: modeling and imaging of a spray-guided direct-injection spark-ignition engine," *Proc. Combust. Inst.* **30**, 2683-91 (2005).
30. A. M. Lippert, T. D. Fansler, M. C. Drake, and A. S. Solomon, "High-speed imaging and CFD modeling of sprays and combustion in a spray-guided spark-ignition direct injection engine," in 6. *AVL Internationales Symposium für Verbrennungsdiagnostik* (Baden-Baden, 2004).
31. T. D. Fansler, M. C. Drake, I. Düwel, and F. P. Zimmermann, "Fuel-Spray and Spark-Plug Interactions in a Spray-Guided Direct-Injection Gasoline Engine," in 7. *AVL Internationales Symposium für Verbrennungsdiagnostik* (Baden-Baden, 2006).
32. J. Marshall, "Clean-burn engine dodges ever tighter regulations," *New Scientist Magazine*, issue 2534 (2006).
33. W. Demtröder, *Laserspektroskopie. Grundlagen und Techniken*, 3 ed (Springer, Berlin-Heidelberg-New York, 1993).
34. P. W. Atkins, *Physikalische Chemie*, 1 ed (VCH-Verlag, Oxford, UK, 1990, 889).
35. J. Kristof, "Untersuchung zweidimensional abbildender lasergestützter Verfahren zur Ermittlung von Tropfengrößen und -geschwindigkeiten in Kraftstoffsprays," Diplomarbeit, Universität Heidelberg (2001).

36. I. Düwel, T. Kunzelmann, J. Schorr, C. Schulz, and J. Wolfrum, "Application of fuel tracers with different volatilities for planar LIF/Mie drop sizing in evaporating systems," in *Proc. of the 9th ICLASS 2003* (Sorrento, Italy, 2003).
37. H. Haken and H. C. Wolf, *Molekülphysik und Quantenchemie. Einführung in die experimentellen und theoretischen Grundlagen*, 3 ed (Springer, Berlin-Heidelberg-New York, 1998).
38. V. Ebert and J. Wolfrum, *Absorption spectroscopy. Optical Measurements - Techniques and Applications*, 2nd corr. edition, ed. F. Mayinger and O. Feldmann (Springer Verlag, Heidelberg, München, 2001, 227- 265).
39. A. C. Eckbreth, *Laser diagnostics for combustion temperature and species*, 2 ed (Gordon and Breach, Amsterdam, The Netherlands, 1996).
40. S. P. Böhnisch, "Die elektrostatische Entladung bei kleinen Abständen und Spannungen," Dissertation, TU Berlin (2004).
41. J. S. Townsend, "Electricity in Gases," Oxford University press, London (1914).
42. D. K. Ottesen, L. L. Baxter, L. J. Radziemski, and J. F. Burrows, "Laser spark emission spectroscopy for in situ, real-time monitoring of pulverized coal particle composition," *Energy and Fuels* **5**, 304 (1991).
43. Y. Ikeda, J. Kojima, and T. Nakajima, "Chemiluminescence based local equivalence ratio measurement in turbulent premixed flames," *AIAA* **2002-0193** (2002).
44. T. D. Fansler, B. Stojkovic, M. C. Drake, and M. E. Rosalik, "Local fuel concentration measurements in internal combustion engines using spark-emission spectroscopy," *Appl. Phys. B* **75**, 577-590 (2002).
45. J. Fischer, B. Xander, A. Veljj, and U. Spicher, "Cycle-Resolved Determination of Local Air-Fuel Ratio at the Spark Gap Using a Direct Injection Gasoline Engine," in *6. AVL Internationales Symposium für Verbrennungsdiagnostik* (Baden-Baden, 2004), 163-173.
46. J. Savard, "Comparative spectrum analysis of o-, m- and p-isomerides of certain benzene derivatives," *Ann. Chim.* **11**, 287-350 (1929).
47. A. M. Bass, "Fluorescence studies of some simple benzene derivatives. in the near ultraviolet. II. Toluene and benzonitrile," *J. Chem. Phys.* **18**, 1403-10 (1950).
48. W. Koban, J. D. Koch, R. K. Hanson, and C. Schulz, "Absorption and Fluorescence of Toluene Vapor at Elevated Temperatures," *Phys. Chem. Chem. Phys.* **6**, 2940-2945 (2004).
49. H. Hippler, J. Troe, and H. J. Wendelken, "Collisional Deactivation of Vibrationally Highly Excited Polyatomic-Molecules.2. Direct Observations for Excited Toluene," *J. Chem. Phys.* **78**, 6709-6717 (1983).
50. B. M. Toselli, J. D. Brenner, M. L. Yerram, W. E. Chin, K. D. King, and J. R. Barker, "Vibrational relaxation of highly excited toluene," *J. Chem. Phys.* **95**, 176-188 (1991).
51. T. Lenzer, K. Luther, K. Reihs, and A. C. Symonds, "Collisional energy transfer probabilities of highly excited molecules from kinetically controlled selective ionization (KCSI). II. The collisional relaxation of toluene: P(E',E) and moments of energy transfer for energies up to 50 000 cm⁻¹," *J. Chem. Phys.* **112**, 4090-4110 (2000).
52. E. H. Kincaid, V. Worah, and M. D. Schuh, "Collision-Induced State-to-State Flow of Vibrational-Energy in S1 Toluene," *J. Chem. Phys.* **94**, 4842-4851 (1991).
53. R. E. Smalley, "Vibrational Randomization Measurements with Supersonic Beams," *J. Phys. Chem.* **86**, 3504-3512 (1982).
54. C. G. Hickman, J. R. Gascooke, and W. D. Lawrance, "The S₁ - S₀ (¹B₂ - ¹A₁) transition of jet-cooled toluene: Excitation and dispersed fluorescence spectra, fluorescence lifetimes, and intramolecular vibrational energy redistribution," *J. Chem. Phys.* **104**, 4887-4901 (1996).

-
55. J. Reboux and D. Puechberty, "A new approach of PLIF applied to fuel/air ratio measurement in the compressive stroke of an optical SI engine," SAE Technical Paper **941988** (1994).
 56. W. Koban, J. D. Koch, V. Sick, N. Wermuth, R. K. Hanson, and C. Schulz, "Predicting Tracer-LIF under engine-related temperature and pressure conditions," *Proc. Combust. Inst.*, 1545-1553 (2005).
 57. C. S. Burton and W. A. Noyes, "Electronic energy relaxation in Toluene vapour," *J. Chem. Phys.* **49**, 1705 (1968).
 58. W. B. Richardson, S. H. Lin, and D. L. Evans, "Analysis of the Molecular Electronic Absorption-Spectra of Shock-Heated Aromatic-Compounds," *J Chem S F2* **78**, 1-15 (1982).
 59. R. G. Brown and D. Phillips, "Quenching of the first excited singlet state of substituted benzenes by molecular oxygen," *Trans. Farad. Soc. II* **70**, 630 (1974).
 60. A. Lozano, B. Yip, and R. K. Hanson, "Acetone: A tracer for concentration measurements in gaseous flows by planar laser-induced fluorescence," *Exp. in Fluids* **13**, 369-376 (1992).
 61. J. B. Ghandhi and P. G. Felton, "On the Fluorescent Behavior of Ketones at High-Temperatures," *Exp. in Fluids* **21**, 143-144 (1996).
 62. F. Ossler and M. Aldén, "Measurements of picosecond laser-induced fluorescence from gas-phase 3-pentanone and acetone: Implications to combustion diagnostics," *Appl. Phys. B* **64**, 493-502 (1997).
 63. M. C. Thurber, F. Grisch, B. J. Kirby, M. Votsmeier, and R. K. Hanson, "Measurements and modeling of acetone laser-induced fluorescence with implications for temperature-imaging diagnostics," *Appl. Opt.* **37**, 4963-4978 (1998).
 64. H. Neij, B. Johansson, and M. Aldén, "Development and Demonstration of 2D-LIF For Studies of Mixture Preparation in SI Engines," *Combust. Flame* **99**, 449-457 (1994).
 65. D. Han and R. R. Steeper, "An LIF equivalence ratio imaging technique for multicomponent fuels in an IC engine," *Proc. Combust. Inst.* **29**, 727-734 (2002).
 66. J. Koch and R. Hanson, "A photophysics model for 3-pentanone PLIF: temperature, pressure and excitation wavelength dependences," *AIAA* 2003-0403 (2003).
 67. M. Thurber and R. K. Hanson, "Pressure and composition dependence of acetone laser-induced fluorescence with excitation at 248, 266 and 308 nm," *Appl. Phys. B* **69**, 229-240 (1999).
 68. W. Koban and C. Schulz, "FARLIF: Myth and reality," in *European Combustion Meeting* (Louvain-la-Neuve, Belgium, 2005).
 69. W. Koban and C. Schulz, "Toluene laser-induced fluorescence (LIF) under engine-related pressures, temperatures and oxygen mole fractions," SAE Technical Paper **2005-012091** (2005).
 70. M. Jacon, C. Lardeux, R. Lopezdelgado, and A. Tramer, "3rd Decay Channel and Vibrational Redistribution Problems in Benzene-Derivatives," *Chemical Physics* **24**, 145-157 (1977).
 71. F. P. Zimmermann, W. Koban, and C. Schulz, "Temperature Diagnostics using Laser-Induced Fluorescence (LIF) of Toluene," in *LACSEA* (Incline Village, Lake Tahoe, CA, 2006).
 72. M. Luong, W. Koban, and C. Schulz, "Novel strategies for imaging temperature distribution using toluene LIF," in *Second International Conference on Optical and Laser Diagnostics (ICO-LAD)* (London, 2005).
 73. R. M. Merer and J. S. Wallace, "Spark Spectroscopy for Spark Ignition Engine Diagnostics," SAE Technical Paper **950164** (1995).

74. R. Maly, "Spark Ignition: Its Physics and Effect on the Internal Combustion Engine," in *Fuel Economy in Road Vehicles Powered by Spark Ignition Engines* (New York, 1984), 91-248.
75. Y. Ikeda, A. Nishiyama, N. Kawahara, E. Tomita, S. Arimoto, and A. Takeuchi, "In-spark-plug Sensor for Analyzing the Initial Flame and Its Structure in an SI Engine," SAE Technical Paper **2005-01-0644** (2005).
76. T. Berg, V. Beushausen, O. Thiele, and H. Voges, "Faseroptischer Zündkerzensensor zur Optimierung motorischer Brennverfahren," MTZ **2006-06** (2006).
77. T. Berg, H. Voges, O. Thiele, V. Beushausen, W. Hentschel, and F. Kallmeyer, "Optical Sensors for Automotive Engine-Research Applications," in *4th IEEE Sensors* (Irvine, CA, 2005).
78. K. B. Ozanyan, T. L. Yeo, F. P. Hindle, N. R. J. Poolton, H. McCann, and K. L. Tan, "Fiber-based UV laser-diode fluorescence sensor for commercial gasolines," IEEE Sensors Journal **4**, 681-690 (2004).
79. J. Hecht, *Understanding Fiber Optics*, 3 ed (Prentice-Hall, Inc., New Jersey, 1999).
80. K.-F. Klein and G. Hillrichs, "Grenzen und Möglichkeiten der Transmission von UV-Licht durch Spezial-Lichtwellenleiter," Proc. of 13th Intern. Scient. Conf. Mittweida, 113-123 (1998).
81. K.-F. Klein, R. Arndt, G. Hillrichs, M. Ruetting, M. Veidemanis, R. Dreiskemper, J. Clarkin, and G. Nelson, "UV-fibers for applications below 200 nm," SPIE-Proc. BiOS'01 **4253**, 42-49 (2001).
82. H. Hitzler, "Transmission von leistungsstarken UV-Laserpulsen durch Quarzfasern und Anwendung von getaperten Einzelfasern sowie Taperbündeln," Dissertation, Physikalisch Chemisches Institut, Universität Heidelberg (1992).
83. R. A. Weeks, "The many varieties of E'-centers: a review," J. Non-Cryst. Solids **179**, 1-9 (1994).
84. C. Pfeleiderer, "Raman- und Absorptionsspektroskopie an Quarzgläsern zur Untersuchung der UV-induzierten Bildung von E'-Zentren," Dissertation, Physikalisch Chemisches Institut, Universität Heidelberg (1992).
85. V. Uhl, "Untersuchung von laserinduzierten Absorptions- und Lumineszenzbanden in thermisch vorbehandeltem synthetischen Quarzglas," Dissertation, Physikalisch Chemisches Institut, Universität Heidelberg (1995).
86. A. d. With, V. Uhl, C. Pfeleiderer, and J. Wolfrum, "A Bundle of Tapered Fibers Transmits 830 mJ/Pulse of 308 nm XeCl Laser Pulses," Ber. Bunsenges. Phys. Chem **97**, 1723-1725 (1993).
87. J. Assmus, J. Gombert, K.-F. Klein, J. P. Clarkin, and G. W. Nelson, "Improvements in UV transmission of all-silica optical fibers with low OH content," SPIE Proceedings **3596**, 108-114 (1999).
88. R. Reichle, C. Pruss, W. Osten, H. Tiziani, F. Zimmermann, and C. Schulz, "Microoptical sensor for integration in a functional spark plug for combustion analysis by UV-laser induced fluorescence spectroscopy," Proc. VDI 4th Conference on Optical Analysis Technology (2004).
89. <http://www.zemax.com>
90. D. J. Wren, "Fluorescence of optical materials stimulated by argon fluoride (ArF) laser radiation at 193 nm," Appl. Spectr. **34**, 627-32 (1980).
91. R. Reichle, C. Pruss, W. Osten, H. J. Tiziani, F. Zimmermann, and C. Schulz, "Fiber optic spark plug sensor for UV-LIF measurements close to the ignition spark," In Wolfgang Osten, Christophe Gorecki, Erik L. Novak (Eds.): "Optical Measurement Systems for Industrial

- Inspection IV", Proceedings of SPIE - The International Society for Optical Engineering **vol. 5856**, 158-168 (2005).
92. R. Reichle, C. Pruss, W. Osten, H. Tiziani, F. Zimmermann, and C. Schulz, "UV-Endoskop mit diffraktiver Aberrationskorrektur für die Motorenentwicklung," Proc. DGaO 107. Tagung, <http://www.dgao-proceedings.de/> (2006).
 93. R. Reichle, C. Pruss, W. Osten, H. Tiziani, F. Zimmermann, and C. Schulz, "Hybrid excitation and imaging optics for minimal invasive multiple-band UV-LIF-measurements in engines," VDI-Berichte 1959, 223-235 (2006).
 94. W. Becker, *Advanced Time-Correlated Single Photon Counting Techniques*. Springer Series in Chemical Physics. Vol. 81 (Springer, 2005, 401).
 95. D. P. Herten, A. Biebricher, M. Heilemann, T. Heinlein, C. Müller, P. Schlüter, P. Tinnefeld, K. D. Westen, M. Sauer, and J. Wolfrum, "Optical single molecule techniques for analytical and biological applications," Recent Res. Devel. Applied Phys. **7**, 345-368 (2004).
 96. D. P. Herten, P. Tinnefeld, and M. Sauer, "Identification of single fluorescently labeled mononucleotide molecules in solution by spectrally resolved time-correlated single photon counting," Appl. Phys. B **71**, 765-771 (2000).
 97. F. P. Zimmermann, W. Koban, D. Herten, C. Roth, and C. Schulz, "Fluorescence lifetime of gas-phase toluene at elevated temperatures," Chem. Phys. Lett. **426**, 248-251 (2006).
 98. G. M. Breuer and E. K. C. Lee, "Fluorescence decay times of photoexcited benzene and toluene in the gas phase," J. Chem. Phys. **51**, 3130-3132 (1969).
 99. C. Orlemann, C. Schulz, and J. Wolfrum, "NO-flow tagging by photodissociation of NO₂. A new approach for measuring small-scale flow structures," Chem. Phys. Lett. **307**, 15-20 (1999).
 100. N. Wermuth and V. Sick, "Absorption and fluorescence data of acetone, 3-pentanone, biacetyl, and toluene at engine-specific combinations of temperature and pressure," SAE Technical Paper **2005-01-2090** (2005).
 101. H. Okabe and W. A. Noyes, "The relative intensities of fluorescence and phosphorescence in biacetyl vapor," J. Am. Chem. Soc. **79**, 810-806 (1957).
 102. H. W. Sidebottom, C. C. Badcock, J. G. Calvert, B. R. Rabe, and E. K. Damon, "Lifetime studies of the biacetyl excited singlet and triplet states in the gas phase at 25°C," J. Am. Chem. Soc. **94**, 13-19 (1972).
 103. C. C. Badcock, H. W. Sidebottom, J. G. Calvert, B. R. Rabe, and E. K. Damon, "A study of the triplet-triplet annihilation reaction in biacetyl vapor excited at 4365 Å and 25°C," J. Am. Chem. Soc. **94**, 19-24 (1972).
 104. B. Hiller, R. A. Booman, C. Hassa, and R. K. Hanson, "Velocity visualization in gas flows using laser-induced phosphorescence of biacetyl," Rev. Sci. Instrum. **55**, 1964 (1984).
 105. B. Stier and M. M. Koochesfahani, "Molecular tagging velocimetry (MTV) measurements in gas phase flows," Exp. in Fluids **26**, 297-304 (1999).
 106. B. Yip, A. Lozano, and R. K. Hanson, "Sensitized phosphorescence: a gas phase molecular mixing diagnostic," Exp. in Fluids **17**, 16-23 (1994).
 107. T. Fujikawa, Y. Hattori, and K. Aklhama, "Quantitative 2-D Fuel Distribution Measurements in an SI Engine Using Laser-Induced Fluorescence with Suitable Combination of Fluorescence Tracer and Excitation Wavelength," SAE Technical Paper **972944** (1997).
 108. J. Fischer, M. Kettner, A. Nauwerck, J. Pfeil, and U. Spicher, "Influence of an Adjustable Tumble-System on In-Cylinder Air Motion and Stratification in a Gasoline Direct Injection Engine," SAE Technical Paper **2002-01-1645** (2002).

-
109. J. Fischer, A. Velji, and U. Spicher, "Investigation of Cycle-to-Cycle Variations of In-Cylinder Processes in Gasoline Direct Injection Engines operating with Variable Tumble Systems," SAE Technical Paper **2004-01-0044** (2004).
 110. J. Pfeil, J. Fischer, M. Kettner, and U. Spicher, "Influence of Spray Propagation on the Gas Phase in a Direct Injection Gasoline Engine," in *10th International Symposium on Flow Visualization* (Kyoto, 2002).
 111. I. Düwel, M. C. Drake, and T. Fansler, "High-Speed, High-Resolution Laser Imaging of Multihole Fuel Sprays in a Firing Spray-Guided Direct-Injection Gasoline Engine," in *19th ILASS Europe 2004* (Nottingham, England, 2004), 278 - 282.
 112. W. Hübner, A. Witt, B. Hoss, T. Albrecht, B. Durst, and A. Abdelfattah, "Methodensatz bei der Entwicklung eines weiterführenden DI Brennverfahrens," in *24. Internationales Wiener Motorensymposium* (15-16 May, 2003).
 113. T. D. Fansler and M. C. Drake, "Designer diagnostics for developing direct-injection gasoline engines," in *Second International Conference on Optical and Laser Diagnostics (ICOLAD 2005)* (City University, London, UK, 2005).
 114. D. Zimmermann and e. al., "Inflammation of Stratified Mixtures in Spray Guided DI Gasoline Engines: Optimization by Application of High Speed Imaging Techniques," in *6. AVL Internationales Symposium für Verbrennungsdiagnostik* (Baden-Baden, 2004).
 115. J. R. Ault and P. O. Witze, "Evaluation and optimization of measurements of flame kernel growth and motion using a fiber-optic spark plug probe," SAE Technical Paper **981427** (1998).
 116. M. J. Hall, "The influence of fluid motion on flame kernel development and cyclic variation in a spark ignition engine," SAE Technical Paper **890991** (1989).

IX APPENDIX

1 Filter transmission plots

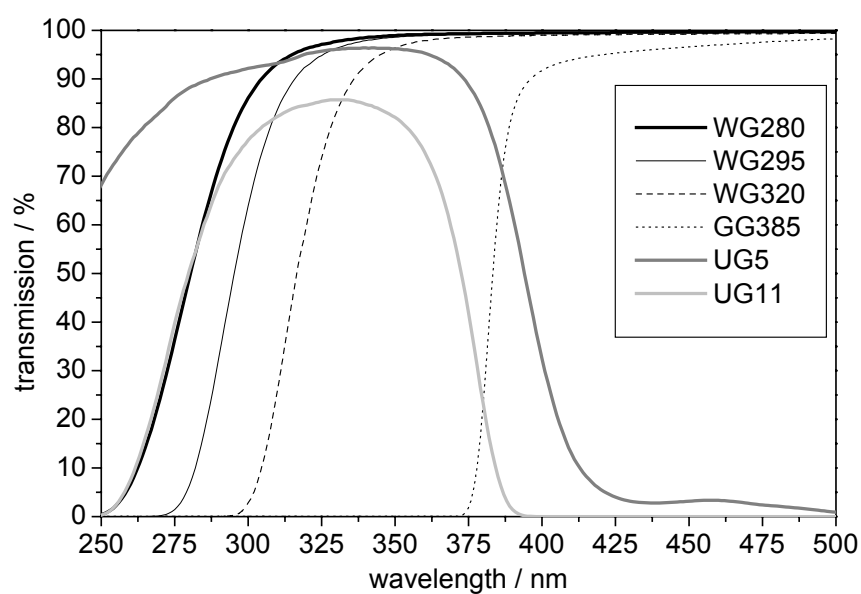


Figure IX-1: Schott glass longpass filters WG280-320, GG385 and bandpass filters UG5, UG11, catalogue transmission curves.

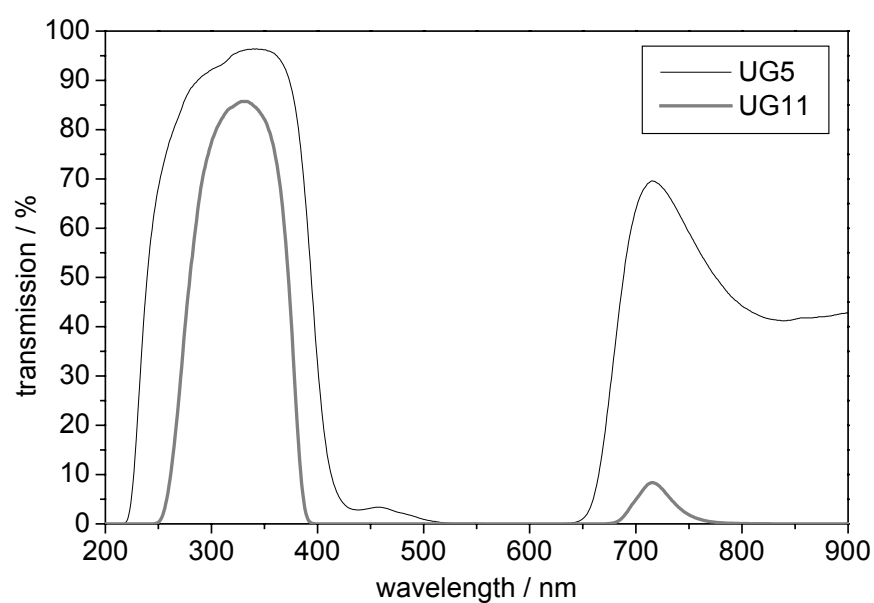


Figure IX-2: Schott glass bandpass filters UG5 and UG11, transmission in UV to IR, catalogue transmission curves.

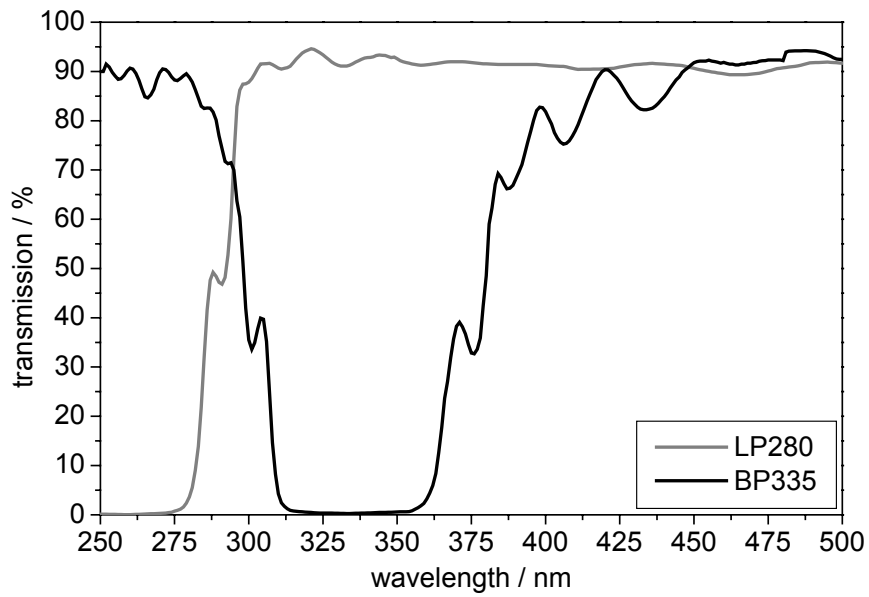


Figure IX-3: Custom dichroic filters longpass 280 nm and negative bandpass 335 nm (Laseroptik), measured transmission curves at 45° angle of incidence.

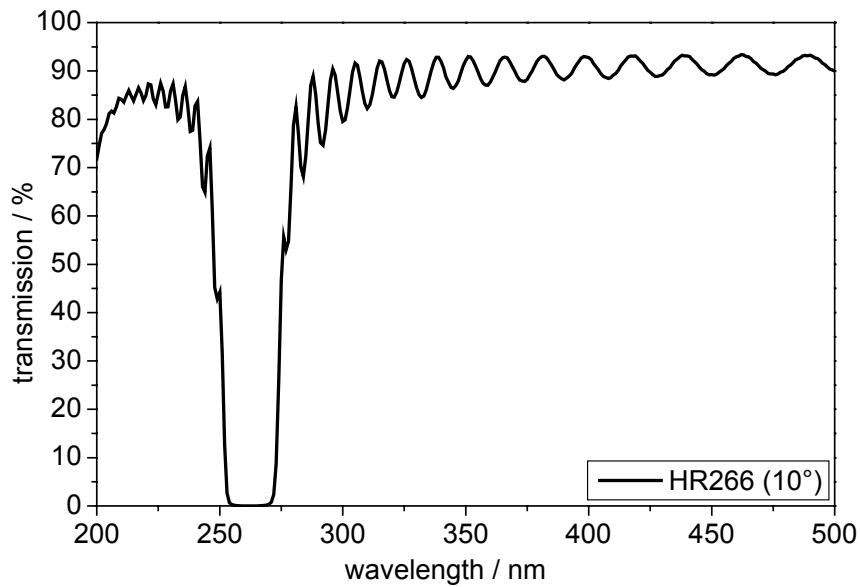


Figure IX-4: Custom dichroic filter HR266 (Laseroptik), measured transmission curve at 10° angle of incidence.

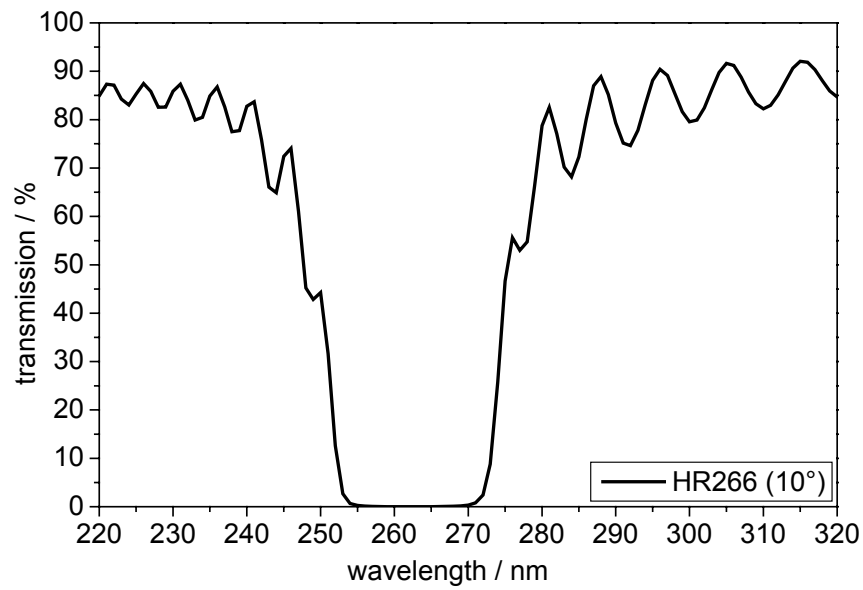


Figure IX-5: Custom dichroic filter HR266 (Laseroptik) zoomed in, measured transmission curve at 10° angle of incidence.

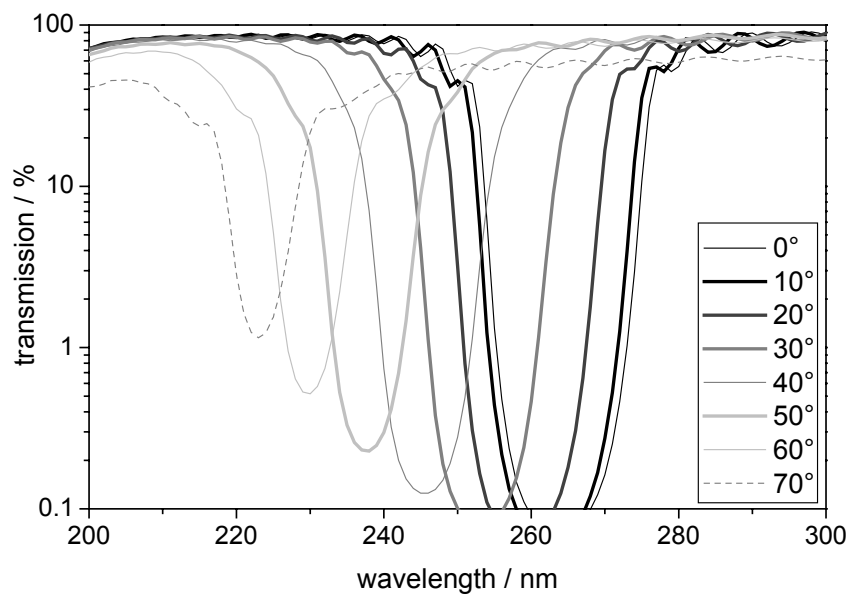


Figure IX-6: Custom dichroic filter HR266 (Laseroptik), dependence on angle of incidence, measured transmission curves.

2 Channel photomultiplier specifications

The detection unit for the fiber-optic spark-plug uses three *PerkinElmer, MH 1943* channel photomultiplier (CPM) modules that each contain a CX34 channel photomultiplier tube (cathode diameter 15 mm) and an adjustable high voltage supply. The photomultiplier sensitivity is shown in Figure IX-7. For easier handling, an electronic control module has been made for each photomultiplier module.

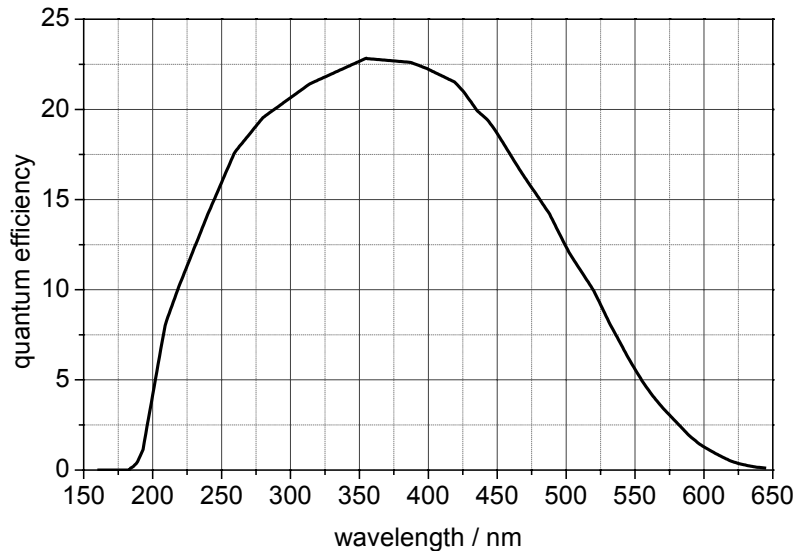


Figure IX-7: Spectral response of used channel photomultiplier tube CX34 (PerkinElmer).

Color	Function	In-/Output	Signal Level
blue	HV Shutdown (kill)	Input	=2.6 V inactive, =2.4 V active
green	V_{set} (Gain cont. volt.)	Input	0 to 3 V (cf. Figure IX-8)
orange	ext. Gate-Input V_{gate}	Input	=3.1 V inactive, = 3.2 V active
red	+5VDC (power supply)	Input	Max. 5.5 V ; Input current < 200 mA
yellow	Monitor Voltage V_{mon}	Output	0 to 3 volts
black	GND (power supply)	Input	Common Ground
Coax, black	Signal Output	Output	Current Pulse, negative

Table IX-1: Connection cables of MH 1943 channel photomultiplier module.

The connection cables (besides the coax signal cable) of the photomultiplier module, shown in Table IX-1, are attached to a 9-pin connector and can flexibly be plugged into connectors in the 19''-rack detection unit for the fiber-optic spark-plug and into the custom made control module. With the potentiometer of the control module the high voltage $V_{\text{ChannelEntrance}}$ (0 – 3000 V) (i.e. the gain, cf. Figure IX-8) is adjusted via the control voltage V_{set} (0 – 3 V). The monitor voltage V_{mon} (0 – 3 V, $V_{\text{ChannelEntrance}}/1000$) is displayed on an illuminated LED. The control module has BNC connectors for applying the HV shutdown signal and the gating TTL signal V_{gate} . Using the gating function, a TTL level of about $V_{\text{gate}} \sim 4$ V is required. When the TTL pulse signal

is set to high it switches the cathode potential higher than the channel entrance potential. Thus, the cathode is switched off only for the time, the input level is at high. Then, no anode signal will be obtained. The response time of the gating function is about 150 μ s. With gate input open or ground, the module will be in standard operating mode. The BNC connector of the coax signal cable can directly be plugged into an oscilloscope. Please note that the **maximum anode output current must never exceed 10 μ A for more than 30 seconds**. Hence, on an oscilloscope **the maximum voltage must never exceed 0.5 mV (with 50 Ω termination)**. For long-term operation **the average anode current should not exceed 100 nA** (0.005 mV with 50 Ω termination). For detection of pulses shorter than 100 ns the maximum anode current can be as high as 1 mA (50 mV with 50 Ω termination) depending on the signal repetition frequency (i.e. the average anode current has to remain lower than 100 nA). The time resolution of the photomultipliers is shorter than 10 ns.

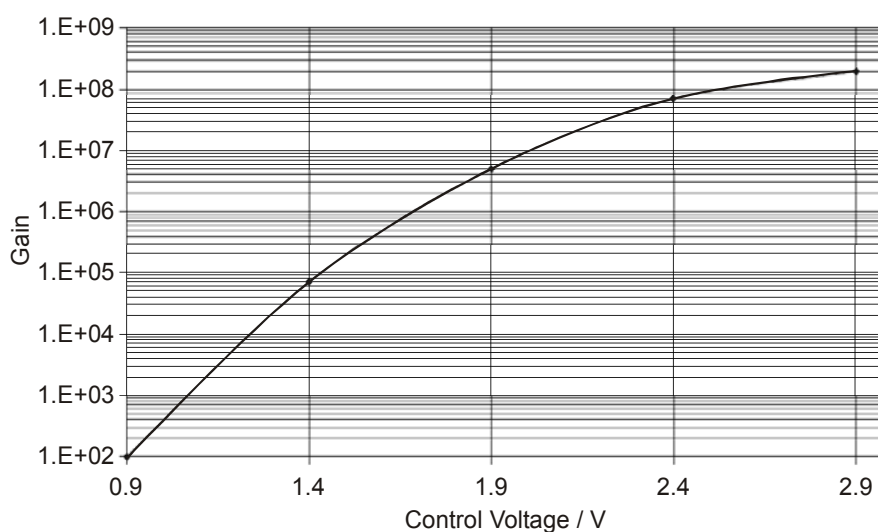


Figure IX-8: Current amplification vs. control voltage.

Before switching on supply voltage, make sure the Channel Photomultiplier is in total darkness. Only operate the photomultipliers in the designated detector unit and make sure it is completely sealed. **Never expose the photomultipliers to high light levels!** If the high voltage is switched on during room-light illumination it would lead to immediate destruction of the photomultiplier. While switching on supply voltage, monitor output signal. In total darkness, count rate is max. about 20 to 30 counts per second (cps). Measuring the output current, the dark current should be in the low pA range. Use 1 M Ω termination to measure dark current: The measured voltage should be below 0.1 mV. If the CPM was exposed to high light levels before operating started, the number of counts can exceed 1kcps or dark current can exceed some nA. In that case, store CPM in darkness for one hour before re-operating. The settling time is < 1 s (time to stabilize HV after supply voltage applied).

The CPM operating temperature is 5 to 40°C and the storage temperature –20 to 50 °C. The weight of the used MH 1943 CPM is approx. 370 g. As shown in Figure IX-9 outer dimensions are of the CPM module are 36x55x116 mm (WxHxL). For more details about CPM operation and technical specifications please refer to *PerkinElmer MH 1900 series manual*.

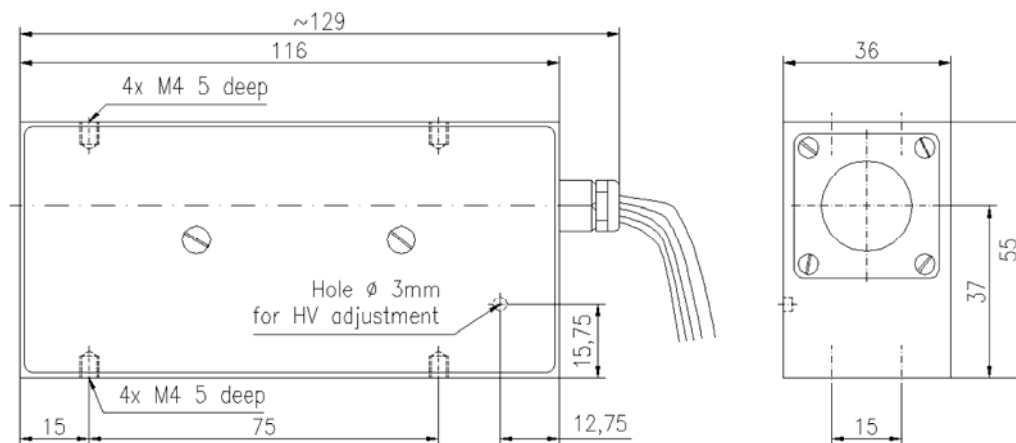


Figure IX-9: Dimensions of PerkinElmer, MH1943 photomultiplier module in mm.

SPECIFICATIONS OVERVIEW

Supply voltage	5 V DC
Supply current	< 200 mA
Settling time	<1 s (time to stabilize HV after supply voltage applied)
Gain	up to 10^8
GATE voltage	V_{gate} 0 V: h to l set time V_{ca} to $V_{\text{ch-ent}} + 140 \text{ V} : \gg 150 \mu\text{s}$ 5 V: l to h set time V_{ca} to $V_{\text{ch-ent}} - 100 \text{ V} : \gg 150 \mu\text{s}$
Monitor voltage out	$V_{\text{ChannelEntrance}} / 1000$
High voltage adjust	by external control voltage (0 - 3 V)
Operating temperature	5 to 40°C
Storage temperature	-20 to 50°C
Weight	approx. 370 g

Maximum ratings:

Input voltage	+5.5 V
Max. anode current	10 μA for max. 30 s for long term operation: max. average anode current of <100 nA is recommended

Anode output current must never exceed 10 μA for more than 30 s!

3 Guideline for using the fiber-optic spark plug

The fiber-optic spark-plug can be used for measurements in any spark-ignited engine that works with the respective electrode length (~6 mm). By using different distance washers the extension into the cylinder can be reduced. When screwing in the spark plug handle the fibers with care and do not twist them too much. Excitation laser – fiber coupling is discussed in chapter IV 1.2 and signal detection is described in chapter IV 1.3. The proper handling of the photomultipliers is shown in the last section (IX 2). This section summarizes the most important specifications of the fiber-optic spark plug. Additionally, it explains how to adjust the probe volume and replace damaged fibers.

FIBER-OPTIC SPARK PLUG SPECIFICATIONS

Probe volume:	~2 mm ³ (6 mm in front of sensor windows)
Max. excitation laser energy:	0.7 mJ/pulse (266 nm, 8 ns/pulse, 10 Hz)
→ Energy available for LIF in probe volume:	~0.3 – 0.4 mJ/pulse
Fiber length:	2 m
Fiber core diameter	of excitation fiber: 400 μm
	of detection fibers: 1000 μm
Fiber material:	high-OH UV enhanced all-silica fibers
Fiber connectors:	SMA (custom PVC SMA connector for detection fibers)
Window material:	UV-sapphire
Spark-plug body material:	Titanium
Spark-plug size:	M14 thread

ADJUSTING AND EXCHANGING FIBERS

Figure IX-10 shows the spark-plug sensor head without its steel tube. The steel tube can be removed after unscrewing three set screws. It has to be disassembled in order to adjust the fiber positions or exchange a damaged fiber. Each quartz fiber is fixed off-axis in a titanium cylinder for adjustment. The position of each cylinder in the spark-plug body is fixed by a set screw (see Figure IX-10). Each positioning cylinder can be rotated about 40° by twisting the corrugated tube that protects the fiber. Because of the off-axis extension of the fibers protruding from the positioning cylinders, the spark-eroded gaps in the spark-plug body limit the rotation angle of the positioning cylinders. Do not try to rotate the cylinders beyond a noticeable stop point. For longitudinal adjustment the cylinders can be shifted further in or out of the spark-plug body. The cylinders should be moved very carefully, because the fragile tilted fiber ends could hit the sensor windows and get damaged. The cylinders must never be pushed in with force. Note that changing the probe volume position also influences its size. An optimum size definition is achieved in 5 – 7 mm in front of the sensor windows. The best way of

adjusting the probe volume is by sending light through all three fibers (e.g., by a HeNe laser) into the probe volume and observing the beam patterns on a piece of paper as illustrated in chapter IV 1.4.3.

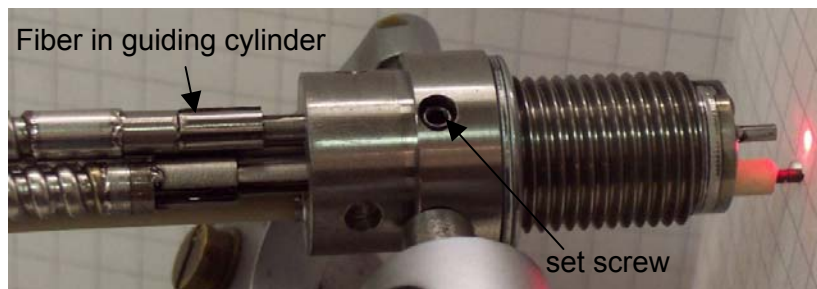


Figure IX-10: Sensor head without shielding steel tube. Each individual fiber can be adjusted after loosening the respective set screw.

For a fast exchange of fibers there is a second set of fibers with tilted ends readily fixed in positioning cylinders and protected by a corrugated steel tube. If a fiber had to be exchanged the broken fiber should be replaced as soon as possible. (Contact FOS Messtechnik GmbH in Schacht-Audorf (<http://www.fos-messtechnik.de>) for the replacement of a fiber in a positioning cylinder.)

4 Guideline for using the hybrid UV endoscope

The UV endoscope can be used in various applications where optical access is limited. With its modular design multi-camera experiments through only one “keyhole” are possible. Examples for the use of the endoscopic system and are given in chapter V 4 also showing the respective experimental setup. In an engine experiment the front endoscope must be fixed in the designated socket in the cylinder wall. In the present concept the endoscope will be used to fix the sealing sapphire window inside the socket. When operating the engine without the endoscope a solid steel dummy is used for sealing the hole in the cylinder wall.

ALIGNMENT OF OPTICAL ELEMENTS

The initial optical alignment of the optical elements of the endoscopic system is crucial for obtaining the specified high resolution and good light collection efficiency. It is important to symmetrically align front endoscope, relay element and CCD on the optical axis. The best performance is achieved for a paraxial object magnification of 0.5. The alignment is best done by adjusting on a target of known size and position. Calculated values for the optimum distances between optical elements are listed in Table IX-2. Many midsize IC engines have bore diameters between 70 and 80 cm. Hence, for imaging the center plane in the cylinder of such an engine the object distance is between 35 and 40 mm. Although the endoscopic system is optimized on an object distance of 35 mm, a good resolution can still be achieved with 40 mm object distance. For further object distances or spectral regions, additional relays for the existing front endoscope can be designed.

object distance of 35 mm and paraxial magnification of 0.5		
<i>Relay element</i>	<i>for 275 – 350 nm</i>	<i>for 380 – 440 nm</i>
<i>Distance between field lens and center of relay</i>	215 mm	228 mm
<i>Distance between field lens and camera chip</i>	358 mm	383 mm

object distance of 40 mm and paraxial magnification of 0.5		
<i>Relay element</i>	<i>for 275 – 350 nm</i>	<i>for 380 – 440 nm</i>
<i>Distance between field lens and center of relay</i>	205 mm	217 mm
<i>Distance between field lens and camera chip</i>	352 mm	376 mm

Table IX-2: Distances between optical elements for an object distance of 35 and 40 mm and a paraxial magnification of 0.5.

When simultaneously imaging both spectral regions on two cameras, two optical paths are defined by a dichroic beam splitter (cf. chapter V 4.2.1). This beam splitter should be installed just before the relay elements. Note that the thickness of the beam splitter influences the optical performance. Best performance is achieved with a thickness of 2 mm or less.

ENDOSCOPE SPECIFICATIONS

Entry diameter:	10 mm
Wavelengths:	275 – 350 nm 380 – 440 nm
Angle of view:	approx. 55°
Object field size:	30 x 30 mm
Image field size:	13 x 13 mm
→ Detector size:	25 mm diameter (intensified CCD camera)
Optimized working distance:	35 mm
Magnification (paraxial):	0.5
Vignette, center/edge better than:	80% (rel. illumination in inner circle of image field)
NA:	0.05 0.058 with enhanced aperture
Resolution:	1.67 LP/mm in object or respective 3.33 LP/mm in image With experimentally measured polychromatic square wave response >0.8 in $r < 30$ mm object space
Resolution at 295 – 315 nm:	up to ~15 LP/mm in image (simulated ideal system and ideal DOE with polychromatic square wave response >0.3 in $r < 30$ mm object space)

5 Automotive history

This paragraph shows a selection of historic milestones regarding the development of cars and engines. All information and figures are taken from various English and German articles in *wikipedia, the free encyclopedia* (<http://wikipedia.org/>). The presented timetables are not exhaustive.

5.1 History of engines and cars

- ul style="list-style-type: none; padding-left: 0;">
- 4000 B.C. The wheel is invented.
- 100 B.C. Heron of Alexandria (Greek) builds a ‘steam engine’ that already works with basic elements of an IC engine (e.g., a piston).
- 1490 Leonardo da Vinci (April 15, 1452 – May 2, 1519) draws a car with propulsion mechanism. 1509 he described a compression-less engine. (His description may not imply that the idea was original with him or that it was actually built.)
- 1673 Dutch physicist, Christian Huygens (April 14, 1629 – July 8, 1695) designed (but never built) an internal combustion engine that was to be fueled with gunpowder. He could be called the pioneer of IC engines. His engine concept was very similar to modern IC engine concepts. (English inventor Sir Samuel Morland already used gunpowder to drive water pumps.)
- 1680 Sir Isaac Newton (January 4, 1643 – March 31, 1727) invented a steam-engine-driven car.
- 1690 Denis Papin (French) built a high-pressure steam engine with piston.
- 1712 English inventor Thomas Newcomen (Dartmouth, Februar 26, 1663 – London, August 5, 1729) improved this steam engine by actually using steam instead of water in the cylinder.
- 1768 Scottish inventor and engineer James Watt (January 19, 1736 – August 19, 1819) further enhanced this steam-engine concept and can be considered as the inventor of the direct-acting steam engine.
- 1769 Nicolas Joseph Cugnot (French) built a steam driven car. This car could transport four persons and reached a top speed of 9 km/h.
- 1780's Alessandro Volta built a toy electric pistol in which an electric spark exploded a mixture of air and hydrogen, firing a cork from the end of the gun.
- 1794 Robert Street (English) built a compression-less engine whose principle of operation would dominate for nearly a century.
- 1801 Richard Trevithick (English) built a steam-driven car that could be called an automobile per definition for the first time.
- 1807 Francois Isaac de Rivaz (Paris, December 19, 1752 – Sion, July 30, 1828) of Switzerland invented an internal combustion engine that used a mixture of hydrogen and

oxygen for fuel. Rivaz designed a car for his engine - the first internal combustion powered automobile. However, his was a very unsuccessful design.

1823 Samuel Brown patented the first internal combustion engine to be applied industrially. It was compression-less and based on what Hardenberg calls the "Leonardo cycle," which, as this name implies, was already out of date at that time. Just as today, early major funding, in an area where standards had not yet been established, went to the best showmen sooner than to the best workers.

1824 Sadi Carnot (June 1, 1796 – August 24, 1832) established the thermodynamic theory of idealized heat engines. This scientifically established the need for compression to increase the difference between the upper and lower working temperatures, but it is not clear that engine designers were aware of this before compression was already commonly used. It may have misled designers who tried to emulate the Carnot cycle in ways that were not useful.



Figure IX-11: Sadi Carnot (1796 - 1832)

1824 English engineer, Samuel Brown adapted an old Newcomen steam engine to burn gas, and he used it to briefly power a vehicle up Shooter's Hill in London.

1826 The American Samuel Morey received a patent for a compression-less 'Gas Or Vapor Engine'.

1829 Walter Hancock (English) commercially built steam-driven cars and buses.

1838 A patent was granted to William Barnet (English). This was the first recorded suggestion of in-cylinder compression. He apparently did not realize its advantages, but his cycle would have been a great advance if developed enough.

1854 The Italians Eugenio Barsanti and Felice Matteucci patented the first working efficient internal combustion engine in London (pt. Num. 1072) but did not get into production with it. It was similar in concept to the successful Otto-Langen indirect engine, but not so well worked out in detail.

1858 Belgian-born engineer, Jean Joseph Étienne Lenoir (Mussy-la-Ville, January 12, 1822 – La Varenne, August 7, 1900) invented and patented (1860) a compression-less, double-acting, electric spark-ignition internal combustion engine fueled by coal gas. In 1863, Lenoir attached an improved engine (using petroleum and a primitive carburetor) to a three-wheeled wagon that managed to complete an historic 90-km road trip from Paris to Joinville-le-Pont.

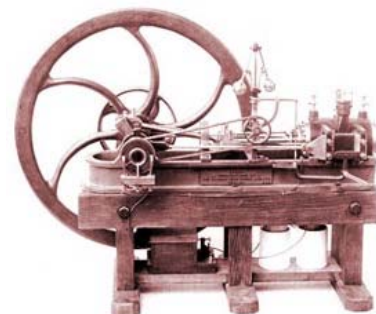


Figure IX-12: Lenoir's two-stroke IC engine (1860)

1862 Alphonse Beau de Rochas, a French civil engineer, patented but did not build a four-stroke engine (French patent #52,593, January 16, 1862).

- 1862 German engineer Nikolaus August Otto (June 14, 1832 – January 28, 1891) designed an indirect-acting free-piston compression-less engine whose greater efficiency won the support of Eugene Langen and then most of the market, which at that time (between 1864 and 1878), was mostly for small stationary engines fueled by lighting gas.
- 1862 – 66 Together with Gottlieb Daimler and Wilhelm Maybach, Nikolaus August Otto developed a practical four-stroke (Otto cycle) engine. 1876 his engine was patented, but 1886 the patent got annulled, because the concept was too similar to that already patented by Lenoir. Nikolaus August Otto founded the 'Gasmotorenfabrik Deutz AG'.
- 1864 Austrian engineer, Siegfried Marcus, built a one-cylinder engine with a crude carburetor, and attached his engine to a cart for a rocky 500-foot drive. Several years later, Marcus designed a vehicle that briefly ran at 10 mph that a few historians have considered as the forerunner of the modern automobile by being the world's first gasoline-powered vehicle.
- 1868 Pierre Michaux und M. Perreaux (French) construct a steam-powered 'motorcycle'.
- 1873 George Brayton, an American engineer, developed an unsuccessful two-stroke kerosene engine (it used two external pumping cylinders). However, it was considered the first safe and practical oil engine.
- 1876 The first successful two-stroke engine was invented by Sir Dougald Clerk.
- 1879 German engineer Carl Friedrich Benz (born as Karl Friedrich Michael Benz) (November 25, 1844 – April 4, 1929) was granted a patent for his internal combustion engine, a reliable two-stroke gas engine, based on Nikolaus Otto's design of the four-stroke engine. Later Benz designed and built his own four-stroke engine that was used in his automobiles, which became the first automobiles in production.
- 1883 French engineer, Edouard Delamare-Deboutville, built a single-cylinder four-stroke engine that ran on stove gas. It is not certain if he did indeed build a car, however, Delamare-Deboutville's designs were very advanced for the time - ahead of both Daimler and Benz in some ways at least on paper.



Figure IX-13: Nikolaus August Otto (1832 – 1891)



Figure IX-14: Karl Benz (1844 – 1929)

1885 Gottlieb Daimler (March 17, 1834 – March 6, 1900) invented what is often recognized as the prototype of the modern gas engine - with a vertical cylinder, and with gasoline injected through a carburetor (patented in 1887). Daimler first built a two-wheeled vehicle the 'Reitwagen' (Riding Carriage) with this engine and a year later built the world's first four-wheeled motor vehicle. Together with Wilhelm Maybach he developed various automobiles.

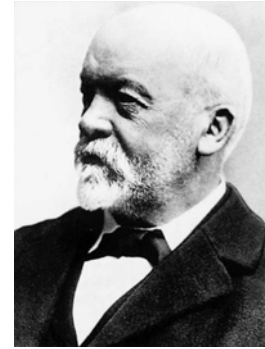


Figure IX-15: Gottlieb Daimler (1834 – 1900)

1886 On January 29, Karl Benz received the first patent (DRP No. 37435) for a gas-fueled car (three wheeled, cf. Figure IX-16). Karl Benz is the first to manufacture a car in mass-production from 1894 – 1902.

1889 Siegfried Marcus, independently of Daimler and Benz, built a car powered by a four-stroke gasoline engine.

1889 Daimler built an improved four-stroke engine with mushroom-shaped valves and two V-slant cylinders.

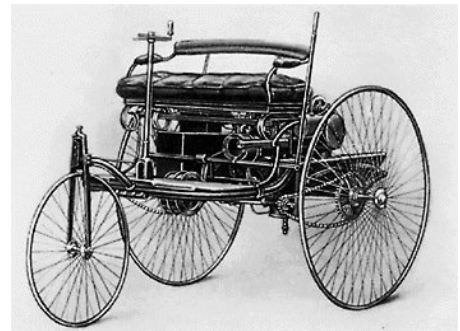


Figure IX-16: Benz Motorwagen (1885)

1890 Wilhelm Maybach (February 9, 1846 – December 29, 1929) built the first four-cylinder, four-stroke engine.

1898 Gaston de Chasseloup-Laubat established the first documented speed record (63.14 km/h) in a car with an electric motor.

1892 Rudolf Diesel (March 18, 1858 – September 30, 1913) filed for a patent at the Imperial Patent Office in Germany. Within a year, he was granted Patent No. 67207 for a "Working Method and Design for Combustion Engines", a new efficient, thermal engine. 1897 he built the first Diesel engine.



Figure IX-17: Wilhelm Maybach (1846 – 1929)

1896 Karl Benz invented the boxer engine, also known as the horizontally opposed engine, in which the corresponding pistons reach top dead centre at the same time, thus balancing each other in momentum.

1900 Rudolf Diesel demonstrated the Diesel engine in the 1900 Exposition Universelle (World's Fair) using peanut oil (bio-diesel).

1900 On April 2, 1900, Emil Jellinek orders a new car as the successor of the 'Phönix' racing car from the Daimler-Motoren-Gesellschaft. Hence, Wilhelm Maybach developed the Mercedes 35 PS (Simplex, cf. Figure IX-19) und delivers it to Jellinek on Dezember 22.

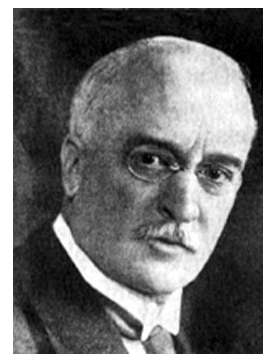


Figure IX-18: Rudolf Diesel (1858 – 1913)

1901 Fredrick Lanchester receives a patent on the disc brake. The first mass-produced car with a disk brake was the Citroën DS in 1955.

1913 Henry Ford (July 30, 1863 – April 7, 1947), founder of the Ford Motor Company, invented the assembly line used for the mass production of large numbers of inexpensive automobiles. His introduction of the Model T automobile revolutionized transportation.



Figure IX-19: Mercedes Simplex (1906)

1914 The first hydraulic brake system is commercialized.

1933 Rotary engines were developed. The most famous one was built in 1957: the Wankel rotary engine.

1940 Automatic transmission was introduced.

1952 Cars with power steering are mass produced.

1954 The first gasoline direct injection engine was employed in the Mercedes 300 SL (cf. Figure IX-20).

1967 Electronic direct injection was developed.

1974 General Motors developed catalytic converters for gasoline engines.

1975 The antilock brake system (ABS) was launched.

1980 Cars with airbag were produced.

1990 Catalytic converters for Diesel engines were developed.

1995 Electronic stability control (ESP) was introduced.

1998 Hybrid vehicles using an on-board rechargeable energy storage system (RESS) and a fueled propulsion power source for vehicle propulsion are mass produced. 'Hybrid vehicle' most commonly refers to petroleum-electric hybrid vehicles, also called hybrid-electric vehicle (HEV) which use internal combustion engines and electric motors.

5.2 History of commercial spark-ignition direct-injection (SIDI) engines

The 1955 Mercedes-Benz 300SL, the first gasoline-powered automobile to use fuel injection, used direct injection. The Bosch fuel injectors were placed into the bores on the cylinder wall used by the spark plugs in other Mercedes-Benz six-cylinder engines (the spark plugs were relocated to the cylinder head). Later, more mainstream applications of fuel injection favoured less expensive indirect injection methods.



Figure IX-20: Mercedes-Benz 300SL Gullwing Coupe (1955)

It was not until 1996 that gasoline direct injection (GDI) reappeared on the market. Mitsubishi Motors was the first with a GDI engine in Japan, the Galant/Legnum's 4G93, which it brought to Europe in 1998. Mitsubishi applied this technology widely, producing over 400,000 GDI engines in four families before 1999, but high-sulphur fuel led to emissions problems, and fuel efficiency was less than expected. PSA Peugeot Citroën also launched a GDI engine (with licensed Mitsubishi technology) in 1999, but both were withdrawn from the market in 2001. DaimlerChrysler produced a special engine for 2000, offered only in markets with low sulphur fuel.

Later GDI engines have been tuned and marketed for their high performance. Volkswagen/Audi led the trend with their 2001 GDI engine, under the product name Fuel Stratified Injection (FSI). The technology, adapted from Audi's Le Mans race cars, induces an electric charge in the fuel-air mixture.

BMW followed with a GDI V12. This initial BMW system used low-pressure injectors and could not enter lean-burn mode, but the company introduced its second-generation High Precision Injection system on the R6 straight-6 in 2006. This system surpasses many others with a wider envelope of lean-burn time, increasing overall efficiency.

General Motors had planned to produce a full range of GDI engines by 2002, but so far only two such engines have been introduced - in 2004, a version of the 2.2 L Ecotec used by the Opel Vectra and in 2005, a 2.0 L Ecotec with VVT technology for the Pontiac Solstice GXP.

In 2004 Isuzu Motors produced the first GDI engine sold in a mainstream vehicle. Standard on the 2004 Axiom and optional on the 2004 Rodeo. Isuzu claimed the benefit of GDI is that the vaporizing fuel has a cooling effect, allowing a higher compression ratio (10.3 to 1 versus 9.1 to 1) that boosts output by 20 horsepower.

Toyota's 2GR-FSE V6 uses a combination of direct and indirect injection. Two injectors per cylinder are employed, a traditional port injector and a new direct injector.

Mazda uses their own version of direct injection in the new Mazdaspeed 6 / Mazda 6 MPS. It is referred to as Direct Injection Spark Ignition.

X ACKNOWLEDGEMENTS

Danken möchte ich Herrn Prof. Dr. Jürgen Wolfrum für die Aufnahme in seinen Arbeitskreis, die Vergabe des Themas für die vorliegende Arbeit und die Bereitstellung der ausgezeichneten Infrastruktur.

Vielen Dank an Herrn Prof. Dr. Christof Schulz für die hervorragende Betreuung, die vielen hilfreichen Tipps während der Durchführung dieser Arbeit und die Anregungen und wertvollen Ratschläge bei ihrer Durchsicht.

Danke auch an meine Arbeitsgruppe am Physikalisch Chemischen Institut (PCI) und an den „Mensa-Club“ für viele lebendige Diskussionen und Hilfe bei kleinen und größeren Problemen. Besonderen Dank an Wieland Koban, Isabell Düwel und Max Hofmann.

Außerdem möchte ich mich bei Herrn Gerhard Schodt und den Mitarbeitern der feinmechanischen Werkstatt des PCI bedanken, ohne deren Hilfe wichtige Teile dieser Arbeit nicht möglich gewesen wären.

Ein Dankeschön geht an die Mitarbeiter des Instituts für Verbrennung und Gasdynamik (IVG) in Duisburg für ihre Hilfe beim schnellen Aufbau der Experimente dort. Vor allem möchte ich mich bei Burkhard Lewerich und Kemal Omerbegovic für ihre tatkräftige Unterstützung im Labor bedanken.

Weiterhin danke ich meinen Projektpartnern René Reichle und Christof Pruss vom Institut für Technische Optik (ITO) in Stuttgart für die gute und gelungene Zusammenarbeit.

Mein Dank für die Finanzierung dieser Arbeit geht an Photonics BW e.V. und die Landesstiftung Baden-Württemberg.

Many thanks to Dr. Mike Drake and Dr. Todd Fansler (General Motors, Detroit, MI) for constant support during my internship at GM and the good cooperation then and later on. It has always been a pleasure to work with you!

Vielen Dank auch an Dr. Jürgen Fischer (damals: Institut für Kolbenmaschinen, IfKM Karlsruhe; jetzt: BMW) für die erfolgreiche Zusammenarbeit.

Last but not least: Vielen Dank, meinen Eltern, meiner Freundin Kaja und allen, die hinter mir standen!

Ich versichere, dass ich diese Arbeit selbständig verfasst und keine anderen als die angegebenen Quellen und Hilfsmittel benutzt habe.

Heidelberg, den 26. September 2006

.....

(Frank Zimmermann)